A comparison study of numerical modeling approaches for simulating the in-plane seismic response of masonry walls

COMPARING UNREINFORCED MASONRY WALLS WITH MASONRY WALLS RETROFITTED WITH THE BED-JOINT REINFORCEMENT TECHNIQUE

Ka Ho Lee

TUDelft
Delft
University of
Technology

A comparison study of numerical modeling approaches for simulating the in-plane seismic response of masonry walls

COMPARING UNREINFORCED MASONRY WALLS WITH MASONRY WALLS RETROFITTED WITH THE BED-JOINT REINFORCEMENT TECHNIQUE

By

Ka Ho Lee

in partial fulfilment of the requirements for the degree of

Master of Science

in Civil Engineering

at the Delft University of Technology,

to be defended publicly on Wednesday April 13, 2022 at 14:00 PM

Student number:	4229436	
Thesis committee:	Prof.dr.ir. J.G. Rots,	TU Delft, chairman
	Dr. A.A. Mehrotra,	TU Delft, daily supervisor
	Dr. R. Esposito,	TU Delft, supervisor
	Dr.ir. G.J.P. Ravenshorst,	TU Delft, supervisor

An electronic version of this thesis is available at http://repository.tudelft.nl/.

Abstract

The extraction of natural gas in the northern part of the Netherlands, from the region of Groningen, has been causing human-induced seismic activities for the past several decades. This is a problem since the existing building stock in this region, which consists of mainly unreinforced masonry buildings and historical structures, are not designed to withstand seismic events due to the lack of empirical earthquake-resistant design features. Further, the combination of a soft topsoil and the gas extraction, is responsible for ground settlements which may compromise the capacity of the existing buildings.

The bed-joint reinforcement technique is a strengthening method which consists of cutting a slot in the bed-joints and installing steel bars embedded in a high-strength repair mortar. Although this strengthening method is commonly applied in the Netherlands to counteract settlement damage, limited investigations on the performance against seismic loading are available in the literature. Therefore, an experimental campaign (Licciardello et al., 2021) was conducted at Delft University of Technology in which a quasi-static cyclic in-plane test on a full scale wall was performed to characterize the performance of the bed-joint reinforcement technique. The wall featured artificially introduced cracks (pre-damage), achieved by the inclusion of plastic sheets between bricks and mortar, to account for the settlement-induced damage. Compared to the un-strengthened walls, tested in a previous experimental campaign (Korswagen et al., 2019) under similar conditions, it is observed that the bed-joint reinforcement technique can provide a significant increment in terms of displacement capacity and ductility of the wall but not in terms of the force capacity.

In this thesis, numerical simulations of both un-strengthened and strengthened walls from the experiments were performed using 2D-models and the nonlinear static analyses (monotonic and cyclic) were carried out in the finite element software DIANA. The objective of this research was to compare different numerical modeling approaches and material models to find the best suited one for simulating the in-plane seismic response of both un-strengthened and strengthened masonry walls. Moreover, the objective was also to extrapolate the experimental results to other wall configurations, which are not experimentally tested, to investigate the combined effect of the bed-joint reinforcement technique and the change in size and location of the window opening on the in-plane response of the wall (parametric study).

In the scope of this thesis, three numerical modeling approaches were investigated (*Figure i*). The bricks and mortar joints are modeled as one homogeneous continuum in the *macro-model*. On the other hand, the bricks and mortar joints are modeled separately for the *continuous* and *detailed micro-model* where interface elements are included at the brick-mortar bonds for the latter one. The *discrete (simplified) micro-model* was not investigated because the reinforcement bars cannot be connected to the mortar joints since they are substituted by zero-thickness interface elements. Moreover, the *Discrete modeling* approach of the reinforcement was used in order to simulate the pull out behavior of the bars. Cracks were modeled using the *discrete cracking approach* and the *smeared cracking approach* where the former one was used at the brick-mortar interfaces and the latter one was used for cracking in the mortar joints (micro-models) and in the masonry composite (macro-model).

The results of the numerical analyses showed that all modeling approaches are able to simulate the main cracks at the main locations for the un-strengthened wall, except for the detailed micro-model using the *Combined Cracking-Shearing-Crushing* material model for the brick-mortar joint interface elements in cyclic analyses. This is due to elastic unloading in tension which results in overly stiff cracks. On the other hand, only the continuous micro-model is best suited to simulate the strengthened wall because the detailed micro-model is not able to capture the behavior of the reinforcements due to the fact that cracks mainly occur in the form of

opening of the brick-mortar joint interfaces. Pre-damage cannot be accurately included in the macro-model. In terms of the constitutive models, the *Total Strain Crack model* is an isotropic material model which is able to capture the crack pattern accurately but is not able to capture the hysteretic behavior in cyclic analyses due to secant unloading. The *Engineering Masonry model* is an orthotropic material model which is able to capture the hysteretic behavior in cyclic analyses due to elastic unloading. However, when applying this material model to the mortar joints in an isotropic way in the continuous micro-model, mainly horizontal cracks are simulated. This is due to the fact that the *Engineering Masonry model* was mainly developed to simulate masonry as a composite material. The bricks were assumed linear elastic in the micro-models since the mortar joints and the bond between the bricks and mortar joints usually are the weakest link in masonry and also to have more efficient analyses since it reduces the computational time significantly.

The numerical results of the parametric study showed that as the opening size increases the in-plane capacity reduces. Moreover, as the opening is moved closer to the toe-side of the wall, the in-plane capacity also decreases. The rate of reduction of the force capacity, due to the location change of the window opening varies differently for different opening sizes. Furthermore, the effect of the bed-joint reinforcement technique on the force capacity becomes less noticeable as the window opening gets bigger. The increment in force capacity, due to the bed-joint reinforcement technique, is relatively larger when the window opening is located close to the middle of the wall.

One important aspect which was not numerically investigated in this thesis research, is the prediction of the ultimate displacement for the parametric study. The same prescribed displacement was used for both un-strengthened and strengthened configurations in order to compare the crack pattern and the increment in force capacity. However, a stopping criteria such as a reduction of 20% of the maximum force capacity is recommended to use for further research. Furthermore, the bricks are kept linear elastic for the micro-models in this research. The compressive stresses in the bricks, at the bottom right corner of the wall, were lower compared to the compressive strength of bricks but larger compared to masonry as a composite material. A new research question could hereby formed whether the continuous micro-model is stronger than the macro-model in terms of compression due to the difference in material properties (composite material vs individual structural component).
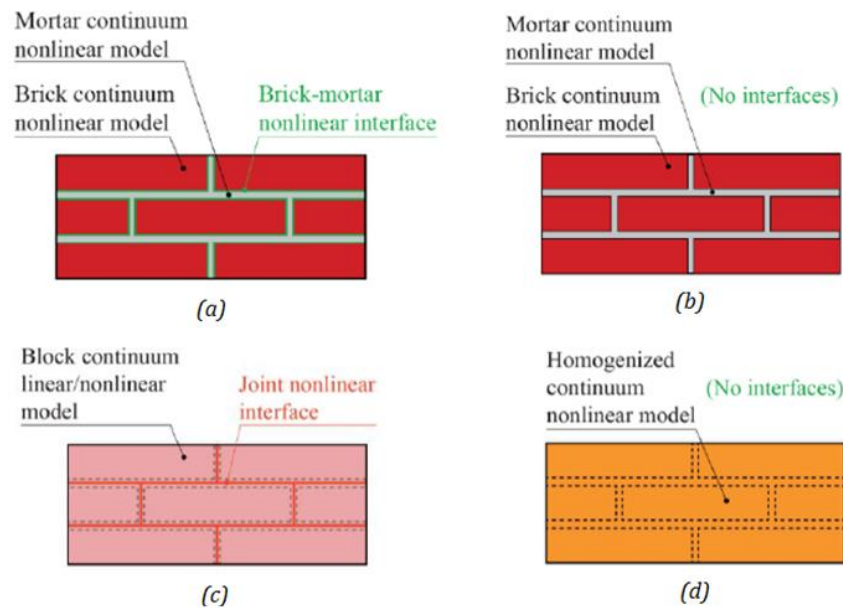

Figure i: (a) Detailed micro-model; (b) continuous micro-model; (c) discrete/simplified micro-model; (d) macro-model (D'Altri et al., 2018)

Acknowledgement

This thesis is written to conclude my Master of Science degree in Structural Engineering at the faculty Civil Engineering and Geosciences at Delft University of Technology. I would like to take this opportunity to express my gratitude to everyone who has supported me during this period.

I would first like to thank my daily supervisor, Dr. Anjali Mehrotra, for her patient guidance during the entire course of my thesis. Thank you for always being available and providing me with constant feedback and encouragement. The meetings with you provided me invaluable support during the challenging months of my thesis. I would also like to thank, Prof. dr. ir. Jan Rots, for helping me to find this interesting and great research topic. Your expertise on the field of masonry and the numerical modeling was invaluable and helped me deepen my understanding of the topic. I would also like to thank, Dr. Rita Esposito, for sharing her valuable knowledge and expertise with me regarding the experiments. Thank you for always providing me with constructive feedbacks on my report and also during the committee meetings. I would also like to thank, Dr. ir. Geert Ravenshorst, for his valuable feedbacks during the committee meetings that pushed me to sharpen my thinking. I am also grateful for the support from Anastasios Drougkas, Langzi Chang and Francesco Messali, thank you for your insight regarding different aspects of the numerical modeling.

Lastly, I would like to thank my parents and my friends for always supporting me and given me encouragement throughout my study.

Ka Ho Lee
Amsterdam, April 2022

Contents

List of Figures

List of Tables

1

INTRODUCTION

1.1 Background information

The extraction of natural gas in the northern part of the Netherlands, from the region of Groningen, has been causing human-induced seismic activities for the past several decades. The Groningen gas field was first discovered in 1959. Since the start of the production in 1963 it has produced over 2,000 billion m^3 of natural gas (Green et al., 2020). The first seismic event linked to the gas production occurred on 4 December 1995 with a magnitude of 2.4 on the Richter scale (NLOG, 2016). The strongest induced earthquake to date occurred near Huizinge on 16 August 2012 with a magnitude of 3.6 on the Richter scale (NAM, 2013).
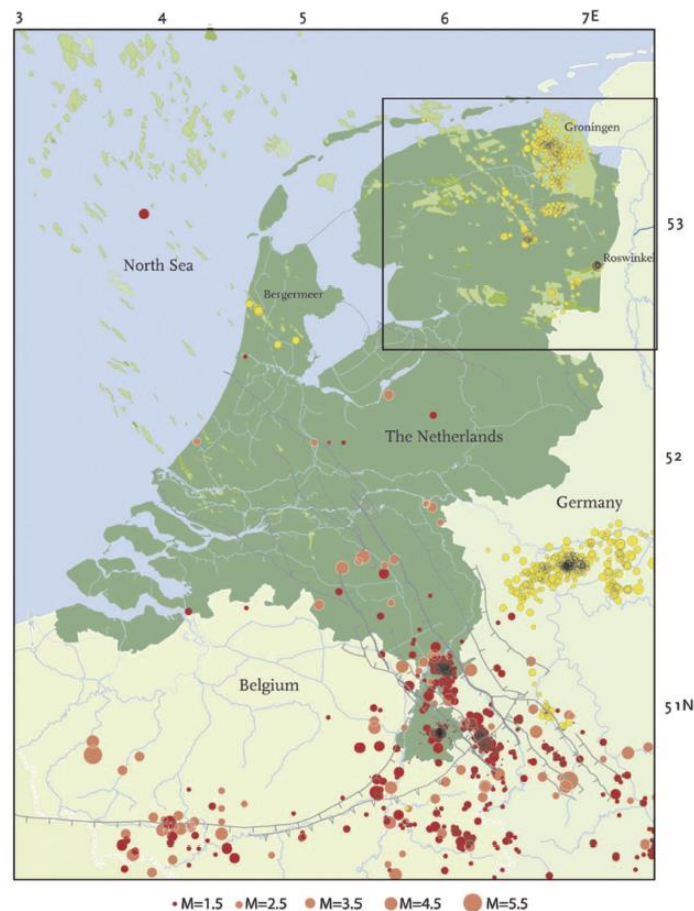
Figure 1.1: General overview of natural tectonic earthquakes (red) and human-induced earthquakes (yellow) (Green et al., 2020)

A general overview of seismic events in the Netherlands is depicted in *Figure 1.1* in which the red circles are indicating the natural tectonic earthquakes, whereas the yellow circles are indicating the human-induced earthquakes. The number of seismic events occurring within the Groningen gas field as function of magnitude and time is illustrated in *Figure 1.2*.
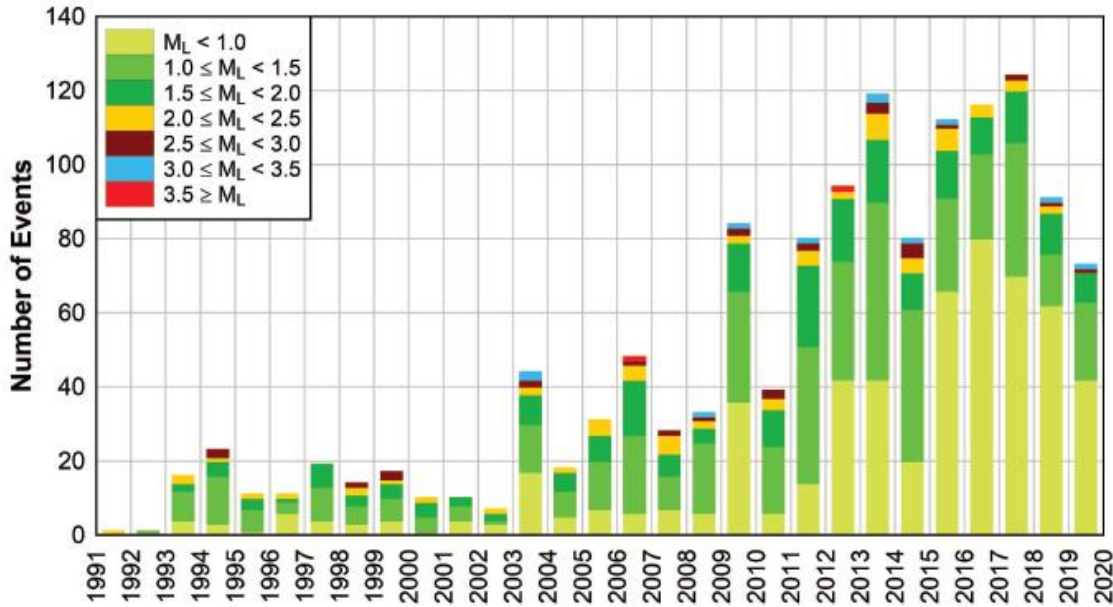
Figure 1.2: Number of seismic events as function of time and magnitude (Green et al., 2020)

In addition, the soil of Groningen varies locally with different layers of peat, clay and sand (Korswagen et al., 2019). The combination of the soft top soil and the extraction of gas are causing ground settlements, which raises the interaction of damage forming in masonry buildings due to seismic activities. Wide-spread damage to existing structures in the region of Groningen have been observed which are the result of the combination of these extensive gas extraction operations, soft top soil, historic lack of naturally occurring seismic activities and the large number of unreinforced masonry (URM) buildings (about 77% of the buildings stock, including aged and historical constructions according to Rots et al., (2016)). These building structures are constructed without empirical earthquake-resistant design features typically encountered in seismic countries. Residential terraced houses are commonly found in the building stock of Groningen. These URM buildings have a large amount of openings and the walls are extremely slender *(Figure 1.3)*.

Figure 1.3: Typical Dutch terraced houses (Esposito et al., 2019)

1.2 Context of present study

Following the strongest seismic event in Huizinge, the Nederlandse Aardolie Maatschappij (NAM), a joint venture between Shell and Exxon Mobil, and the Dutch government initiated an extensive research program to get a better understanding of the seismic events. A large number of experimental and numerical campaigns have been carried out at Delft University of Technology in which the in-plane loading of URM walls has been researched extensively. One field of the experiments is focused on the application and assessment of a retrofitting technique, namely the bed-joint reinforcement (funded by the Rijksdienst voor het cultureel Erfgoed (RCE) according to Licciardello et al., 2021). This retrofitting technique is commonly applied in URM structures in the Netherlands to prevent/ repair vertical cracks which are caused by ground settlements (Drougkas et al., 2020). The application of this strengthening technique consists of cutting a groove in the bed-joints and installing steel bars embedded in a high-strength repair mortar. Subsequently, a second layer of repair mortar is injected in the grooves ensuring a full coverage. The application procedure of this retrofitting technique is illustrated in *Figure 1.4*. The bars are typically mounted near the surface of the masonry, in a one- or two-sided configuration (Drougkas et al., 2020).

This thesis research will be focusing on addressing the following research gap:

> *Although the bed-joint reinforcement technique has been widely applied in practice for damaged masonry walls due to ground settlements, there is a lack of extensive and systematic research on the application of this intervention technique for damage due to seismic activities.*

Figure 1.4: Application procedure bed-joint reinforced repointing (Corradi et al., 2020)

As mentioned before, numerical campaigns have been carried out alongside with the experiments. Numerical modeling is not only an important aspect for the evaluation and verification of the experimentally-obtained results, but also for the extrapolation of results to other configurations than what is possible to test in the laboratory. Moreover, numerical investigations are helpful to assist the interpretation of the experimental results. A wide range of Finite Element modeling approaches are herein available to model masonry where each one of them are distinguished from another by its specific strength and the preferred range of applications. The choice for using one model over the other depends on finding the right balance between the desired level of accuracy in results and the associated computational expenses. The applied models in this study are the *macro-model*, *continuous micro-model* and the *detailed micro-model*. These models are discussed in more detail in Section 1.5.

1.3 Objective and scope of research

The scope of this MSc thesis research is the numerical modeling of the masonry wall retrofitted with the bed-joint reinforcement technique, from the experiment by Licciardello et al., (2021) and the experimentally tested URM wall by Korswagen et al., (2019). A quasi-static cyclic in-plane test, up to the Near Collapse state (refers to the state where a structure has sustained heavy damage, close to structural collapse), was conducted for both walls from both papers. Considering the wall specimens from the experiment by Licciardello et al., (2021), prior to the installation of the strengthening measure, the un-strengthened wall was tested under similar conditions to simulate the behavior in the Damage Limitation state (refers to the state where a structure has sustained visible, light but repairable damage). The un-strengthened walls from both papers have the same geometry, material properties, loading and boundary conditions. The focus of this research is on the in-plane seismic behavior of both un-strengthened and strengthened masonry walls. The results are discussed by interpreting the capacity curves, crack patterns and failure mechanisms. The behavior of the reinforcements in the strengthened wall is evaluated based on the amount of slip and the potential of yielding in the bars. Moreover, this research is focused on the numerical approach of the Finite Element Method (FEM) for which the analyses are conducted in the commercial software DIANA FEA version 10.4.

The objectives of this research are summarized as follows:

- *Create accurate and valid finite element models of the experimentally tested un-strengthened wall by Korswagen et al., (2019) and strengthened wall by Licciardello et al., (2021) to investigate the effect of the bed-joint reinforcement technique*

- *Performing sensitivity analyses to investigate the influence of different numerical settings and input parameters on the in-plane seismic behavior of the experimentally tested wall*

- *Performing a parametric study to investigate the influence of the opening size and location on the in-plane seismic behavior of both URM walls and masonry walls retrofitted with the bed-joint reinforcement.*

1.4 Research questions

The main research question is formulated as follows:

> *Which modeling approach is best suited for simulating the in-plane seismic behavior of both URM walls and masonry walls retrofitted with the bed-joint reinforcement, and what are the influences on the in-plane response when changing the size and location of the window opening?*

The main research question can be stepwise answered by finding the answers to the following sub-questions:

1) *What is the most suited finite element modeling approach (macro vs continuous micro vs detailed micro) to simulate the in-plane behavior of un-strengthened masonry walls?*

2) *What is the most suited finite element modeling approach (macro vs continuous micro vs detailed micro) to simulate the in-plane behavior of strengthened masonry walls?*

3) What is the effect of changing the size and location of the opening on the in-plane behavior of both un-strengthened and strengthened masonry walls?

1.5   Research method

The numerical modeling can be divided into three main parts. Part 1 is focused on the numerical modeling of the un-strengthened masonry walls, whereas Part 2 is focused on the masonry walls strengthened with the bed-joint reinforcement technique. The numerical models in Part 1 are compared to the experimental results of the un-strengthened wall from the paper by Korswagen et al., (2019). The numerical models of the strengthened walls in Part 2 are compared to the experimental results of the strengthened wall from the paper by Licciardello et al., (2021). Furthermore, Part 3 is focused on the parametric study to investigate the influence of the opening size and location on the in-plane seismic behavior of both un-strengthened and strengthened walls. The three main parts are described in more detail below as follows:

Part 1: numerical modeling of the un-strengthened wall

Several numerical modeling approaches are available to simulate masonry. The different modeling approaches are listed below as follows:

1. *Macro-model*: The masonry bricks and mortar joints are modeled as one homogeneous continuum.

2. *Continuous micro-model*: The masonry bricks and mortar joints are modeled separately.

3. *Discrete (simplified) micro-model:* The masonry bricks are expanded up to half of the thickness of the mortar joints. Consequently, the geometry of the mortar joints are not being modeled directly but instead, represented with zero-thickness interface elements which connect the expanded bricks to each other.

4. *Detailed micro-model*: The masonry bricks and mortar joints are modeled separately, where interface elements are also incorporated at the interfaces between the bricks and the mortar joints.

In the scope of this thesis research, all numerical modeling approaches described above are used, except for the *Discrete (simplified) micro-model*. The reason for this is because the reinforcement bars cannot be connected to the mortar joints since they are represented with zero-thickness interface elements.

The objective is to find the most suited model and compare the differences in accuracy of obtained results with the associated computational expenses. The steps for each modeling approach are the same, namely starting off by doing a monotonic pushover analysis as the base model for the sensitivity analysis. The next step is to use this base model and perform a sensitivity analysis to investigate the influence of different numerical settings and parameters (for example mesh size, load-step size, convergence criteria etc.) on the in-plane response of the masonry walls. Moreover, the objective of the sensitivity analysis is to find the most optimum configuration of numerical parameters, in terms of accurate results (crack pattern and capacity curves) with a reasonable associated computational time, to perform a cyclic pushover analysis. The results of the monotonic and cyclic analysis are compared to each other per modeling approach as well as between the three different modeling approaches. All three modeling approaches are used for the analyses in the Damage Limitation state. Subsequently, the best suited model is chosen and used for the analysis up to the Near Collapse state.

Part 2: numerical modeling of the strengthened wall

The same three modeling approaches are used to simulate the strengthened wall. The most optimum configuration of numerical parameters for each model, which is found with the sensitivity analyses in Part 1, is used for the monotonic analyses for the strengthened walls in the Damage Limitation state. The results of the strengthened walls are compared to the results of the un-strengthened walls from Part 1. Again, the best suited model is chosen and used for the analysis up to the Near Collapse state.

Part 3: parametric study

Part 3 is a parametric study in which different wall-opening configurations are used for both un-strengthened and strengthened walls to investigate the combined effect of the bed-joint reinforcement technique and the change in size and location of the window opening on the in-plane seismic response. One chosen modeling approach, based on the results in Part 1 and 2, is used for the simulations of all configurations.

Three different window opening sizes are investigated in this study:

1. _Group 1_: configurations with the _original_ size window opening (780 x 1510 mm)

2. _Group 2_: configurations with the _medium_ size window opening (1000 x 1930 mm)

3. _Group 3_: configurations with the _large_ size window opening (1660 x 2050 mm)

The original size window opening of Group 1 has the same dimensions as in the experiment. The dimensions of the medium and large size opening are based on measurements which can be found in typical Dutch terraced houses in the region of Groningen (illustrated in the paper by Miglietta et al., (2019)). For all groups, five different opening locations are investigated, resulting in a total of 15 different configurations. For this study, the opening is only moved sideways where the height location is kept the same within each group. The different configurations, in terms of the location of the central point of the opening measured from the left edge of the wall, are indicated with a letter. These five configurations for all groups are:

1. _Configuration A_: central point of the window opening is moved to the left (with respect to the window opening location from the experiment)

2. _Configuration B_: central point of the window opening is the same as the experiment

3. _Configuration C_: central point of the window opening is moved to half the width of the wall

4. _Configuration D_: mirrored version of configuration B

5. _Configuration E_: mirrored version of configuration A

Configurations 1B is essentially the wall from the experiment. In summary, the distance to the central point of the opening is the same for configurations "B", "C" and "D" of each group. This also holds for configuration "A" and "E", except for Group 3 in order to maintain a minimum size for the pier at the toe-side of the wall. The wall-opening dimensions of configuration "B" of each group are illustrated in _Figure 1.5_. The location of the central point of the opening are herein indicated for all configurations for each group.

Group 1: Original size window opening

Central point locations

Group 1 opening diagram:
- Position of Central Point window opening → 1B
- Vertical: 650, 755, 1510, 755, 530, 2690
- Horizontal: 870, 390, 390, 1420, 780, 3070

Group 1 central point locations:
- Position of Central Point window opening
- Points: 1A 1B 1C 1D 1E
- Vertical: 1395, 2690, 1295
- Horizontal: 930, 330, 275, 275, 330, 930, 3070

Group 2: Medium size window opening

Central point locations

Group 2 opening diagram:
- Position of Central Point window opening → 2B
- Vertical: 410, 965, 1930, 965, 350, 2690
- Horizontal: 760, 500, 500, 1310, 1000, 3070

Group 2 central point locations:
- Position of Central Point window opening
- Points: 2A 2B 2C 2D 2E
- Vertical: 1375, 2690, 1315
- Horizontal: 930, 330, 275, 275, 330, 930, 3070

Group 3: Large size window opening

Central point locations

Group 3 opening diagram:
- Position of Central Point window opening → 3B
- Vertical: 350, 1025, 2050, 1025, 290, 2690
- Horizontal: 430, 830, 830, 980, 1660, 3070

Group 3 central point locations:
- Position of Central Point window opening
- Points: 3A 3B 3C 3D 3E
- Vertical: 1375, 2690, 1315
- Horizontal: 1040, 275, 275, 1040, 220, 220, 3070

Figure 1.5: Geometry wall-opening configurations and central point locations of window opening for all 3 window opening sizes

7

1.6   Report outline

The final project outline is illustrated using a flowchart (*Figure 1.6*) in which the approach and the corresponding chapters are summarized.
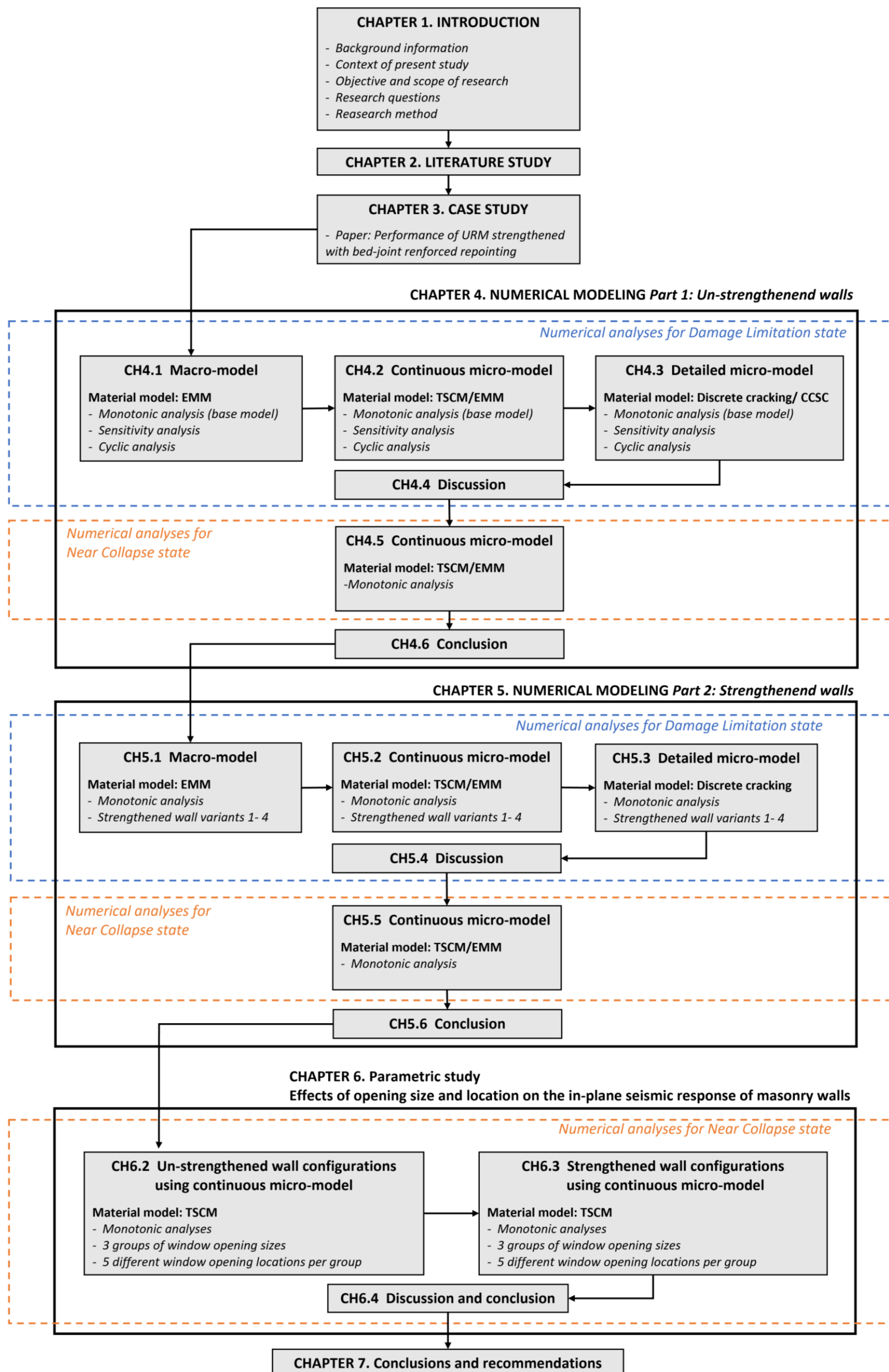
Figure 1.6: Project outline flowchart

2

LITERATURE STUDY

The literature study is conducted in order to obtain a better insight into the general aspects of unreinforced masonry, the bed-joint reinforcement technique, material behaviors, different types of seismic responses and different aspects regarding the numerical modeling. Several references to previously conducted papers are made to determine what is known and available in the literature. The literature study is a first step to determine the knowledge gaps and find the possibilities for new contributing research. Drougkas et al., (2020 & 2020b) performed several numerical investigations using both macro- and continuous micro-model for the simulation of the strengthened full scale wall which was tested at Delft University of Technology (Licciardello et al., 2021). Moreover, Mahmoudimotlagh (2020) conducted a MSc thesis research in which the macro-model was used to investigate the effect of different lay-outs for the bed-joint reinforcement. However, both studies are focused only on the same wall-opening configuration from the experiment. The investigation on different wall-opening configuration is yet to be studied to expand on the observations and results yielded in the previous studies. A parametric study with different configurations can be used for the extrapolation of results to other configurations than what is possible to test in the laboratory. Compared to the previous studies, the detailed micro-model is an additional modeling approach in this research for which the results are compared to the other numerical modeling approaches. Moreover, different material models are used for each modeling approach and compared to each other as well in this research.

2.1   Material properties of masonry

The general aspects of unreinforced masonry and different terminologies regarding masonry construction are discussed in Section 2.1.1. Furthermore, different material behavior of masonry are elaborated in Section 2.1.2.

2.1.1   Material types and masonry terminologies

Unreinforced masonry (URM) is one of the oldest and diverse building material (FEMA, 1998). Different types of masonry material have been applied in practice. Clay-brick masonry, calcium silicate brick masonry, concrete masonry and stone masonry are common types of masonry materials. In the scope of this thesis project, the focus will be on the clay brick masonry which are typically found in the majority of the URM building stocks in the region of Groningen. According to Jafari et al. (2017), the clay brick masonry including solid, perforated and frogged unit can be categorized as the pre-war period (until 1945) and post-war period (after 1945) masonry. The analyzed calcium silicate brick masonry belong to the period before 1985.
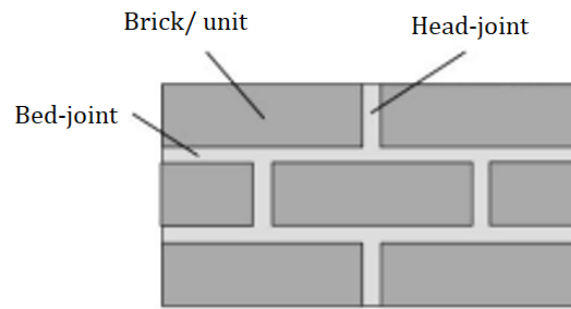
Figure 2.1: Different components of masonry (Campbell & Duran, 2017)

Masonry is an orthotropic material, meaning that the properties are dependent on the direction of loading with respect to the mortar joints. This is due to the arrangement of stacking and placing of the masonry units and binding them with mortar. The mortar joints can be categorized into bed-joints and head-joints *(Figure 2.1)*. Bed-joints are the horizontal joints which are continuous over the width of the wall. On the other hand, head-joints are the vertical joints which can go discontinuous or continuous over the height of the wall depending on the bond pattern. One of the most common bond pattern for the stacking of units is the running bond as depicted in *Figure 2.2*.
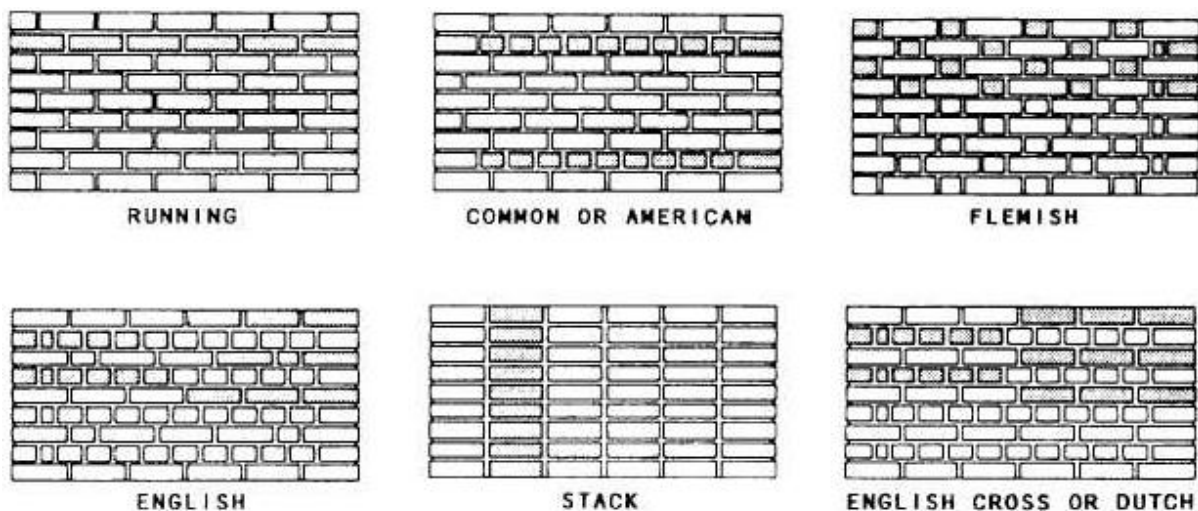
Figure 2.2: Types of masonry bond pattern (Buza, 1993)

The mortar usually consists of Ordinary Portland cement, hydrated lime and fine sand. The final mix proportions in weight may vary. The construction mortar used in the experiment (Licciardello et al., 2021) had a final weight ratio of 1: 2: 9 (cement: lime: sand).

URM buildings in the region of Groningen typically consists of baked-clay bricks which are placed with a running bond pattern and arranged in single- or double- leaf walls. Many of the masonry structures (constructed after 1970) are built with cavity walls consisting of an outer clay-brick façade and an inner calcium-silicate load-bearing wall (Korswagen et al., 2020). Thin steel ties are used to connect the inner and the outer leaf. The cavity can be filled with air or insulation materials. Different types of cross-sectional configurations of masonry walls are illustrated in *Figure 2.3*. A single leaf wall is used for the full scale wall in the experiment and the numerical models in this research.
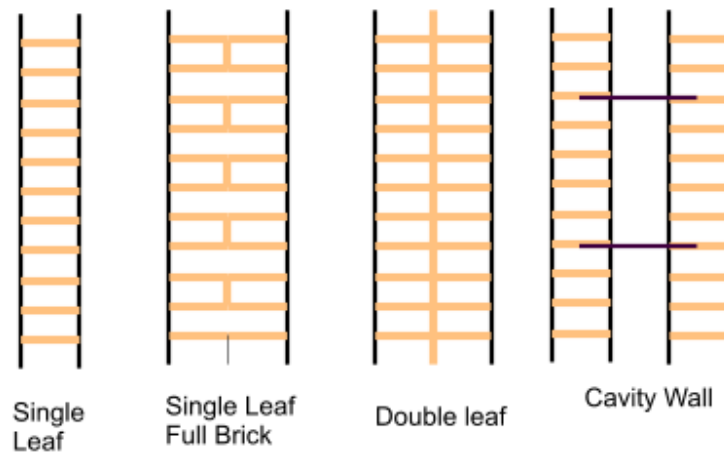
Figure 2.3: Types of masonry walls (Beardmore, 2012)

2.1.2 Material behavior of masonry

Masonry is a quasi-brittle material in uniaxial tension and compression for which the force capacity not immediately drops back to zero, but gradually decreases (Lourenco, 1996). It is characterized by a softening behavior after the peak stress (post-peak stage). Softening is defined as a gradual decrease of mechanical resistance under a continuous increase of deformation forced upon a material specimen or structure (Lourenco, 1996). Quasi-brittle materials fail due to a process of progressive internal crack growth (microcracks). The growth of these microcracks will accelerate after peak stress and develop into unstable macrocracks, meaning that the load has to decrease to avoid uncontrollable crack growth.

The characterization of the material properties is an important aspect for the assessment of seismic behavior of masonry structures. The findings of these material properties can serve as input parameters for numerical and analytical models. According to Jafari et al. (2017) and Esposito et al. (2016), an extensive experimental testing campaign has been carried out at the Delft University of Technology. Destructive laboratory tests have been conducted on samples which were extracted from existing masonry buildings. The objective of these experiments was to provide a database in order to characterize the compression, bending and shear properties of Dutch URM. The determinations for the compression, bending (flexural) and shear properties are elaborated in this section.

Compression properties

The compressive strength can be determined for each constituent material (units and mortar) and for masonry as a composite material.

1. ***Units***: The compressive strength of units can be determined following *EN 772-1:2011*. Due to the restraint effect of the solid platens in the test setup, the obtained compressive strength (in the relevant direction of loading) is multiplied by an appropriate shape/ size factor d of the bricks. This results in a normalized compressive strength of the masonry unit f_b (Lourenco, 1996). An example of a compression test on a masonry unit is depicted in *Figure 2.4*.

Figure 2.4: Compression test on masonry units (Mishra, 2021)

2. **_Mortar_**: The compressive strength of mortar can be determined following *EN 1015-11:1999*. Mortar samples are collected and cast in molds for the test. According to Esposito et al. (2016), the compressive mortar strength f_m can be calculated with *equation (1)*:

$$f_m = \frac{F_{max}}{t_m l_p} \qquad (1)$$

where F_{max} is the maximum load, t_m is the thickness of the mortar specimen and l_p is the length of the loading plate. The test set-up is illustrated in *Figure 2.5*.

Figure 2.5: Compression test mortar (Esposito et al., 2016)

3. **_Masonry composite_**: The compressive strength of masonry as a composite material can be determined following *EN 1052-1:1998*. For the investigation of the orthotropic behavior of masonry, the compression tests can be performed in vertical configuration (loading perpendicular to the bed-joints) and horizontal configuration (loading parallel to the bed-joints). The two configurations are illustrated in *Figure 2.6*.
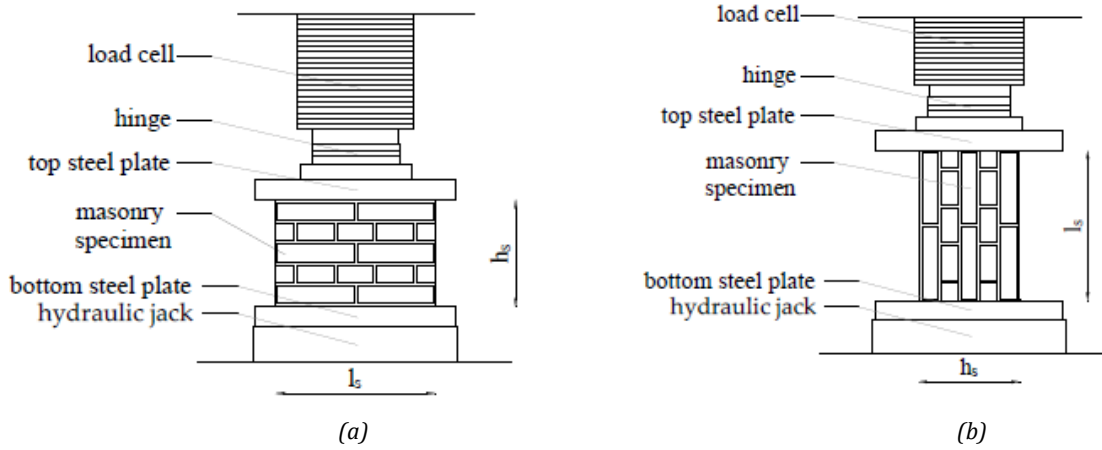
Figure 2.6: Compression test on masonry composite with (a) vertical configuration; (b) horizontal configuration (Esposito et al., 2016)

According to Esposito et al. (2016), the compressive masonry strength for the vertical (f'_m) and horizontal ($f'_{m,h}$) configuration can be determined with *equation (2)* and *equation (3)* based on the assumption that the stress is constant over the cross-section of the specimen:

$$f'_m = \frac{F_{max}}{t_s l_s} \tag{2}$$

$$f'_{m,h} = \frac{F_{max}}{t_s h_s} \tag{3}$$

where F_{max} is the maximum load, t_s, l_s, and h_s are the dimensions of the masonry specimen as built. The force and displacement are measured continuously during the test in order to determine the stress-strain relation. The elastic modulus of masonry E_m can be obtained as the slope of the most linear part of the stress-strain curve.

According to the test results (Esposito et al., 2016), the stress-strain curves for both configurations showed similar trends in the normal direction (parallel to the loading direction). Moreover, the stress-strain relation for calcium silicate masonry was characterized by an initial linear-elastic behavior followed by a nonlinear hardening behavior until the peak. This transition occurred at a stress level of approximately 1/10 of the maximum peak stress. The post-peak was characterized by a linear softening behavior for the vertical configuration, while an exponential trend was observed for the horizontal configuration. The stress-strain relation for the clay masonry showed similar trends as the calcium silicate masonry. The nonlinearity for the vertical configuration started at approximately 1/3 of the maximum peak stress while for the horizontal configuration between 1/10 and 1/3 of the peak stress. An exponential softening behavior was observed for both configuration for the clay masonry. In general, a typical compressive behavior for masonry is depicted in *Figure 2.7*. A relatively large ductility can be observed compared to the typical tensile behavior of masonry (discussed in next section). The compressive fracture energy is defined as the area under the stress-relative displacement curve.
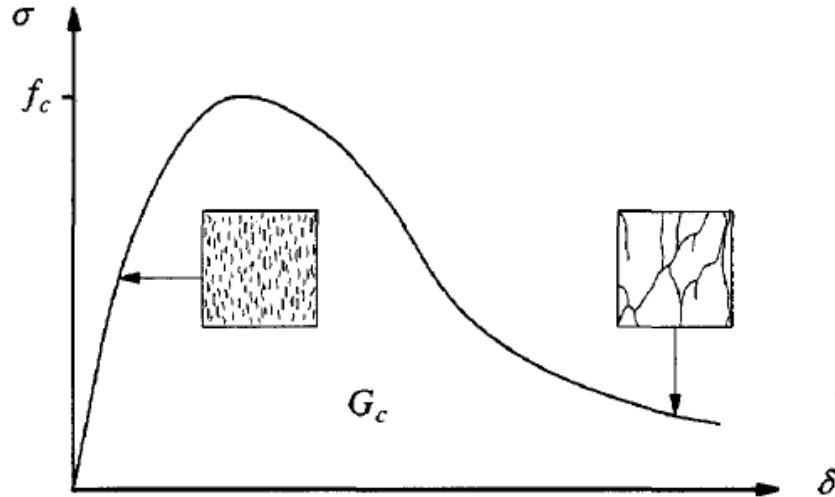
Figure 2.7: General compressive behavior of masonry (Lourenco, 1996)

Bending (flexural) properties

The flexural strength can be determined for each constituent material (units and mortar) and for masonry as a composite material. Moreover, the tensile strength for the interfaces between the units and mortar can also be determined.

1. **_Units_**: The flexural strength of units can be determined following *NEN 6790: 2005* with a three-point bending test (*Figure 2.8*). According to Esposito et al. (2016), the flexural strength of masonry units f_{bt} can be determined with *equation (4)*:

$$f_{bt} = \frac{3\,F_{max}\,d_1}{2\,h_u\,t_u^2} \tag{4}$$

where F_{max} is the maximum load, d_1 is the distance between the supports, h_u is the height of the masonry unit, t_u is the thickness of the masonry unit. Moreover, the elastic modulus E_b of the masonry units can be determined using *equation (5)* with the assumption that the stress distribution over the height of the cross-section is linear:

$$E_b = \frac{F_{el}\,d_1^3}{48\,v_{el}\,I} \tag{5}$$

where F_{el} and v_{el} are the load and vertical deflection in the linear elastic stage, respectively and I is the moment of inertia of the masonry unit along the cross-section, d_1 is the distance between the supports (Esposito et al., 2016).
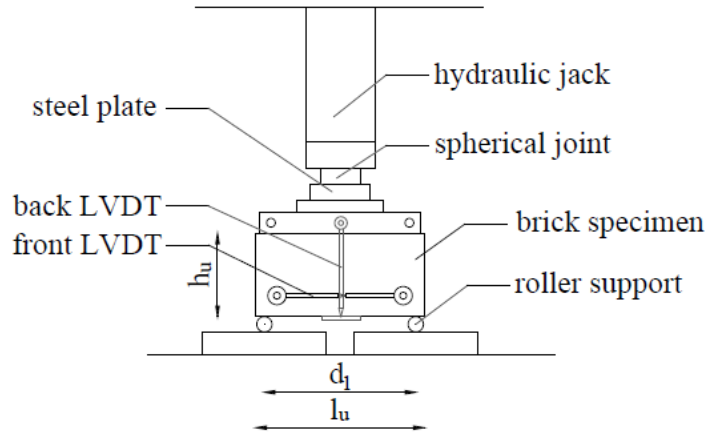
Figure 2.8: Three-point bending test on masonry unit (Esposito et al., 2016)

2. **_Mortar_**: The flexural strength of mortar can be determined following *EN 1015-11:1999* with a three-point bending test *(Figure 2.9)*. According to Esposito et al. (2016), the flexural strength of mortar f_{mt} can be determined with *equation (6)*:

$$f_{mt} = \frac{3 F_{max} d_1}{2 t_m h_m^2} \tag{6}$$

where F_{max} is the maximum load, d_1 is the distance between the supports, t_m is the thickness of the mortar specimen and h_m is the height of the mortar specimen.
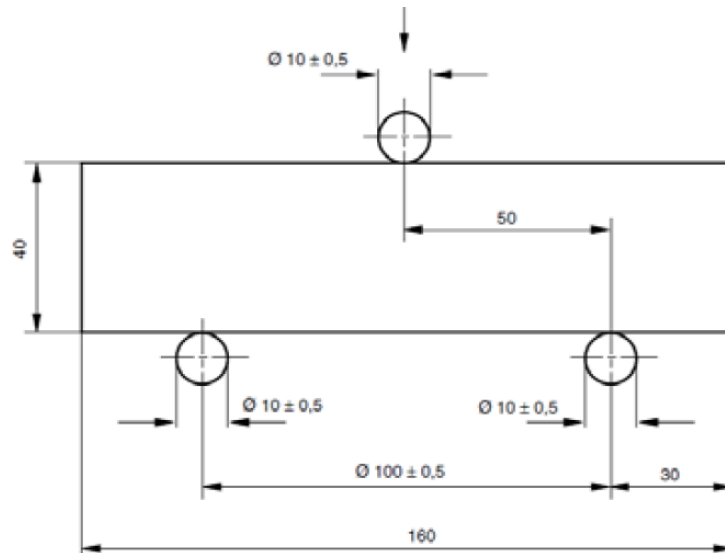
Figure 2.9: Three-point bending test on masonry mortar specimen (Esposito et al., 2016)

3. **_Masonry composite_**: According to Esposito et al. (2016), the flexural strength of masonry can be determined for three different configurations in which the first two were performed following *EN 1052-2:1999*, while the last one was a standarized test:

   a. **_Out-of-plane vertical bending test (OOP1)_**: is a four-point bending test with the moment vector parallel to the bed-joints (*Figure 2.10a*).

16

b. **_Out-of-plane horizontal bending test (OOP2)_**: is a four-point bending test with the moment vector orthogonal to the bed-joints (*Figure 2.10b*).

c. **_In-plane vertical bending test (IP)_**: is a four-point bending test with the moment vector orthogonal to the plane of the wall (*Figure 2.10c*).

(a)   *(b)*   *(c)*
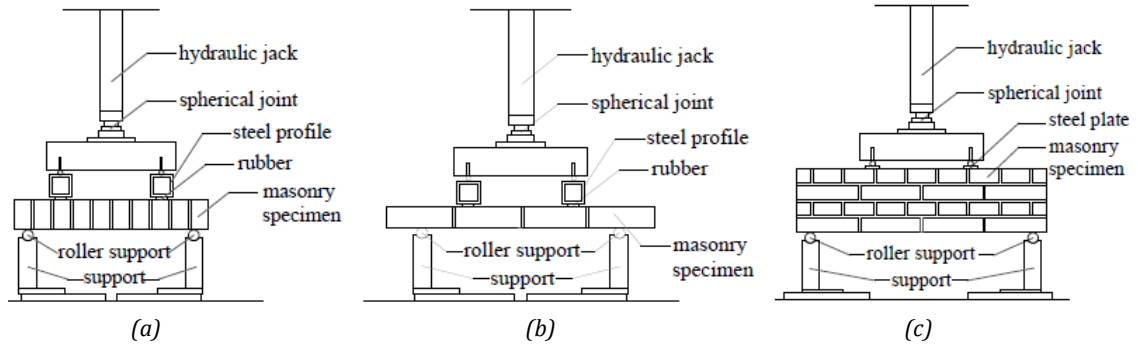
Figure 2.10: Four-point bending test wit (a) OOP1; (b) OOP2; (c) IP (Esposito et al., 2016)

The flexural strength of the masonry f_x can be determined for all configurations with *equation (7)*:

$$f_x = \frac{M_{max}}{W} = \frac{F_{max}\, d_3}{2W} \qquad\qquad (7)$$

where M_{max} is the maximum bending moment, W is the section modulus verified for the different configurations, F_{max} is the maximum load at failure, d_3 is the distance between the loading and the bearing support (Esposito et al., 2016).

According to the experimental results (Esposito et al., 2016), the OOP1 tests for both calcium silicate masonry and clay masonry showed brittle failure in the force-displacement curve where the cracking mostly occurred along one bed-joint in the constant moment zone. On the other hand, step-wise cracking patterns were observed in both bed-and head-joints in the constant moment zone for both materials for OOP2 as well as for IP test. This resulted in a softing behavior at the post-peak stage. Moreover, It has been concluded by Jafari et al. (2017) that the obtained value of the flexural masonry strength is higher in case when the cracks are passing vertically straight through head- and bed-joints and units than when the cracks are only following trough the head- and bed-joints joints as stair-case cracks.

4. **_Unit-mortar interface (Mode-I tensile failure)_**: The bond between the unit and mortar is often considered the weakest link in a masonry assemblage (Lourenco, 1996). The bond strength between masonry units and mortar can be determined following *EN 1052-5:2002* with a bond wrench test *(Figure 2.11)*.
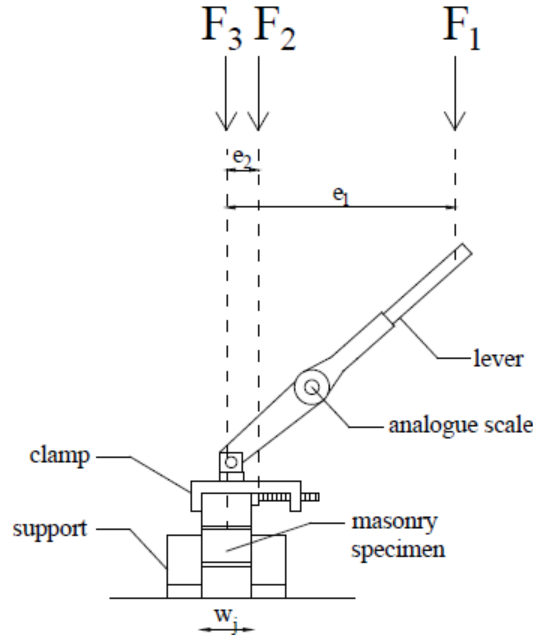
Figure 2.11: Bond wrench test (Esposito et al., 2016)

According to Esposito et al. (2016), the tests are performed for every bed-joint of a stack bonded specimen. The bond wrench strength f_w can be determined with *equation (8)*:

$$f_w = \frac{F_1 e_1 + F_2 e_2 - \frac{2}{3} t_u (F_1 + F_2 + \frac{F_3}{4})}{\frac{l_j w_j^2}{6}} \tag{8}$$

where F_1 is the failure load which is calculated from the lever arm length and the bending moment registered by the bond wrench scale. F_2 is the normal force as a result of the weight of the bond wrench apparatus. F_3 is the weight of the masonry unit pulled off from the specimen, including the weight of adherent mortar. e_1 is the distance from the applied load to the tension face of the specimen, e_2 is the distance from the center of gravity of the clamp to the tension face of the specimen, l_j is the mean length of the bed joint, and w_j is the mean width of the bed joint (Esposito et al., 2016).

The tensile failure in the unit-mortar interfaces is considered as the Mode-I failure. the tensile fracture energy G_f^I is determined as the area under the capacity curve. It is defined as the amount of energy needed to create a unitary area of a crack along the unit-mortar interface (Lourenco, 1996). In general, a typical tensile behavior under a uniaxial loading is illustrated in *Figure 2.12*. A quasi-brittle failure can be observed with softening after the peak load.
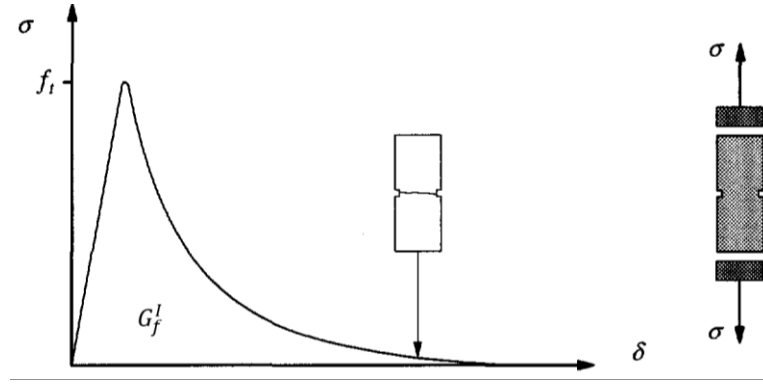
Figure 2.12: Tensile behavior under uniaxial loading (Lourenco, 1996)

Shear properties (Mode-II failure)

According to Esposito et al. (2016), the initial shear properties of unit-mortar interfaces can be determined following *EN 1052-3:2002* in which a displacement control procedure is used rather than a prescribed force control procedure. A triplet shear test as depicted in *Figure 2.13* has been carried out where the tested specimen was kept under constant lateral pre-compression.
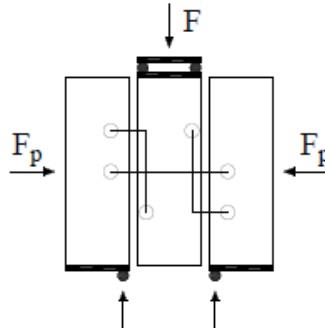
Figure 2.13: Triplet shear test (Esposito et al., 2016)

The shear strength of the interfaces f_v can be determined with *equation (9)*:

$$f_v = \frac{F_{max}}{2\,A_s} \tag{9}$$

where F_{max} is the maximum load, A_s is the cross-sectional area of the specimen parallel to the bed-joint. Moreover, the pre-compression stress f_p can be determined with *equation (10)*:

$$f_p = \frac{F_p}{A_s} \tag{10}$$

where F_p is the pre-compression force. Moreover, the residual shear strength $f_{v,res}$ can be determined because the test was carried out in displacement control. According to Esposito et al. (2016), the residual shear strength occurred at an almost constant load where a plateau of large sliding displacement was observed in which the resistance can be associated to friction only. When plotting the shear strength against the pre-compression stress obtained from equation (9) and (10), respectively, the initial shear properties can be determind with the Coulomb friction formulation in *equation (11)* and *equation (12)*:

$$f_v = f_{v0} + \mu f_p \tag{11}$$

$$f_{v,res} = f_{v0,res} + \mu_{res} f_p \tag{12}$$

Because a linear regression of the data is considered, the initial shear strength f_{v0} can be determined as the intercept with the horizontal axis and the coefficient of friction μ as the slope of the line (Esposito et al., 2016). The residual initial shear strength $f_{v0,res}$ and the residual coefficient of friction μ_{res} can be found in the same way. The graphical representation for the shear behavior of calcium silicate masonry is illustrated in *Figure 2.14*. The shear behaviour of masonry is characterized by a quasi-brittle failure of cohesion and a long plastic plateau (Rots et al., 2016).

(a)   *(b)*
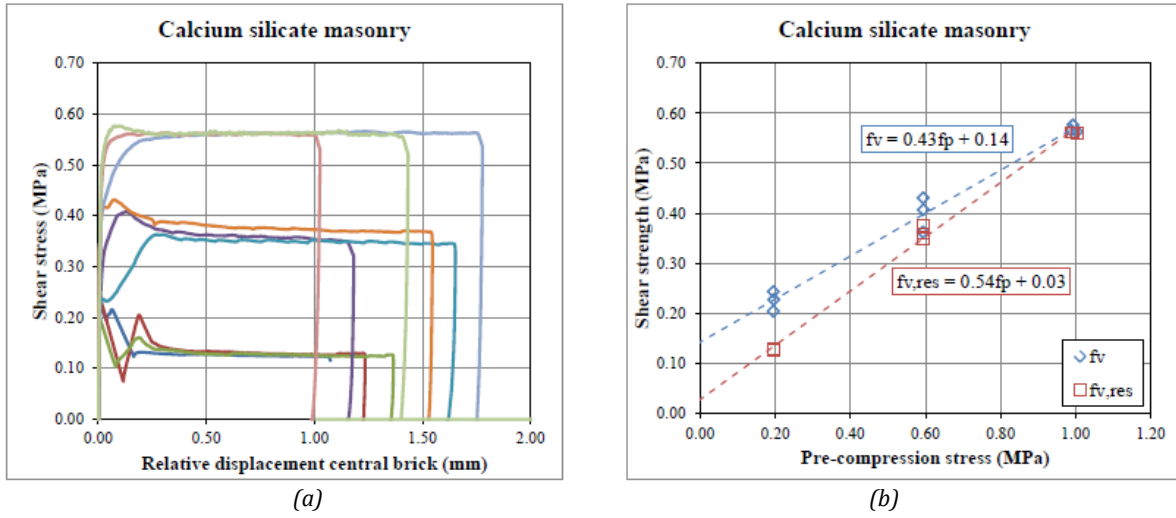
Figure 2.14: Shear behavior calcium silicate masonry wit (a) shear stress vs relative displacement central brick; (b) shear strength vs pre-compression stress (Esposito et al., 2016)

Furthermore, the shear failure in the unit-mortar interfaces is considered as the Mode-II failure for which the shear fracture energy G_f^{II} is defined as the area under the stress- relative displacement curve. In general, a typical behavior of masonry under shear loading is illustrated in *Figure 2.15*.
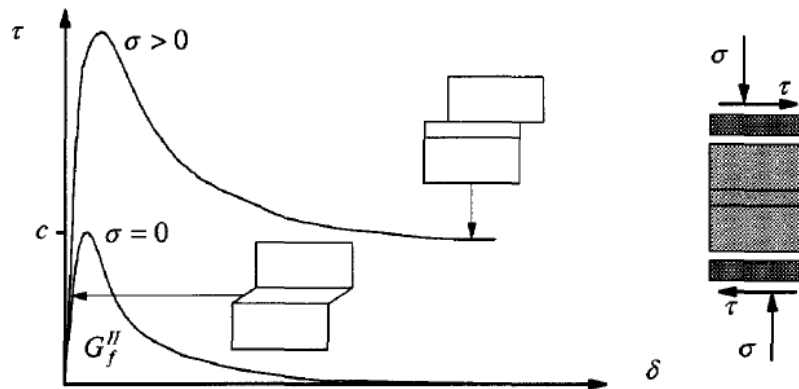
Figure 2.15: Shear behavior of masonry (Lourenco, 1996)

20

2.2 Failure modes of URM walls under seismic loading

Different failure mechanisms may occur when URM walls are subjected to seismic loading. The different types of seismic behavior are introduced in Section 2.2.1. The in-plane seismic responses for solid URM walls without openings are discussed in Section 2.2.2, whereas the perforated URM walls are discussed in Section 2.2.3. Moreover, the out-of-plane seismic responses for URM walls are discussed in Section 2.2.4.

2.2.1 Types of seismic behavior

The box-behavior of a masonry structure is illustrated in *Figure 2.16*. Different types of failure modes can be associated to the in-plane and out-of-plane behavior. The walls perpendicular to the direction of the seismic action are subjected to out-of-plane bending. On the other hand, the walls parallel to the direction of the seismic action are resisting the in-plane seismic actions. The failure modes (overturning) of the walls loaded out-of-plane are prevented by the connected in-plane shear walls. In general, the out-of-plane failure modes are the most vulnerable because they can cause total or partial overturning of the walls (Alejo et al., 2017). Out-of-plane walls are very flexible and weak, whereas the in-plane walls usually are relatively stiff and strong in their plane.
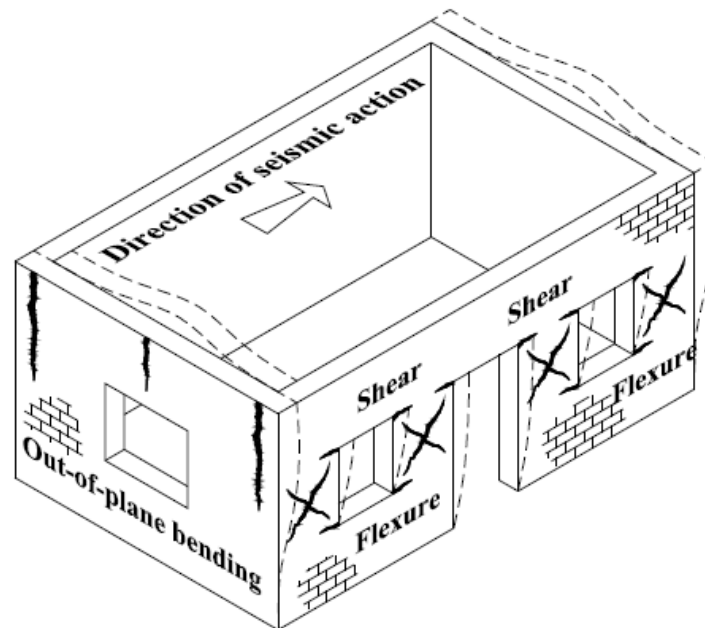
Figure 2.16: Box-behavior of masonry building including out-of-plane and in-plane walls (Alejo et al., 2017)

2.2.2 In-plane seismic behavior of URM walls

The occurrence of different type of failure modes *(Figure 2.17)* is dependent on the following parameters: the geometrical characteristics of the wall (including aspect ratio of units); the mechanical characteristics of the different masonry components (mortar, units and interfaces);

the boundary conditions and the vertical compression load (Calderini et al., 2009). It is often difficult to distinguish the occurrence of specific type of mechanism since sequences and combinations may occur. The classification of observed seismic failure modes for masonry walls loaded in-plane can be divided into two typical types of behaviors which are elaborated below:

1. ***Flexural behavior failure modes***: Due to the lateral loading on the masonry wall, one bottom corner will get lifted up whereas the other corner will get compressed. Two different failure modes are herein involved where the ultimate limit state for both cases is reached by failure at the compressed corner (Calderini et al., 2009):

    a. ***Rocking***: When the vertical applied load is low with respect to the compressive strength of the masonry, the lateral load will cause tensile flexural cracks at the heel of the wall. In this case, the wall starts to behave as a nearly rigid body rotating about the toe. Rocking failure tends to occur in slender walls which is in line with the experimental results (Esposito & Ravenshorst, 2017).

    b. ***Crushing***: Significant flexural cracking will be prevented when the vertical loading is high and close to the compressive strength of the masonry. A wide spread damage pattern consisting of vertical sub-cracks will form towards the compressed corner.

2. ***Shear behavior failure modes***: The sliding failure can be divided into two different failure modes:

    a. ***Bed-joint sliding***: horizontal shear cracks are formed along the horizontal bed-joint plane. This form of sliding shear failure is usually located at the base of the wall. Bed-joint sliding tends to occur only in very squat walls which is in line with the experimental results (Esposito & Ravenshorst, 2017).

    b. ***Diagonal cracking***: A diagonal "stair-stepped" path is formed usually starting from the center of the wall and developing towards the corners. The crack may develop only through head- and bed-joints or also through the bricks. The head-joints open and close to allow for movement (sliding) of the bed-joints (FEMA, 1998). In moderately slender piers, diagonal cracking tends to occur over rocking and bed-joint sliding for increasing levels of vertical compression (Calderini et al., 2009).
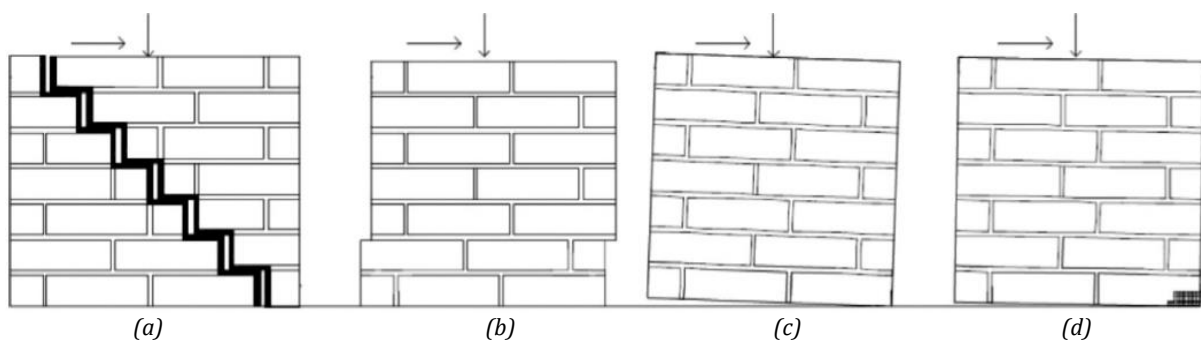
Figure 2.17: In-plane failure modes of URM walls: (a) diagonal cracking; (b) bed-joint sliding; (c) rocking; (d) crushing (Khan et al., 2017)

2.2.3　　　In-plane seismic behavior of perforated URM walls

A masonry wall with openings can be sub-divided into two types of panels. The "piers" are the principal vertical resistant elements for both dead and seismic load. On the other hand, the "spandrels" are the secondary horizontal elements, coupling piers in case of seismic loads (Calderini et al., 2009). According to FEMA, (1998), URM walls are subdivided into different components types for the specification of behavior modes on component level. The components which are relevant for perforated URM walls are illustrated in *Figure 2.18* and listed below:

1. ***Weak piers (type URM2)***: The inelastic deformations are located in the weak piers of a perforated URM wall. The previously mentioned behavior modes for solid URM walls can also be applied on component level for the weak piers.

2. ***Weak Spandrels (type URM3)***: The inelastic deformations are located first in the weak spandrels of a perforated URM wall. This could lead to multistory piers when all the spandrels in a system are failed. Additional failure modes are specified for the component of the weak spandrel:

   a. ***Spandrel Joint Sliding***: is a form of bed-joint sliding which are located at the end of the spandrels. It resembles the pulling apart effect of interlocked fingers which are commonly observed in running bond masonry. The presence of a lintel can allow for large drifts resulting in a relatively ductile failure mode of the spandrel.

   b. ***Spandrel Unit Cracking***: is a type of damage in which the in-plane moment at the end of the spandrel is not relieved by spandrel joint sliding. But instead, brittle vertical cracks are formed through the units which can lead to local falling hazard of spandrels. Consequently, the height of the piers might get altered .

   c. ***Spandrel Diagonal Tension***: is a behavior mode in which diagonal "X" cracks propagate through units without significant ductile response. The combination of strong mortar, weak units and high compressive loading can lead to this failure mode after which the vertical load capacity is quickly dropped.
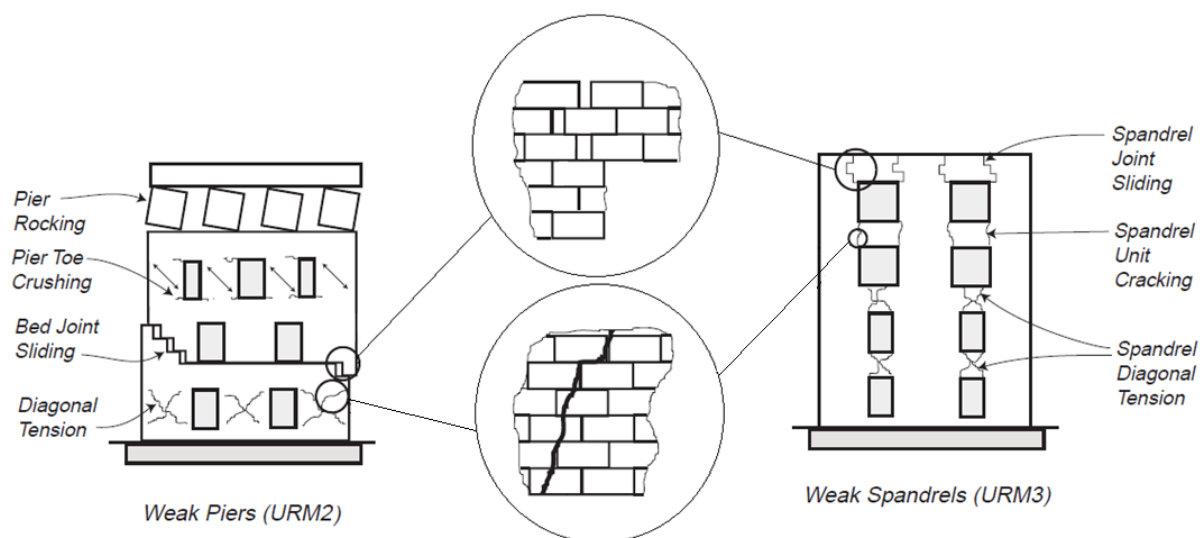
Figure 2.18: Perforated URM wall components and behavior modes (FEMA, 1998)

2.2.4   Out-of-plane seismic behavior of URM walls

The out-of-plane behavior is dependent on the quality and strength of the connections with the other structural elements, such as the internal and external load-bearing walls, floors and roof structures. According to the studies (D'Ayala & Speranza, 2003), it is assumed that the friction of the contact surface is the only governing restraint to overturning of a particular wall in case the structure is not strengthened. One example of strengthening technique is the insertion of metallic ties to anchor the facades to the other connected structural elements. The overturning of external masonry walls commonly occurs involving portions of connected walls. Different overturning failure mechanisms are illustrated in *Figure 2.19*. Moreover, it is assumed that every mechanism can be triggered within the whole façade involving any number of stories.
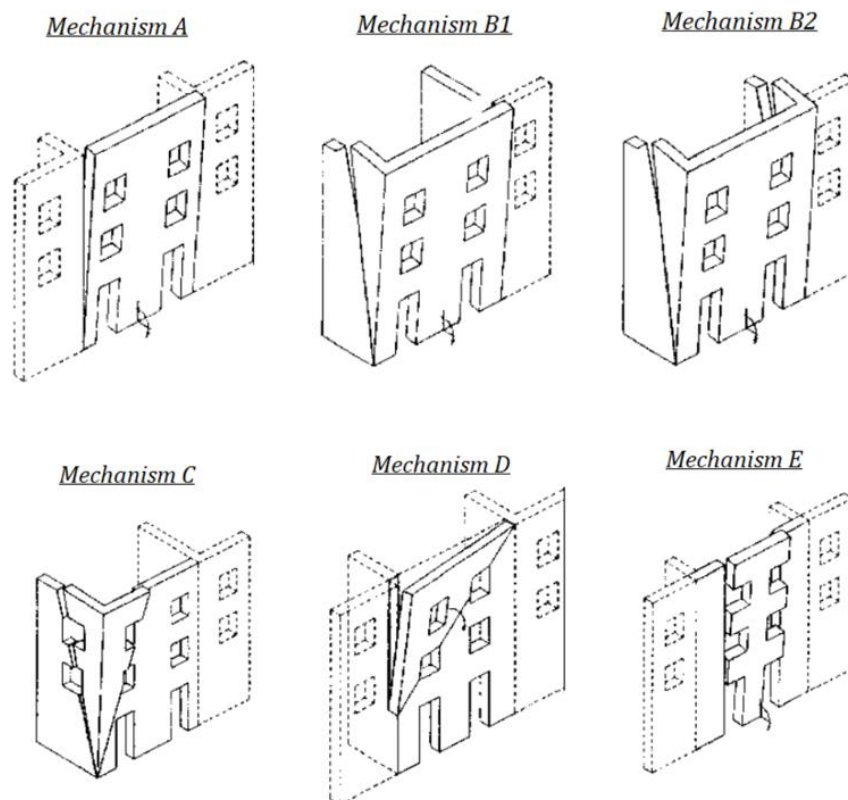
Figure 2.19: Overturning failure mechanisms (D'Ayala & Speranza, 2003)

On the other hand, if the connections with the other structural elements are strong enough, the overturning can be prevented, while out-of-plane failure mechanisms based on the arch effect may develop. Two variants of the arch effect failure mechanism are studied by D'Ayala & Speranza (2003) and also recognized in Eurocode 6 (EN-1996-1-1, 2005):

1. ***Vertical arch mechanism***: is characterized by out-of-plane deflection of vertical strips of the façade. In the analytical model (*Figure 2.20*), the presence of the strengthening ties are simulated by identifying two (hinge) points along the height for which the lateral deflection is constrained. It is assumed that these points are located at the floor and roof levels only. A third hinge will form in between the initial two points along the height of the façade when the failure mechanism is triggered. This is identified by a horizontal crack.
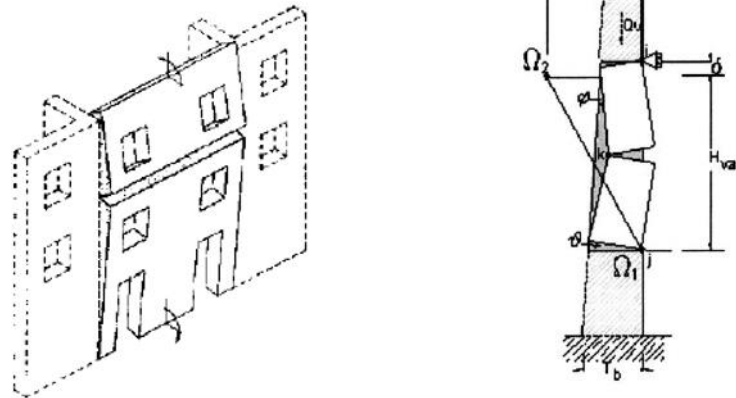
Figure 2.20: Arch effect failure mechanism F with analytical model (D'Ayala & Speranza, 2003)

2. ***Horizontal arch mechanism***: is characterized by a central trapezoidal portion which tends to deflect outwards from the façade plane (*Figure 2.21*). The failure mechanism is triggered by the formation of a imaginary vertical cylindrical hinge along the vertical symmetry of the façade. The horizontal crack at the bottom of the trapezoidal is simulated by two horizontal sliding rollers. Furthermore, both diagonals of the trapezoidal are simulated by cylindrical hinges.
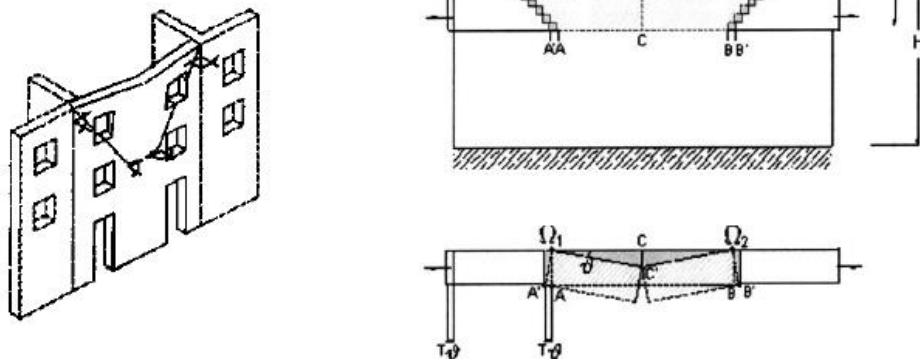
Figure 2.21: Arch effect failure mechanism G with analytical model (D'Ayala & Speranza, 2003)

2.3   Bed-joint reinforcement technique

The bed-joint reinforcement is a strengthening and repair method often applied in the Netherlands to counteract damage caused by ground settlement in URM buildings. This technique is often used to preserve the historical and artistic aspects of cultural heritage buildings, because its application is not invasive and does not influence the aesthetic aspect of the building (Licciardello etal., 2021).

Due to the increase in seismic activities in the region of Groningen (northern part of the Netherlands), triggered by gas extraction, it is of interest to investigate the effectiveness of the bed-joint reinforcement technique against seismic loading. Therefore, an experimental campaign has been conducted at Delft University of Technology to investigate the performance of masonry strengthened with bed-joint reinforcement. See Chapter 3 for the case study on the experiment.

The application of this strengthening technique consists of cutting a groove in the mortar joint and installing reinforcement (twisted steel bars, stainless steel or Fiber-Reinforced Polymer bars) embedded in a high-strength repair mortar (*Figure 2.22*). Subsequently, a second layer of repair mortar is injected in the groove ensuring a full coverage. The bars are typically mounted near the surface of the masonry, in a one- or two-sided configuration (Drougkas et al., 2020).

Figure 2.22: Execution of the bed-joint reinforcement technique (Licciardello etal., 2021)

2.4 Numerical modeling

Numerical analyses are important for the safety assessment of URM structures which are subjected to seismic events. The response and the failure modes observed during earthquakes need to be accordingly simulated. A wide range of models are herein available where each one of them are distinguished from another by its specific strengths and the preferred range of applications. The choice for using one model over the other depends on finding the right balance between the desired level of accuracy in results and the associated computational expenses. Such studies requires pragmatic discretization at the structural scale. The concept for modeling masonry in Finite Element Method is elaborated in Section 2.4.1. The modeling of reinforcement in Finite Element Method is discussed in Section 2.4.2. The implicit solution procedure is discussed in Section 2.4.3. Moreover, the modeling of cracking (discrete and smeared cracking approach) is discussed in Section 2.4.4. Lastly, the constitutive models for simulating the nonlinear material behavior of the construction materials for masonry walls are discussed in Section 2.4.5 for the *Total Strain crack model* and in Section 2.4.6 for the *Engineering Masonry model*.

2.4.1 Modeling masonry in Finite Element Method

In this thesis research, the Finite Element Method (FEM) is used in which the masonry is discretized into a number of finite elements. A suitable constitutive law is adopted after which a nonlinear incremental analysis can be performed. Masonry can be modeled in the FEM on different level of details. The following models are available and illustrated in *Figure 2.23*:

a) **_Detailed micro-model_**: is a discontinuum based model in which the bricks and mortar joints are modeled independently. Continuum elements are used for both units and mortar joints. Interface elements are included at the brick-mortar joint interfaces in which the nonlinearities are localized to allow for possible joint opening and frictional sliding failure. Detailed micro-models represent the material very accurately but is computationally expensive.

b) **_Continuous micro-model_**: is an "adapted" version of the detailed micro-model where the organized and periodic micro-structure of the masonry is kept. Both units and mortar are modeled separately, but the interface elements are left out.

c) **_Discrete micro-model_**: is also called a _Simplified micro-model_ which finds a better balance between the desired level of accuracy and the computational expenses. The masonry bricks are herein expanded up to half of the thickness of the mortar joints. Consequently, the geometry of the mortar joints are not being modeled directly but instead, represented with zero-thickness interface elements which connect the expanded bricks to each other (Pulatsu et al., 2020).

d) **_Macro-model_**: is a continuum based approach in which the masonry is represented by a homogeneous orthotropic continuum where no distinction is made between the units and the mortar. For this reason, the internal structure of the masonry cannot be described explicitly where the damage within the structure is smeared out through the continuous medium (Pulatsu et al., 2020). For this reason, macro-modeling requires much less computational costs and is therefore a efficient and practical option.

In the scope of this thesis research, all numerical modeling approaches described above will be used, except for the _Discrete micro-model_. The reason for this is because the reinforcement bars cannot be connected to the mortar joints since they are represented with zero-thickness interface elements.
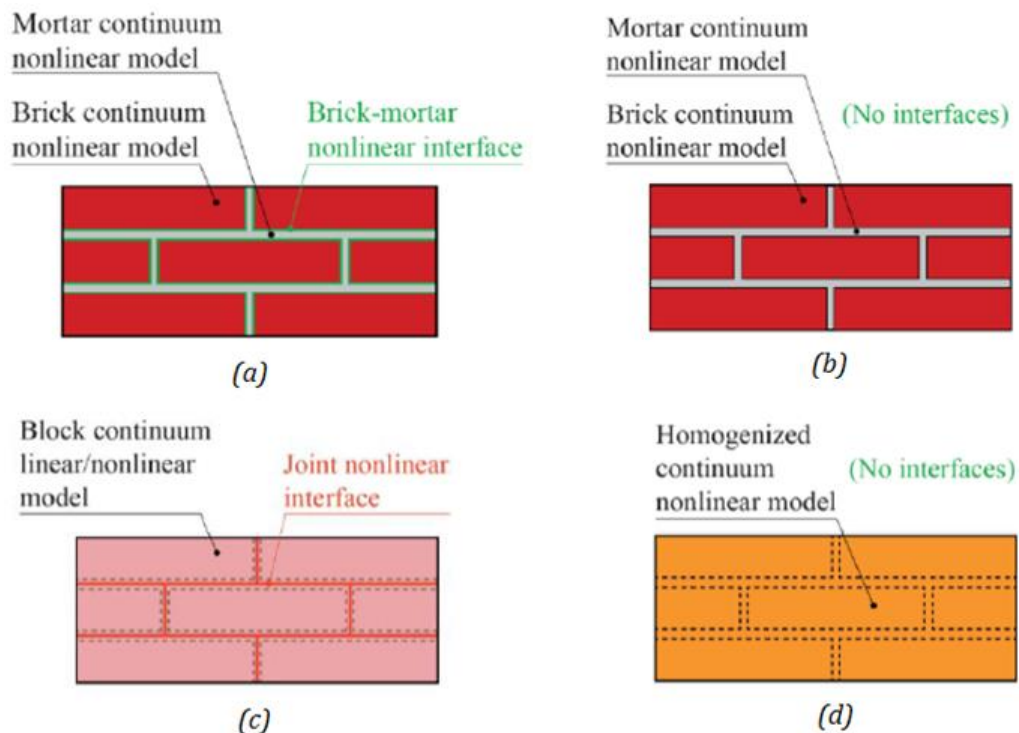
Figure 2.23: (a) Detailed micro-model; (b) continuous micro-model; (c) discrete micro-model; (d) macro-model (D'Altri et al., 2018)

2.4.2   Modeling reinforcement in Finite Element Method

The reinforcement bars which are implemented in the bed joint reinforcement technique can be simulated in the numerical models using two different modeling approaches:

1. ***Discrete modeling***: The reinforcement bars are physically and independently modeled within the model. Truss elements and beam elements can be used to represent the reinforcements. While the former element type only capture the axial behavior, the latter one also accounts for the bending stiffness. Furthermore, the reinforcements are fully bonded to the continuum elements (mortar) because they are sharing the same nodes. For this reason, the freedom in creating the mesh is reduced because the mesh lines do have to coincide with the positions of the reinforcements. On the other hand, the pull-out behavior of the reinforcement bars can be simulated through the introduction of interface elements, assigned with bond-slip behavior, between the truss/beam elements and the mortar continuum.

2. ***Embedded reinforcements***: The reinforcements are embedded in the continuum elements which means that no additional degrees of freedom are added because they do not have nodes of their own. The displacements and strains of the reinforcements are derived at the location points within the mother continuum elements (mortar) which are illustrated in *Figure 2.24*. One disadvantage of this method is that the slip between the mortar and bars are not explicitly modeled because they are both based on the same displacement field. Consequently, the reinforcements are fully bonded in this model.

In the scope of this thesis research, the *Discrete modeling* approach of the reinforcement will be used in order to simulate the pull out behavior of the bars. Since the lay-out of the reinforcement bars is quit simple because they are connected only to the bed-joints, it will not overcomplicate the discretization of the model. Moreover, Mahmoudimotlagh ([2020](#)) already performed numerical modeling using embedded reinforcements.

Figure 2.24: Embedded reinforcement: (a) bar in plane stress elements; (b) bar in curved shell elements; (c) bar in solid elements (Ferreira, [2021](#))

2.4.3   Implicit solution procedures

FEM uses an implicit solver that assembles the global stiffness matrix in all steps and pursues satisfaction of constitutive behavior and equilibrium (Rots et al., 2016). The nonlinear implicit solution procedure can be explained with the equilibrium path which is a graphical representation of the global response (force-displacement). Each point on the equilibrium path represent a equilibrium point or equilibrium configuration (Hendriks et al., Lecture 4, 2019). The stiffness matrix of a system can be found by finding the envelope of this equilibrium path. This is done by using a incremental-iterative solution procedure in which the solution for each step requires a series of trial solutions (iterations) to establish equilibrium within a certain tolerance (LS-DYNAsupport, 2021). The following incremental-iterative solution procedure are available:

1. ***Full Newton-Raphson***: updates the stiffness in every iteration

2. ***Modified Newton-Raphson***: updates the stiffness only in the first iteration of every load increment

3. ***Initial stiffness method***: uses the initial (linear) stiffness for every iteration of every load increment

A graphical representation of the implicit solution procedure is illustrated in *Figure 2.25*. The procedure starts with a guess for the nodal displacements (using element stiffness) which will be differentiated and interpolated to the integration points to find the strains and stresses. Subsequently, the internal forces are found by integrating the stresses over the volume of the elements and extrapolating these to the nodes. The equilibrium is found when the internal forces are almost equal to the external forces.

Figure 2.25: Nonlinear implicit solution procedure (Hendriks et al., Lecture 4, 2019)

The iteration procedure is stopped when the convergence criterion and tolerance, which measure how well the obtained solution satisfied the equilibrium, are met. The right balance between accurate and economical solutions can be found by carefully choosing the convergence criteria and tolerances. The following options are available (Hendriks et al., Lecture 4, 2019):

1. ***Force-based convergence norm***: the remaining force imbalance is a small fraction of the total applied force

2. ***Displacement-based convergence norm***: the last update of the displacement increment is a small fraction of the initial displacement increment

3. ***Energy-based convergence norm***: the last update of the stored energy is a small fraction of the initial stored energy.

2.4.4   Modeling of cracking

Cracking is a material nonlinearity which can be modeled in the numerical analyses for masonry structures using two different approaches, namely the *Discrete cracking approach* and the *Smeared cracking approach*. The concept of these two approaches are discussed in this section separately.

Discrete cracking approach

The appearance of cracks in masonry walls indicate that discontinuities are formed in the system. The simulation of these discontinuities can be achieved by incorporating discrete elements using either spring elements or interface elements at those locations. The Discrete cracking approach is based on the concept of having discontinuities in a system initially from the start. This means that the discontinuities are predefined in the mesh of the model at which the opening and the closure will be simulated. The essence is that the deformations and nonlinearities are lumped or localized into a point, line or plane using spring or interface elements. Moreover, the nonlinear material behavior are only described within the aforementioned discrete elements while the bulk material (surrounding continuum elements) are kept linear elastic.

Two types of spring elements are available, namely the translational and the rotational spring elements which relate the stress versus the relative displacement and the moment versus the relative rotation, respectively. Furthermore, spring elements can also be implemented as bedding, connected to the continuum elements. For instance, a building on top of a soil layer. However, this becomes difficult and inconvenient, especially for models with irregular meshes and/ or higher order elements. This is due to the fact that spring elements attached to the nodes of the adjacent continuum elements do not all have the same stiffnesses. Because of the contribution of neighboring elements, different stiffnesses need to be assigned to different spring elements. This becomes worse for quadratic elements where the middle nodes are showing larger reaction forces compared to the corner nodes, even when the system is uniformly loaded. This can be explained by the fact that an unit displacement at a corner node activates a relatively small part of the element in comparison to an unit displacement at a middle node (shape functions). For the case of 3D quadratic solid elements, the stiffnesses related to the corner nodes are even negative (conceptionally impossible as input parameters in finite element programs). The aforementioned phenomena's are illustrated by *Figure 2.26* including the shape functions. The solution is to use interface elements.

An interface element can be seen as a row of "smeared spring elements" in which the interface area is accounted for automatically instead of manually for spring elements. Interface elements relate stresses versus relative displacement instead of forces versus relative displacement. In a masonry wall, the interface elements can be located in the mortar joints or within the brick units. Usually, the bond between the bricks and the mortar joints are the weakest link in masonry where either the vertical head-joints are opened by pulling (Mode-I tensile failure) or the horizontal bed-joints are shifted through slipping (Mode–II shear failure).

(a) *(b)*
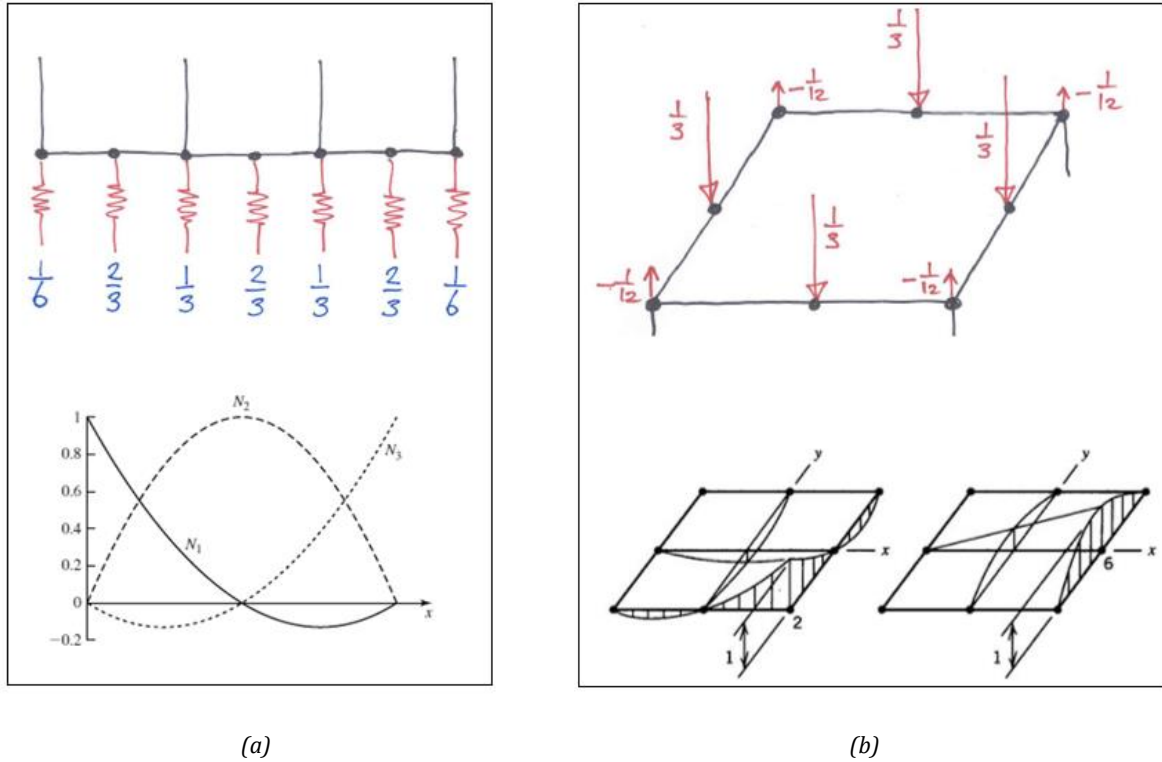
Figure 2.26: Spring stiffness ratio's including the shape functions for: (a) 2D quadratic elements; (b) 3D quadratic elements (Hendriks et al., Lecture 6, 2019; Nagendran, 2020; Lecture, 2008)

On the other hand, interface elements which are located within the brick units represent possible cracking. A crack starts to form when the tensile strength of the material has been exceeded. This means that up until this point, the predefined discontinuities should not really be there from the start. The initial elastic deformation of the interface elements should be negligible compared to the deformations of the surrounding continuum elements (Hendriks et al., Lecture 4, 2019). This can be achieved by assigning an initially high "dummy" stiffness (or penalty stiffness) to the interface elements. For this reason, the normal stiffness k_n and the tangential stiffness k_t of the interface elements should be set initially high. However, extreme large stiffness differences should be avoided because of numerical difficulties and ill-conditioning during the analyses.

The constitutive behavior in tension (Mode-I) for the interface elements are described as follows. A linear loading branch with an initially high stiffness goes up until it reaches the tensile strength of the material. From this point, cracks start to form and the function goes into a nonlinear tension softening curve until it reaches zero stress level. Subsequently, the unloading branch goes horizontally back to the origin at zero stress (because the open cracks do not contain any tensile strength). When the cracks are closed, they become stiff again because of the compressive strength and the function goes into the branch of the compressive behavior. The

aforementioned material behavior is illustrated in *Figure 2.27* in which it can be observed that the loading and unloading behavior is a closed cycle, meaning that energy is dissipated. This fracture energy G_f, the tensile strength f_t, the two stiffness components k_n and k_t, together with the choice of a predefined tension softening function by specification of the curve name, are the input parameters for the material constitutive behavior in tension. Different tension softening curves are shown in *Figure 2.28*.
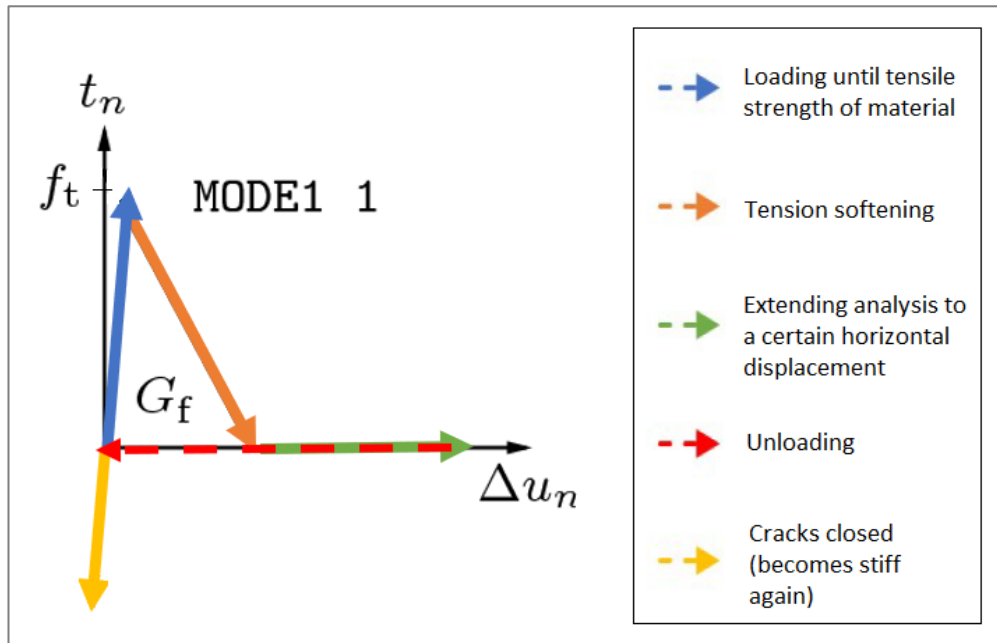
Figure 2.27: Constitutive model for tension behavior
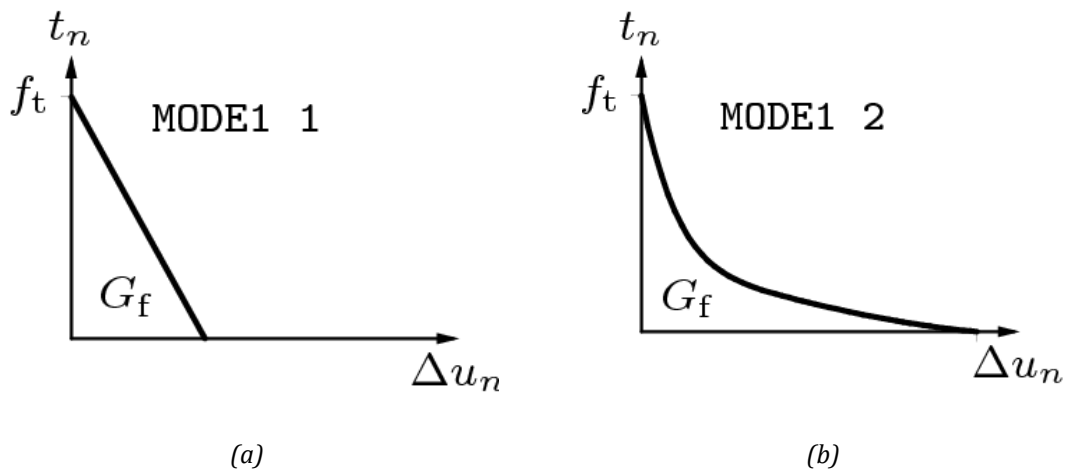
Figure 2.28: Tension softening models: (a) linear; (b) nonlinear Hordijk et al. (Ferreira, 2021)

Smeared cracking approach

In contrast to the Discrete cracking approach, the discontinuities are not predefined in the Smeared cracking approach. Sometimes it is difficult to define beforehand where to put the interface elements (including their orientations) because of not knowing where the cracks might occur. This is why the Smeared cracking approach can be used in which the effect of cracking is spread over the area that belongs to an integration point within a continuum element as shown in *Figure 2.29*. The advantage of using this model is that cracking can occur anywhere in the mesh in any direction.
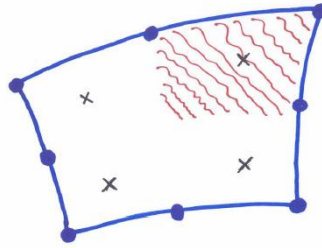
Figure 2.29: Smeared cracking over area of an integration point (Hendriks et al., CIE5148 Lecture 7, 2019)

A crack is initiated when the principal tensile stress σ_1 exceeds the value of the tensile strength f_t. The direction of the crack is perpendicular to the direction of the principal tensile stress (Hendriks et al., CIE5148 Lecture 7, 2019). The Smeared cracking approach relates the principal stress versus the principal strain instead of the principal stress versus the relative displacement (crack opening) for the Discrete cracking approach, illustrated in *Figure 2.30*. The spreading of cracks over a continuum element is defined by the strain ε which is the total crack openings W within a continuum element, divided by the crack bandwidth h. The crack bandwidth is an additional input parameter which is related to the element size, defined for different types of elements. It is important to note that this numerical parameter h enters into the constitutive material model which means that the material model behavior is dependent on the element size.

(a)   *(b)*
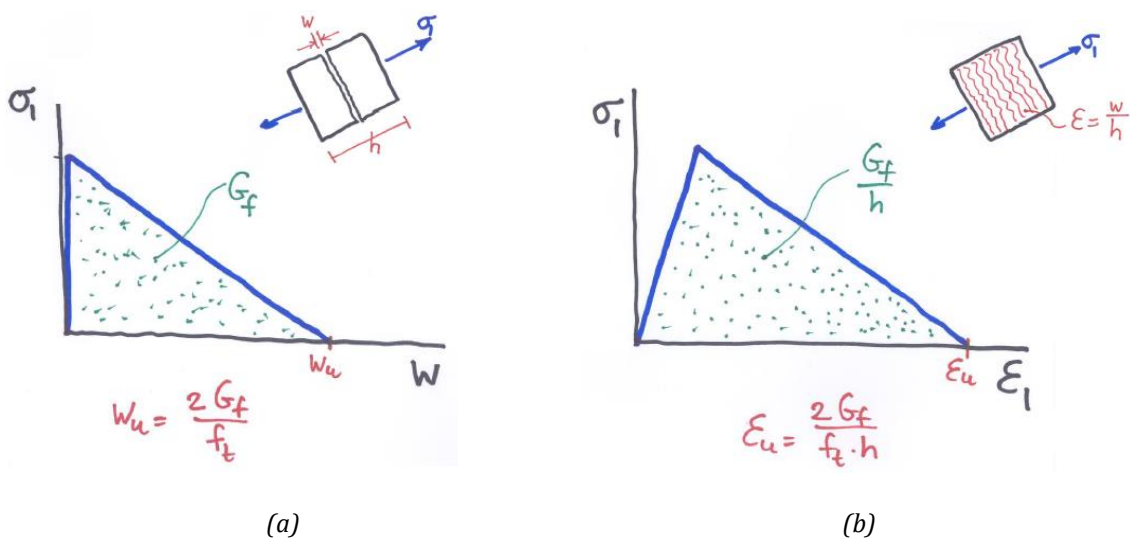
Figure 2.30: Tensile material behavior: (a) Discrete cracking model; (b) Smeared cracking (Hendriks et al., CIE5148 Lecture 7, 2019)

2.4.5   Total Strain Crack Model

The constitutive models which are based on total strain were originally developed for concrete and assume an isotropic material with secant unloading and reloading behavior (Rots et al., 2016). The Total Strain Crack Model (TSCM) follows a smeared failure approach for the fracture energy in which the tensile and compressive behavior of a material is described with one stress-strain relation (Ferreira, 2021).

The required input parameters for this model consist of two parts: (1) the basic linear elastic properties like the Young's modulus E and the Poisson's ratio v; and (2) the parameters which describes the tensile and compressive behavior including the specification of the predefined function. Different types of predefined tensile and compressive curves are presented in *Figure 2.31* and *Figure 2.32* respectively. Important to note is that type (d), (e) and (f) for tension and type (g) for compression are based on the fracture energy G_f including the numerical parameter for the crack bandwidth h. The Rots' element based method determines the crack bandwidth h based on the size, the shape and interpolation function of the used finite element. Different specifications can be found for different types of elements (Ferreira, 2021).
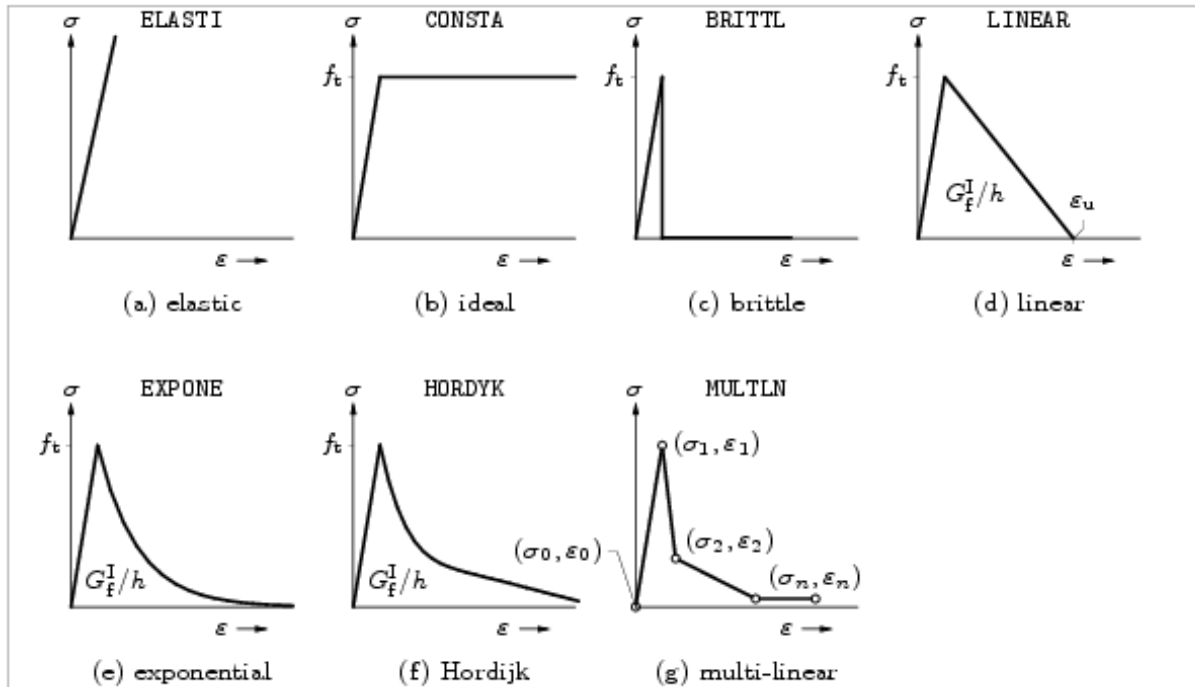
Figure 2.31: Predefined tension softening functions for the Total Strain Crack Model (Ferreira, 2021)
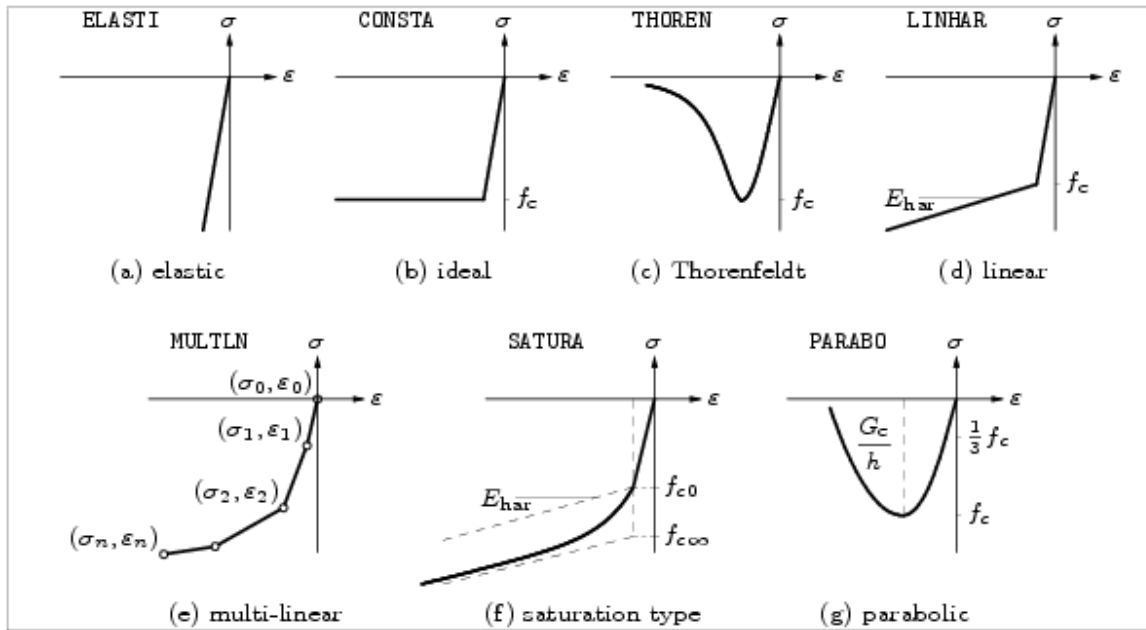
Figure 2.32: Predefined compression functions for the Total Strain Crack Model (Ferreira, 2021)

Non-proportional loading is a reason why there are multiple models specified for the simulation of cracking. This can be due to fact that the structure is loaded in a non-proportional way or due to the redistribution of forces in the structure. Consequently, the principal stresses might rotate resulting in shear stresses along the open cracks. The TSCM is subdivided into two models (illustrated in *Figure 2.33*):

1. ***Total Strain Fixed Crack Model***: is a shear retention model in which the orientation of the crack is kept the same. The stress-strain relations are evaluated in the fixed coordinate system

2. ***Total Strain Rotating Crack Model***: cracks are rotated to be perpendicular again to the direction of the principal stresses in order to have no shear stresses along the cracks. The stress-strain relations are evaluated in the principal directions of the strain vector.
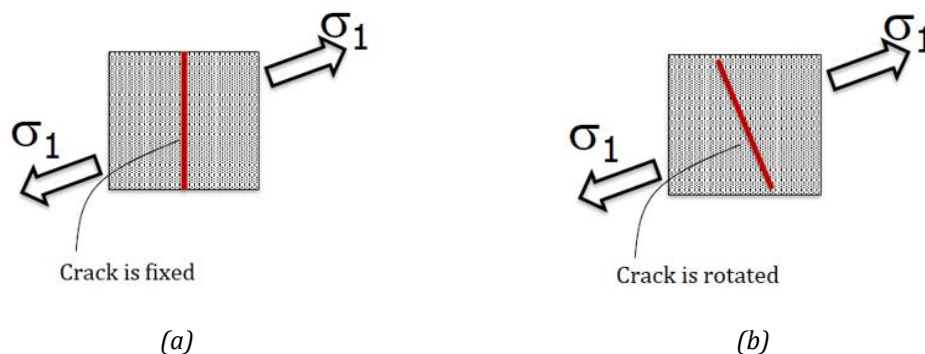
Figure 2.33: (a) Total Strain Fixed Crack Model; (b) Total Strain Rotating Crack Model (Hendriks et al., Lecture 4, 2019)

Although the failure load is well described by the model, one disadvantage of using the TSCM is that the orthotropic property of masonry is not taken into account. Moreover, the model does not distinguish between tensile cracks (normal either to bed-or head-joints) and shear cracks (Rots et al., 2016). Consequently, the model might fail to accurately reproduce the different failure modes of the masonry. Furthermore, because the model is based on only secant

unloading and reloading behavior, the energy absorption is usually underestimated. This is the reason why the cyclic unloading and reloading are not captured well in this model. This is in line with the numerical results found in the MSc thesis by Xu (2018) which are illustrated in *Figure 2.34* (showing small hysteretic loops without dissipated energy during unloading and reloading). The model is herein compared to the Engineering Masonry Model which will be discussed in the next section.
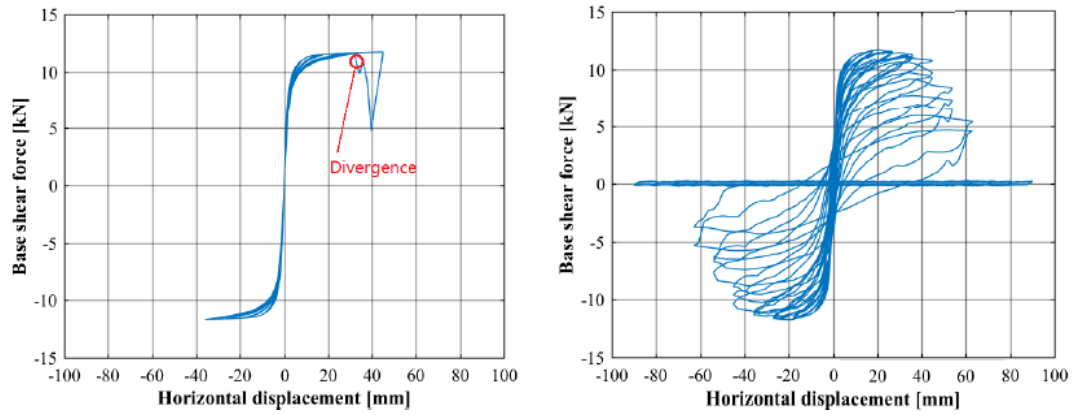
Figure 2.34: Capacity curves showing the difference between the Total Strain Crack Model (left) and the Engineering Masonry model (right) in cyclic pushover analysis (Xu, 2018)

2.4.6 Engineering Masonry Model

The Engineering Masonry Model (EMM) is also based on the smeared failure approach and is developed by DIANA FEA B.V. together with professor J. G. Rots of Delft University of Technology for modeling failure of masonry walls (Schreppers et al., 2017). The previously mentioned disadvantages that come with the Total Strain based crack model can be overcome by this new model.

Each single failure mechanism (cracking, crushing and sliding failure) are captured with the EMM in which the in-plane shear failure is based on the standard Coulomb friction failure criterion. Furthermore, the orthotropic property of masonry is included in the model by introducing different elastic properties in the direction of the bed-and head-joints (Rots et al., 2016). The local element x-direction is hereby aligned with the bed-joints and the local element y-direction with the head-joints as depicted in *Figure 2.35*.
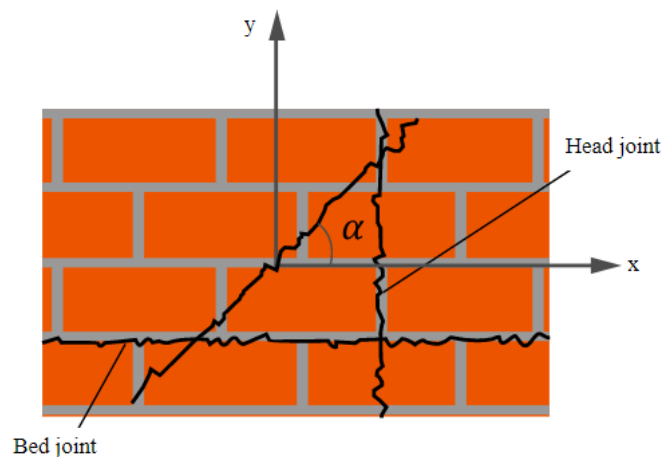
Figure 2.35: Orientations of local axis (Ferreira, 2021)

Four different cracks in the plane of the elements are predefined, namely in the direction of the bed-joints, head-joints and in two diagonal directions at a predefined angle α (defined as the angle between the bed-joints and the diagonal stair step crack).

The constitutive model is characterized by the elastic, tensile, compressive and shear behaviors. The tensile, compressive and shear failure modes are defined by different post-peak and unloading/ reloading behavior. Several input parameters which characterized each failure mode need to be determined by either experimental tests or by using empirical relations when additional parameters may not be readily available. The aforementioned constitutive behaviors are presented separately below.

Elastic behavior

The orthotropic behavior of masonry is considered in the elastic phase of the tensile, compressive and shear behavior. This is achieved by introducing different elastic parameters in the directions of the x- and y-coordinate system as specified before. For the improvement of the stability of the numerical procedure, it is assumed that there is no coupling between the stiffness of the normal component and the in-plane shear component in both x- and y-directions (Rots et al., 2016). Moreover, any interactions between the normal components are neglected. In addition, the Poisson's ratio ν is set to zero for simplicity and robustness. This is assumed to be reasonable accurate enough since the value of Poisson's ratio for typical Dutch brick masonry are small according to Rots et al. (2016).

The elastic phase is characterized by three input parameters, namely the Young's moduli E_x and E_y, and the shear modulus G_{xy}. From literature, the following empirical relations can be applied in case when info regarding the input parameters are not available. The Young's modulus in the direction parallel to the bed-joints E_x might be set as a fraction of the modulus normal to the bed-joints E_y. Accordingly, different ratio values for clay bricks and calcium silicate brick are specified in the literature. These values are compared to the experimental determined ones which are listed in (Schreppers et al., 2017). Furthermore, the shear modulus can be estimated as 40 % of the Young's modulus normal to the bed-joints according to EN-1996-1-1 (2005).

Tensile (cracking) behavior

The cracking behavior is described by a tension softening function which is assumed to be linear as illustrated in *Figure 2.36*. The maximum strain ever reached is called $\alpha_{tensile}$ and the corresponding stress is $\sigma_{rf,tensile}$. The ultimate tensile strain ε_{ult} is defined as the stage in which the crack is fully open where no stresses can be further transferred.

The tensile stress-strain curve is characterized by the Young's modulus E, tensile strength f_t and tensile fracture energy G_{ft} for each local x-and y-direction. However, the same value for the fracture energy is assumed in both directions (Rots et al., 2016) and can be determined with the empirical expression of *equation (13)* according to Schreppers et al. (2017). The relation between the aforementioned input parameters can be expressed by the geometric relation of *equation (14)* in which the crack bandwidth h is included.

$$G_{ft} = 0.025(2f_t)^{0.7} \tag{13}$$

$$\varepsilon_{ult} = \frac{2G_{ft}}{hf_t} \tag{14}$$

37

Moreover, the model is based on secant unloading and reloading (similar to the behavior used in the Total Strain based crack model) where the stress and strain follow a straight line to the origin (Rots et al., 2016).
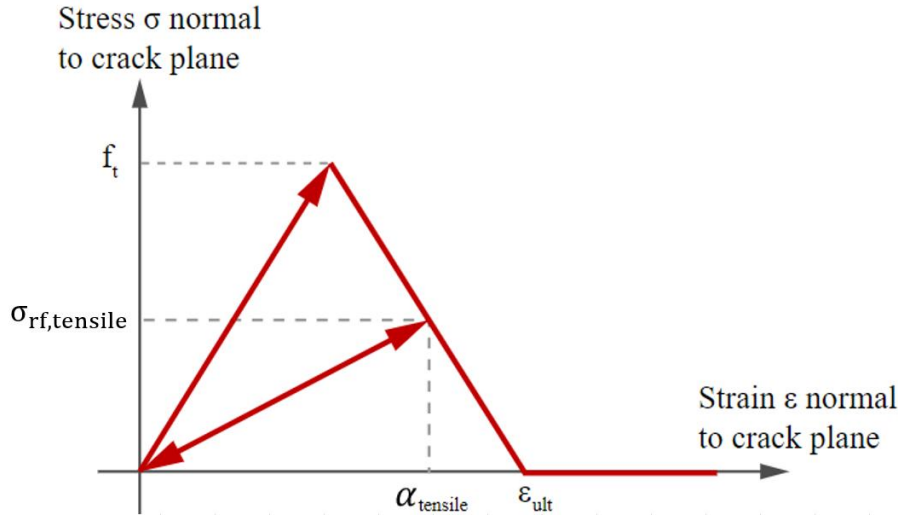
Figure 2.36: Cracking behavior of Engineering Masonry model (Schreppers et al., 2017)

Tensile cracking is assessed in the directions normal to the four different crack planes as mentioned before. While the input parameters normal to the bed-joints (input parameters with y-index) are necessary to detect the tensile failure of the masonry, cracking in the direction normal to the head-joints (input parameters with x-index) and to the diagonal planes are provided with different user defined options in DIANA FEA according to Schreppers et al. (2017). The four different syntax options are listed below:

1) *(HEADTP=NONE)*: The head-joints do not fail in this option. Only cracking in the direction normal to the bed-joints are considered, thus the local y-direction (only specifying input parameters with y-index). Diagonal cracks are not considered.

2) *(HEADTP=EXPLIC)*: Failure of the bed-joints and head-joints are both considered. Input parameters with both x-and y-indices are specified. Diagonal cracks are not considered.

3) *(HEADTP=DIAGON)*: Diagonal cracks are considered together with cracking in the direction normal to the bed-and head-joints. In this option, the head-joint failure is assumed to occur as part of the diagonal crack. The tensile strength of the diagonal cracks $f_{t\alpha}$ is a function of the input parameter α which is defined as the angle between the bed-joints and the diagonal stair-case crack, presented in *equation (15)*. The shear release of the diagonal cracks are also considered by the fact that slip occurs along the bed-joints. This is expressed with the tensile strength normal to the head-joint f_{tx} which is a function of the maximum frictional shear stress τ_{max} in the bed-joint expressed in *equation (16)*. f_{ty} is defined as the bed-joint tensile strength.

$$f_{t\alpha} = \frac{f_{tx}f_{ty}}{f_{tx}^2 sin^2\left(\frac{\pi}{2} - \alpha\right) + f_{ty}^2 cos^2\left(\frac{\pi}{2} - \alpha\right)} \tag{15}$$

$$f_{tx} = \frac{\tau_{max}}{\tan(\alpha)} \tag{16}$$

4) **(HEADTP=FRICTI)**: Failure of the bed-joints and head-joints are both considered. In this case, the tensile strength normal to the head-joint f_{tx} is evaluated and calculated from the friction shear stress in the bed-joints like in option 3. Optionally, a minimum head-joint tensile strength could be provided.

Compressive (crushing) behavior

Compressive crushing is assessed in the direction normal to the bed-and head-joints only (Rots et al., 2016). The compressive behavior is characterized by linear softening as depicted in *Figure 2.37*. The minimum strain ever reached is called α_{comp} and the corresponding stress is $\sigma_{rf,comp}$. Furthermore, the compressive fracture energy G_{fc} can be estimated with the empirical expression of *equation (17)* according to Schreppers et al. (2017).
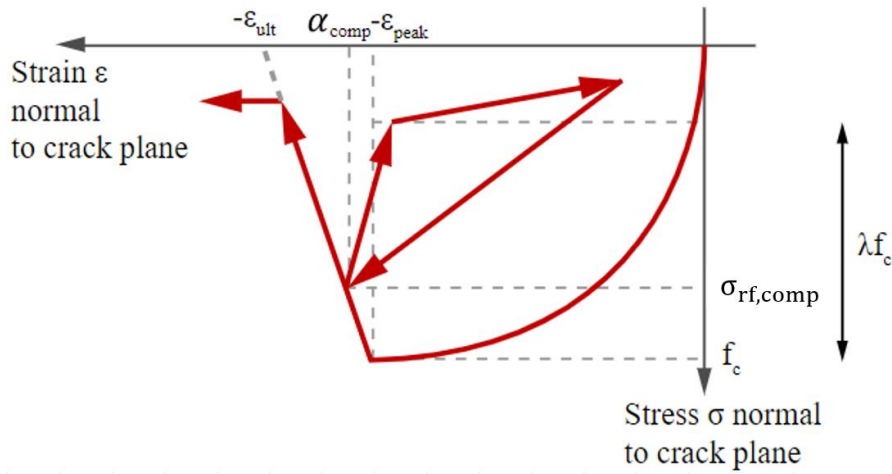
Figure 2.37: Crushing behavior of Engineering Masonry model (Schreppers et al., 2017)

$$G_{fc} = 15 + 0.43f_c - 0.0036f_c^2 \qquad (17)$$

Instead of using the initial Young's modulus E to find the peak strain ε_{peak} by going up linearly in a straight line until the compressive strength f_c is reached, this value for ε_{peak} is found by "prolonging" the curve using the factor n. Resulting in a predefined curve which consist of a third order and a parabolic curve up until the compressive strength f_c has been reached. Consequently, a larger ductility is shown for the compressive behavior. The factor n is defined by *equation (18)*.

$$n = \frac{E\varepsilon_{peak}}{f_c} \qquad (18)$$

Subsequently, a linear softening curve is assumed until a residual stress of 10% of the compressive strength f_c has been reached. The ultimate compressive strain ε_{ult} is defined as the strain value for which the linear softening curve would have reached a zero stress level.

Unlike secant unloading and reloading for the tensile cracking behavior, the compressive behavior follow a bilinear unloading curve (Rots et al., 2016). For this, an unloading factor λ (value between 0 and 1) has been defined. The unloading starts with a linear elastic branch using the initial stiffness E until the compressive stress level of $\lambda\sigma_{rf,comp}$ has been reached. Subsequently, a secant stiffness E_{sec} to the origin is followed, expressed in *equation (19)*. At

reloading a straight line to the last loading point is followed. As a result, $\lambda = 0$ corresponds to the case in which the unloading goes linearly to zero stress level using the initial stiffness E. On the other hand, $\lambda = 1$ correspond to the case with a secant unloading to the origin with a stiffness of $\frac{\sigma_{rf,comp}}{\alpha_{comp}}$ (Schreppers et al., 2017).

$$E_{sec} = \frac{\lambda \sigma_{rf,comp}}{\alpha_{comp} - \lambda \frac{\sigma_{rf,comp}}{E}} \tag{19}$$

Shear (sliding) behavior

The in-plane shear behavior is described by the function which is depicted in *Figure 2.38*. The in-plane shear stress τ is a function of the in-plane shear strain γ and the stress normal to the bed-joint σ_{yy}. The shear stress cannot exceed the value of the maximum friction stress τ_{max} which is defined by the Coulomb friction criterion in *equation (20)*.

$$\tau_{max} = \max[0, c - \sigma_{yy}\tan(\phi)] \tag{20}$$

The function is characterized by the input parameters for cohesion c, friction angle ϕ, shear fracture energy G_{fs} and the initial shear stiffness G. Furthermore, the cohesion will be reduced to zero when an integration point of an element is cracked (Schreppers et al., 2017). The function consist of an linear elastic branch going from zero up until τ_{max}, followed by a linearly descending branch, due to the reduction of the cohesion, until it reaches zero at ultimate shear strain γ_{ult}. The ultimate shear strain can be derived with *equation (21)* where h is the crack bandwidth of the element. During unloading, the function goes into the opposite side of the graph (sliding in opposite direction). Accordingly, shear failure is characterized by quasi-brittle failure of cohesion followed by a plastic plateau and elastic unloading (Rots et al., 2016).

$$\gamma_{ult} = \frac{2G_{fs}}{ch} - \frac{c}{G} \tag{21}$$
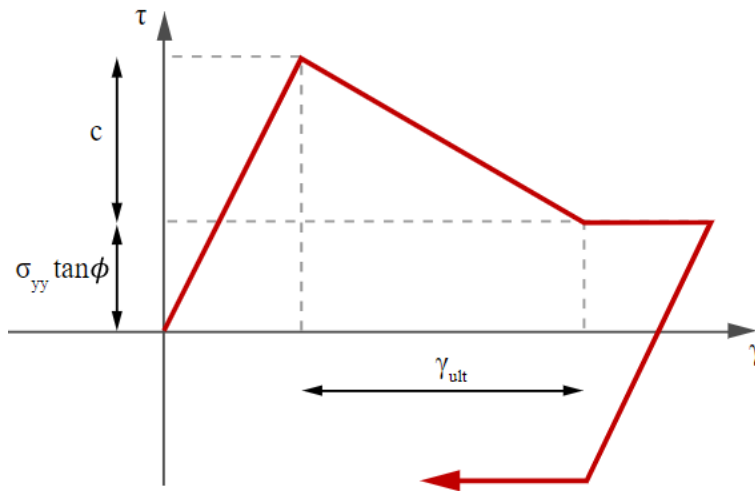
Figure 2.38: Shear behavior of Engineering Masonry model (Schreppers et al., 2017)

40

2.5   Conclusions

Four numerical modeling approaches with varying level of detail are found in the literature for simulating masonry structures. The bricks and mortar joints are modeled as one homogeneous continuum in the *macro-model*. On the other hand, the bricks and mortar joints are modeled separately for the *continuous* and *detailed micro-model* where interface elements are included at the brick-mortar bonds for the latter one. Considering the *discrete (simplified) micro-model*, the bricks are expanded up to half the thickness of the mortar joints and connected to each other with zero thickness interface elements. For this reason, the bed-joint reinforcement bars cannot be connected to the mortar joints. Within the scope of this thesis research, all aforementioned modeling approaches will be used, except for the discrete (simplified) micro-model.

In the scope of this thesis research, the *Discrete modeling* approach of the reinforcement will be used in order to simulate the pull out behavior of the bars. Since the lay-out of the reinforcement bars is quit simple because they are connected only to the bed-joints, it will not overcomplicate the discretization of the model.

The characterization of the material properties is important because they can serve as input parameters for numerical and analytical models. An extensive experimental testing campaign has been carried out at the Delft University of Technology. Destructive laboratory tests have been conducted on samples which were extracted from existing masonry buildings. The objective of these experiments was to provide a database in order to characterize the compression, bending and shear properties of Dutch URM. The material properties for masonry as a composite material will be used for the macro-model, whereas the material properties for each structural component (brick and mortar) will be used for the two micro-models.

Cracks can be modeled using the *discrete cracking approach* or the *smeared cracking approach* where the former one will be used at the brick-mortar interfaces and the latter one will be used for cracking in the mortar joints (micro-models) and in the masonry composite (macro-model). Both *Total Strain Crack model* and *Engineering Masonry model* are based on the smeared cracking approach where the former one is an isotropic material model which only allows for secant unloading and the latter one is an orthotropic material model which allows for elastic unloading.

3

CASE STUDY

Paper: Performance of unreinforced masonry strengthened with bed joint reinforced repointing

Experimental tests have been conducted at Delft University of Technology with the goal to investigate the performance of the bed-joint reinforcement technique as a strengthening measure against seismic loading for the residential terraced houses in the Groningen area. An experimental campaign was conducted within the project "Lab tests and studies towards retrofitting measures in Groningen heritage" funded by the OCW-RCE subsidies (Licciardello et al., 2021). The experimental results provide a first insight on the effectiveness of the technique as well as support the validation of the numerical analeyses. In this chapter, the experimental tests are briefly summarized in order to provide context for the numerical simulations conducted in this thesis. Note that in the experiment and in this thesis, the retrofitted wall is compared with an un-damaged URM wall *(TUD_COMP-41)* from another experimental campain, conducted under similar conditions at Delft University of Technology (Korswagen et al., 2019).

First, a brief discription of the test setup for both un-strengthnened and strengthened walls according to the experiment is given in Section 3.1. Subsequently, the adopted loading protocol is discussed in Section 3.2. A description of the reinforcements and the retrofitted wall specimen is given in Section 3.3. Moreover, the experimental results are briefly discussed in Section 3.4.

3.1 Description of the test setup

The test setup for the quasi-static cyclic in-plane test, on the full-scale walls including the dimensions, is illustrated in *Figure 3.1*. The tested masonry wall specimens were built in single-leaf running bond using clay-bricks. A single window opening was eccentrically included in the walls. A single-row concrete lintel was constructed above the window opening. Moreover, the walls were glued to a bottom HEB300 steel beam and a top HEB600 steel beam to prevent sliding. The two steel beams were connected to each other via two steel columns. This steel supporting frame was set in a cantiliver configuration, allowing free displacement and rotation of the top beam while the bottom beam was fully fixed to the setup frame. The self-weight of the top beam (inlcuding some setup components) provided an uniform, initial vertical stress (overburden) of $0.12 \ MPa$. A hydraulic jack was attached to the center of the top beam to impose the horizontal displacement in the plane of the wall. The out-of-plane displacement of the wall was restrained by the supporting frame. Important to note is that the test setup is the same for both un-strengthened and strengthened walls.
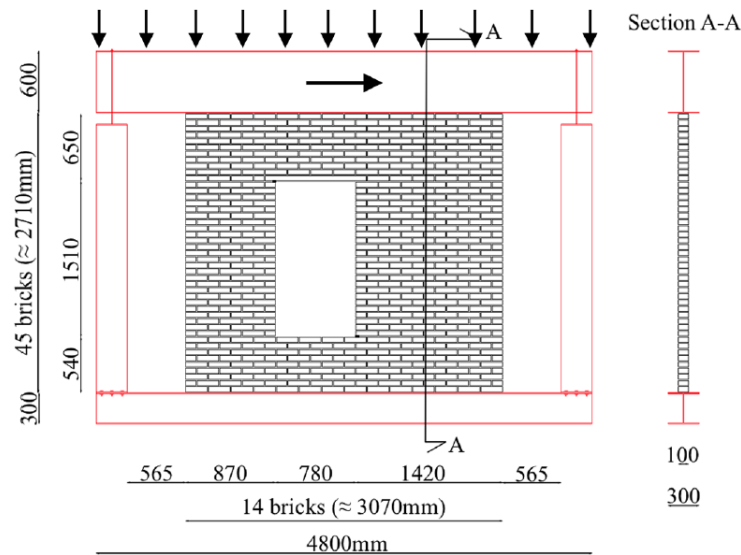
Figure 3.1: Test setup and dimensions of the un-strengthened wall from the experiment by (Korswagen et al., 2019)

3.2 Loading protocol

The same loading protocol was adopted for the un-strengthened and the strengthened walls. The lateral load was applied in three phases. The first, repetitive (one-way cyclic) quasi-static loading section is referred to as Phase 1. This section consists of five cycles in the positive x-direction. The second, cyclic (two-way) quasi-static loading section is referred to as Phase 2 and consists of seven cycles in both loading directions. Each cycle consist of 30 runs for both phases. A run is defined as the loading sequence after which the target displacement is applied in both loading directions up to returning to the original position of the wall. Phase 1 and Phase 2 are referred to as the Damage Limitation (DL) state, while Phase 3 is referred to as the Near Collapse (NC) state. The loading protocol for Phase 3 was determined considering the dynamic response of a typical Dutch terraced house experimentally tested on a shaking table by adopting a "Groningen type" loading sequence (Licciardello et al., 2021). Phase 3 consists of eight cycles. The first two cycles consists of two runs each, while the remaining six cycles consists of one run each. The loading scheme with its phases is illustrated in *Figure 3.2*.

(a)   *(b)*
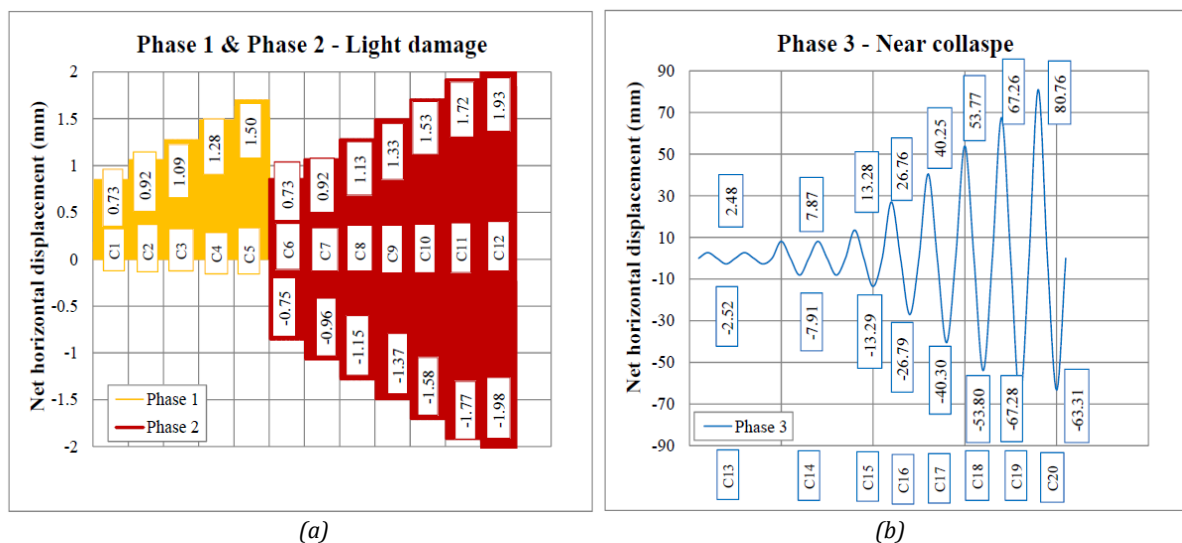
Figure 3.2: Loading scheme: (a) DL state Phase 1 and 2; (b) NC state Phase 3 (Licciardello et al., 2021)

3.3 Description of reinforcement and wall specimens

The strengthening technique consists of the placement of twisted steel bars in 4 cm cut-out grooves in the bed-joints, embedded in high-strength repair mortar (*Figure 3.3b*). The diameter of the steel bars are 6 *mm*. The lay-out of the steel reinforcing bars in the bed-joints of the full scale wall are illustrated in *Figure 3.3a*. The bars are placed in pairs every 3 joints (marked in green) above and below the window opening. The piers on both side of the opening are strengthened with a single bar every 5 or 6 joints (marked in purple). Furthermore, the diagonal bars (marked in blue) are placed at the corners of the opening. This is done by inserting diagonal ties across the width of the wall in drilled holes.
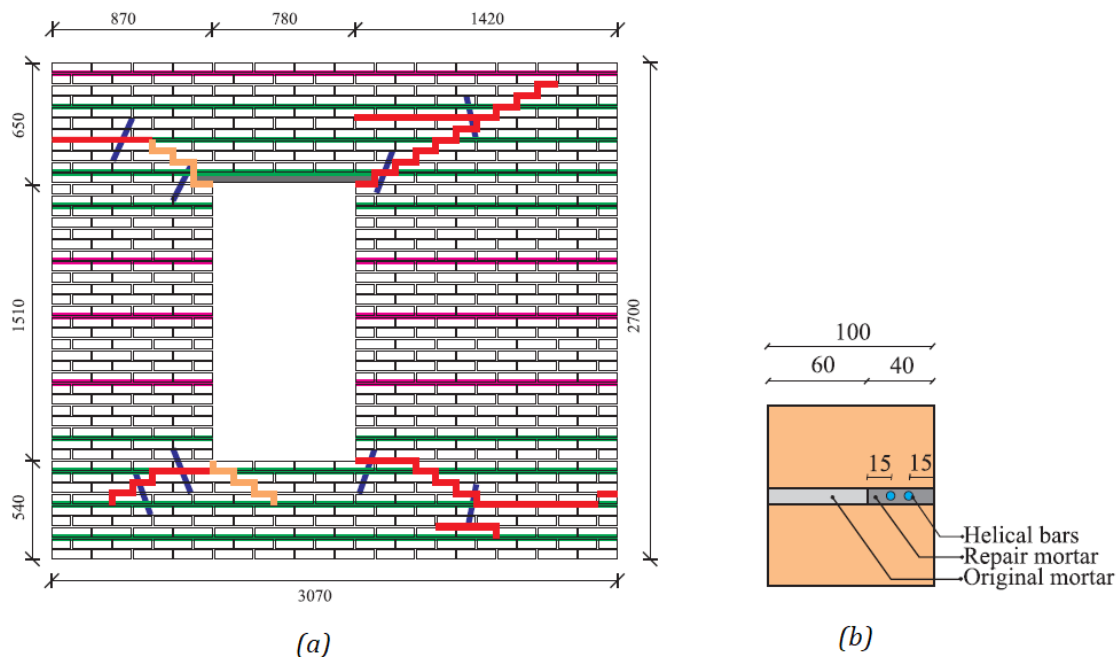
Figure 3.3: (a) Geometry of strengthened wall (TUD_COMP-45) with locations of pre-/ post- damage and lay-out reinforcements; (b) cross-section reinforced bed-joint (Drougkas et al., 2020)

The strengthening of the wall specimen took place at the end of Phase 2, after which the entire loading protocol was restarted. This means that the wall was already damaged prior to strengthening. This damage is referred to as "post-damage" for which the cracks are marked in red in *Figure 3.3a* and *Figure 3.5*. Moreover, the cracks that are marked in orange (*Figure 3.3a* and *Figure 3.5*) are referred to as "pre-damage". These cracks are the result of the placement of thin plastic sheets between the bricks and mortar to account for the artificial absence of bond to simulate cracking due to soil subsidence (Drougkas et al., 2020).The section of the bed-joints that were reinforced and do not intersect with the pre-/post-damage are referred to as "strengthened joints", while the section of the bed-joints that were reinforced and intersect with the pre-/post-damage are referred to as "repaired joints". An overview is provided in *Figure 3.4* of the loading sequences for the different walls. In summary, three different walls can be distinguised from each other, namely the un-damaged/ un-strengthened wall (TUD_COMP-41), the pre-damaged/ un-strengthened wall (TUD_COMP-45) and the pre-damaged/ strengthened wall (TUD_COMP-45). An illustration is made in *Figure 3.5* for the three different walls.
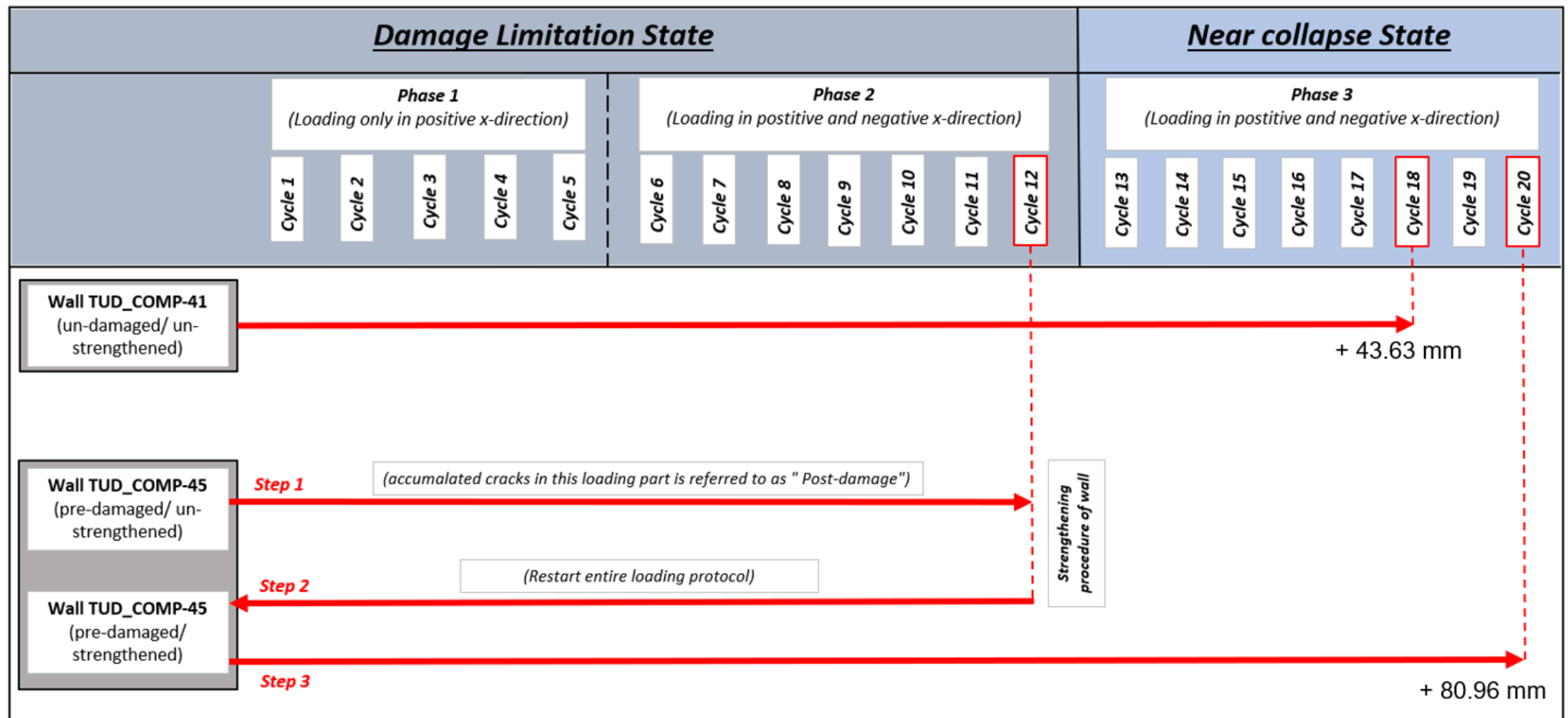
Figure 3.4: Overview experiment of loading sequences for the tested wall specimens

Un-damaged/ un-strengthened wall
(TUD_COMP-41)

Pre-damaged/ un-strengthened wall
(TUD_COMP-45)

Pre-damaged/ strengthened wall
(TUD_COMP-45)
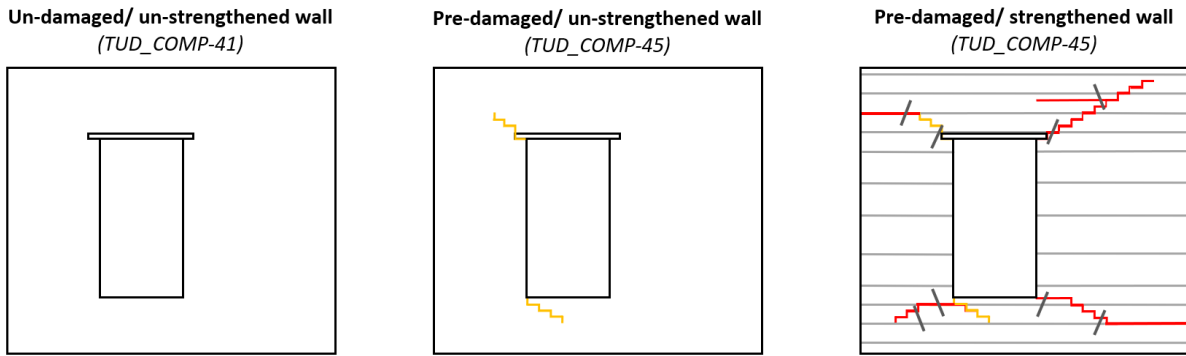
Figure 3.5: Three different tested wall specimens

3.4 Summary of experimental results

For the DL state (Phase 1 and 2), the comparison is made between the same wall *(TUD_COMP-45)* that was initially tested as un-strengthened wall and later strengthened. On the contrary, for the NC state (Phase 3), the comparison of the strengthened wall *(TUD_COM-45)* is made with the un-damaged/ un-strengthened wall *(TUD_COMP-41)*.

The experimental results are discussed in terms of base shear force versus net horizontal displacement (capacity curves), crack pattern and failure mechanisms. According to Licciardello et al. ([2021](#)), the cracks in the un-strengthened wall mainly developed diagonally from the window corners while the cracks in the strengthened wall were mainly horizontal in the masonry portion above the window opening and more spread out in the area below the window opening (both in mortar joints and bricks). The crack pattern and base shear force versus net horizontal displacement for both un-strengthened and strengthened wall are illustrated in *Figure 3.7* for the DL state as well as the NC state. The orange and red colored cracks are accumulated during Phase 1 and Phase 2, respectively. The cracks which are formed during Phase 3 are indicated in blue. Furthermore, the superscript "a" is added to the crack numbers to highlight the small differences between the two un-strengthened walls. Additionally, an asterisk is added as superscript to the crack number in case when the crack shape or location is significantly modified in the strengthened wall.

Considering the DL state, an average reduction of 20~25% in crack width and 25~50% in crack length was observed for the strengthened wall compared to the un-strengthened wall. The obtained values for the crack width and length (at the end of Phase 2) for both strengthened and un-strengthened wall from the experiment are listed in *Table 1*. Furthermore, the presence of the bed-joint reinforcement contributes to a delay in the crack process for the DL state. Considering the NC state, different failure mechanisms was observed for the un-strengthened wall when approaching the end of the analysis. According to Licciardello et al. ([2021](#)), the following failure mechanisms of masonry components are identified:

- *Rocking* mechanism of the piers
- *Sliding* mechanism between two parts of the wall
- *Arch mechanism* of the masonry portion below the window opening
- *Toe crushing* (compression failure) at the bottom or top corner of one of the piers

The prevailing mechanism for the un-strengthened wall was rocking of both piers until Cycle 14. Sliding between the masonry portion above the window opening and the two piers occurred during Cycle 15 for loading in the negative x-direction. Subsequently, the L-shaped portion of

the wall composed by the masonry portion on the top of the window and the right pier (P2) started to slide with respect to the rest of the wall (during Cycle 18 for loading in the positive x-direction). Rocking of both piers was also the initial failure mechanism for the strengthened wall for both loading directions. However, an arching mechanism was formed at the base of the wall during Cycle 18 for both loading directions. Subsequently, toe crushing occurred during Cycle 20 for loading in positive x-direction and sliding of the masonry portion above of the window opening with respect to the piers for the negative x-direction. The relevant failure mechanisms at the end of the NC state (Phase 3) are illustrated for both un-strengthened and strengthened wall in *Figure 3.6*.

(a)   *(b)*   *(c)*   *(d)*
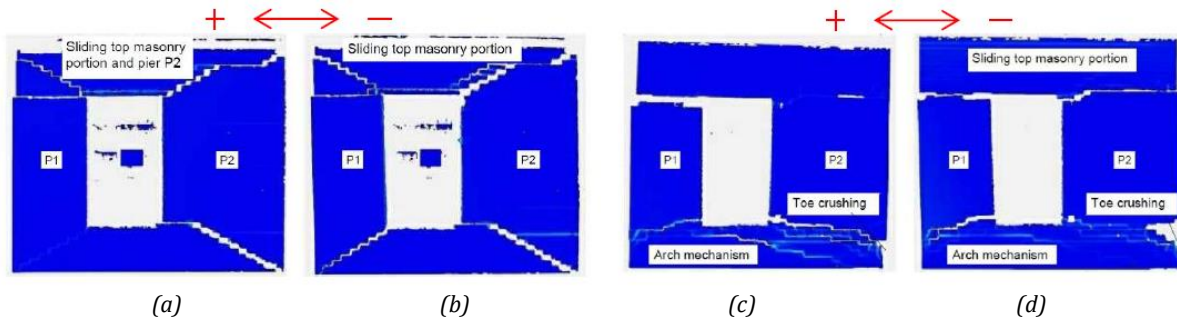
Figure 3.6: Relevant failure mechanism at the end of NC state (Phase 3): (a)-(b) un-strengthened wall; (c)-(d) strengthened wall (Licciardello et al., 2021)

According to Licciardello et al. (2021), no significant increment in force capacity was observed. For the un-strengthened wall, the maximum base shear force was equal to 20.72 kN and -19.54 kN for the positive and negative loading direction, respectively. Considering the strengthened case, the maximum base shear force was equal to 25.14 kN and -23.46 kN for the positive and negative loading direction, respectively. The strengthened wall showed a more ductile behavior with an increased displacement capacity (+40%) with respect to the un-strengthened wall for both loading directions. However, the damage in the strengthened wall is more extended in terms of number, width and length (both in mortar and bricks, due to the forming of an arch mechanism at the portion below the window opening induced by the bed-joint reinforcement). Furthermore, the application of the strengthening technique results in an increase in out-of-plane deformations during the NC state (Phase 3) due to the asymmetric placement of reinforcing bars within the thickness of single-wythe wall. The test was stopped for the strengthened wall because out-of-plane deformation occurred in both piers.

Table 1: Results for crack width (w) and length (l) obtained from the experiment by (Licciardello et al., 2021)

	Un-strengthened wall		Strengthened wall		Percentage difference	
	Crack width w	Crack length l	Crack width w	Crack length l	Crack width w	Crack length l
	[mm]	[mm]	[mm]	[mm]	[%]	[%]
Crack 1	0.44	1017	0.51	676	+13	-34
Crack 2	2.13	1056	1.06	871	-51	-18
Crack 3	0.55	767	0.44	580	-20	-25
Crack 4	0.52	1651	0.4	741	-25	-56
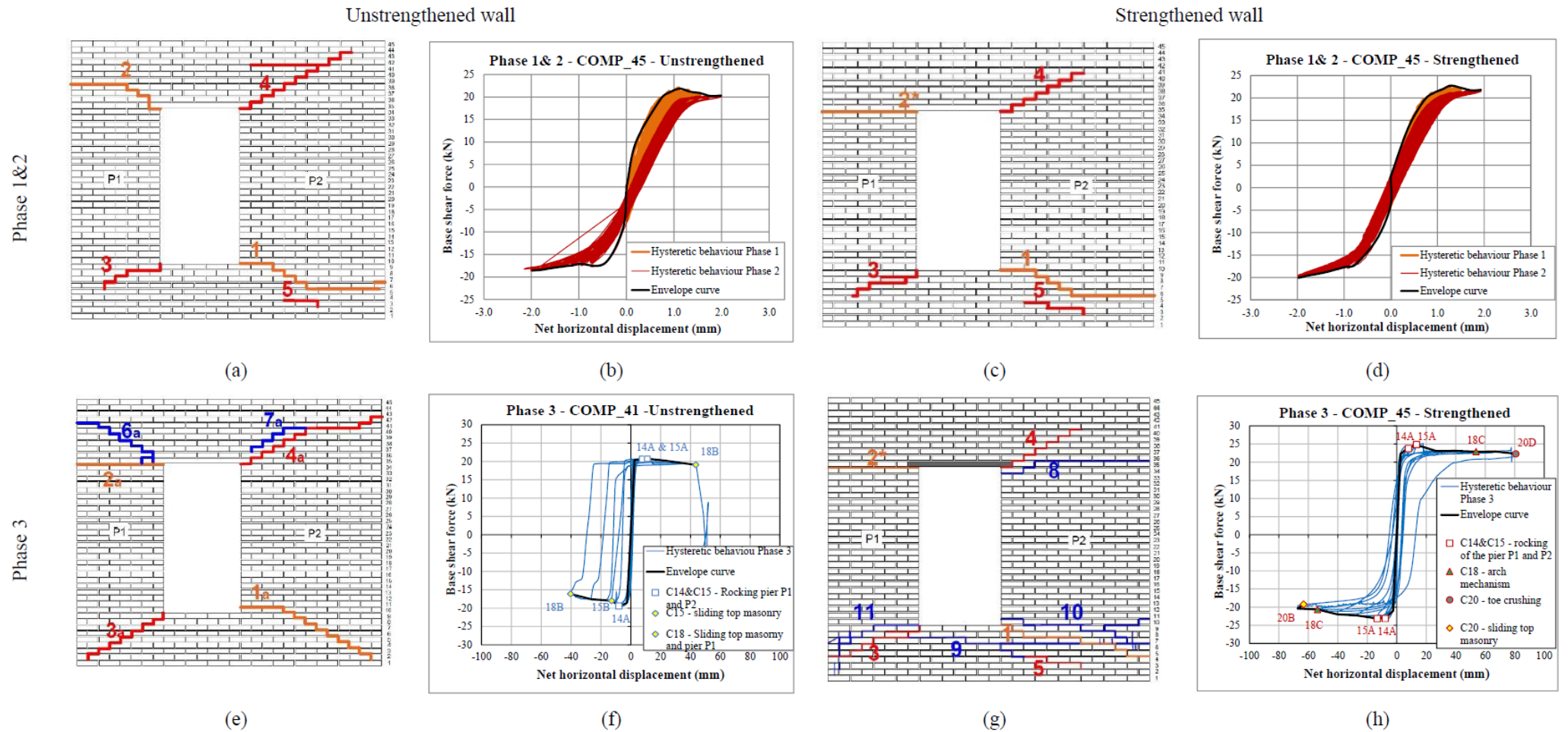
Figure 3.7: Crack pattern and base shear force versus net horizontal displacement curve: (a)-(b) un-strengthened wall during DL state; (c)-(d) strengthened wall during DL state; (e)-(f) un-strengthened wall during NC-state; (g)-(h) strengthened wall during NC state (Licciardello et al., 2021)

4

NUMERICAL MODELING
Part 1: Un-strengthened walls

The URM wall from the experiment can be modeled on different levels of detail. Three different modeling approaches are used; the *macro-model*, the *continuous micro-model* and the *detailed micro-model*. The *discrete (simplified) micro-model* is not included in this thesis research because the reinforcement bars cannot be connected to the mortar joints since they are represented with zero-thickness interface elements. The wall specimens from the experiment are simulated in the commercial software DIANA FEA version 10.4. All numerical analyses are performed on a computer with an Intel Core i7 9th Gen processor. The steps for the three modeling approaches are the same, namely starting off with a monotonic analysis as the base model for the sensitivity analysis. The sensitivity analysis is used to investigate the influence of different numerical settings and parameters as well as to find the most optimum configuration of parameters with the lowest associated computational costs, without compromising the accuracy of the results. This obtained configuration is used to perform the cyclic analysis. The URM wall tested up to the DL state is modeled using all three modeling approaches. After this, the most suited modeling approach is used to model the wall tested up to the NC state. Important to note is that pre-/post-damage are not included in the numerical models of the un-strengthened wall in this chapter, meaning that the results are compared with wall specimen (TUD_COMP-41). The models with the pre-/post-damage are investigated in Chapter 5 for the strengthened wall.

The numerical modeling of the macro-model, continuous micro-model and the detailed micro-model are elaborated for the DL state in Section 4.1, Section 4.2 and Section 4.3, respectively. Both monotonic and cyclic pushover analyses are discussed for each model. Subsequently, the numerical results of the three modeling approaches in the DL state are discussed and compared to each other in Section 4.4. The numerical analyses for the NC state are discussed in Section 4.5. Lastly, the conclusions for Chapter 4 are provided in Section 4.6.

4.1 Finite element model using macro-modeling approach

In this section, the URM wall is modeled for the DL state with a macro-modeling approach. The geometry of the FE-model including the boundary conditions are discussed in Section 4.1.1. Different adopted FE-types including information about the mesh of the model are discussed in Section 4.1.2. The adopted material models for all components are presented in Section 4.1.3. Moreover, the monotonic pushover analysis is discussed in Section 4.1.4, followed by a sensitivity analysis in Section 4.1.5. Lastly, the cyclic pushover analysis is discussed in Section 4.1.6.

4.1.1   Geometry and boundary conditions

The masonry wall is modeled with a macro-modeling approach, meaning that the bricks and the mortar joints are modeled as one homogeneous continuum. The masonry wall and the concrete lintel are simulated with 2D plane stress elements while the steel beams are simulated with beam elements. The full dimensions of the masonry wall are 3070 x 2690 x 100 mm^3 (length x height x thickness). The window opening has an area of 780 x 1510 mm^2 (length x height). The location of the opening is based on the experiment (illustrated in *Figure 3.1*). Furthermore, the concrete lintel above the window opening has a dimension of 975 x 50 x 100 mm^3. The FE macro-model including its loading and boundary conditions is illustrated in *Figure 4.1*. The cross-sectional properties per component are listed in *Table A 2* of Appendix A. Moreover, pre-/post-damage are not included in this case for the un-strengthened macro-model.

The steel beams are connected to the nodes of the bottom and top edge of the wall. This means that the steel beams are fully bonded to the wall which simulates the effect of the them being glued to the wall. It is important to note that the applications of the boundary conditions at the bottom and the vertical pre-compressive stress (overburden) at the top, are on the nodes of the side of the steel beams and not of the wall. This also holds for the application of the boundary conditions at the top left corner, where the horizontal prescibed displacement is applied to the side of the center of the top steel beam. The boundary conditions at the bottom are simulated using a line support where the displacement in x-and y-direction (u_x, u_y) and the rotation around the z-axis (φ_z) are restrained. Moreover, the boundary conditions at the top left corner is simulated using a point support where the displacement in x-direction (u_x) is restrained.
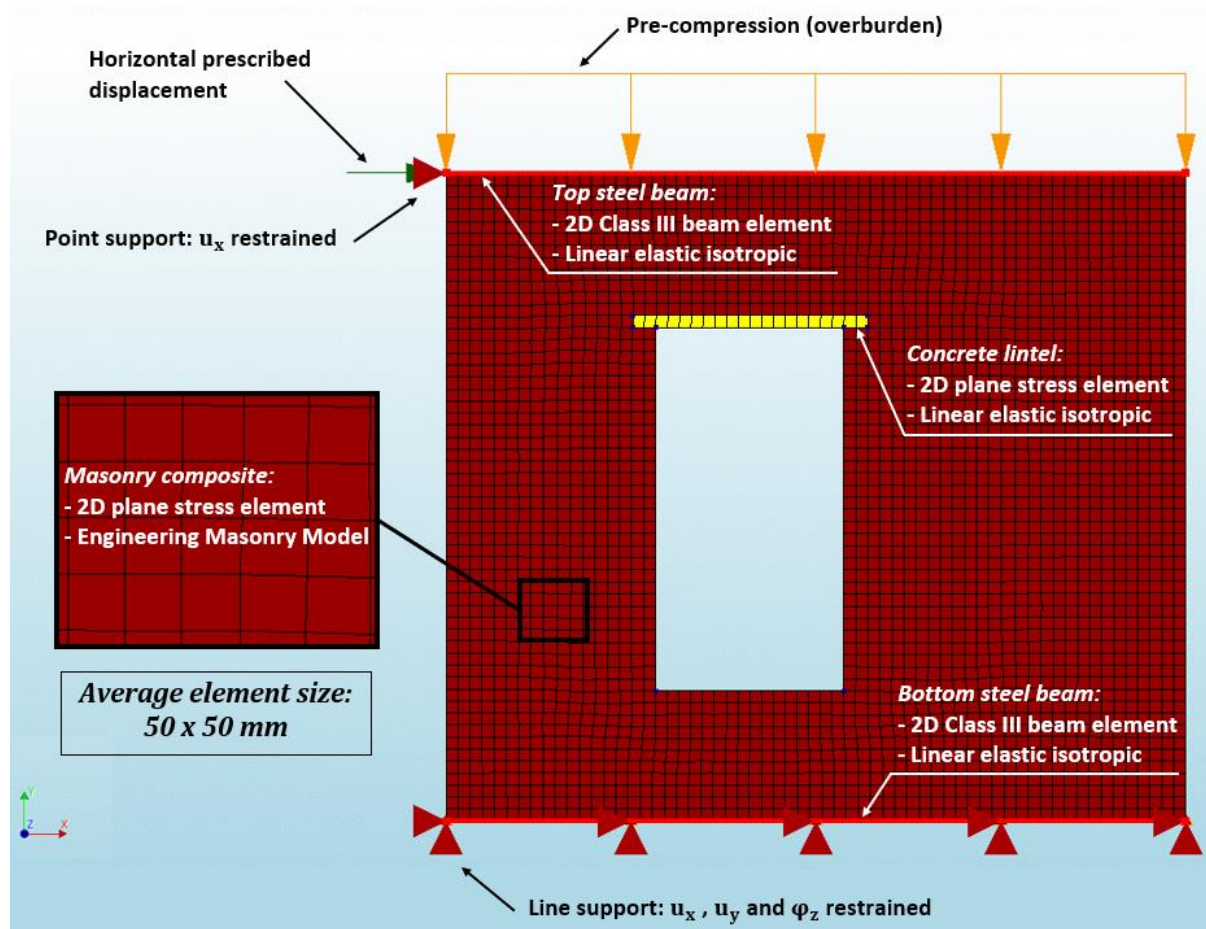
Figure 4.1: FE-model using macro-modeling approach (un-strengthened wall)

4.1.2 Finite element discretization and mesh properties

The characteristics of different FE-types which are used to simulate the macro-model and the properties of the mesh are listed in *Table A 3* of Appendix A. The top and bottom steel beams are simulated with 2-noded Class III-beam elements (L6BEA). The masonry wall and the concrete lintel are simulated with 4-noded plane stress elements (Q8MEM). An element size of 50 mm is chosen as the base model value for the macro-model.

4.1.3 Constitutive laws

The material properties for the masonry wall as a composite material are listed in *Table 2*. The smeared, continuum Engineering Masonry Model (EMM) is used to capture the nonlinear and orthotropic properties of the masonry wall. The values are taken from Table 6 from the paper by Korswagen et al. ([2019](#)). The material properties for the steel beams (*Table 3*) and the concrete lintel (*Table 4*) are kept linear elastic since the strength of these materials are much higher compared to the masonry wall. Moreover, the crack bandwidth h is determined based on the *Rot's Element Based Model* using *equation (22)* for linear 2D elements (Ferreira, [2021](#)):

$$h = \sqrt{2A} \tag{22}$$

where A is the total area of the element.

Table 2: Material properties - masonry wall as a composite material

Masonry as a composite material			
Material class	Concrete and masonry		
Material model	Engineering Masonry Model		
Elasticity parameters			
Young's modulus	E_x	2157	N/mm^2
	E_y	3087	N/mm^2
Shear modulus	G_{xy}	1354	N/mm^2
Mass density	ρ	1708	kg/m^3
Cracking parameters			
Head-joint failure type	Diagonal stair-case cracks		
Bed-joints tensile strength	f_t	0.09	N/mm^2
Fracture energy in tension	G_f^I	0.007527	N/mm
Angle between stepped diagonal crack and bed-joint	α	0.5	rad
Crushing parameters			
Compressive strength	f_c	11.35	N/mm^2
Fracture energy in compression	G_c	26.05	N/mm
Factor to strain at compressive strength	n	4	-
Unloading factor, 1= secant, 0= linear	λ	1	-
Shear failure parameters			
Friction angle	φ	0.669	rad
Cohesion	c	0.14	N/mm^2
Crack bandwidth			
Crack bandwidth specification	Rots		
Crack bandwidth	h	70.71	mm

Table 3: Material properties - steel beams

Steel beams					
	Top steel beam		Bottom steel beam		
Material class	Steel		Steel		
Material model	Linear elastic isotropic		Linear elastic isotropic		
Young's modulus	E	210000	N/mm^2	E	210000	N/mm^2
Poisson's ratio	ν	0.3	-	ν	0.3	-
Mass density	ρ	-	kg/m^3	ρ	7850	kg/m^3

Table 4: Material properties - concrete lintel

Concrete lintel			
Material class	Concrete and masonry		
Material model	Linear elastic isotropic		
Young's modulus	E	31000	N/mm^2
Poisson's ratio	ν	0.2	-
Mass density	ρ	2400	kg/m^3

4.1.4 Monotonic pushover analysis (base model)

A monotonic pushover analysis is adopted for the macro-model. This analysis is used as the base model for the sensitivity analysis (discussed in Section 4.1.5). The overburden with a value of 0.12 MPa is multiplied with the thickness of the masonry wall (100 mm) in order to obtain an uniformely distributed load of 12 N/mm, which is applied on top of the steel beam over the full length of the wall. Important to note is that the self-weight of the top steel beam is included in the overburden and therefore the mass density of this component is set to zero. Displacement-controlled load application is used for the lateral loading in order to capture the post-peak response. A prescribed displacement of 1 mm is assigned to the top left corner of the wall in order to have a load-factor (percentage of load applied) which will be equal to the load-step size. According to the experimental test by Licciardello et al. ([2021](#)), the maximum top lateral displacement of the wall (DL state) is 1.93 mm in the positive x-direction and 1.98 mm in the negative x-direction. First, the self-weight and the overburden are vertically applied with a load-step of 1.0. Subsequently, the wall is in the horizontal positive x-direction incrementally displaced with load-steps of 0.01 (193 load steps are prescribed with step sizes of 0.01 mm). Finally, the wall is in the horizontal nagative x-direction incrementally displaced with load-steps of 0.01 (391 load steps are prescribed with step sizes of 0.01 mm). The applied numerical settings and parameters are listed in *Table A 1* of Appendix A.

The numerical results are discussed in terms of interpreting the capacity curves (force-displacement curves) and the contour plots of the crack patterns. The capacity curve for the monotonic analysis is depicted in *Figure 4.2*. Several points (load-steps) are selected and marked in the graph which help to better understand the evolution and propagation of the crack pattern in the wall. These load-steps are:

1. ***Load-step A***: indicates the onset of cracking at the corners of the window when loading in the positive x-direction

2. ***Load-step B***: indicates the onset of cracking at the base of the left pier when loading in the positive x-direction

3. ***Load-step C***: indicates the maximum base shear force at maximum top lateral displacement in positive x-direction

4. ***Load-step D***: indicates the zero position

5. ***Load step E***: indicates the onset of cracking at the base of the right pier when loading in the negative x-direction

6. ***Load step F***: indicates the maximum base shear force at maximum top lateral displacement in negative x-direction

The complete set of contour plots, which correspond to each selected load-step, for showing the evolution of the crack pattern, can be found in *Figure A 1* of Appendix A.1. In this section, only the contour plots for load-step C (*Figure 4.3a*) and load-step F (*Figure 4.3b*) are presented with the final crack pattern for both loading directions at maximum top lateral displacement.

The rocking behavior of the left pier, when loading in the positive x-direction, is simulated with the macro-model which is in line with the experimental results. The stair-case crack at the bottom right corner of the opening is not captured as prominently as the one at the top right corner. Moreover, the horizontal crack at the base of the right pier starts to develop into a stair-case crack.
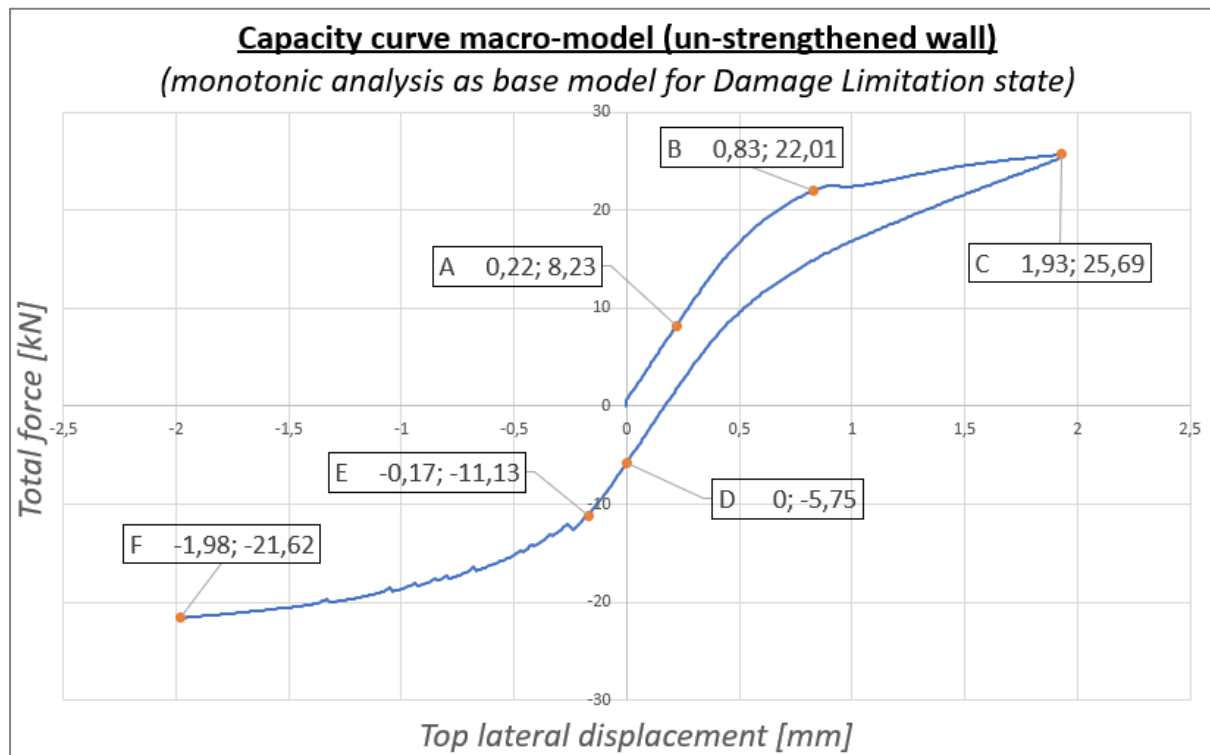
Figure 4.2: Capacity curve for monotonic pushover analysis of un-strengthened macro-model (base model)
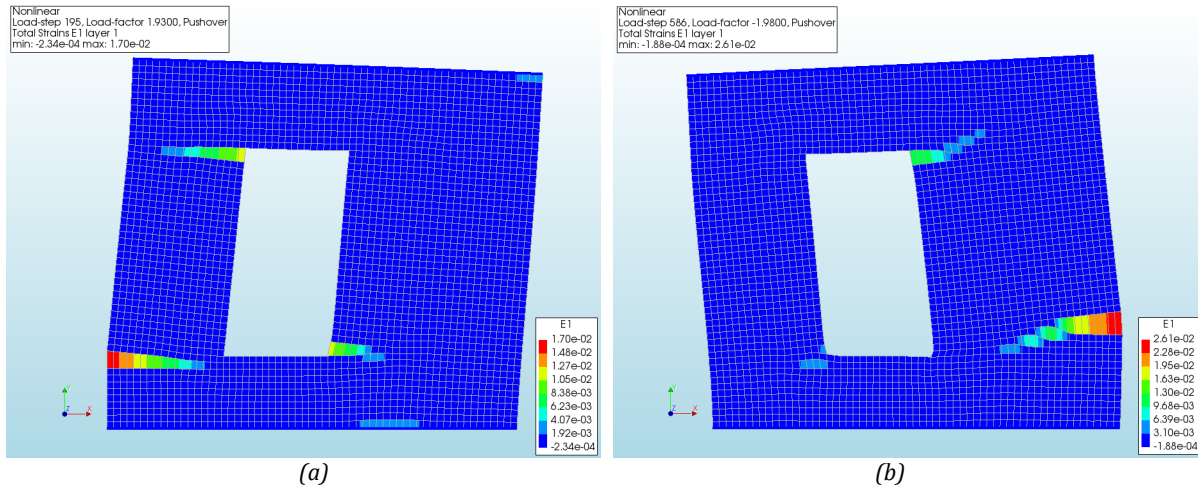
Figure 4.3: Crack pattern for monotonic pushover analysis of un-strengthened macro-model (base model) using principal strain E1 contour plots (scaling factor = 100): (a) positive x-direction; (b) negative x-direction

4.1.5 Sensitivity analysis

A sensitivity study is conducted for the macro-model using monotonic pushover analyses. The objective is to examine the influence on the results, in terms of the capacity curves and crack patterns, when changing different numerical parameters. Moreover, the objective is to find the most suitable configuration of numerical parameters with the lowest associated computational costs, without compromising the accuracy of the results, to perform the cyclic pushover analysis. The results are listed in *Table 5* where the maximum base shear forces in both loading directions are compared to the experimental found results. The numerical parameters which are checked and compared for the sensitivity analysis are: *mesh size*, *element order*, *convergence tolerance*, *satisfaction of all specified norms*, *source of nonlinearity*, *load-step size*, *iterative method* and *head-joint failure type*.

The previously conducted monotonic pushover analysis for the macro-model including all assigned properties and parameters is used as the base model for the sensitivity analysis where only one specified parameter is changed at a time. The results are presented and discussed in more detail for each numerical parameter separately in Appendix A.2. In summary, the diagonal stair-case cracks at the corners of the window opening are only well captured when choosing the head-joint failure type: *Diagonal stair-case cracks*. Some small differences can be spotted when looking at specific cracks, but the results of the sensitivity analysis consistently display the main cracks which capture the rocking failure behavior of both piers. Moreover, large diagonal cracks running across the right pier can be observed in some of the results of the sensitivity analysis (also observed in the MSc thesis by Mahmoudimotlagh, 2020). This was however not observed during the experiments. The results of the sensitivity analysis indicate that these large diagonal cracks tend to occur in the right pier when refining the numerical settings, meaning in terms of; using smaller elements, using quadratic elements, using a tighter convergence tolerance and satisfying all specified norms.

The most suitable configuration of numerical parameters must be carefully chosen so as to provide accurate yet economical solutions. When the convergence criterion is specified too tight, a lot of effort is spent in obtaining unnecessary accuracy. On the other hand, when it is specified too loose, the obtained results are inaccurate. The results of the crack pattern and the capacity curve need to be weighted against the associated computational time. Accordingly, the most optimum option for each numerical parameter comparison is highlighted in green in *Table 5*. This combination is used for the cyclic pushover analysis in Section 4.1.6.

Table 5: Results sensitivity analysis monotonic loading for macro-model (un-strengthened wall)

Results sensitivity analysis *Macro-model (un-strengthened wall)*			*Loading in positive x-direction*		*Loading in negative x-direction*		**Computational time**
			Max. base shear force	**Difference compared to experiment**	**Max. base shear force**	**Difference compared to experiment**	
			[kN]	[%]	[kN]	[%]	[min]
Experimental results: un-strengthened wall (TUD_COMP-41)			**22.05**	**-**	**-18.72**	**-**	**-**
Mesh size	25 x 25 mm		25.60	+ 16.10 %	-21.83	+ 16.61 %	28
	50 x 50 mm	*(base model)*	25.69	+ 16.51 %	-21.62	+ 15.49 %	6
	100 x 100 mm		25.84	+ 17.19 %	-21.76	+ 16.24 %	2
Element order	Linear: 50 x 50 mm	*(base model)*	25.69	+ 16.51 %	-21.62	+ 15.49 %	6
	Quadratic: 50 x 50 mm		25.01	+ 13.42 %	-21.12	+ 12.82 %	9
Convergence tolerance	Displacement (0.01)	Force (0.01)	23.88	+ 8.30 %	-21.66	+ 15.71 %	15
	Displacement (0.05)	Force (0.05) *(base model)*	25.69	+ 16.51 %	-21.62	+ 15.49 %	6
	Displacement (0.1)	Force (0.1)	25.69	+ 16.51 %	-21.37	+ 14.16 %	6
Satisfy all specified norms	Yes		23.97	+ 8.71 %	-22.43	+ 19.82 %	9
	No	*(base model)*	25.69	+ 16.51 %	-21.62	+ 15.49 %	6
Source of nonlinearity	Physical nonlinearity	*(base model)*	25.69	+ 16.51 %	-21.62	+ 15.49 %	6
	Physical + Geometric nonlinearity		25.77	+ 16.87 %	-21.68	+ 15.81 %	6
Load-step size	0.005(386) -0.005(782)		25.95	+ 17.69 %	-21.71	+ 15.97 %	12
	0.01(193) -0.01(391)	*(base model)*	25.69	+ 16.51 %	-21.62	+ 15.49 %	6
	0.02(97) -0.02(196)		25.75	+ 16.78 %	-21.44	+ 14.53 %	4
Iterative method	Regular Newton-Raphson	*(base model)*	25.69	+ 16.51 %	-21.62	+ 15.49 %	6
	Modified Newton-Raphson		25.69	+ 16.51 %	-21.16	+ 13.03 %	7
	Secant (Quasi-Newton)		30.85	+ 39.91 %	-22.92	+ 22.44 %	6
Head-joint failure type	Head- joints failure not considered		26.94	+ 22.18 %	-22.48	+ 20.09 %	6
	Direct input head-joint tensile strength		26.16	+ 18.64 %	-21.35	+ 14.05 %	6
	Diagonal stair-case cracks	*(base model)*	25.69	+ 16.51 %	-21.62	+ 15.49 %	6
	Tensile strength head-joint defined by friction		26.24	+ 19.00 %	-21.62	+ 15.49 %	6

Marked in green = most optimum configuration of numerical parameters in terms of accurate results (crack pattern and capacity curve) with reasonable associated computational time

4.1.6   Cyclic pushover analysis

A cyclic pushover analysis is conducted for the un-strengthened macro-model. The cyclic pushover analysis is based on the loading protocol which is adopted in the experiment. The first, repetitive (one-way cyclic) quasi-static loading section is referred to as Phase 1. This section consists of five cycles with 30 runs per cycle. The second, cyclic (two-way) quasi-static loading section is referred to as Phase 2 and consists of seven cycles of 30 runs each. A cyclic analysis with the full loading protocol is highly likely to be computationally expensive. Therefore, the loading protocol is reduced to only one run per cycle of loading. The adopted loading scheme is illustrated in *Figure 4.4*.
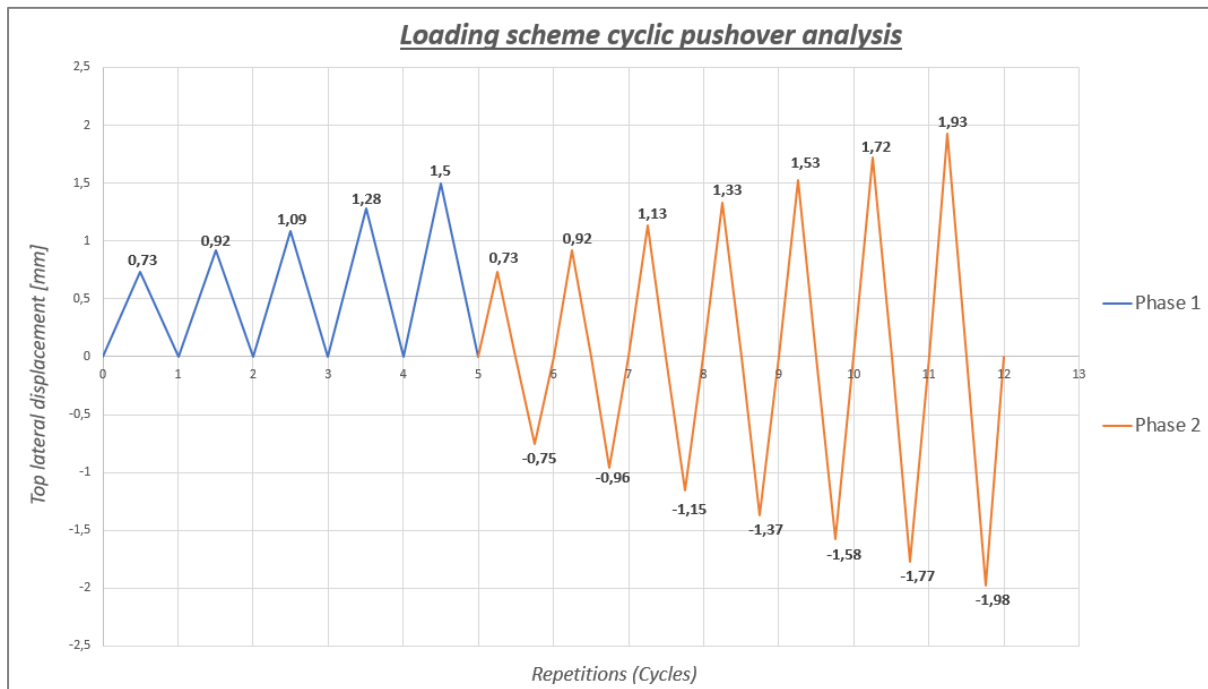
Figure 4.4: Loading scheme cyclic pushover analysis

For the cyclic pushover analysis, a prescribed displacement of 1 *mm* is also applied at the top left support in order to have a load-factor (percentage of load applied) which will be equal to the load-step size. First, the self-weight and the overburden is vertically applied with a load-step of 1.0. Subsequently, the cyclic loading is applied using a load step size of 0.02 *mm* with the corresponding amount of steps per cycle to obtain the maximum horizontal displacements according to the cyclic loading scheme (*Figure 4.4*).

The results of the cyclic and monotonic analyses are compared with each other, as well as with the experimental results. The comparison is done by interpreting the capacity curves and the crack pattern. The most optimum configuration of numerical parameters and settings, obtained from the sensitivity analysis, is used for the monotonic and cyclic analysis.

The capacity curves are illustrated in *Figure 4.5*. The pattern of the capacity curves are in a reasonable agreement with the experiment. Important to note is that the force reduction is not captured by the numerical model. The maximum base shear force is located at the maximum horizontal displacement (see capacity curve monotonic loading). The peak force for the experiment is located at around a horizontal displacement of 1.25 mm, after which the capacity

is gradually decreasing. According to Drougkas et al. (2020), the force reduction can be partly attributed to the influence of out-of-plane deflection which is not simulated with a 2D model where the deformation is captured perfectly in-plane. Moreover, the numerical models are expected to be stronger due to perfect conditions. Imperfections such as weak brick-mortar bonds can occur locally in the wall in the experiment. Because of these reasons, the maximum base shear forces are overestimated in both loading directions for the numerical models. Moreover, the energy dissipation is slightly underestimated compared with the experiment. On the other hand, the initial stiffness in both loading directions are in good agreement with the experiment.
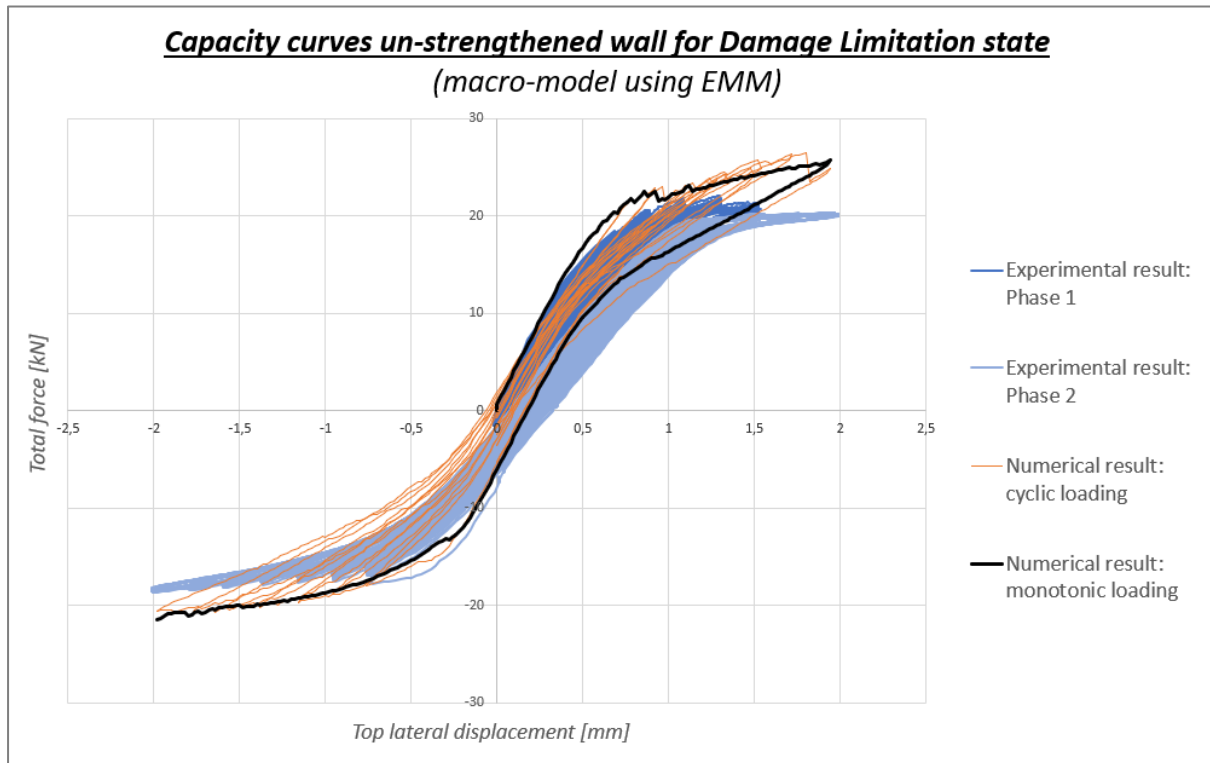
Figure 4.5: Capacity curve monotonic and cyclic pushover analysis comparison for macro-model (un-strengthened wall)

The final crack patterns for both monotonic and cyclic analysis are illustrated in *Figure 4.6*. Considering the crack pattern for the positive x-direction, the crack at the top of the left pier (crack number 2a) is in good agreement with the experiment. This crack starts from the top left corner of the window and develops horizontally over the width of the pier. However, the separation of the left pier with respect to the top spandrel is not simulated by the numerical model because the length of the crack is underestimated compared to the experiment. The propagation of the crack, starting at the bottom right corner of the window (crack number 1a), is mainly diagonal. This crack initiates as a horizontal crack and then develops into a diagonal stair case crack which is in line with the experiment. Furthermore, the rocking failure behavior of the left pier can be observed due to the horizontal crack occurring along the base of the pier.

Considering the crack pattern for the negative x-direction, the diagonal stair-case crack starting at the top right corner of the window (crack number 4a) is simulated accordingly to the experiment. However, the stair-case crack starting at the bottom left corner of the window (crack number 3a) is underestimated in its length. Moreover, the horizontal crack at the base of

the right pier develops from a horizontal crack into a diagonal stair-case crack. In contrary, this crack is a pure horizontal crack in the experiment.

The capacity curve obtained from the monotonic analysis follows the outline of the capacity curves for the cyclic analysis as the envelope curve. The results for both loading cases are very similar in terms of the shape of the obtained capacity curve and the crack pattern. The maximum base shear forces in both loading directions for both monotonic and cyclic analysis are listed in *Table 6*. The values are close when comparing both analyses with each other. The computational time for the cyclic analysis is larger. When looking at the results in terms of the crack pattern, small differences can be spotted when comparing specific cracks. Considering the cyclic analysis, the cracks at the top and the bottom of the left pier are propagating more as a stair-case crack, while these cracks are propagating more in the horizontal direction for the monotonic analysis. As was observed in the results of the sensitivity analysis, diagonal cracks running across the right pier start to occur at the end of the cyclic analysis. Although some small differences can be spotted, the results of the monotonic and cyclic analysis consistently display the main cracks which capture the rocking failure behavior of both piers.

Lastly, the maximum crack width w for each main crack is also indicated in *Figure 4.6*. However, because the pre-/post-damage are not included in the numerical models in this chapter, a direct comparison with the experiment cannot be made since the experimental obtained values (*Table 1*) are for the pre-damaged/ un-strengthened wall (TUD_COMP-45). The results of the crack width for the un-strengthened wall in this chapter are compared with the strengthened wall in Chapter 5. It can be observed that the results of the cyclic analysis are close to the monotonic analysis in terms of the maximum crack width and also the crack length. The largest difference (in terms of crack width) is 20% for the horizontal crack at the base of the left pier.

Table 6: Comparison numerical results monotonic vs cyclic analysis for macro-model (un-strengthened wall)

	Positive x-direction		Negative x-direction		Time
	Max. base shear force	Difference compared to experiment	Max. base shear force	Difference compared to experiment	
	[kN]	[%]	[kN]	[%]	[min]
Experimental results	**22.05**	**-**	**-18.72**	**-**	**-**
Monotonic analysis	25.75	+ 16.78 %	-21.44	+ 14.53 %	4
Cyclic analysis	26.47	+ 20.05 %	-20.94	+ 11.86 %	29

Macro-model (un-strengthened wall)

(Crack pattern numerical results vs experimental results for Damage Limitation state with the maximum crack width w [mm] indicated)
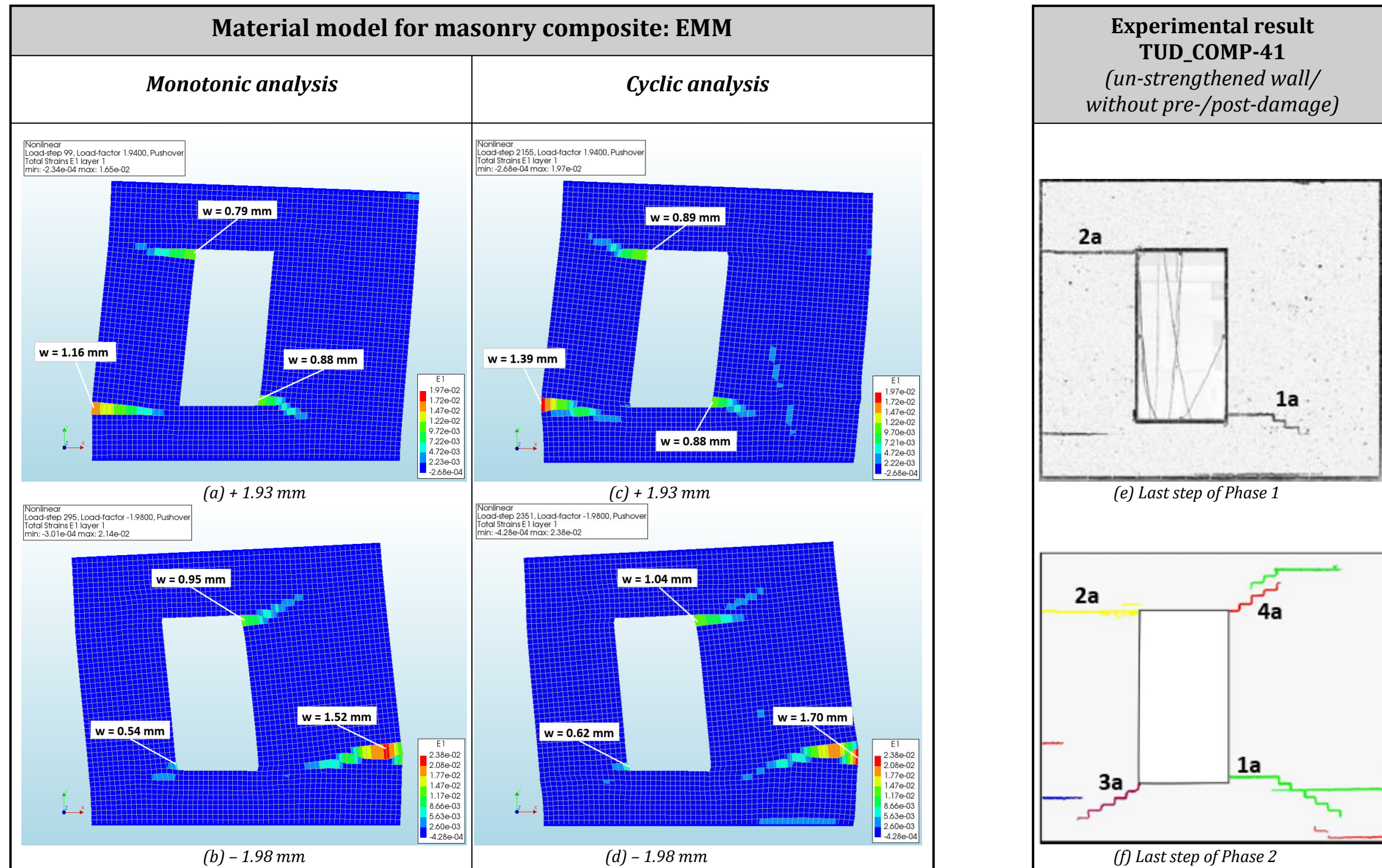
Figure 4.6: Cracking pattern at maximum top displacement of monotonic and cyclic analysis (DL state) for macro-model using contour plots principal strain E1 (scaling factor = 100)

4.2 Finite element model using continuous micro-modeling approach

In this section, the URM wall is modeled for the DL state with a continuous micro-modeling approach. The properties of the model with the adopted assumptions are presented in a similar order like the previously discussed macro-model. The geometry of the FE-model including the boundary conditions are discussed in Section 4.2.1. Different adopted FE-types including information about the mesh of the model are discussed in Section 4.2.2. The adopted material models for all components are presented in Section 4.2.3. Moreover, the monotonic pushover analysis is discussed in Section 4.2.4, followed by a sensitivity analysis in Section 4.2.5. Lastly, the cyclic pushover analysis is discussed in Section 4.2.6.

4.2.1 Geometry and boundary conditions

The geometry and boundary conditions for the continuous micro-model are the exact same as the previously discussed macro-model (see Section 4.1.1). However, the bricks and the mortar joints are modeled separately, each with their own material properties assigned. The dimensions of the clay bricks are 210 x 50 x 100 mm^3 (length x height x thickness). The thickness of the mortar joints is 10 mm. The bricks, mortar joints and concrete lintel are simulated with 2D plane stress elements while the steel beams are simulated with beam elements. The FE continuous micro-model including its loading and boundary conditions is illustrated in *Figure 4.7*. The cross-sectional properties are also the same as the previous model (*Table A 2* of Appendix A). However, separate thicknesses for the bricks and mortar joints are specified for the continuous micro-model which are both 100 mm. Again, the pre-/post-damage are not included in this case for the un-strengthened continuous micro-model.
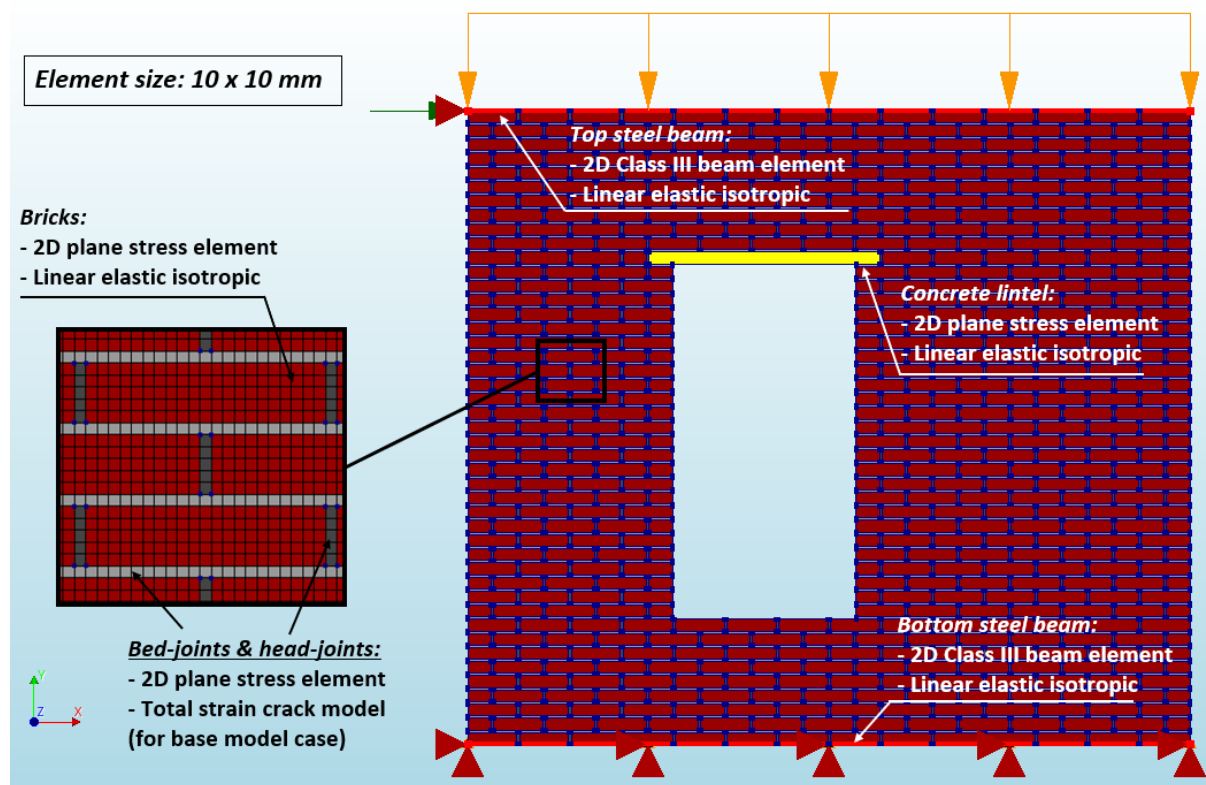
Figure 4.7: FE-model using continuous micro-modeling approach (un-strengthened wall)

4.2.2   Finite element discretization and mesh properties

The characteristics of all different FE-types which are used to simulate the continuous micro-model are listed in *Table A 3* of Appendix A. The top and bottom steel beams are again simulated with 2-noded Class III-beam elements (L6BEA). The masonry bricks, concrete lintel and mortar joints are simulated with 4-noded plane stress elements (Q8MEM). An element size of 10 *mm* is chosen for the analyses of the continuous micro-models to match the thickness of the mortar joints. The properties for the mesh are listed in *Table B 2* of Appendix B.

4.2.3   Constitutive laws

According to Korswagen et al. ([2019](#)), no damage was observed in the masonry bricks during the experiment. For this reason, the material properties of the bricks (*Table 8*) are kept linear elastic, meaning that all nonlinear properties are gathered in the mortar joints. This is also done in order to reduce the computational expenses. The material properties for the steel beams and the concrete lintel are kept linear elastic just like the macro-model and are listed in *Table 3* and *Table 4*, respectively in Section 4.1.3. The nonlinear material properties of the mortar joints are listed in *Table 7*. The *Toal Strain Crack model (TSCM)* is used for the mortar joints since the material by itself is an isotropic material. It should be noted that the material properties for the bed-joint and the head-joints are specified separately. The values are taken from Table 5 from the paper by Korswagen et al. ([2019](#)). Moreover, the crack bandwidth h is also determined based on the *Rot's Element Based Model* using *equation (22).*

Table 7: Material properties - mortar joints

Mortar joints						
Material class	Concrete and masonry					
Material model	Total strain based crack model					
Crack orientation	Rotating					
Linear material properties						
	Bed-joints			**Head-joints**		
Young's modulus	E	1000	N/mm^2	E	4600	N/mm^2
Poisson's ratio	ν	0.14	-	ν	0.14	-
Mass density	ρ	1708	kg/mm^3	ρ	1708	kg/mm^3
Tensile behavior						
Tensile curve	Linear-crack energy					
Tensile strength	f_t	0.09	N/mm^2	f_t	0.05	N/mm^2
Mode-I tensile fracture energy	G_f^I	0.00753	N/mm	G_f^I	0.00499	N/mm
Crack bandwidth specification	Rots					
Crack bandwidth	h	14.14	mm	h	14.14	mm
Compressive behavior						
Compression curve	Parabolic			Elastic		
Compressive strength	f_c	3.81	N/mm^2	f_c	-	N/mm^2
Compressive fracture energy	G_c	6.4	N/mm	G_c	-	N/mm

Table 8: Material properties - masonry bricks

Masonry bricks			
Material class		Concrete and masonry	
Material model		Linear elastic isotropic	
Young's modulus	E	8049	N/mm^2
Poisson's ratio	ν	0.16	-
Mass density	ρ	1708	kg/m^3

4.2.4   Monotonic pushover analysis (base model)

A monotonic pushover analysis is adopted for the continuous micro-model. This analysis is used as the base model for the sensitivity analysis (discussed in Section 4.2.5). The same loading cases as for the macro-model are used for the continuous micro-model. The used numerical settings and parameters are listed in *Table B 1* of Appendix B. The load-step size for the pushover loading is 0.04 *mm* with the corresponding amount of load-steps to reach the maximum top lateral displacement (+1.93 mm in the positive x-direction and -1.98 mm in the negative x-direction for the DL state).

The results are discussed in terms of interpreting the capacity curves and the contour plots of the crack patterns. The capacity curve for the monotonic analysis is depicted in *Figure 4.8*. Several points (load-steps) are selected and marked in the curve which help to better understand the evolution and propagation of the crack pattern in the wall. It should be noted that the maximum base shear forces in both loading direction are not occurring at the maximum top lateral displacement. The load-steps are identified as follow:

1. ***Load-step A*:** indicates the onset of cracking at the corners of the window when loading in the positive x-direction

2. ***Load-step B*:** indicates the onset of cracking at the base of the left pier when loading in the positive x-direction

3. ***Load-step C*:** indicates the peak load in positive x-direction

4. ***Load-step D*:** indicates the maximum top lateral displacement in the positive x-direction

5. ***Load-step E*:** indicates the zero position

6. ***Load-step F*:** indicates the onset of cracking at the right base of the wall when loading in the negative x-direction

7. ***Load-step G*:** indicates the peak load in negative x-direction

8. ***Load-step H*:** indicates the maximum top lateral displacement in the negative x-direction

The complete set of contour plots, which correspond to each selected load-step, for showing the evolution of the crack pattern are illustrated in *Figure B 1* of Appendix B.1. In this section, only the contour plots for load-step D (*Figure 4.9a*) and load-step H (*Figure 4.9b*) are presented with the final crack pattern for both loading directions at maximum top lateral displacement.

The diagonal stair-case cracks starting at the corners of the window opening are well captured by the continuous micro-model. However, instead of a crack running horizontally at the top of the left pier, which was simulated by the previously discussed macro-model, the crack at the top left corner of the window is developing into a diagonal stair-case crack. Moreover, the horizontal crack (loading in negative x-direction) is occuring at the right base of the wall rather than at the base of the right pier.
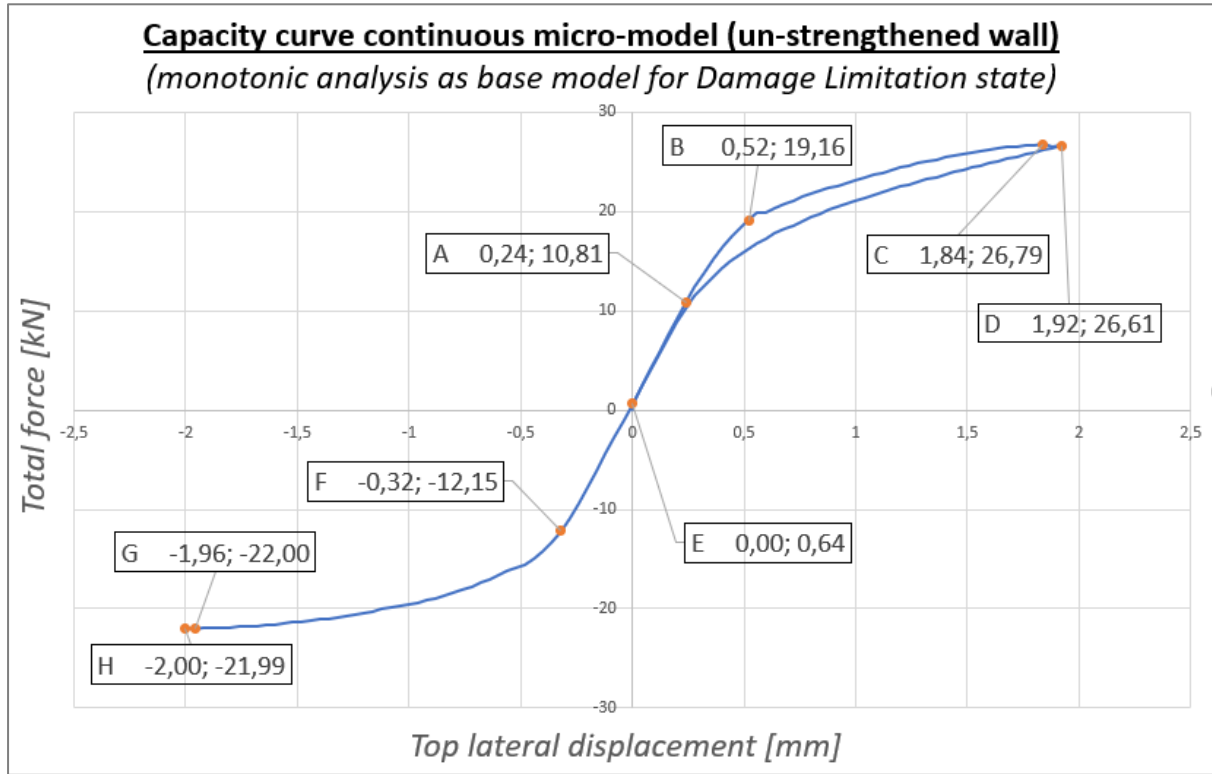
Figure 4.8: Capacity curve for monotonic pushover analysis of un-strengthened continuous micro-model (base model)
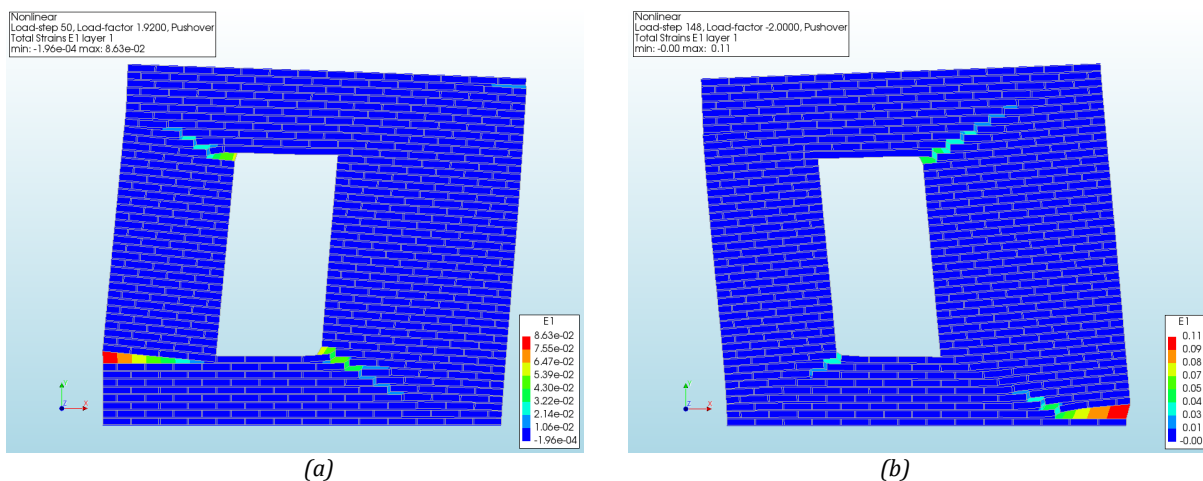
Figure 4.9: Crack pattern for monotonic pushover analysis of un-strengthened continuous micro-model (base model) using principal strain E1 contour plots (scaling factor = 100): (a) positive x-direction; (b) negative x-direction

4.2.5   Sensitivity analysis

A sensitivity study is also conducted for the monotonic pushover analysis for the continuous micro-model. It should be noted that the sensitivity analysis is only done for the continuous micro-model using the *TSCM* for the mortar joints. The results are listed in *Table 9* in which the maximum base shear forces in both loading directions are compared to the experimental found results. The parameters which are checked and compared for the sensitivity analysis are the same as for the macro-model, except for the material input parameters since the mortar joints are modeled separately. The material properties are herein checked for different combinations of Young's modulus and tensile strength for the bed- and head-joints. Important to note is that when changing the values of the tensile strength f_t for the mortar joints, the fracture energy G_{ft} also needs to be changed proportionally because these two parameters are linked to each other according to *equation(13)*.

The performed monotonic pushover analysis for the continuous micro-model with all assigned properties and parameters is used as the base model for the sensitivity analysis where only one specified parameter is changed at a time. The results are presented and discussed in more detail for each numerical parameter separately in Appendix B.2. In summary, the diagonal stair-case cracks starting at the corners of the window opening are only well captured when choosing an element size which matches the thickness of the mortar joints (10 mm). This is because the nonlinearity are only located in the mortar joints. It can be observed that the crack pattern is very sensitive to changes in the numerical settings and parameters. This is especially the case for the crack at the top of the left pier. Depending on the numerical settings and the material properties, this crack can develop from a diagonal stair-case crack into a horizontal crack, running across the entire width of the left pier. Moreover, this crack is not always propagating perfectly as a continuous stair-case crack. Although small differences can be spotted when looking at specific cracks, the results of the sensitivity analysis consistently display the main cracks which capture the main rocking failure behavior of the left pier.

When comparing the values of the obtained maximum base shear forces in both loading directions for each category of numerical settings (*Table 9*), it can be observed that the differences are rather small. This can also be seen in the results of the capacity curves (*Figure B 7* of Appendix B.2) where the graphs are overlapping each other because the results are very close to each other. However, large differences can be found when looking at the computational time.

Similar to the sensitivity analysis for the monotonic pushover analysis of the macro-model, the most suitable configuration of numerical parameters must be carefully chosen so as to provide accurate yet economical solutions. The most optimum option for each numerical parameter comparison is highlighted in green in *Table 9*. This combination is used for the cyclic pushover analysis which is discussed in Section 4.2.6.

Table 9: Results sensitivity analysis monotonic loading for continuous micro-model using TSCM for mortar joints (un-strengthened wall)

Results sensitivity analysis *Continuous micro-model (un-strengthened wall)*				*Loading in positive x-direction*		*Loading in negative x-direction*		**Computational time**
				Max. base shear force	**Difference compared to experiment**	**Max. base shear force**	**Difference compared to experiment**	
				[*kN*]	[%]	[*kN*]	[%]	[*min*]
Experimental results: un-strengthened wall (TUD_COMP-41)				**22.05**	-	**-18.72**	-	-
Mesh size	10 x 10 mm		*(base model)*	26.79	+ 21.50 %	-22.00	+ 17.52 %	60
	50 x 50 mm			25.04	+ 13.56 %	-21.27	+ 13.62 %	10
	100 x 100 mm			25.17	+ 14.15 %	-21.26	+ 13.57 %	6
Element order	Linear: 10 x 10 mm		*(base model)*	26.79	+ 21.50 %	-22.00	+ 17.52 %	60
	Quadratic: 10 x 10 mm			26.45	+ 19.95 %	-21.40	+ 14.32 %	190
Convergence tolerance	Displacement (0.01)	Force (0.01)	Energy (0.001)		26.31	+ 19.32 %	-21.78	+ 16.35 %	174
	Displacement (0.005)	Force (0.005)	Energy (-)		26.48	+ 20.09 %	-21.83	+ 16.61 %	128
	Displacement (0.01)	Force (0.01)	Energy (-)	*(base model)*	26.79	+ 21.50 %	-22.00	+ 17.52 %	60
	Displacement (0.05)	Force (0.05)	Energy (-)		26.84	+ 21.72 %	-22.44	+ 19.87 %	31
Satisfy all specified norms	Yes		*(base model)*	26.79	+ 21.50 %	-22.00	+ 17.52 %	60
	No			26.71	+ 21.13 %	-22.01	+ 17.57 %	58
Source of nonlinearity	Physical nonlinearity		*(base model)*	26.79	+ 21.50 %	-22.00	+ 17.52 %	60
	Physical + Geometric nonlinearity			26.92	+ 22.09 %	-22.09	+ 18.00 %	72
Load-step size	0.01(193) -0.01(391)			26.37	+ 19.59 %	-21.76	+ 16.24 %	254
	0.02(97) -0.02(196)			26.52	+ 20.27 %	-21.69	+ 15.87 %	132
	0.04(48) -0.04(98)		*(base model)*	26.79	+ 21.50 %	-22.00	+ 17.52 %	60
Iterative method	Regular Newton-Raphson		*(base model)*	26.79	+ 21.50 %	-22.00	+ 17.52 %	60
	Modified Newton-Raphson			26.84	+ 21.72 %	-21.92	+ 17.09 %	63
	Secant (Quasi-Newton)			26.26	+ 19.09 %	-21.64	+ 15.60 %	102
Material input parameters	*Different combinations Young's modulus comparison*							
	$E_{bed\,joints} = 1000 N/mm^2$	$E_{head\,joints} = 4600 N/mm^2$	*(base model)*	26.79	+ 21.50 %	-22.00	+ 17.52 %	60
	$E_{bed\,joints} = 1000 N/mm^2$	$E_{head\,joints} = 500 N/mm^2$		26.28	+ 19.18 %	-21.59	+ 15.33 %	51
	$E_{bed\,joints} = 1000 N/mm^2$	$E_{head\,joints} = 1000 N/mm^2$		26.55	+ 20.41 %	-21.82	+ 16.56 %	50
	Different combinations mortar tensile strength comparison							
	$f_{t,\,bed-joints} = 0.09\,N/mm^2$ $G_{ft,\,bed-joints} = 0.00753\,N/mm$	$f_{t,\,head-joints} = 0.05\,/mm^2$ $G_{ft,\,head-joints} = 0.00499\,N/mm$	*(base model)*	26.79	+ 21.50 %	-22.00	+ 17.52 %	60
	$f_{t,\,bed-joints} = 0.09\,N/mm^2$ $G_{ft,\,bed-joints} = 0.00753\,N/mm$	$f_{t,\,head-joints} = 0.09\,/mm^2$ $G_{ft,\,head-joints} = 0.00753\,N/mm$		26.45	+ 19.95 %	-22.05	+ 17.79 %	68

Marked in green = most optimum configuration of numerical parameters in terms of accurate results (cracking pattern and capacity curve) with reasonable associated computational time

4.2.6   Cyclic pushover analysis

Cyclic pushover analyses are conducted using the continuous micro-modeling approach. Both the *Total Strain Crack Model (TSCM)* and the *Engineering Masonry model (EMM)* are used for the mortar joints for separate models. The results of these two material models are compared to each other as well as to the experiment. The material properties for the EMM are listed in *Table B 3* of Appendix B. Furthermore, the loading protocol is also reduced to only one run per cycle of loading for the continuous micro-model (Korswagen et al., 2019). First, the self-weight and the overburden is vertically applied with a load-step of 1.0. Subsequently, the cyclic loading is applied in load steps of 0.04 (step sizes of 0.04 mm) with the corresponding amount of steps per cycle to obtain the maximum horizontal displacement according to the loading scheme presented in *Figure 4.4*.

The results of the cyclic and monotonic analyses are compared with each other, as well as with the experimental results. The comparison is done by interpreting the capacity curves and the crack pattern. The most optimum configuration of numerical parameters and settings, obtained from the sensitivity analysis, is used for both monotonic and cyclic analysis. Important to note is that the EMM is mainly developed to simulate masonry as a composite material, for which the orthotropic behavior can be captured by using different properties for the elasticity, strength and toughness. However, the bricks in the model for this study are kept linear elastic which means that cracking can only occur in the mortar joints. For this reason, the EMM is adapted by setting the aforementioned properties the same in both x-and y-directions, since mortar by itself is an isotropic material. This is done according to previous numerical simulations which were carried out by researchers at the TU-Delft (Korswagen et al., 2019b).

The capacity curves for the continuous micro-model using TSCM and EMM for the mortar joints are illustrated in *Figure 4.10* and *Figure 4.11*, respectively. The pattern of the capacity curves are in a reasonable agreement with the experiment. Similar to the results of the previously discussed macro-model, the force reduction is not captured by the continuous micro-model for both material models. Again, this can be explained by the fact that the numerical models are expected to be stronger due to perfect conditions, resulting in an overestimation of the obtained maximum base shear forces in both loading directions. A limitation of the TSCM is the underestimation of the energy dissipation, meaning that the hysteretic behavior is not captured because the material model does not allow for elastic unloading (only secant). For this reason, the capacity curve always goes back to the origin after each cycle. On the other hand, the improvement in the energy dissipation can be seen when using the EMM for the mortar joints because this model does allow for elastic unloading. Moreover, the initial stiffness in both loading directions for both material models are in good agreement with the experiment.

The final crack patterns for both material models using both monotonic and cyclic analysis are illustrated in *Figure 4.12*. Some differences in the crack patterns can be observed between the two different material models. The results for the model using the TSCM for the mortar joints are discussed first. Considering the crack pattern for the positive x-direction, the crack at the top of the left pier (crack number 2a) is simulated slightly different compared with the experiment. This crack starts to from at the top left corner of the window opening and develops from a diagonal stair-case crack into a horizontal crack, resulting in a separation of the left pier with respect to the top spandrel. However, this crack is a pure horizontal crack in the experiment. The propagation of the crack, starting at the bottom right corner of the window (crack number 1a), is mainly diagonal in the numerical model. This crack initiates as a horizontal crack and then develops into a diagonal stair case crack in the experiment. Furthermore, the rocking failure behavior of the left pier can be observed due to the horizontal crack occurring along the bed-joint at the base of the pier. Considering the crack pattern for the negative x-direction, both diagonal stair-case cracks at the corners of the window are simulated.

However, the stair-case crack, starting at the bottom left corner of the window (crack number 3a), is underestimated in its length. Moreover, rocking of the wall is simulated numerically with a horizontal crack occurring at the bottom right corner of the wall. No rocking of the right pier is simulated by the model using the TSCM for the mortar joints.

When looking at the crack pattern for the model using the EMM for the mortar joints and considering the positive x-direction, the crack at the top of the left pier (crack number 2a) is also simulated slightly different compared with the experiment. No separation of the left pier with respect to the spandrel can be observed since the crack is not running along the full width of the pier. The diagonal stair-case crack, starting at the bottom right corner of the window (crack number 1a) and the horizontal crack at the base of the left pier, are similar to the model using the TSCM and in a good agreement with the experiment. Considering the crack pattern for the negative x-direction, the rocking failure behavior of the right pier can be observed due to the horizontal crack occurring along the bed-joint at the base of the pier. The diagonal stair-case crack starting at the top right corner of the window (crack number 4a) is in a good agreement with the experiment. On the other hand, the diagonal stair-case crack starting at the bottom left corner of the window (crack number 3a) is underestimated in its length.

The capacity curves obtained from the monotonic analyses for both material models follows the outline of the capacity curves for the cyclic analyses as the envelope curves. The results for both loading cases, when looking at both material models seperately, are very similar in terms of the shape of the obtained capacity curves and the crack patterns. The maximum base shear forces in both loading directions for both monotonic and cyclic analysis are listed in *Table 10*. The values are close when comparing both analyses with each other. The computational time for the cyclic analysis is significantly larger compared to the monotonic anlysis. When looking at the results in terms of the crack pattern (*Figure 4.12*), the monotonic analysis is almost identical to the cyclic analysis for both material models.

Table 10: Comparison numerical results monotonic vs cyclic analysis for continuous micro-model (un-strengthened wall)

		Positive x-direction		*Negative x-direction*		**Time**
		Max. base shear force	**Difference compared to experiment**	**Max. base shear force**	**Difference compared to experiment**	
		$[kN]$	$[\%]$	$[kN]$	$[\%]$	$[min]$
Experimental results		**22.05**	**-**	**-18.72**	**-**	**-**
TSCM	Monotonic analysis	26.71	+ 21.13 %	-22.01	+ 17.57 %	58
	Cyclic analysis	26.24	+ 19.00 %	-21.91	+ 17.04 %	322
EMM	Monotonic analysis	26.38	+ 19.64 %	-21.70	+ 15.92 %	36
	Cyclic analysis	26.18	+ 18.73 %	-21.25	+ 13.51 %	275

Lastly, the maximum crack width *w* for each main crack is also indicated in *Figure 4.12* for both material models. Again, because the pre-/post-damage are not included in the numerical models in this chapter, a direct comparison with the experiment cannot be made since the experimental obtained values (*Table 1*) are for the pre-damaged/ un-strengthened wall (TUD_COMP-45). The results in this chapter are compared with the strengthened wall in Chapter 5. On the other hand, it can be observed that the values for the continuous micro-model using the EMM are overall larger than the ones obtained with the model using the TSCM. The results of the monotonic and cyclic analysis are very close in terms of the maximum crack width and also the crack length. The largest difference (in terms of crack width) is 13% for crack number 3a in the model using the TSCM and 24% for crack number 1a in the continuous micro-model using the EMM.
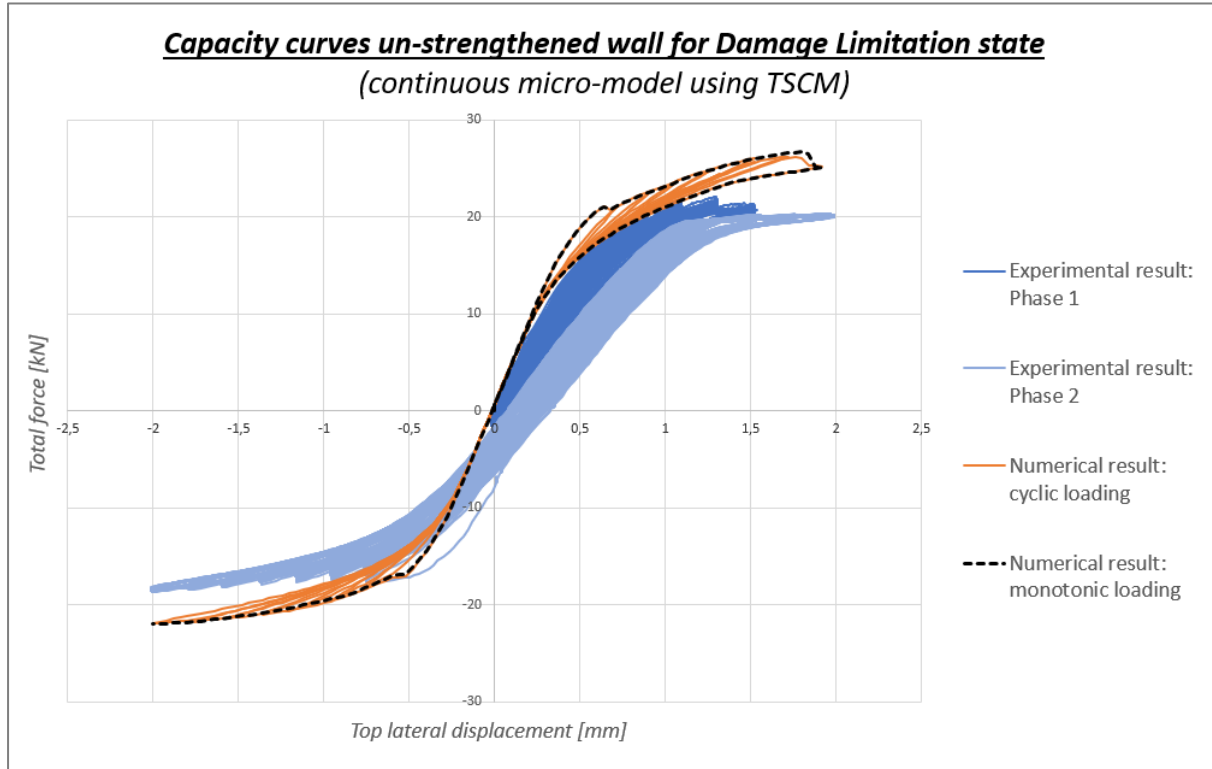
Figure 4.10: Capacity curve monotonic and cyclic pushover analysis vs experiment for continuous micro-model using TSCM for the mortar joints (un-strengthened wall)
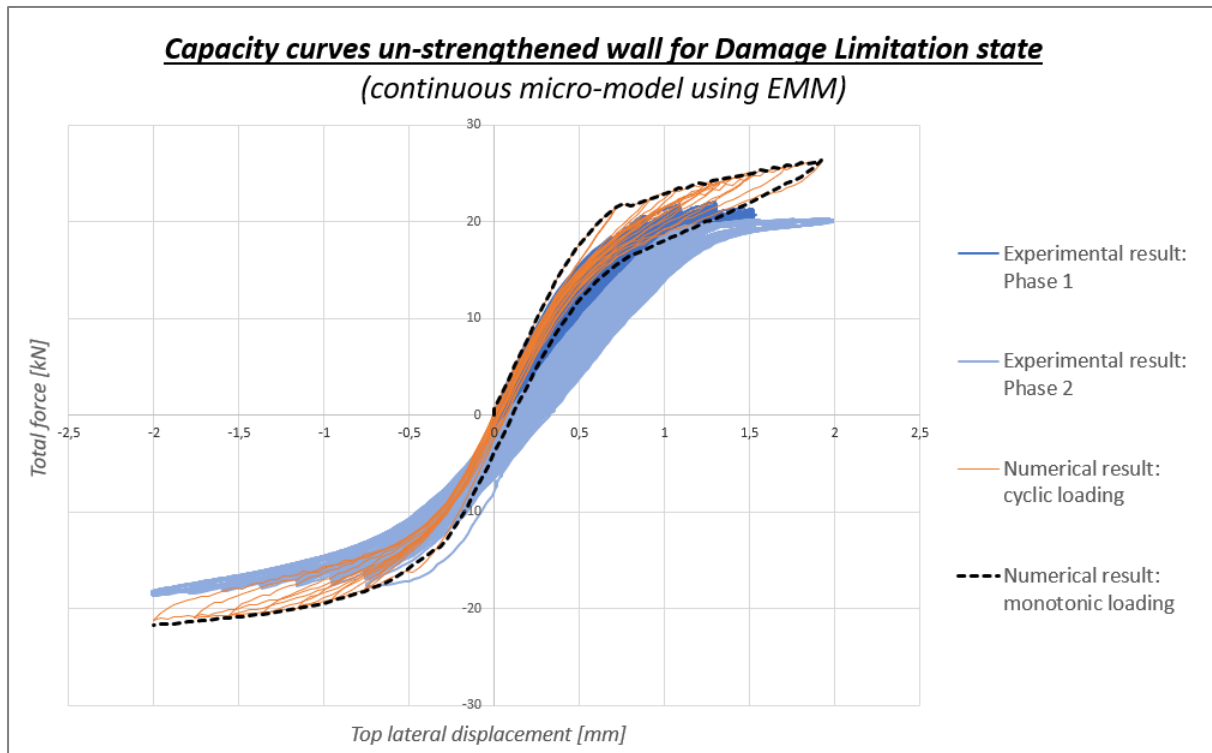
Figure 4.11: Capacity curve monotonic and cyclic pushover analysis vs experiment for continuous micro-model using EMM for the mortar joints (un-strengthened wall)

Continuous micro-model (un-strengthened wall)

(Crack pattern numerical results vs experimental results for Damage Limitation state with the maximum crack width w [mm] indicated)
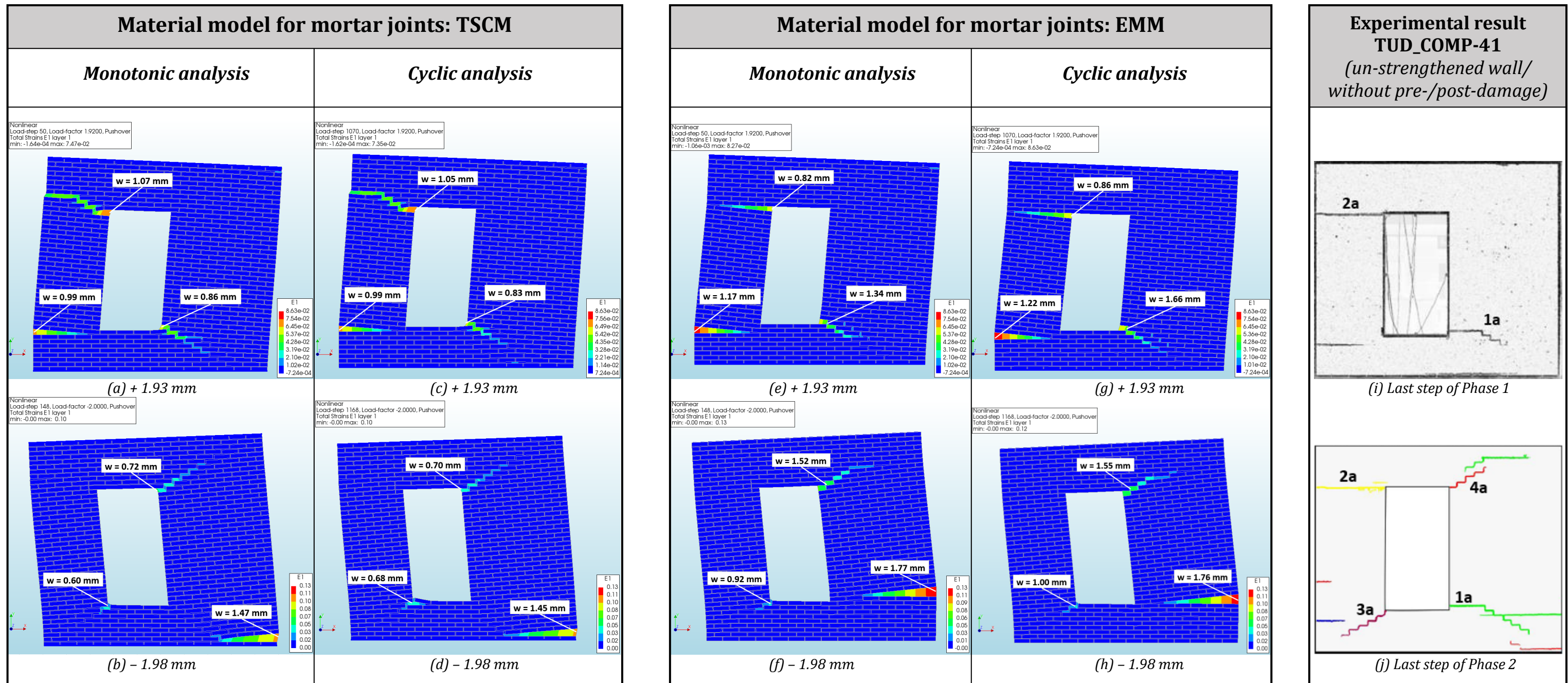
Figure 4.12: Crack pattern at maximum top displacement monotonic and cyclic pushover analysis (DL state) for continuous micro-model using contour plots principal strain E1 (scaling factor = 100)

4.3 Finite element model using detailed micro-modeling approach

In this section, the URM wall is modeled for the DL state with a detailed micro-modeling approach. The properties of the model with the adopted assumptions are discussed in a similar order like the previous two models. The geometry of the FE-model including the boundary conditions are discussed in Section 4.3.1. Different adopted FE-types including information about the mesh of the model are discussed in Section 4.3.2. The adopted material models for all components are presented in Section 4.3.3. Moreover, the monotonic pushover analysis is discussed in Section 4.3.4, followed by a sensitivity analysis in Section 4.3.5. Lastly, the cyclic pushover analysis is discussed in Section 4.3.6.

4.3.1 Geometry and boundary conditions

The boundary conditions for the detailed micro-model (*Figure 4.13*) are the exact same as the previously discussed continuous micro-model (see Section 4.2.1). However, the geometry of the bed-joints are modified (divided into sections) to include interface elements between the bricks and the bed-and head-joints in order to allow for the stair-case cracks to propagate. The interface elements (marked in yellow in *Figure 4.14*) are herein only placed at one side of the mortar joints. According to the numerical experiment carried out by D'Altri et al. (2018), this modeling approach reduces the number of interface elements and thus the computational costs, without compromising the model accuracy. Furthermore, the concrete lintel and the two steel beams are also included in the model. The cross-sectional properties of all components are the same as the continuous micro-model. The thickness of the interface elements (100 mm) is an additional input value in this model. Again, the pre-/post-damage are not included in this case.
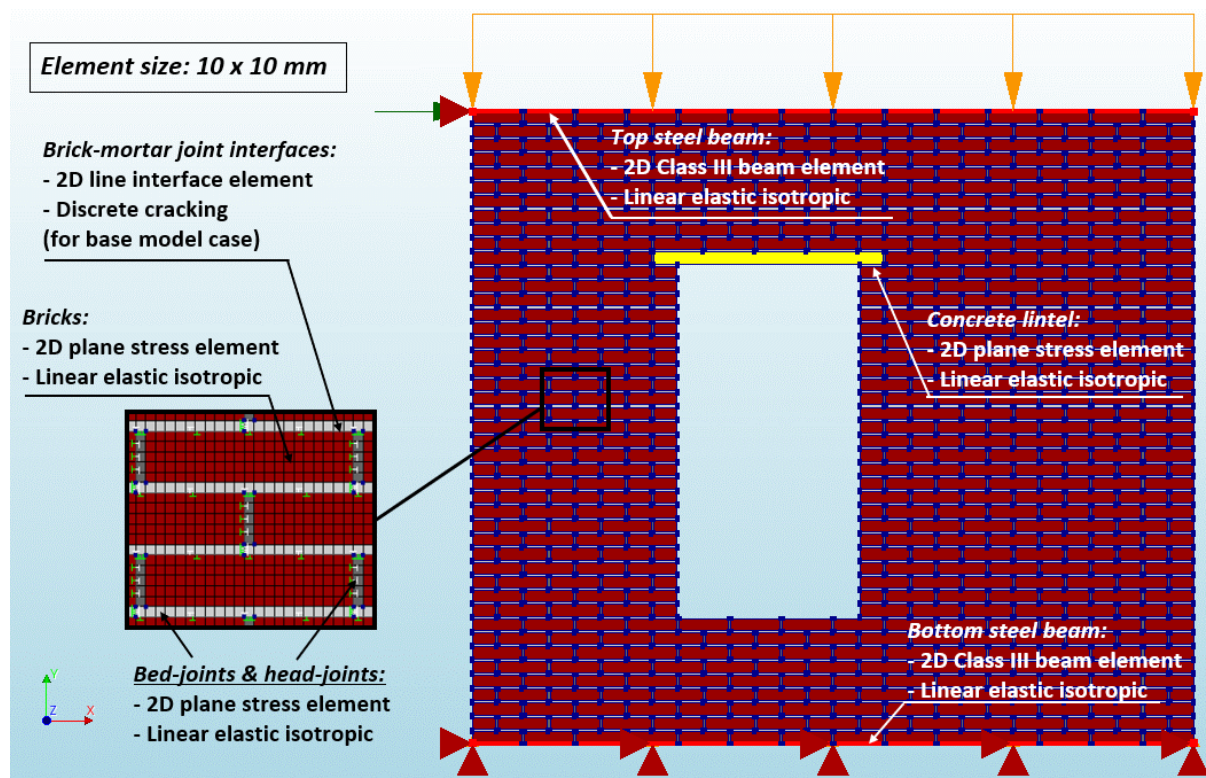
Figure 4.13: FE-model using detailed micro-modeling approach (un-strengthened wall)
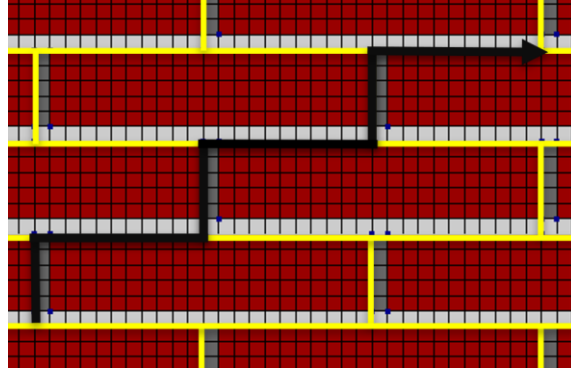
Figure 4.14: Location of line interface elements (marked in yellow) according to (D'Altri et al., 2018)

4.3.2 Finite element discretization and mesh properties

The characteristics of different FE-types which are used to simulate the detailed micro-model are the same as the previous two modeling approaches. However, one additional FE-type is incorporated in the model at the brick-mortar joint interfaces. These interfaces are simulated with 2+2 nodes, line interface elements (L8IF). The properties of the FE mesh and the characteristics of the interface elements are listed in *Table C 2* and *Table C 3* of Appendix C, respectively. An element size of 10 *mm* is chosen to match the thickness of the mortar joints.

4.3.3 Constitutive laws

The material properties for the steel beams (*Table 3*), the concrete lintel (*Table 4*) and masonry bricks (*Table 8*) are kept linear elastic like the continuous micro-model. Two approaches are considered for the detailed micro-model. In *Approach 1*, the nonlinearities are located only in the interface elements (Discrete cracking) which means that the material properties of the mortar joints are kept linear elastic. In *Approach 2*, the nonlinearities are located both in the interface elements (Discrete cracking) as well as in the mortar joint (smeared cracking using EMM). The results for both approaches are very similar, namely cracks mainly occur in the form of opening of the interfaces while smeared cracking is limited in the mortar joints. For this reason, the crack pattern and capacity curve are also very similar. Therefore, only *Approach 1* is considered in this chapter, while the results of *Approach 2* are presented in Appendix C.3. The material properties of the mortar joints and the interface elements are listed in *Table 11* and *Table 12*, respectively. The values are taken from Table 6 of the paper by Korswagen et al. (2019).

According to Hendriks et al. (2019), the initial normal stiffness k_n, the shear stiffness k_t and the shear modulus G for the interfaces can be determined with *equation (23)*, *equation (24)* and *equation (25)*, respectively.

$$k_n = \frac{500\ E}{l} \tag{23}$$

$$k_t = \frac{500\ G}{l} \tag{24}$$

$$G = \frac{E}{2(1 + \nu)} \tag{25}$$

where E is the Young's modulus, G is the shear modulus, v is the Poisson's ratio and l is the element size.

Table 11: Material properties of mortar joints

Mortar joints (linear material)						
Material class	Concrete and masonry					
Material model	Linear elastic isotropic					
	Bed-joints			Head-joints		
Young's modulus	E	1000	N/mm^2	E	500	N/mm^2
Poisson's ratio	v	0.14	-	v	0.14	-
Mass density	ρ	1708	kg/m^3	ρ	1708	kg/m^3

Table 12: Material properties of interfaces between bricks and mortar joints

Brick-mortar interfaces						
Class	Interface elements					
Material model	Discrete cracking					
Linear material properties						
Type	2D line interface					
	Bed-joints			Head-joints		
Normal stiffness modulus-y	k_n	50000	N/mm^3	k_n	25000	N/mm^3
Shear stiffness modulus-x	k_t	21930	N/mm^3	k_t	10965	N/mm^3
Discrete cracking						
Tensile strength	f_t	0.09	N/mm^2	f_t	0.05	N/mm^2
Mode-I tension softening criterion	Linear					
Fracture energy	G_{ft}	0.00753	N/mm	G_{ft}	0.00499	N/mm
Mode-I unloading/ reloading model	Secant					
Mode-II shear criterion for crack development	Zero shear traction					

4.3.4   Monotonic pushover analysis (base model)

A monotonic pushover analysis is adopted for the detailed micro-model. This analysis is used as the base model for the sensitivity analysis (discussed in Section 4.3.5). The same loading cases as for the previous two modeling approaches are used for the detailed micro-model (base model). The applied numerical settings and parameters are listed in *Table C 1* of Appendix C. The load-step size for the pushover loading is 0.04 *mm* with the corresponding amount of load-steps to reach the maximum top lateral displacement (+1.93 mm in the positive x-direction and -1.98 mm in the negative x-direction for the DL state).

The results are discussed in terms of interpreting the capacity curves and the contour plots of the crack patterns. The capacity curve for the monotonic analysis is depicted in (*Figure 4.15*). Several points (load-steps) are selected and marked in the curve which help to better understand the evolution and propagation of the crack pattern in the wall. The load-steps are identified as follow:

1. ***Load-step A:*** indicates the onset of cracking at the corners of the window when loading in the positive x-direction

2. **_Load-step B_**: indicates the onset of cracking at the base of the left pier when loading in the positive x-direction

3. **_Load-step C_**: indicates the peak load in positive x-direction

4. **_Load-step D_**: indicates the maximum top lateral displacement in the positive x-direction

5. **_Load-step E_**: indicates the zero position

6. **_Load-step F_**: indicates the onset of cracking at the base of right pier when loading in the negative x-direction

7. **_Load-step G_**: indicates the peak load in negative x-direction

8. **_Load-step H_**: indicates the maximum top lateral displacement in the negative x-direction

The complete set of contour plots, which correspond to each selected load-step for showing the evolution of the crack pattern, are illustrate in _Figure C 1_ of Appendix C. In this section, only the contour plots for load-step D (_Figure 4.16a_) and load-step H (_Figure 4.16b_) are presented with the final crack pattern for both loading directions at maximum top lateral displacement.
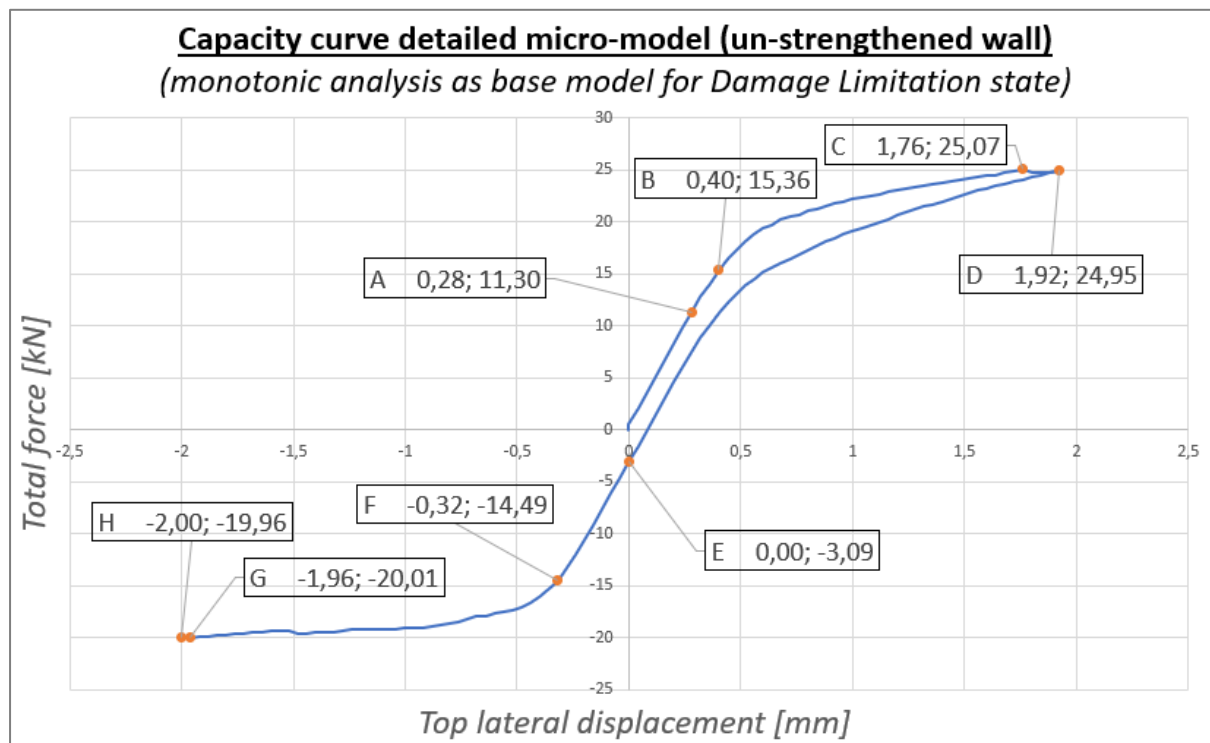
Figure 4.15: Capacity curve for monotonic pushover analysis of un-strengthened detailed micro-model (base model)

The stair-case cracks are well captured with the detailed micro-model. However, the stair-case cracks at the top right and bottom right corner of the window opening are shifted with one or two width of a brick to the side and thus not propagating diagonally in line with the corners of the window opening. The rocking failure behavior of the left pier is well captured where the stair-case crack at the top develops into a horizontal crack. Moreover, the horizontal crack (loading in negative x-direction) is occuring at the base of the right pier.
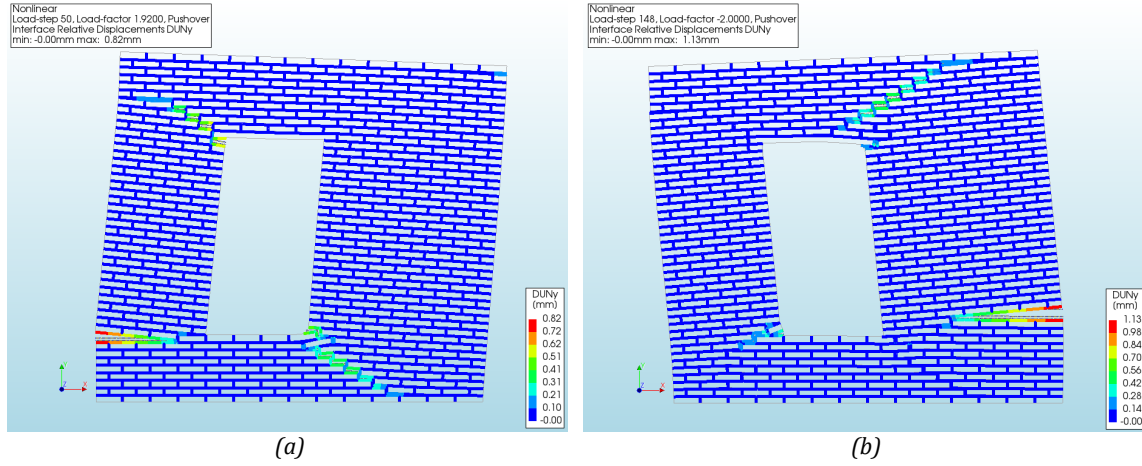
Figure 4.16: Crack pattern for monotonic analysis of un-strengthened detailed micro-model (base model) using Interface relative vertical displacement DUNy [mm] (scaling factor = 100): (a) positive x-direction; (b) negative x-direction

4.3.5   Sensitivity analysis

A sensitivity study is also conducted for the detailed micro-model using monotonic pushover analyses. It should be noted that the sensitivity analysis is only done for the detailed micro-model using *Discrete cracking* for the interface elements. The results are listed in (*Table 13*) in which the maximum base shear forces in both loading directions are compared to the experimental found results. The element size is set to 10 mm since it has been observed from the sensitivity analysis for the continuous micro-model that stair-case cracks are only well captured when the elements size matches the thickness of the mortar joints.

The performed monotonic pushover analysis for the detailed micro-model with all assigned properties and parameters is used as the base model for the sensitivity analysis where only one specified parameter is changed at a time. The numerical parameters which are checked and compared for the sensitivity analysis are: *element order, convergence tolerance*, *satisfaction of all specified norms*, *load-step size*, *iterative method* and different combinations of initial stiffnesses and tensile strengths for the bed- and head-joint interface elements. Again, important to note is that when changing the values of the tensile strength f_t for the bed- and head-joint interface elements, the fracture energy G_{ft} also needs to be changed proportionally because these two parameters are linked to each other according to *equation(13).*

The results for the sensitivity analysis of the detailed micro-model are very similar when changing different numerical parameters. This can be observed from the contour plots which show similar crack patterns and also from the results of the capacity curves where the graphs are overlapping each other. Small differences can be spotted when comparing specific cracks in terms of the crack length and some diagonal cracks are shifted more to the side compared to the others. The only noticeable difference is with the results of the analysis using the Secant (Quasi-Newton) iterative method in which no cracking (opening of interface elements) can be observed in the wall. For this reason, the maximum base shear force in both loading directions are overestimated by a lot. The results of the crack patterns and the capacity curves can be found in Appendix C.2. Although small differences can be spotted, the results of the sensitivity analysis consistently display the main cracks which capture the rocking failure behavior of both piers.

Since the results are every similar for different comparisons of numerical parameters, the same configuration as used for the base model is applied for the cyclic pushover analysis which is discussed in Section 4.3.6.

Table 13: Results sensitivity analysis monotonic loading for detailed micro-model using Discrete cracking for brick-mortar joint interfaces (un-strengthened wall)

Results sensitivity analysis *Detailed micro-model (un-strengthened wall)*				*Loading in positive x-direction*		*Loading in negative x-direction*		**Computational time**
				Max. base shear force	**Difference compared to experiment**	**Max. base shear force**	**Difference compared to experiment**	
				[kN]	[%]	[kN]	[%]	[min]
Experimental results: un-strengthened wall (TUD_COMP-41)				**22.05**	**-**	**-18.72**	**-**	**-**
Element order	Linear: 10 x 10 mm		*(base model)*	25.07	+ 13.70 %	-20.01	+ 6.89 %	27
	Quadratic: 10 x 10 mm			25.09	+ 13.79 %	-20.13	+ 7.53 %	41
Convergence tolerance	Displacement (0.005)	Force (0.005)	Energy (-)	25.34	+ 14.92 %	-20.12	+ 7.48 %	103
	Displacement (0.01)	Force (0.01)	Energy (-)	25.28	+ 14.65 %	-19.50	+ 4.17 %	63
	Displacement (0.05)	Force (0.05)	Energy (-) *(base model)*		25.07	+ 13.70 %	-20.01	+ 6.89 %	27
Satisfy all specified norms	Yes			25.08	+ 13.74 %	-19.99	+ 6.78 %	127
	No		*(base model)*	25.07	+ 13.70 %	-20.01	+ 6.89 %	27
Load-step size	0.01(193) -0.01(391)			25.44	+ 15.37 %	-19.69	+ 5.18 %	146
	0.02(97) -0.02(196)			25.63	+ 16.24 %	-19.97	+ 6.68 %	58
	0.04(48) -0.04(98)		*(base model)*	25.07	+ 13.70 %	-20.01	+ 6.89 %	27
Iterative method	Regular Newton-Raphson		*(base model)*	25.07	+ 13.70 %	-20.01	+ 6.89 %	27
	Modified Newton-Raphson			*Diverging at load-step 4*				
	Secant (Quasi-Newton)			73.80	+ 234.69 %	-75.10	+ 301.18 %	15
Material input parameters	*Different combination interface initial stiffnesses comparison*							
	$k_{n, \text{ bed-joints}} = 50000 \text{ N/mm}^3$ $k_{t, \text{ bed-joints}} = 21930 \text{ N/mm}^3$	$k_{n, \text{ head-joints}} = 25000 \text{ N/mm}^3$ $k_{t, \text{ head-joints}} = 10965 \text{ N/mm}^3$	*(base model)*	25.07	+ 13.70 %	-20.01	+ 6.89 %	27
	$k_{n, \text{ bed-joints}} = 25000 \text{ N/mm}^3$ $k_{t, \text{ bed-joints}} = 10965 \text{ N/mm}^3$	$k_{n, \text{ head-joints}} = 25000 \text{ N/mm}^3$ $k_{t, \text{ head-joints}} = 10965 \text{ N/mm}^3$		25.19	+ 14.24 %	-20.09	+ 7.32 %	26
	Different combinations interface tensile strength comparison							
	$f_{t, \text{ bed-joints}} = 0.09 \text{ N/mm}^2$ $G_{ft, \text{ bed-joints}} = 0.00753 \text{ N/mm}$	$f_{t, \text{ head-joints}} = 0.05 \text{ /mm}^2$ $G_{ft, \text{ head-joints}} = 0.00499 \text{ N/mm}$	*(base model)*	25.07	+ 13.70 %	-20.01	+ 6.89 %	27
	$f_{t, \text{ bed-joints}} = 0.09 \text{ N/mm}^2$ $G_{ft, \text{ bed-joints}} = 0.00753 \text{ N/mm}$	$f_{t, \text{ head-joints}} = 0.09 \text{ N/mm}^2$ $G_{ft, \text{ head-joints}} = 0.00753 \text{ N/mm}$		25.64	+ 16.28 %	-19.40	+ 3.63 %	24

Marked in green = most optimum configuration of numerical parameters in terms of accurate results (cracking pattern and capacity curve) with reasonable associated computational time

4.3.6   Cyclic pushover analysis

Cyclic pushover analyses are conducted using the detailed micro-modeling approach. The results of the model using the *Discrete cracking* material model for the interface elements are herein compared to the results of the model using the *Combined cracking-shearing-crushing* (CCSC) material model. The material properties for the brick-mortar interfaces using the CCSC model are listed in *Table C 4* of Appendix C. Furthermore, the loading protocol is reduced to only one run per cycle of loading for the detailed micro-model. A prescribed displacement of 1 *mm* is applied at the top left support. First, the self-weight and the overburden is vertically applied with a load-step of 1.0. Subsequently, the cyclic loading is applied in load steps of 0.04 (step sizes of 0.04 *mm*) with the corresponding amount of steps per cycle to obtain the maximum horizontal displacement according to the cyclic loading scheme (*Figure 4.4*).

The results of the cyclic and monotonic analyses are compared with each other, as well as with the experimental results. Again, the comparison is done by interpreting the capacity curves and the crack pattern. It has been concluded from the results of the sensitivity analysis that the influences are small when changing different numerical parameters for the detailed micro-model. For this reason, the same configuration of numerical settings as the base model is used for the cyclic analysis.

The consitutive relation for Discrete cracking is based on a total deformation theory in which the normal traction is expressed as a function of the crack width and the shear traction is expressed as a function of the the crack slip (Ferreira, 2021). Discrete cracking is specified as initiation of Mode-I (tensile) and Mode-II (shear). For the model in this case, Mode-I and Mode-II are uncoupled. On the other hand, the CCSC material model ("Composite Interface model") is able to simulate fracture, frictional slip as well as crushing along material interfaces, at the joints in masonry.

The capacity curves are illustrated in (*Figure 4.18*) for the model using Discrete cracking for the interfaces and in (*Figure 4.19*) for the model using the CCSC for the interfaces. The pattern of the capacity curve for the case when using Discrete cracking for the interfaces is in a reasonable agreement with the experiment. However, when looking at the capacity curve for the case when using CCSC for the interfaces, the energy dissipation is overestimated by a lot compared to the experimental result. The residual displacements at zero-force are very large in both loading directions. This can also be seen from the crack pattern for the cyclic analysis where the cracks are not closing when loading the wall in the opposite x-direction, meaning that the cracks are getting larger after each cycle. This can be explained by the fact that elastic un-loading is taking place when looking at the tensile (Mode-I) failure behavior. The constitutive behavior in tension (Mode-I) for the interface elements (*Figure 4.17*) is described as follows. A linear loading branch with an initially high stiffness goes up until it reaches the tensile strength of the material. From this point, cracks start to form and the function goes into a tension softening branch until it reaches the zero stress level. Subsequently, the unloading branch goes horizontally back to the origin at zero stress level (because the open cracks do not contain any tensile strength). For the CCSC material model however, instead of going horizontally back to the origin at zero stress level, elastic un-loading takes place and the curve goes into the branch of the opposite sign, meaning that the cracks become stiff again. This is the reason why the cracks are not closing and are getting larger after each unloading of the cycle. The phenomena described above is a short-coming of the CCSC material model when applying it for cyclic analyses where unloading is taking place. On the other hand, the initial stiffness in both loading directions for both material models are in good agreement with the experiment.
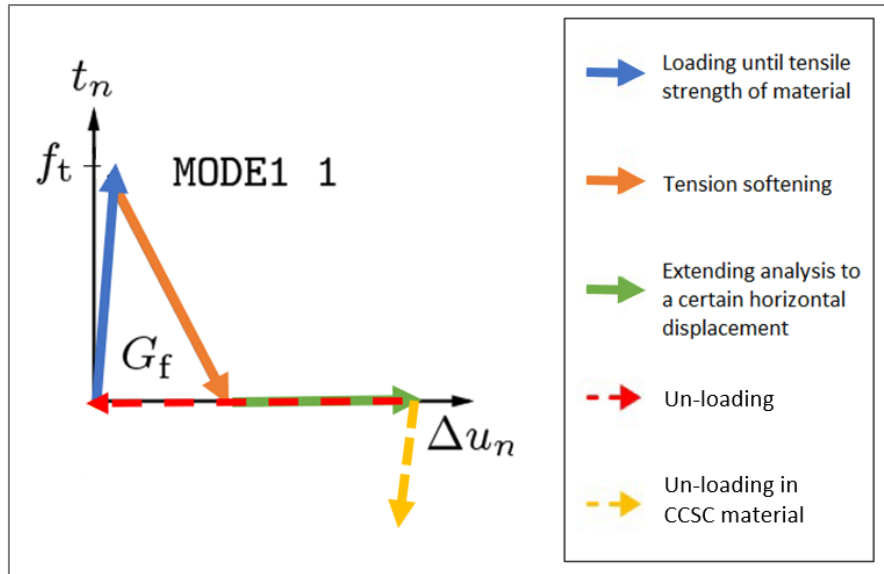
Figure 4.17: Constitutive model for tensile (Mode-I) failure

The final crack patterns for both material models using both monotonic and cyclic analysis are illustrated in *Figure 4.20*. Some differences in the crack patterns can be observed between the two different material models. The results for the model using Discrete cracking are discussed first. Considering the crack pattern for the positive x-direction, the crack at the top of the left pier (crack number 2a) is simulated slightly different compared with the experiment. This crack starts from the top left corner of the window and develops from a diagonal stair-case crack into a horizontal crack. However, separation of the left pier with respect to the top spandrel is only for the case of cyclic analysis, since this crack does not propagate over the full width of the wall for the monotonic analysis. The propagation of the crack, starting at the bottom right corner of the window (crack number 1a), is mainly diagonal and is shifted with one width of a brick to the left. Furthermore, the rocking failure behavior of the left pier can be observed due to the horizontal crack occurring along the bed-joint at the base of the pier.

Considering the crack pattern for the negative x-direction, both diagonal stair-case cracks at the corners of the window are simulated. The diagonal stair-case crack starting at the bottom left corner of the window (crack number 3a) is underestimated in its length for the monotonic analysis. The stair-case crack starting at the top right corner of the window (crack number 4a) is in a good agreement with the experiment, except that the crack is shifted to the left by the width of two bricks. Moreover, rocking of the right pier is simulated numerically with a horizontal crack occurring at the base of the pier. Furthermore, the crack at the top of the left pier (crack number 2a) is also visible in the negative x-direction for the case of the cyclic analysis.

When looking at the crack pattern for the model using the CCSC for the brick-mortar interfaces and considering the positive x-direction, the crack at the top of the left pier (crack number 2a) is propagating only in horizontal direction which is in line with the experiment. However, no separation of the left pier with respect to the spandrel can be observed since the crack is not running along the full width of the pier. The diagonal stair-case crack starting at the bottom right corner of the window (crack number 1a) and the horizontal crack at the base of the left pier are simulated. When looking at the crack pattern of the cyclic analysis, the cracks are not closing when loading the wall in the opposite x-direction. Subsequently, the cracks are getting larger (in width and length) after each cycle. This phenomena for the CCSC is explained and discussed in the section above.

Unlike the results of the previously discussed two modeling approaches (macro-model and continuous micro-model), the capacity curve of the monotonic analysis, for the model using *Discrete cracking* for the interfaces, is not exactly enveloping the capacity curve of the cyclic analysis. It can be observed from (*Figure 4.18*) that the last cycle of the cyclic analysis is showing a larger residual displacement at zero force. The explanation for this is as follows; when the maximum top lateral displacement was reached in the positive x-direction, the left pier was returned to its original zero position in one load-step after unloading. This happened while the L-shape portion of the wall (consisting of the right pier and the top spandrel) was slowly returning to its original zero postion. When the L-shape part of the wall met the top of the left pier again at the zero position, it pushed the left pier a bit to the left. This is the reason why the diagonal stair-case crack at the top of the left pier is also visible when loading the wall in the negative x-direction for the cyclic analysis (*Figure 4.20d*). Moreover, this also explains why the residual displacement at zero force is larger for the last cycle of the cyclic analysis. Although the capacity curve of the monotonic analysis does not exatly follow the outline of the cyclic analyis, the shape of both capacity curves are in a reasonable agreement with the experiment. However, this material model does not capture Mode-II (shear) failure as well as the model using the CCSC. On the other hand, eventhough the CCSC is able to capture fracture, slip and compressive failure in a realistic manner, one short-coming is that the material model is not able to model the behavior of the wall for cases when unloading is taking place.

The maximum base shear forces in both loading directions, for both monotonic and cyclic analysis, are listed in *Table 14*. The values are close when comparing both analyses with each other. The computational time for the cyclic analysis is significantly larger compared to the monotonic anlysis.

Table 14: Comparison numerical results monotonic vs cyclic analysis for detailed micro-model (un-strengthened wall)

	Positive x-direction		Negative x-direction		Time
	Max. base shear force	Difference compared to experiment	Max. base shear force	Difference compared to experiment	
	$[kN]$	$[\%]$	$[kN]$	$[\%]$	$[min]$
Experimental results	**22.05**	**-**	**-18.72**	**-**	**-**
Discrete cracking					
Monotonic analysis	25.07	+ 13.70 %	-20.01	+ 6.89 %	27
Cyclic analysis	24.74	+ 12.20 %	-20.52	+ 9.62 %	395
Combined cracking-shearing-crushing					
Monotonic analysis	23.59	+ 6.98 %	-21.64	+ 15.60 %	20
Cyclic analysis	27.30	+23.81 %	-21.37	+ 14.16 %	392

Lastly, the maximum crack width *w* for each main crack is also indicated in *Figure 4.20* for the model using Discrete cracking for the interfaces. Again, because the pre-/post-damage are not included in the numerical models in this chapter, a direct comparison with the experiment cannot be made since the experimental obtained values (*Table 1*) are for the pre-damaged/ un-strengthened wall (TUD_COMP-45). The results in this chapter are compared with the strengthened wall in Chapter 5. Compared to the previously discussed macro- and continuous micro-model, a larger difference in obtained values for the maximum crack width can be observed between the monotonic and cyclic analysis. The largest difference is 73% for crack number 3a. Moreover, the crack length for crack number 2a and 3a is also larger in the cyclic analysis. The values for the model using the CCSC for the interfaces are not indicated because the cracks are getting larger after unloading and therefore a direct comparison cannot be made between the monotonic and cyclic analysis.
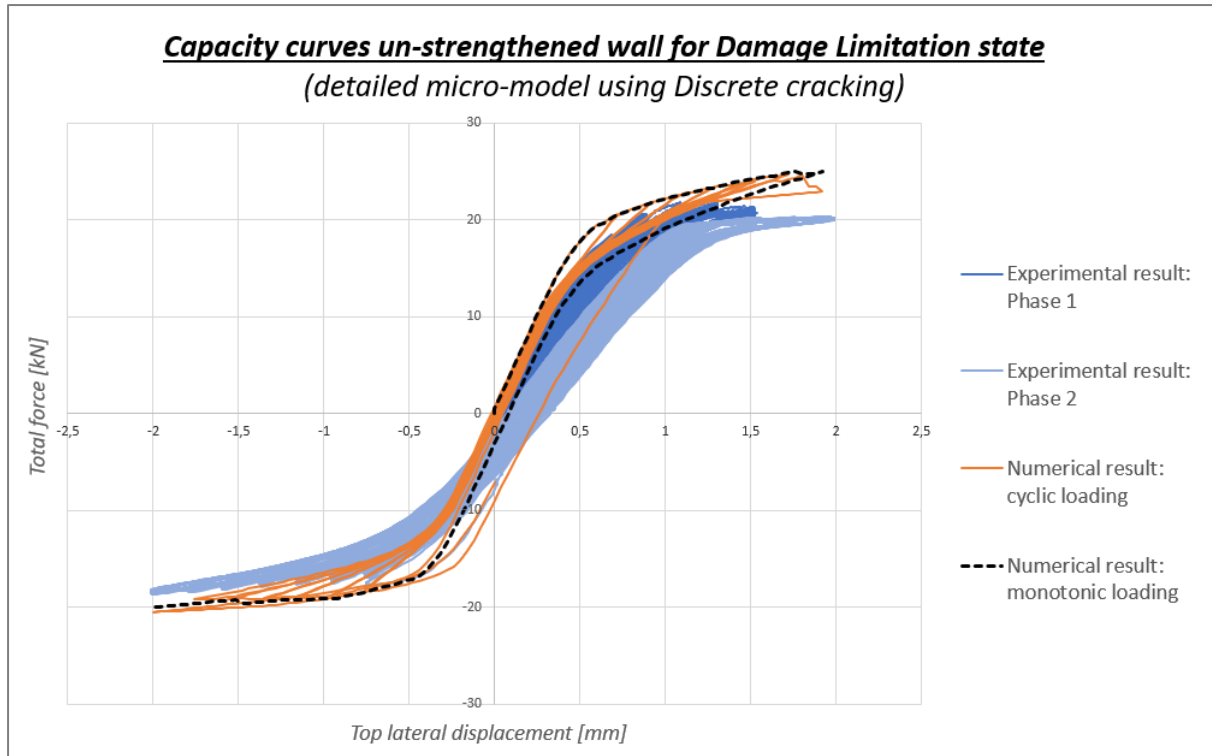
Figure 4.18: Capacity curves detailed micro-model using Discrete cracking for brick-mortar joint interface elements
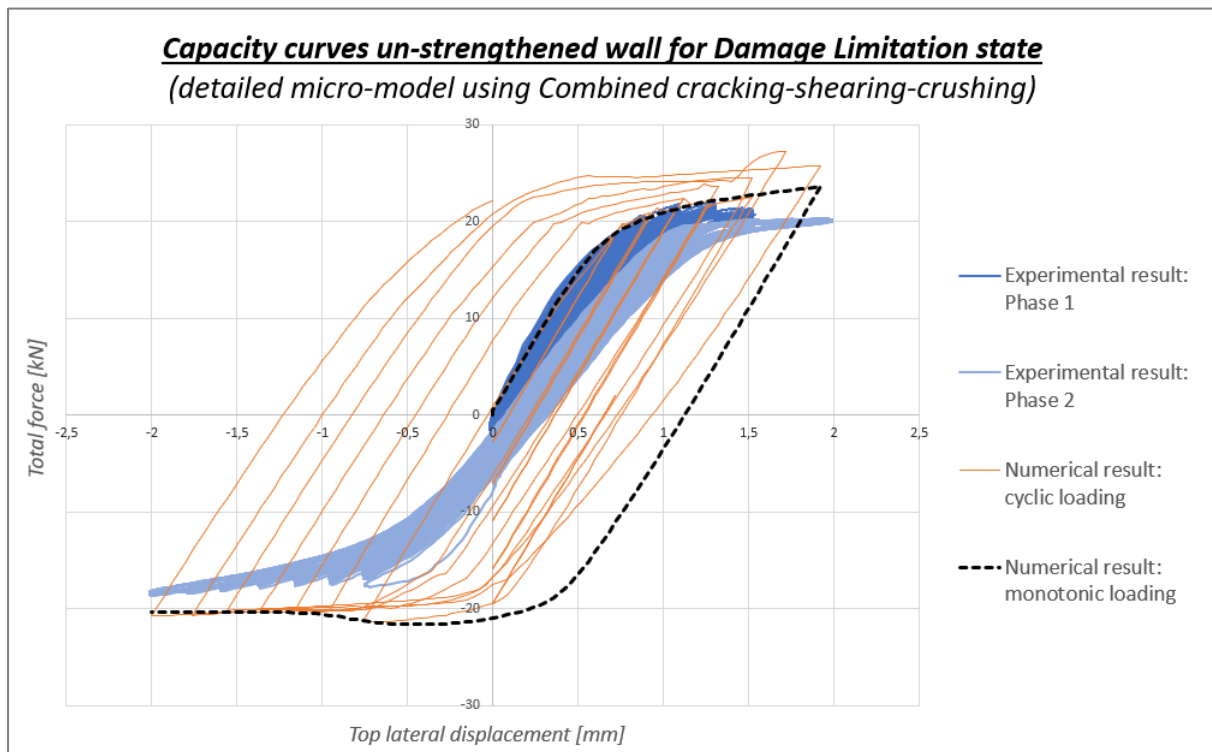
Figure 4.19: Capacity curves detailed micro-model using Combined cracking-shearing-crushing for brick-mortar joint interface elements

Detailed micro-model (un-strengthened wall)

(Crack pattern numerical results vs experimental results for Damage Limitation state with the maximum crack width w [mm] indicated)
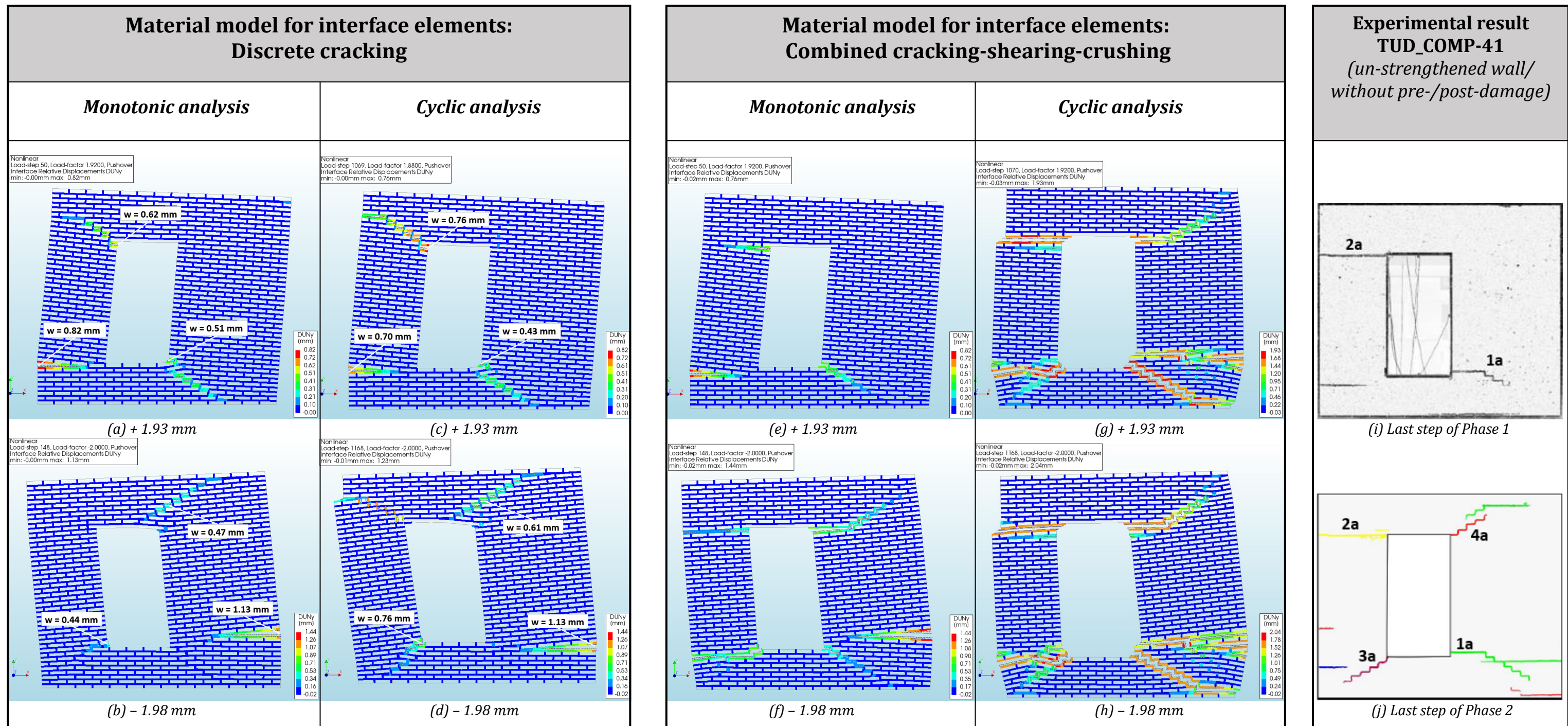
Figure 4.20: Crack pattern at maximum top displacement monotonic and cyclic pushover analysis (DL state) for detailed micro-model using contour plots interface relative displacement DUNy [mm] (scaling factor = 100)

4.4 Discussion numerical analyses for the Damage Limitation state

The results of the crack patterns are compared for all three modeling approaches. The contour plots with the crack pattern for all models are put next to each other for the monotonic analyses in *Figure 4.21* and for the cyclic analyses in *Figure 4.22*. The crack patterns are simulated in a reasonable agreement with the experiment for all three modeling approaches with the applied material models. Some differences can be noticed between the models for the crack at the top of the left pier. For the macro-model and the detailed micro-model using the CCSC material model, this crack propagates horizontally over the width of the pier. On the contrary, this crack develops from a diagonal stair-case crack into a horizontal crack for the continuous micro-model using the TSCM for the mortar joints and the detailed micro-model using Discrete cracking for the brick-mortar joint interfaces. Moreover, only the continuous micro-model using the TSCM is showing a horizontal crack along the bed-joint at the right base of the wall when loading in the negative x-direction, whereas this crack is located at the base of the right pier for the other models.

The detailed micro-model using the CCSC material model for the brick-mortar interfaces is less suitable when unloading is taking place (cyclic analysis). In summary, the reasoning for this is because elastic unloading takes place for the CCSC material model in tension. This means that the cracks become stiff again and the crack width keeps increasing after each cycle, resulting in an overestimation of the energy dissipation. The macro-model is able to simulate the diagonal stair-case cracks starting at the corners of the window. However, in case when pre-/post-damage needs to be included in the model (Chapter 5), the continuous and detailed micro-model are more suited since these modeling approaches allow for a more precise modeling where the geometry of the mortar joints are modeled explicitly. This allows for a direct assignment of modified material properties to each component. The results of the continuous and detailed micro-model are comparable in terms of crack pattern and capacity curve. However, the modeling effort is significantly lower for the continuous micro-model. According to Rots ([1997](#)), a disadvantage of the continuous micro-modeling approach is that the transverse contraction of the mortar joints cannot be included in the model because of the absence of interface elements. This is the phenomena where the relatively weak joints (compared to the masonry bricks) tend to expand laterally under vertical compression but are restrained because of the bonding with the bricks. Consequently, this results in a stress field with compression in the joints and lateral tension in the bricks. However, this is the case for problems in which the behavior under compression is governing. For the case of the experiment, failure behavior under tension and shear is governing.

The monotonic pushover analyses are good estimations for the cyclic pushover analyses when comparing the results with each other in terms of the crack patterns and the enveloping of the capacity curves. However, the computational time increases significantly when performing a cyclic analysis. The two detailed micro-models are the only models which are showing some differences in results when comparing the monotonic analysis with the cyclic analysis. Moreover, the obtained values for the maximum crack width from a detailed micro-model are relatively smaller compared to the macro- and continuous micro-model. The maximum base shear forces in both loading directions for all models are listed and compared with each other as well as with the experiment in *Table 15*. The results of the detailed micro-model using Discrete cracking for the brick-mortar joint interfaces is the closest to the experiment in terms of the obtained maximum base shear forces.

The maximum force capacity in both loading directions are presented in *Table 15* for all modeling approaches and the corresponding applied material models. The percentage differences with respect to the experiment and the associated computational time for each model are herein indicated.

Table 15: Comparison maximum base shear forces and computational time for all modeling approaches (un-strengthened wall)

	Positive x-direction		Negative x-direction		Time
	Max. base shear force	Difference compared to experiment	Max. base shear force	Difference compared to experiment	
	$[kN]$	$[\%]$	$[kN]$	$[\%]$	$[min]$
Experimental results	**22.05**	**-**	**-18.72**	**-**	**-**
Macro-model using EMM for masonry composite					
Monotonic analysis	25.75	+ 16.78 %	-21.44	+ 14.53 %	4
Cyclic analysis	26.47	+ 20.05 %	-20.94	+ 11.86 %	29
Continuous micro-model using TSCM for mortar joints					
Monotonic analysis	26.71	+ 21.13 %	-22.01	+ 17.57 %	58
Cyclic analysis	26.24	+ 19.00 %	-21.91	+ 17.04 %	322
Continuous micro-model using EMM for mortar joints					
Monotonic analysis	26.38	+ 19.64 %	-21.70	+ 15.92 %	36
Cyclic analysis	26.18	+ 18.73 %	-21.25	+ 13.51 %	275
Detailed micro-model using Discrete cracking for interface elements					
Monotonic analysis	25.07	+ 13.70 %	-20.01	+ 6.89 %	27
Cyclic analysis	24.74	+ 12.20 %	-20.52	+ 9.62 %	395
Detailed micro-model using Combined cracking-shearing-crushing for interface elements					
Monotonic analysis	23.59	+ 6.98 %	-21.64	+ 15.60 %	20
Cyclic analysis	27.30	+23.81 %	-21.37	+ 14.16 %	392

Crack pattern comparison of all modeling approaches (un-strengthened wall)

(Monotonic analysis for Damage Limitation state with the maximum crack width w [mm] indicated)
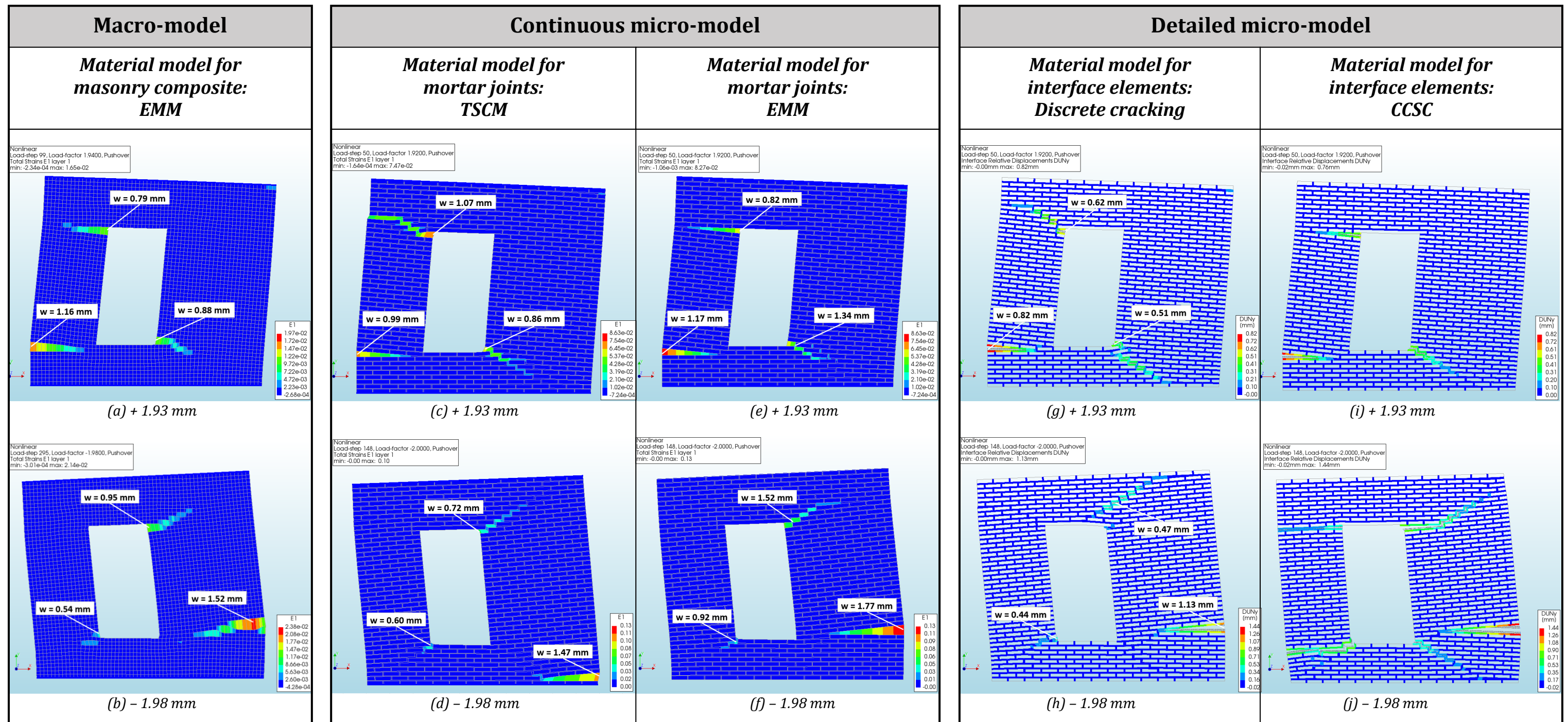
Figure 4.21: Crack pattern comparison of all modeling approaches for monotonic analyses (DL state)

Crack pattern comparison of all modeling approaches (un-strengthened wall)

(Cyclic analysis for Damage Limitation state with the maximum crack width w [mm] indicated)
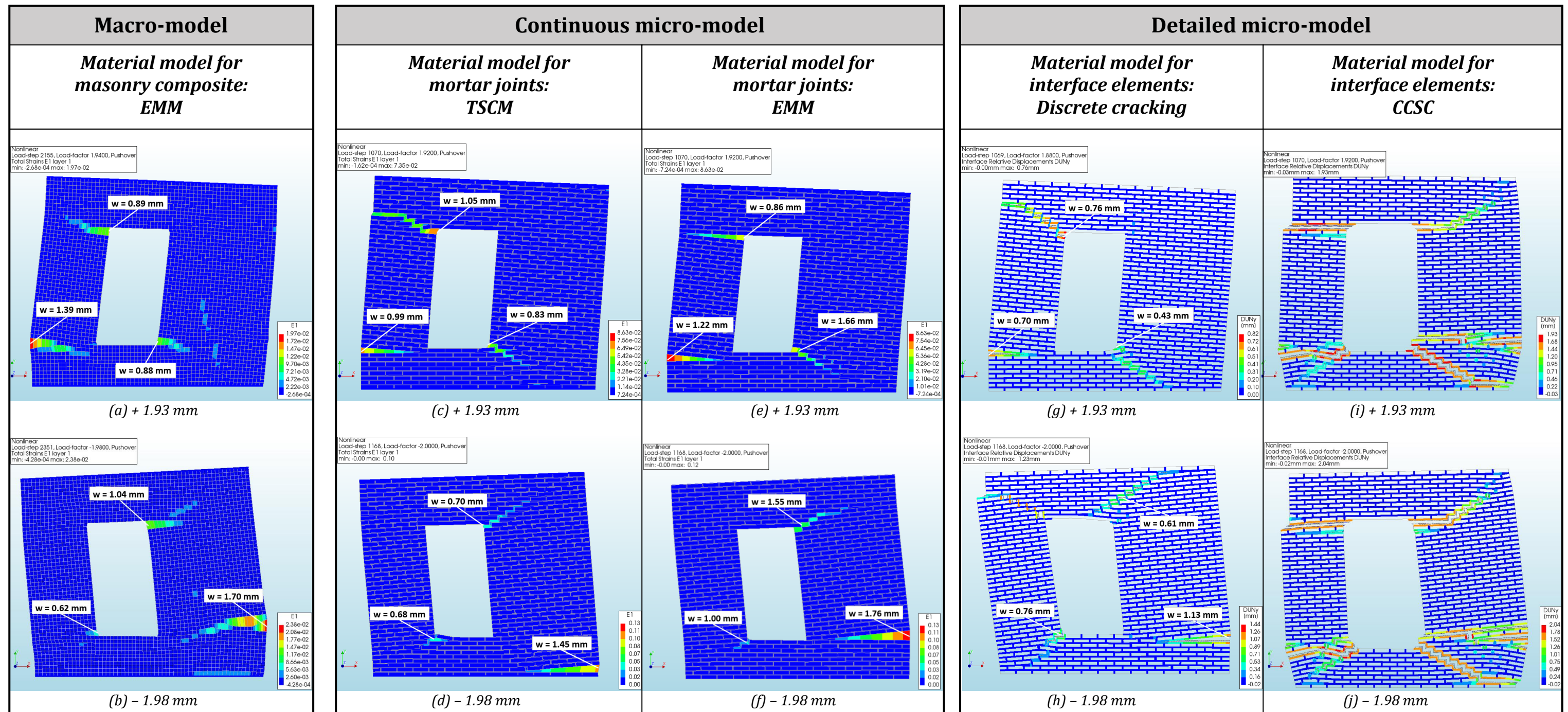
Figure 4.22: Crack pattern comparison of all modeling approaches for cyclic analyses (DL state)

4.5   Numerical analyses for the Near Collapse state

The continuous micro-modeling approach has been chosen to simulate the loading of the experimental tested wall up to the Near Collapse (NC) state. The choice is based on the numerical results which are obtained and discussed in the previous sections. The diagonal stair-case cracks are captured more precisely with the continuous micro-model compared to the macro-model. On the other hand, the continuous micro-modeling approach has a comparable accuracy in simulating the cracks compared to the detailed micro-modeling approach. However, the modeling effort is significantly lower for the continuous micro-modeling approach. Again, both the TSCM and the EMM are used as the material models for the mortar joints in separate models and the results are compared with each other. Both monotonic and cyclic analyses are conducted.

The loading protocol for the NC state (*Figure 4.23*) is also simplified to only one run per cycle of loading. The total loading protocol (DL state + NC state) is applied for the analyses in this section. The loading protocol for the DL state is presented in (*Figure 4.4*) in Section 4.1.6. Important to note is that unlike the performed monotonic analyses for the DL state, the monotonic analyses for the NC state are preformed separately for the positive and negative x-direction. Moreover, the applied numerical settings and parameters for the continuous micro-model using the TSCM and EMM for the mortar joints are listed in *Table E 1* of Appendix E.
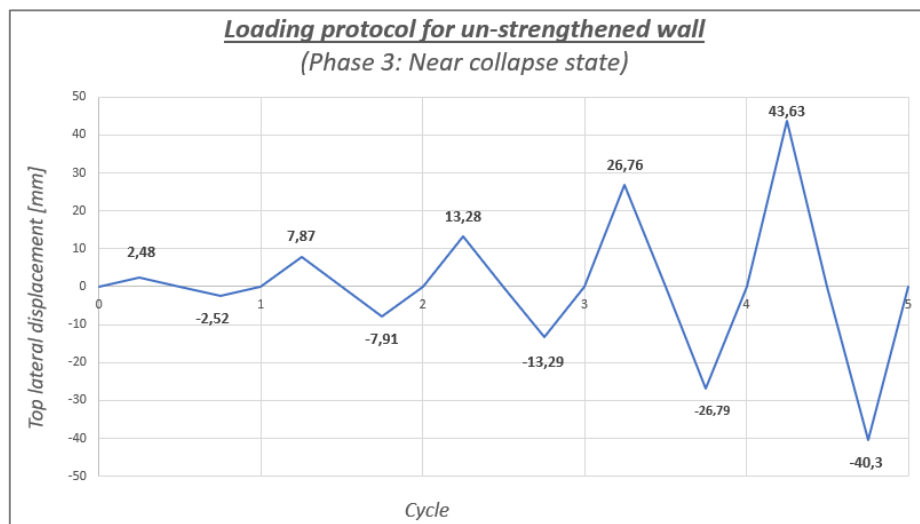
Figure 4.23: Loading protocol for un-strengthened wall (NC state)

The results of the cyclic and monotonic analyses are compared with each other, as well as with the experimental results. Again, the comparison is done by interpreting the capacity curves and the crack patterns. The capacity curves for the monotonic analyses, for both material models, are compared with the envelope curve of the experiment in *Figure 4.24a*. The pattern of the capacity curves are in a reasonable agreement with the experiment. However, the maximum force capacity is overestimated for both material models. This can be explained by the fact that the numerical models could be expected to be stronger than the experiment because of perfect conditions. The strength of the bond between the bricks and mortar joints might not be consistent over the entire wall in the experiment, which results in local weaker spots in the wall. Moreover, the bricks are kept linear elastic for the numerical models which means that cracks can only occur in the mortar joints.

Capacity curves and bilinear approximations

For the comparison of different parameters, obtained from the experiment, the bilinear approximation curves are calculated for the numerical capacity curves. According to Licciardello et al. ([2021](#)), the initial stiffness K_{el} is determined as the secant stiffness which intersect the capacity curve at 0.7 times the maximum base shear force. The ultimate displacement u_u is determined from the capacity curve at a residual capacity of 0.8 times the maximum base shear force. By imposing that the area underneath the capacity curve and the bilinear curve up to the ultimate displacement are the same, the maximum base shear force V_u of the bilinear curve can be determined. The elastic displacement is determined as $u_{el} = V_u / K_{el}$. The ductility factor is determined as $\mu_b = u_u / u_{el}$. The ultimate drift is determined as $d_{r-b} = 100 * u_u / h_{wall}$, where h_{wall} is the height of the wall. The bilinear curves are illustrated in *Figure 4.24b* for both material models. The parameters obtained from the bilinear curves are listed in *Table 16* and compared with the experimental results.

The capacity curves of the cyclic and monotonic analyses are compared with each other, as well as with the experiment in *Figure 4.25a* for the continuous micro-model using the TSCM for the mortar joints and in *Figure 4.25b* for the continuous micro-model using the EMM for the mortar joints. The capacity curves for the monotonic analyses follows the outline of the capacity curves for the cyclic analyses as the envelope curve. Again, the hysteretic behavior is not captured with the model using the TSCM for the mortar joints. The capacity curve always goes back to the origin after each cycle, resulting in an underestimation of the energy dissipation. On the other hand, the EMM is able to capture the hysteretic behavior because the material model allows for elastic unloading.

Table 16: Numerical results vs experiment (Licciardello et al., [2021](#)) for un-strengthened wall using parameters obtained from the bilinear approximation curves with percentage difference from experiment in parentheses

		Un-strengthened wall					
		Continuous micro-model using TSCM		Continuous micro-model using EMM		Experiment TUD_COMP-41	
		Pos.	Neg.	Pos.	Neg.	Pos.	Neg.
Initial stiffness K_{el}	$[kN/mm]$	36.19 (+29.0%)	37.07 (+49.9%)	36.52 (+30.2%)	22.41 (-9.4%)	28.06	24.73
Max. base shear force V_u	$[kN]$	25.38 (+26.3%)	-22.58 (+27.8%)	29.81 (+48.3%)	-27.54 (+56.9%)	20.10	-17.67
Elastic displacement u_{el}	$[mm]$	0.70 (-2.8%)	-0.61 (-15.3%)	0.82 (+13.9%)	-1.23 (+70.8%)	0.72	-0.72
Ultimate displacement u_u	$[mm]$	43.60 (-0.1%)	-40.40 (+0.3%)	43.50 (-0.3%)	-40.50 (+0.5%)	43.63	-40.30
Ductility factor μ_b	$[-]$	62.29 (+2.3%)	66.23 (+17.4%)	53.05 (-12.9%)	32.93 (-41.6%)	60.90	56.40
Ultimate drift d_{r-b}	$[\%]$	1.62 (+0.6%)	-1.50 (+0.7%)	1.62 (+0.6%)	-1.51 (+1.3%)	1.61	-1.49
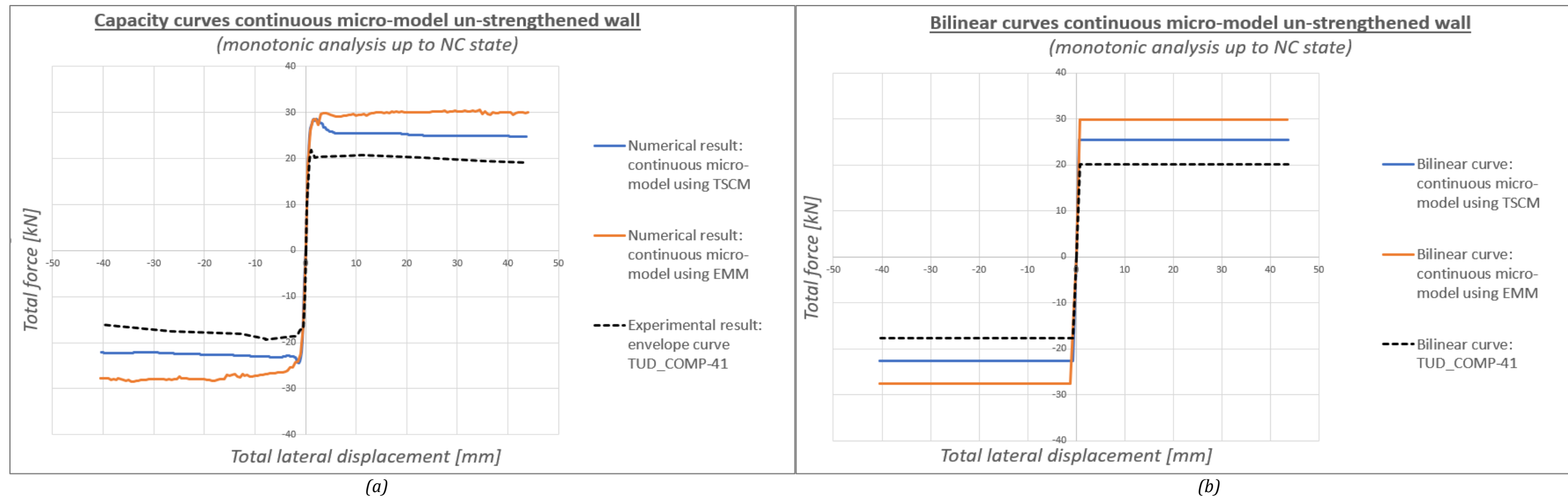
Figure 4.24: Continuous micro-model un-strengthened wall monotonic analyses up to NC state: (a) capacity curves; (b) bilinear approximations
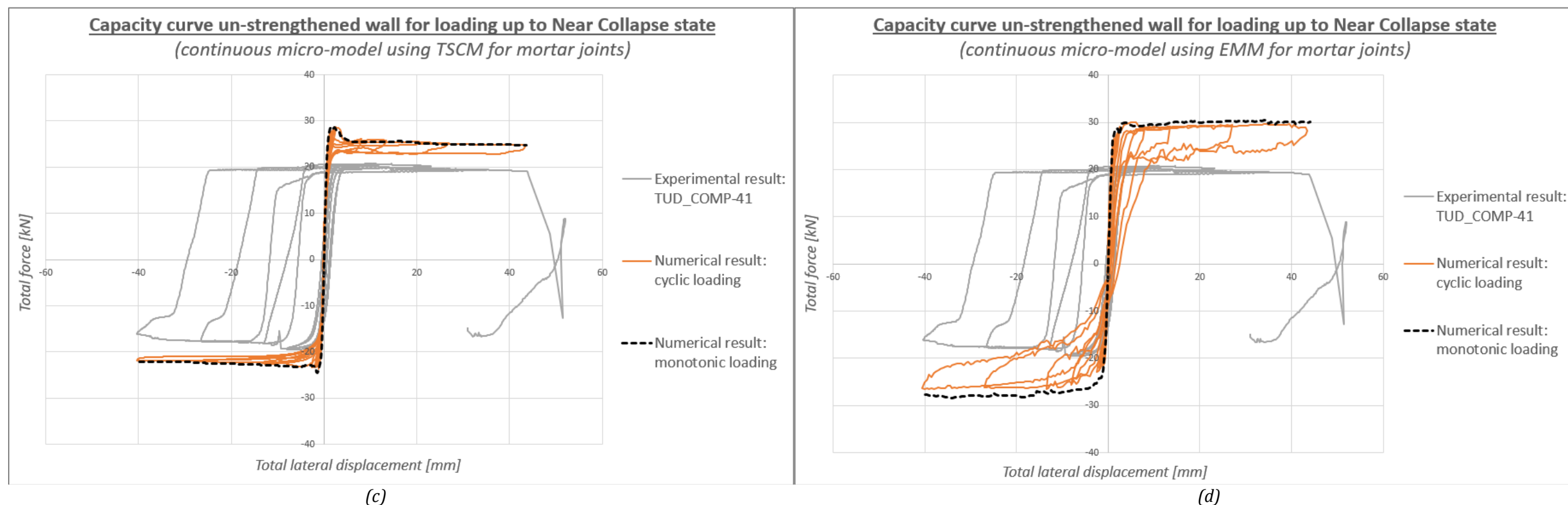
Figure 4.25: Capacity curves un-strengthened wall monotonic and cyclic analyses up to NC state: (a) continuous micro-model using TSCM; (b) continuous micro-model using EMM

Crack pattern

The contour plots of the principal strain E_1 are used to present the numerical results of the crack pattern. These contour plots are scaled for a better display of the cracks (same approach as Mahmoudimotlagh, 2020). The scaled E_1 contour plots are related to the constitutive law of the masonry wall. In this case, three contour levels are specified:

1. $E_1 < \varepsilon_{cr}$ (uncracked)
2. $\varepsilon_{cr} < E_1 < \varepsilon_{ult}$ (partially cracked)
3. $E_1 > \varepsilon_{ult}$ (fully cracked)

The cracking strain ε_{cr} and the ultimate strain ε_{ult} are calculated with *equation (26)* and *equation (27)*, respectively. The material properties for the bed-joints are used for the calculations:

$$\varepsilon_{cr} = \frac{f_t}{E} = \frac{0.09}{1000} = 0.00009 \qquad (26)$$

$$\varepsilon_{ult} = \frac{2G_f}{f_t h} = \frac{2G_f}{f_t\sqrt{2A}} = \frac{2*0.00753}{0.09*\sqrt{2*10*10}} = 0.0118 \qquad (27)$$
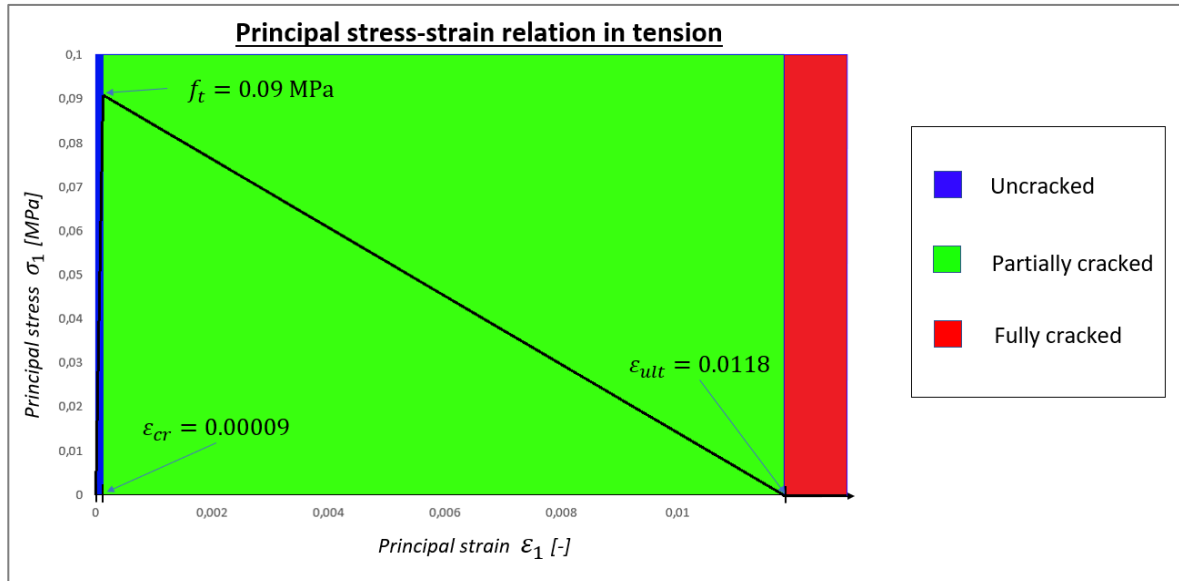
Figure 4.26: Principal stress-strain relation in tension

The principal stress-strain relation in tension is illustrated in *Figure 4.26*. The contour levels for different types of cracks are herein marked using different colors. These colors correspond to the contour levels in the scaled E_1 plots.

According to Licciardello et al. (2021), the existing cracks mainly evolved by increasing their length and width during the NC state (Phase 3). The final crack patterns for both material models using both monotonic and cyclic analysis are illustrated in *Figure 4.27*. Again, some differences in the crack patterns can be observed between the two different material models. The results for the model using the TSCM for the mortar joints are discussed first. It can be

observed that the existing cracks, accumulated during the DL state, are extended in their length which is in line with the experiment. However, the cracks in the numerical model are more distributed compared with the single crack lines in the experiment. Considering the crack pattern for the positive x-direction, the crack at the top of the left pier (crack number 2a) and the newly formed diagonal stair-case crack (crack number 6a) are simulated in a good agreement with the experiment. The combination of these two cracks results in a separation of the left pier with respect to the top spandrel. The propagation of the crack, starting at the bottom right corner of the window (crack number 1a), is mainly diagonal in the numerical model and is extended in its length to the bottom right corner of the wall, which is in line with the experiment. Furthermore, the rocking failure behavior of the left pier can be observed due to the horizontal crack occurring along the bed-joint at the base of the pier. Considering the crack pattern for the negative x-direction, both diagonal stair-case cracks at the corners of the window are extended in their length to the corners of the wall. Moreover, rocking of the right pier is simulated numerically with horizontal cracks occurring along the bed-joints at the bottom of the pier. The crack pattern obtained with the monotonic analysis are very close to the cyclic analysis for the continuous micro-model using the TSCM for the mortar-joints.

The cracks obtained with the model using the EMM for the mortar joints are also more distributed compared with the single crack lines in the experiment. Considering the crack pattern in the positive x-direction, the crack at the top of the left pier (crack number 2a) is simulated in a good agreement with the experiment. However, the newly formed diagonal stair-case crack starting at the top left corner of the window (crack number 6a) is not simulated. The rocking failure behavior of the left pier is captured because of the horizontal cracks occurring at the base of the pier. Furthermore, the diagonal stair-case crack, starting at the bottom right corner of the window (crack number 1a) is widely distributed where the cracks are also running across the base of the right pier. Considering the crack pattern for the negative x-direction, no rocking of the right pier is being simulated with the monotonic analysis. Instead, rocking of the wall is captured by having horizontal cracks occurring along the bed-joints at the bottom right corner of the wall. On the other hand, rocking of the right pier is simulated with the cyclic analysis. The diagonal stair-case crack starting at the top right corner of the window (crack number 4a) is in a less good agreement with the experiment compared with the model using the TSCM for the mortar joints. This diagonal stair-case crack is not extended to the corner of the wall and is also propagating in horizontal direction along the bed-joints. On the other hand, the diagonal stair-case crack starting at the bottom left corner of the window (crack number 3a) is extended to the corner of the wall but is also widely distributed.

In summary, the capacity curves obtained from the monotonic analyses for both material models follows the outline of the capacity curves for the cyclic analyses as the envelope curves. The results for both loading cases, when looking at both material models separately, are very similar in terms of the obtained capacity curves and the crack patterns. The model using the EMM for the mortar joints is able to capture the hysteretic behavior when doing a cyclic analysis. However, the crack pattern of the model using the TSCM for the mortar joints are in a better agreement with the experiment. This could be because of the assumption that is made for the numerical models where the bricks are kept linear elastic. As a result, the EMM was adapted and applied in an isotropic manner to only the mortar joints. However, because the EMM was mainly developed to capture masonry as an orthotropic material, this could be the reason why the full potential of the material model could not be carried out because it was limited by the assumption that was made for this case.

Continuous micro-model (un-strengthened wall)

(Crack pattern numerical results vs experimental results for Near Collapse state)
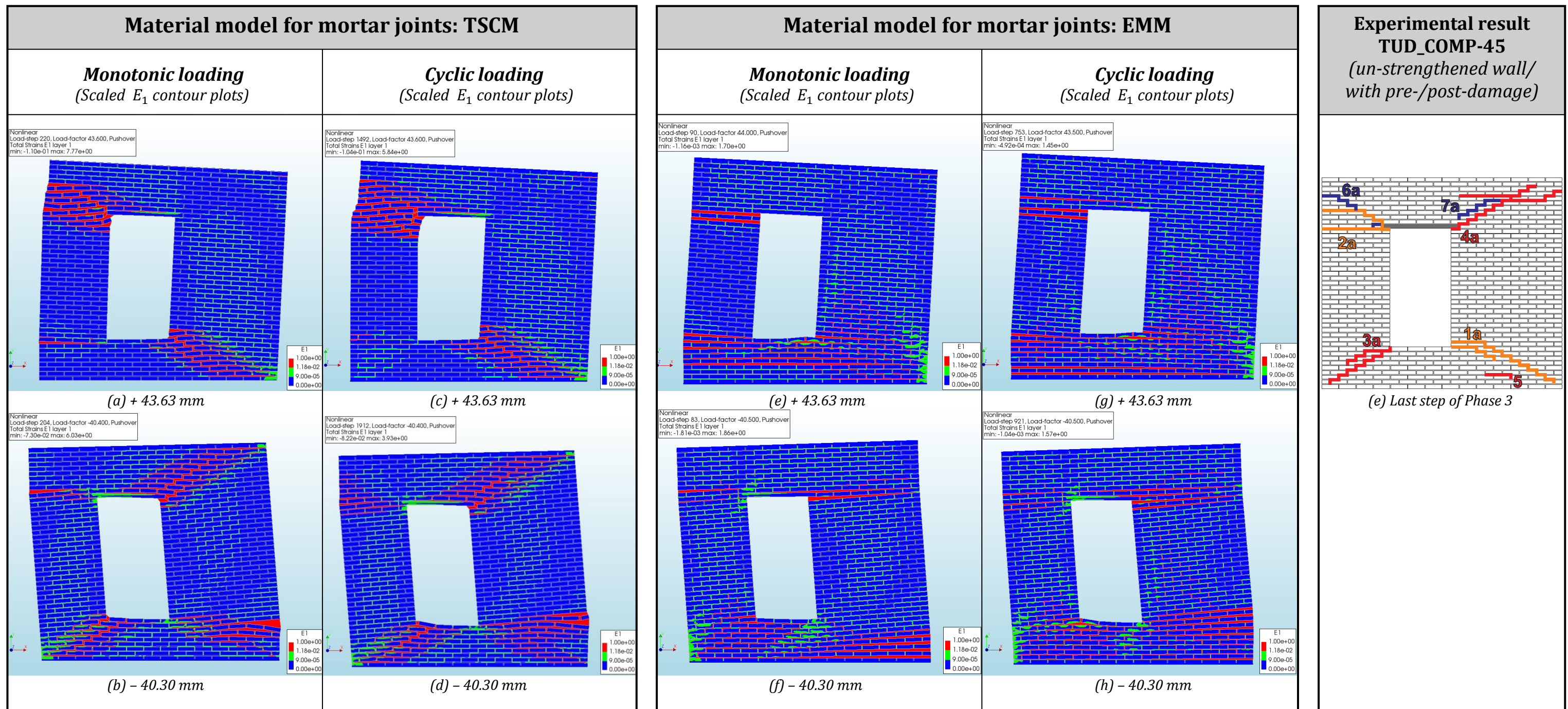
Figure 4.27: Crack pattern at maximum top displacement monotonic and cyclic pushover analysis (up to NC state) for continuous micro-model using contour plots scaled principal strain E1 [-]

4.6   Conclusions

Analyses for the Damage Limitation state

Considering the numerical analyses for the un-strengthened wall in the Damage Limitation state, all modeling approaches are able to simulate the main individual cracks at the main locations accurately, except for the detailed micro-model using the *Combined cracking-shearing-crushing* model for the brick-mortar joint interfaces. This material model is not accurate for cyclic analyses because of the fact that elastic unloading in tension takes place, resulting in overly stiff cracks.

The numerical settings and parameters such as the mesh size, load-step size and convergence criteria do have influence on the crack pattern. Although small differences can be spotted, the results of the sensitivity analyses consistently display the main cracks which capture the main rocking failure behavior of both piers.

Large diagonal cracks tend to occur in the right pier for the macro-model when refining the numerical settings, meaning in terms of; using smaller elements, using quadratic elements, using a tighter convergence tolerance etc. However, these diagonal cracks running across the right pier are not observed in the experiments. On the other hand, the diagonal stair-case cracks are only well captured in the two micro-model when choosing an element size which matches the thickness of the mortar joints.

The hysteretic behavior in cyclic analyses cannot be captured with the *Total Strain Crack model (TSCM)* since this material model only allows for secant unloading, whereas the *Engineering Masonry model (EMM)* allows for elastic unloading.

Approach 1 and 2 for the detailed micro-model are very similar because cracks mainly occur in the form of opening of the interface elements at the brick-mortar bonds, while smeared cracking in the mortar joints is limited. This means that Approach 1 is a reasonable simplification of Approach 2.

The monotonic analyses are very similar to the cyclic analyses in terms of the crack pattern and the capacity curves where the monotonic analyses follows the outline of the cyclic analyses as the envelope curve. However, the computational time for the cyclic analyses are significantly higher compared to the monotonic analyses.

Analyses for the Near Collapse state

The continuous micro-model is chosen for the analyses in the Near Collapse state since the diagonal stair-case cracks are much better captured compared to the macro-model. Moreover, the modeling effort is significantly lower compared to the detailed micro-model, without losing much accuracy in obtained results.

The maximum force capacity in both loading directions is closer to the experiment when using the *TSCM* for the mortar joints. Furthermore, the continuous micro-model using the *EMM* for the mortar joints mainly display horizontal cracks, whereas the stair-case cracks are captured with the *TSCM*. The results of the monotonic analyses are also similar to the cyclic analyses in the Near Collapse state in terms of the capacity curves and the crack patterns for both material models. The cracks obtained with the analyses in the Near Collapse state are more distributed compared to the individual crack lines which are obtained in the experiment and also the numerical analyses in the Damage Limitation state.

5

NUMERICAL MODELING
Part 2: Strengthened walls

The effect of the bed-joint reinforcement technique is investigated in this chapter. The three modeling approaches from the previous chapter are used again for simulating the strengthened wall. This chapter follows the same sequence for the discussion of the numerical models, namely starting off by doing simulations for the Damage Limitation (DL) state. Subsequently, the continuous micro-model is used again for the simulations up to the Near Collapse (NC) state. The pre-/post-damage are not included in the un-strengthened models from the previous chapter. However, the strengthened wall from the experiment was damaged prior to strengthening. For this reason, in order to make the comparison possible with the numerical models of the un-strengthened wall, as well as with the strengthened wall from the experiment, four variants are herein considered as illustrated in *Figure 5.1*. Variant 1 and Variant 2 are the models *without* pre-/post-damage where the former one only has bed-joint reinforcement and the latter one has both bed-joint reinforcement and diagonal bars. These two variants are compared with the numerical models of the un-strengthened wall. On the other hand, Variant 3 and Variant 4 are the models *with* pre-/post-damage where the former one only has bed-joint reinforcement and the latter one has both bed-joint reinforcement and diagonal bars. These two models are compared with the strengthened wall from the experiment. As described before in Chapter 3, the damages which were accumulated prior to the strengthening process are referred to as the *post-damage*, while the *pre-damage* is the result of the placement of thin plastic sheets between the bricks and mortar to account for the artificial absence of bond to simulate cracking due to soil subsidence.
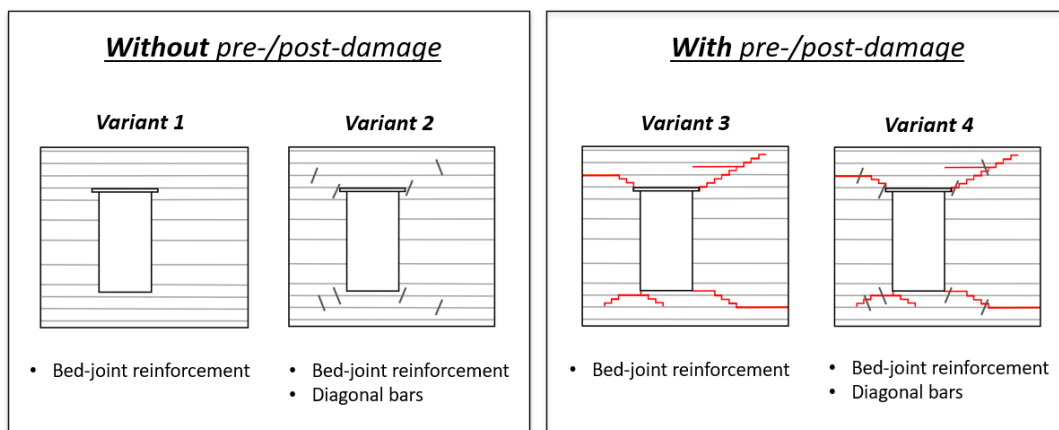
Figure 5.1: Four variants to investigate the effect of the bed-joint reinforcement, diagonal bars and pre-/post-damage

The monotonic analyses (in the DL state) for the macro-model, continuous and detailed micro-model are presented and discussed in Section 5.1, Section 5.2 and Section 5.3, respectively. The results of the analyses in the DL state for all three modeling approaches are discussed in Section 5.4. Furthermore, the numerical simulations of the strengthened wall up to the NC state are

presented and discussed in Section 5.5. Both monotonic and cyclic analysis are herein conducted. Lastly, the conclusions for Chapter 5 are provided in Section 5.6.

5.1 Finite element model using macro-modeling approach

The macro-modeling approach is used to model the strengthened wall in this section for the DL state. The numerical model and the results are presented in a similar order like the un-strengthened walls from the previous chapter. The geometry of the FE-model including the boundary conditions are discussed in Section 5.1.1. Different adopted FE-types including information about the mesh of the model are discussed in Section 5.1.2. The adopted material models for all components are presented in Section 5.1.3. Moreover, the results of the monotonic analyses are presented and discussed in Section 5.1.4.

5.1.1 Geometry and boundary conditions

The geometry and boundary conditions of the strengthened wall are the same as for the un-strengthened wall, which are discussed in the previous chapter. The same element type and material model for each structural component are used as for the un-strengthened wall (illustrated in *Figure 4.1* of Section 4.1.1). The pre-/post-damage is included in the macro-model by dividing the wall into sections and assigning modified material properties to the damaged areas. This method of modeling is according to the paper by Drougkas et al. (2020b). The FE-model of the strengthened wall is illustrated in *Figure 5.2*. The steel reinforcing bars, which are placed in pairs in some of the bed-joints, are modeled as one single equivalent reinforcement bar with a circular cross-section equal to the sum of the areas of the original bars. The diameter of all steel bars are $6\ mm$. The diameter of the equivalent steel bar is $8.49\ mm$.
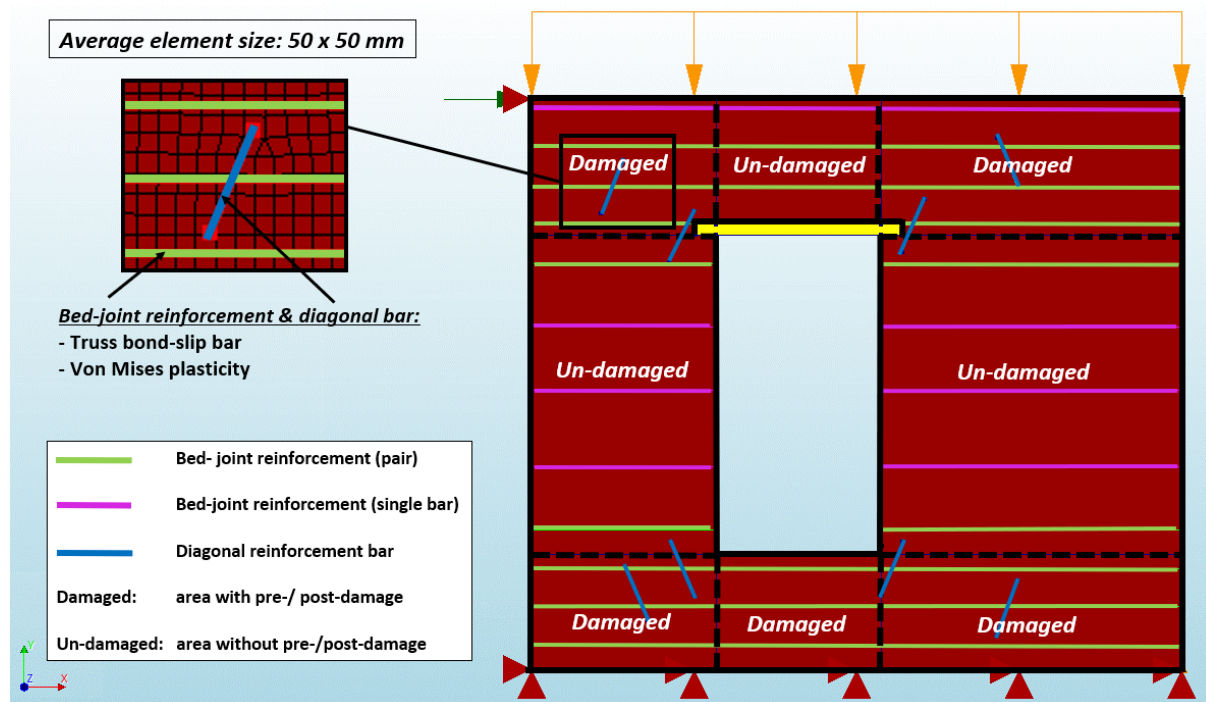
Figure 5.2: FE-model using macro-modeling approach (strengthened wall)

5.1.2 Finite element discretization and mesh properties

The same FE-types are used for the strengthened wall as for the un-strengthened macro-model where the characteristics are listed in *Table A 3* of Appendix A. The steel reinforcing bars are simulated with truss elements where interface elements are incorporated between the trusses and the plane stress elements for the bed-joints. By assigning a bond-slip constitutive relation, the pull-out behavior of the steel bars can be modeled. The material properties are presented in Section 5.1.3. Furthermore, the same mesh size as for the un-strengthened macro-model of 50 *mm* is used.

5.1.3 Constitutive laws

The material properties for the top/ bottom steel beams and the concrete lintel are the same as for the un-strengthened walls which are listed in *Table 3* and *Table 4*, respectively. The material properties for the un-damaged areas of the masonry wall are also the same as for the un-strengthened wall and listed in *Table 2*. However, the Young's modulus is reduced by 50% in all damaged areas. Furthermore, the tensile strength, as well as the tensile and shear fracture energy, are reduced to zero to account for the artificial absence of bond in the pre-damage and the loss of interface cohesion in the post-damage due to crack opening (Drougkas et al., 2020b).

The material properties for the steel reinforcing bars are listed in *Table 17*. The Von Mises plasticity model is used to simulate the nonlinearity of the reinforcement. The stress-strain relationship for the reinforcing bars is illustrated in *Figure 5.3*. Furthermore, to simulate the pull-out behavior of the reinforcing bars, the material type of the "Truss bond-slip bar" is used, where interface elements are introduced between the truss elements for the reinforcement and the plane stress elements for the bed-joints. According to Drougkas et al. (2020), the pull-out test stress-slip cruves are fitted to the bond-slip model proposed in the CEB-FIB Model Code 2010. The shear bond stress τ_0 is herein expressed as a piecewise function of the slip s. The numerical parameters for the bond-slip model are taken from Table 4 from the paper by Drougkas et al. (2020). The normal and shear stiffness for the bond-slip interfaces are determined based on the Young's modulus of the plane stress elements for which the truss elements for the reinforcement bars are connected to.

Figure 5.3: Stress-strain relation reinforcement bars

Table 17: Material properties – steel reinforcing bars

Steel reinforcing bars				
Material type			Truss bond-slip bar	
Reinforcement bar				
Young's modulus	E	N/mm^2	194000	
Poisson's ratio	ν	-	0.3	
Mass density	ρ	kg/m^3	7850	
Nonlinear model			Von Mises plasticity	
Hardening function			Total strain-yield stress	
Hardening hypothesis			Strain hardening	
Hardening type			Isotropic hardening	
Yield strength	f_y	N/mm^2	205	
Tensile strength	f_s	N/mm^2	515	
Bond-slip interface				
Normal stiffness modulus	k_n	N/mm^2	6174	
Shear stiffness modulus	k_t	N/mm^2	61.74	
Bond-slip interface failure model		CEB-FIB 2010 bond-slip function		
			Bed-joint reinforcement	Diagonal bars
Maximum shear stress	τ_{max}	N/mm^2	2	1.3
Ultimate shear stress	τ_f	N/mm^2	0.05	0.05
Linearized initial slip section	S_0	mm	0.06	0.06
Relative slip section	S_1	mm	5	20
Relative slip section	S_2	mm	110	45
Relative slip section	S_3	mm	120	50
Exponent	α	-	0.7	0.7

5.1.4 Monotonic pushover analysis

Monotonic analyses are conducted for all four variants of the strengthened wall with a macro-modeling approach. The loading conditions and the configuration of numerical parameters and settings are the same as for the most optimum configuration which was found with the sensitivity analysis for the un-strengthened wall (*Table 5* in Section 4.1.5). However, a looser convergence criteria of 0.1 (instead of 0.05 from the sensitivity analysis) is used for the numerical models of the strengthened wall because large diagonal cracks occurred across the right pier when using a tighter convergence criteria.

The capacity curves for Variant 1 and 2 of the strengthened wall are compared with the un-strengthened wall in *Figure 5.4a*, while Variant 3 and 4 of the strengthened wall are compared with the experiment in *Figure 5.4b*. From the results of the capacity curve and the obtained maximum base shear forces in both loading directions (*Table 18*), it can be observed that the increase in force capacity is very small for the DL state. This can also be concluded from the results of the contour plots (*Figure 5.5*) where the crack pattern are almost identical when comparing the un-strengthened wall with Variant 1 and 2 of the strengthened wall.

Although the results of Variant 3 and 4 of the strengthened wall are close to the experiment in terms of the shape of the capacity curve (*Figure 5.4b*) and the obtained maximum base shear forces in both loading directions (*Table 18*), the results are not accurate because of the following reason; the pre-/post-damage are included in the macro-model by dividing the wall into damaged and un-damaged areas by identifying the loacations of the cracks according to the

experiment, and assigning modified material properties to those areas. For this reason, the pre-/post-damage is "smeared" over the whole damaged areas which means that the maximum force capacity is underestimated. Moreover, the material properties for the high-strength repair mortar, used for the embedment of the reinforcement bars, cannot be assigned to the model since the geometry of the bed-joints are not modeled seperately. The implementation of pre-/post-damage can be refined in a continuos micro-model where the bricks and mortar joints are modeled seperately (see Section 5.2).

The maximum occurred axial stresses and bond-slip in the reinforcement bars for all four variants of the strengthened wall are listed in *Table 19*. No yielding of the reinforcement bars occurred in the DL state for all four variants since the maximum axial stresses are all below the yield strength of 205 N/mm^2. Moreover the maximum occurred bond-slip in the bed-joint reinforcement and the diagonal bars are well below the corresponding maximum elastic bond-slip of 5 mm and 20 mm, respectively.

Lastly, the maximum crack width w for each main crack is also indicated in *Figure 5.5*. However, because the crack pattern for the strengthened wall Variant 3 and 4 are smeared over the damaged areas and thus not accurate, the comparison with the experiment is therefore not made. The comparison with the experiment is more accurate with a continuous and detailed micro-modeling approach which are discussed in the next sections. The obtained values of the maximum crack width for the un-strengthened wall, from the previous chapter, are compared with the strengthened wall Variant 1 and 2. It can be observed that the values are close when comparing the un-strengthened wall with the two strengthened wall variants. The only noticeable decrease in crack width is for the crack at the base of the left pier (loading in positive x-direction) and crack number 3 (loading in negative x-direction) with 11~12% and 26~31%, respectively. On the other hand, the maximum crack width for the crack at the base of the right pier (loading in negative x-direction) is increased with 16% for the two strengthened wall variants with respect to the un-strengthened wall.

Table 18: Comparison maximum base shear forces for strengthened wall-Variant 1 and 2 with un-strengthened wall and experiment for the macro-model

	Positive x-direction		Negative x-direction	
	Max. base shear force	Percentage difference	Max. base shear force	Percentage difference
	[kN]	[%]	[kN]	[%]
Un-strengthened wall	**25.75**	**-**	**-21.44**	**-**
Strengthened wall-Variant 1	26.53	+ 3.03 %	-21.94	+ 2.33 %
Strengthened wall-Variant 2	26.65	+ 3.50 %	-21.98	+ 2.52 %
Experiment	**22.72**	**-**	**-20.10**	-
Strengthened wall-Variant 3	21.81	- 4.01 %	-18.31	- 8.91 %
Strengthened wall-Variant 4	21.86	- 3.79 %	-18.12	- 9.85 %
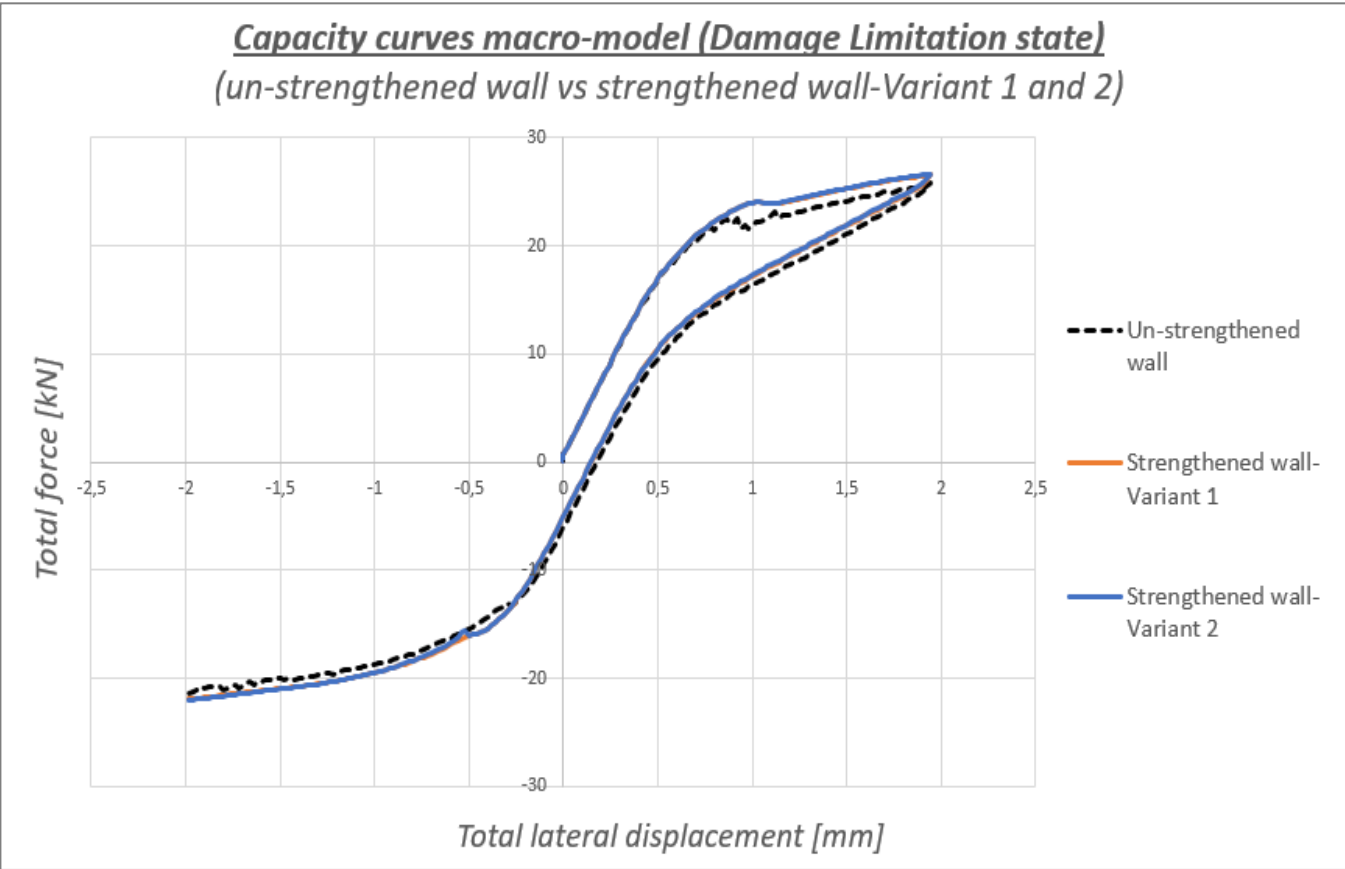
(a)
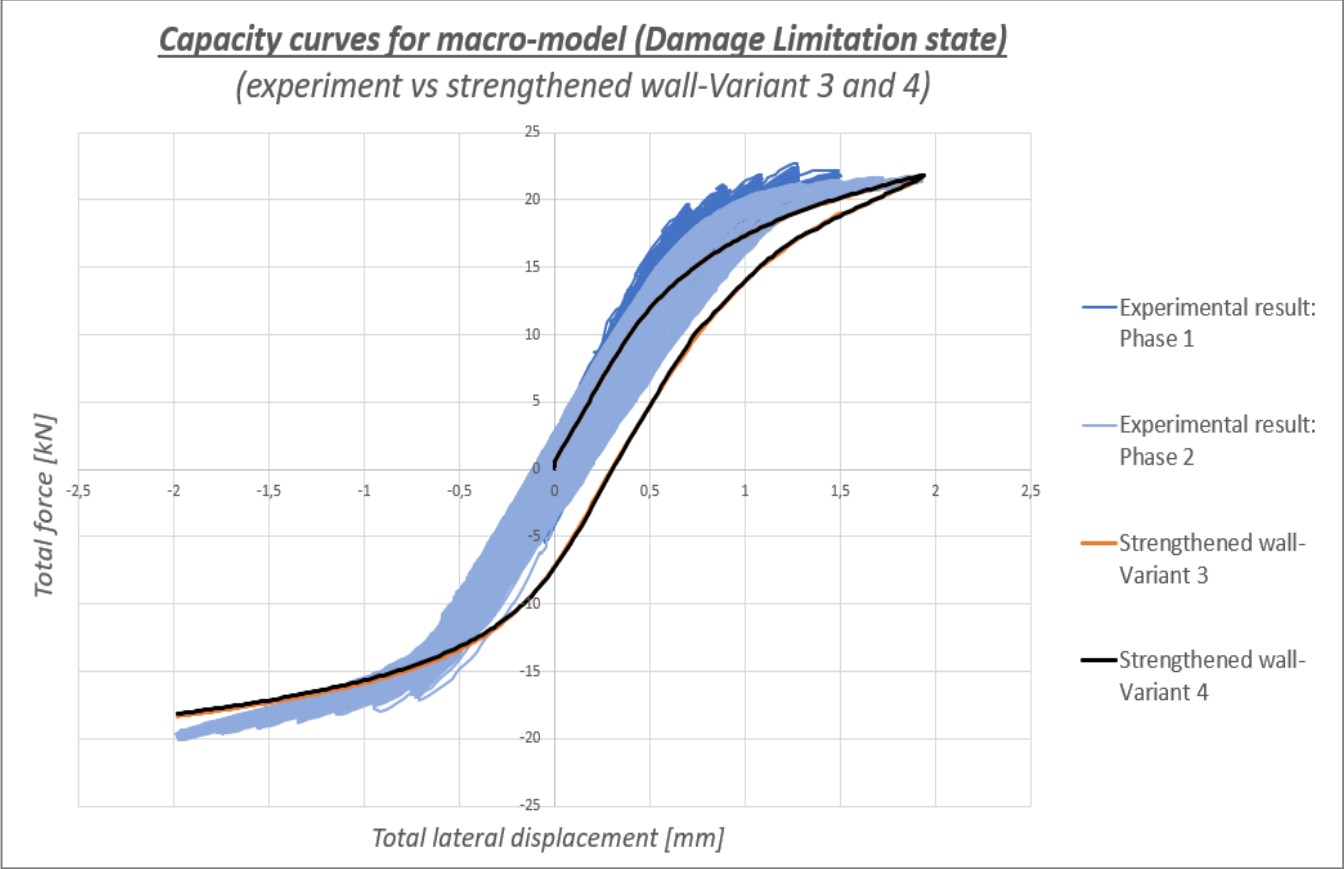
(b)

Figure 5.4: Comparison of capacity curves using the macro modeling approach: (a) un-strengthened wall vs strengthened wall-Variant 1 and 2; (b) experiment vs strengthened wall-Variant 3 and 4

Table 19: Numerical results strengthened wall macro-model for all four variants

Macro-model (strengthened wall)		Loading in positive x-direction					Loading in negative x-direction					Total Time
		Max. base shear force	Maximum axial stress		Maximum bond-slip		Max. base shear force	Maximum axial stress		Maximum bond-slip		
			Bed-joint reinforcement	Diagonal bar	Bed-joint reinforcement	Diagonal bar		Bed-joint reinforcement	Diagonal bar	Bed-joint reinforcement	Diagonal bar	
		$[kN]$	$[N/mm^2]$	$[N/mm^2]$	$[mm]$	$[mm]$	$[kN]$	$[N/mm^2]$	$[N/mm^2]$	$[mm]$	$[mm]$	$[min]$
Without pre-/post-damage	Variant 1: Only bed-joint reinforcement	26.53	33.27	-	0.0601	-	-21.94	28.89	-	0.0648	-	3
	Variant 2: Bed-joint reinforcement & diagonal bars	26.65	33.46	0.84	0.06	0.23	-21.98	28.76	0.46	0.07	0.36	3
With pre-/post-damage	Variant 3: Only bed-joint reinforcement	21.81	25.62	-	0.0514	-	-18.31	44.44	-	0.10	-	4
	Variant 4: Bed-joint reinforcement & diagonal bars	21.86	26.24	0.49	0.05	0.23	-18.12	55.22	0.34	0.13	0.09	4

Macro-model using EMM for masonry composite (strengthened wall)

(Crack pattern monotonic analysis for Damage Limitation state with maximum crack width w [mm] indicated)
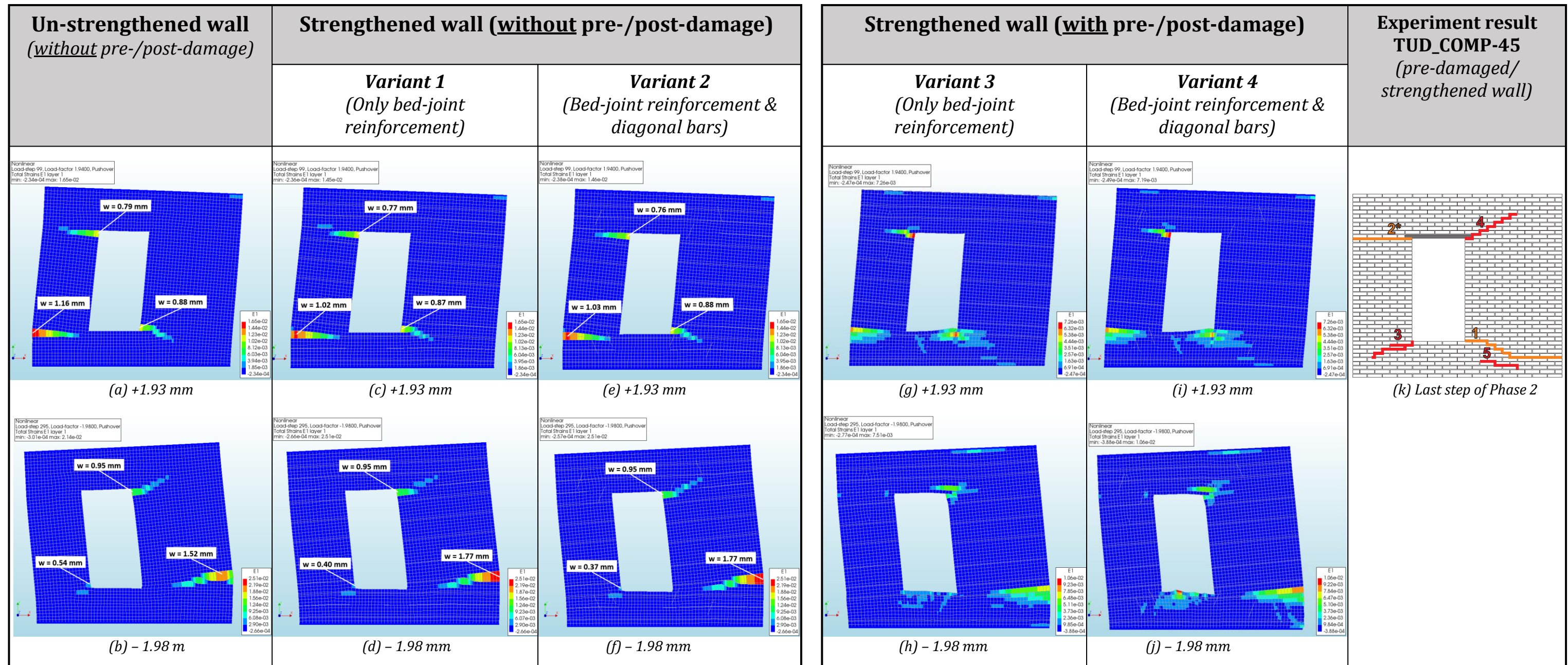
Figure 5.5: Crack pattern at maximum top displacement monotonic analysis (DL state) for macro-model using contour plots principal strain E1

5.2 Finite element model using continuous micro-modeling approach

The continuos micro-modeling approach is used to model the strengthened wall in this section for the DL state. The numerical model and the results are presented in a similar order like the un-strengthened walls from the previous chapter. The geometry of the FE-model including the boundary conditions are discussed in Section 5.2.1. Different adopted FE-types including information about the mesh of the model are discussed in Section 5.2.2. The adopted material models for all components are presented in Section 5.2.3. Moreover, the the results of the monotonic analysis are presented and discussed in Section 5.2.4.

5.2.1 Geometry and boundary conditions

The geometry and boundary conditions of the strengthened wall are the same as for the un-strengthened wall, which are discussed in the previous chapter. The same element type and material model for each structural component are used as for the un-strengthened wall (illustrated in *Figure 4.7* of Section 4.2.1). Because the bricks and the mortar joints are modeled separately with a continuous micro-modeling approach, it allows for the direct geometrical definitions of the pre-/post-damage in the mortar joints. Consequently, it allows for the direct assignment of material properties to each structural component. For this reason, the use of high strength repair mortar in only the reinforced bed-joints can be simulated directly. The FE-model of the strengthened wall is illustrated in *Figure 5.6*. The diagonal bars are herein numbered and the rows of reinforced bed-joints are indicated with a letter. Again, the steel reinforcing bars which are placed in pairs in some of the bed-joints are modeled as one single equivalent reinforcement bar with a circular cross-section equal to the sum of the areas of the original bars. The diameter of all steel bars are 6 *mm*. The diameter of the equivalent steel bars are 8.49 *mm*.
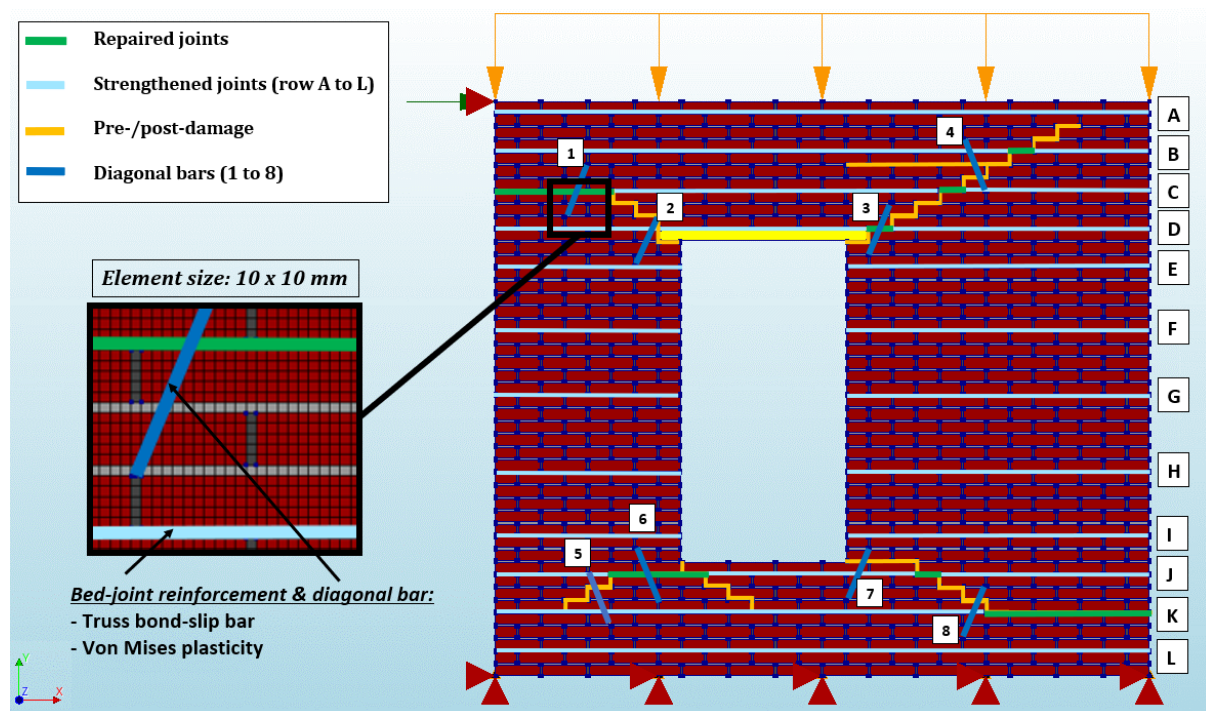
Figure 5.6: FE-model using continuous micro-modeling approach (strengthened wall)

5.2.2   Finite element discretization and mesh properties

The same FE-types are used for the strengthened wall as for the un-strengthened wall where the characteristics are listed in *Table A 3* of Appendix A. The steel reinforcing bars are simulated with truss elements where interface elements are incorporated between the trusses and the plane stress elements for the bed-joints. By assigning a bond-slip constitutive relation, the pull-out behavior of the steel bars can be modeled (same as for the macro-model). The material properties are discussed in Section 5.2.3. Furthermore, a mesh size of 10 *mm* is used to match the thickness of the mortar joints in order to capture the diagonal stair-case cracks.

5.2.3   Constitutive laws

The material models of the top/ bottom steel beams, concrete lintel and masonry bricks are the same as for the un-strengthened walls which are listed in *Table 3*, *Table 4* and *Table 8*, respectively. On the other hand, the material properties for the reinforced bed-joints are different since a change in the material composition of the mortar joints, along the thickness of the wall, is introduced with the strengthening technique. Because the mortar joints for the strengthened wall consist of a layer of 6 cm construction mortar and a layer of 4 cm high-strength repair mortar, the "rule of mixtures" is applied for the determination of the mechanical properties of the composite joint (Drougkas et al., 2020). For this reason, the material composition of the mortar joints can be indirectly considered in a 2D plane-stress continuous micro-model. The material properties for the strengthened and repaired joints are taken from Table 5 from the paper by Drougkas et al. (2020). The material properties of all different joints for both TSCM and EMM are listed in *Table E 2* and *Table E 3*, respectively in Appendix E.

The material properties for the steel reinforcing bars and the bond-slip model are the same as for the macro-model (see *Table 17*). Moreover, the pre-/post-damage can be simulated by reducing the Young's modulus by 50% and reducing the tensile strength, as well as the tensile and shear fracture energy to zero according to Drougkas et al. (2020).

5.2.4   Monotonic pushover analysis

Monotonic analyses are conducted for all four variants of the strengthened wall with a continuous micro-modeling approach. The loading conditions and the configuration of numerical parameters and settings are the same as for the most optimum configuration which was found with the sensitivity analysis for the un-strengthened wall (*Table 9* from Section 4.2.5).

The capacity curves for Variant 1 and 2 of the strengthened wall are compared with the un-strengthened wall in *Figure 5.7* for the continuous micro-model using the TSCM for the morta joints, whereas in *Figure 5.8* for the continous micro-model using the EMM for the mortar joints. Moreover, the capacity curves for the strengthened wall Variant 3 and 4 for both material models are compared with the experiment in *Figure 5.9*. From the results of the capacity curves and the obtained maximum base shear forces in both loading directions (*Table 20*), it can be observed that the increase in force capacity is very small when comparing the strengthened wall Variant 1 and 2 with the un-strengthened wall for both material models in the DL state. This can also be concluded from the results of the contour plots (*Figure 5.10* and *Figure 5.11*) where the crack pattern are almost identical when comparing the un-strengthened wall with Variant 1 and 2 of the strengthened wall. Only Variant 2 of the continuous micro-model using the TSCM for the mortar joints (*Figure 5.10*) is showing a difference in terms of crack length for crack number 2*.

The crack pattern for the strengthened wall Variant 3 and 4, for the continuous micro-model using the TSCM (*Figure 5.10*), are close to the experiment. The cracks mainly follow the geometry of the pre-/post-damage. This also holds for the continuous micro-model using the EMM (*Figure 5.11*). Only crack number 2 is different compared to the experiment and the crack length for crack number 3 is underestimated for both material models.

The maximum occurred axial stresses and bond-slip in the reinforcement bars for all four variants of the strengthened wall are listed in *Table 22* for both material models. No yielding of the reinforcement bars occurred in the DL state for all four strengthened wall variants and both material models since the maximum axial stresses are all below the yield strength of 205 N/mm^2. Moreover, it can be observed that the maximum axial stresses are smaller in both loading directions for the continuous micro-model using the EMM. The obtained values for the maximum bond-slip are comparable for both material models. Moreover the maximum occurred bond-slip in the bed-joint reinforcement and the diagonal bars are well below the corresponding maximum elastic bond-slip of 5 mm and 20 mm, respectively. This holds for both material models.

Lastly, the maximum crack width w for each main crack is also indicated in *Figure 5.10* and *Figure 5.11*. The obtained values of the maximum crack width for the un-strengthened wall, from the previous chapter, are compared with the strengthened wall Variant 1 and 2 for both material models. Considering the model using the TSCM for the mortar joints, the largest percentage increment, with respect to the un-strengthened wall, is +61% for the horizontal crack at the base of the left pier (Variant 2), while the largest reduction is -47% for crack number 2 (Variant 2). Considering the model using the EMM for the mortar joints, the largest percentage increment, with respect to the un-strengthened wall, is +26% for crack number 2 (Variant 1), while the largest reduction is -37% for crack number 4 (both Variant 1 and 2). On the other hand, the values for the maximum crack width for the strengthened wall Variant 3 and 4 are compared to the experiment in *Table 21*. As was observed before in Chapter 4, the obtained values for the maximum crack width are larger with the continuous micro-model using the EMM for the mortar joints.

Table 20: Comparison maximum base shear forces of strengthened wall variants with un-strengthened wall and experiment for the continuous micro-model using TSCM and EMM

		Positive x-direction		Negative x-direction	
		Max. base shear force	Percentage difference	Max. base shear force	Percentage difference
		[kN]	[%]	[kN]	[%]
TSCM	***Un-strengthened wall***	**26.71**	**-**	**-22.01**	**-**
	Strengthened wall-Variant 1	27.08	+ 1.39%	-22.98	+ 4.41%
	Strengthened wall-Variant 2	27.16	+ 1.68%	-23.07	+ 4.82%
	Experiment	**22.72**	-	**-20.10**	-
	Strengthened wall-Variant 3	26.81	+ 18.00%	-22.38	+ 11.34%
	Strengthened wall-Variant 4	27.04	+ 19.01%	-22.46	+ 11.74%
EMM	***Un-strengthened wall***	**26.38**	**-**	**-21.70**	**-**
	Strengthened wall-Variant 1	27.00	+ 2.35%	-22.58	+ 4.06%
	Strengthened wall-Variant 2	27.17	+ 2.99%	-22.63	+ 4.29%
	Experiment	**22.72**	-	**-20.10**	-
	Strengthened wall-Variant 3	27.04	+ 19.01%	-21.45	+ 6.72 %
	Strengthened wall-Variant 4	27.15	+ 19.50%	-21.57	+ 7.31 %
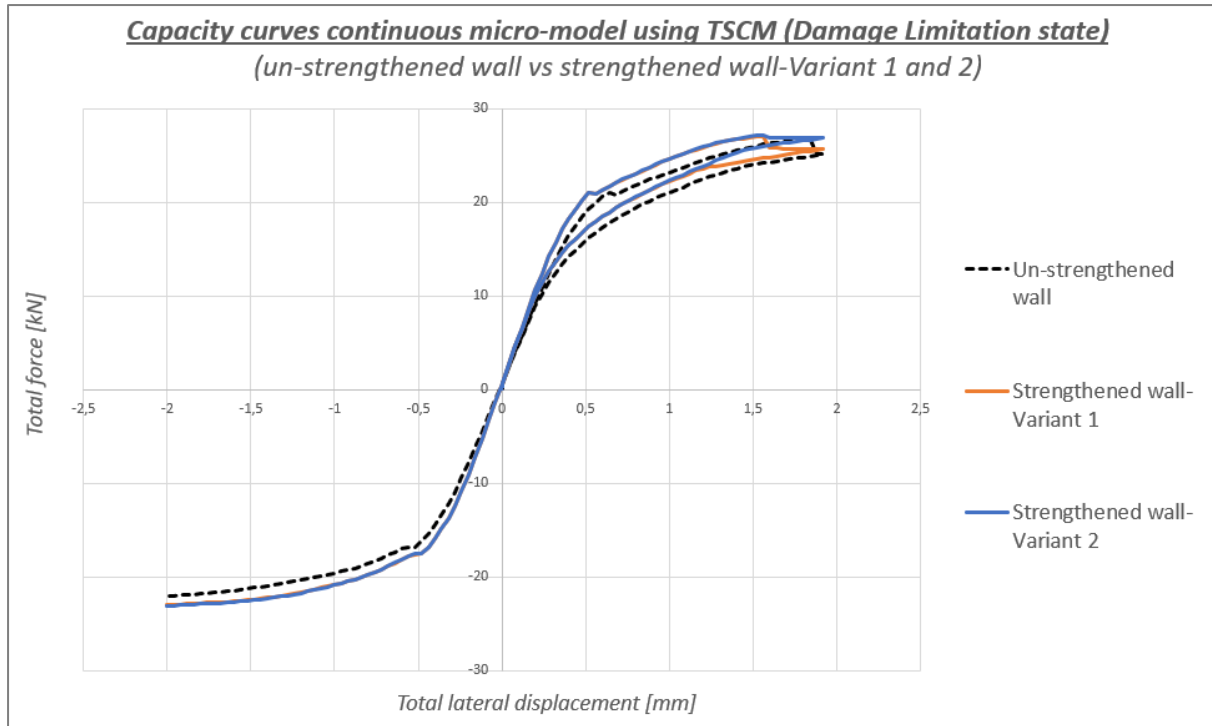
Figure 5.7: Comparison capacity curves for un-strengthened wall vs strengthened wall Variant 1 and 2 for continuous micro-model using TSCM for mortar joints
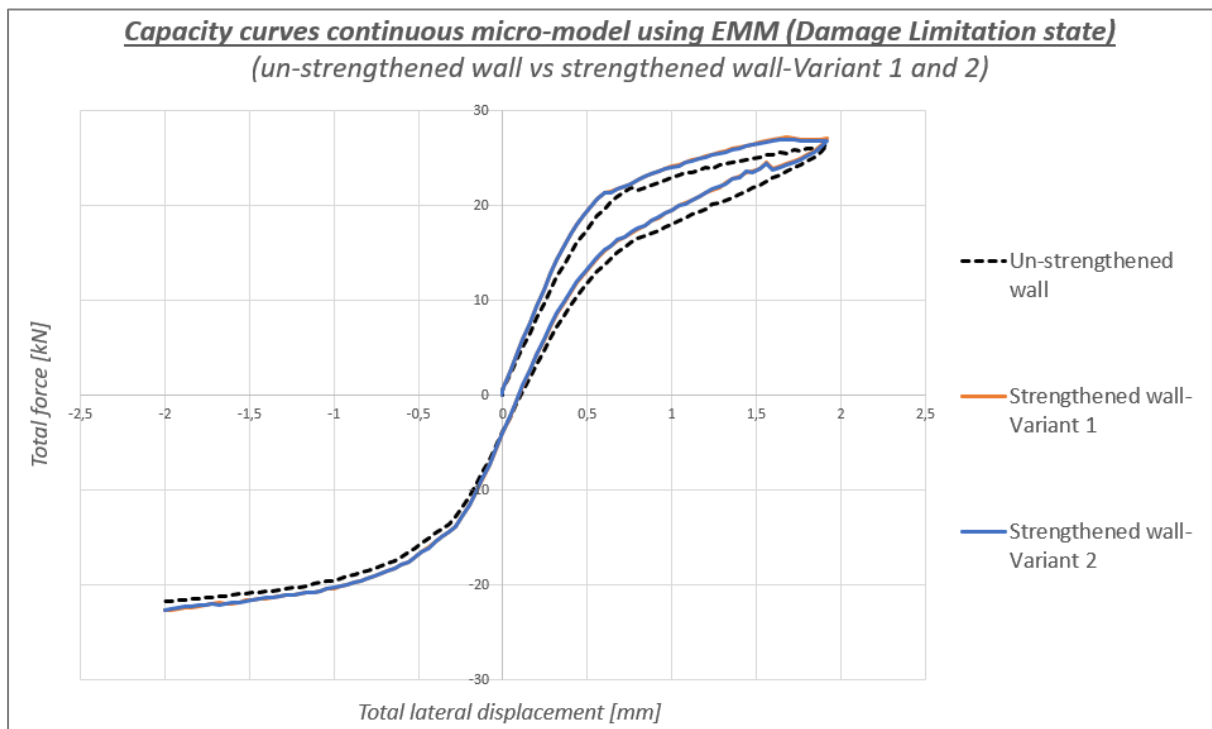
Figure 5.8: Comparison capacity curves for un-strengthened wall vs strengthened wall Variant 1 and 2 for continuous micro-model using EMM for mortar joints
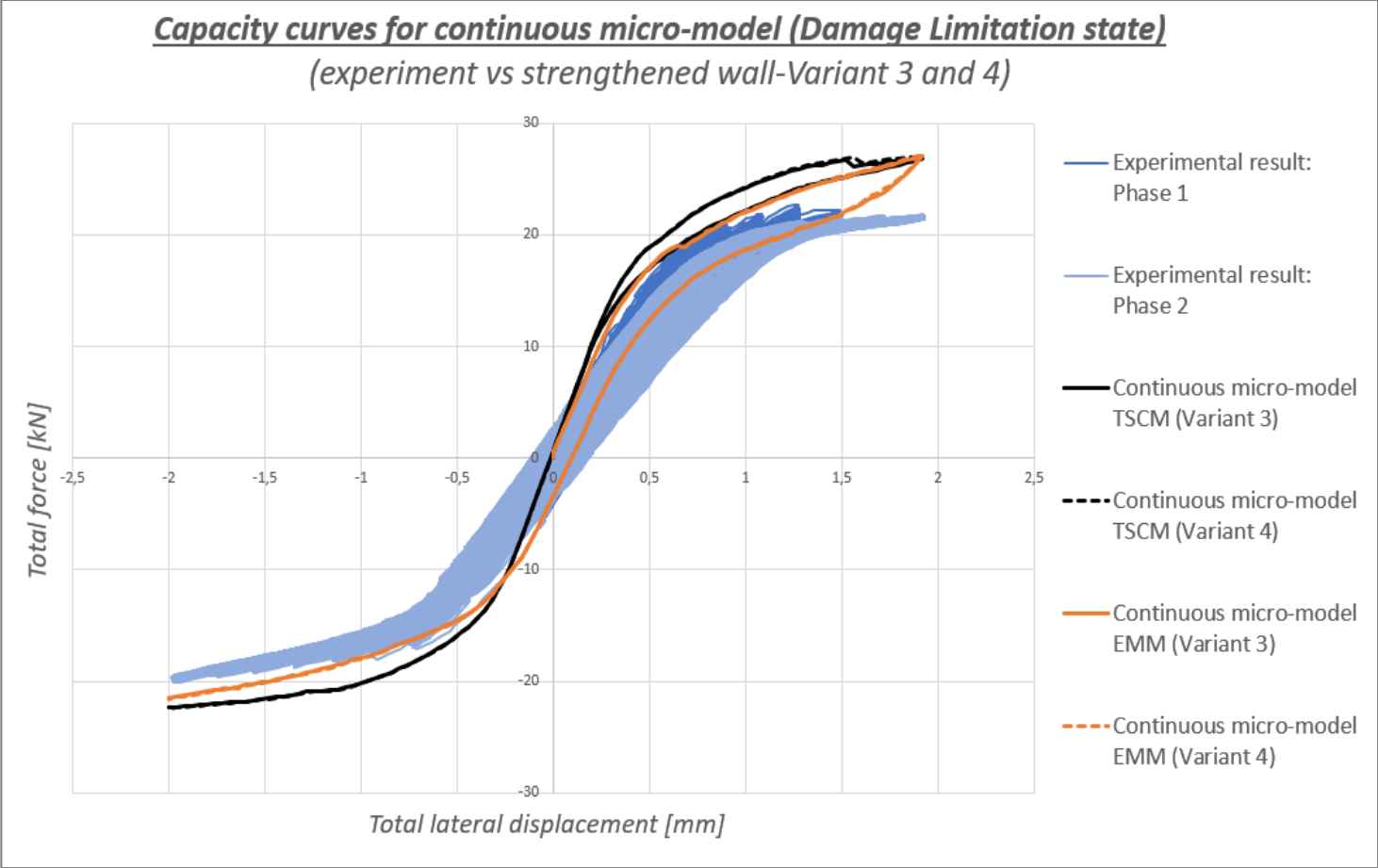
Figure 5.9: Comparison capacity curves for experiment vs strengthened wall Variant 3 and 4 for continuous micro-model using TSCM and EMM for mortar joints in separate models

Table 21: Maximum crack width w [mm] comparison between the experiment (TUD_COMP-45) and strengthened wall Variant 3 and 4 for continuous micro-model using TSCM and EMM for mortar joints in separate models

	Crack width for pre-damaged/ strengthened wall (TUD_COMP-45)	Crack width for strengthened wall using TSCM for mortar joints		Crack width for strengthened wall using EMM for mortar joints	
		Variant 3	*Variant 4*	*Variant 3*	*Variant 4*
	[mm]	[mm]	[mm]	[mm]	[mm]
Crack 1	**0.51**	0.66 (+29%)	0.65 (+27%)	1.02 (+100%)	1.01 (+98%)
Crack 2	**1.06**	0.96 (-9%)	0.94 (-11%)	1.48 (+40%)	1.48 (+40%)
Crack 3	**0.44**	0.63 (+43%)	0.63 (+43%)	1.00 (+127%)	0.99 (+125%)
Crack 4	**0.40**	0.55 (+38%)	0.55 (+38%)	1.30 (225%)	1.28 (+220%)

Table 22: Numerical results strengthened wall continuous micro-model for all four variants

Continuous micro-model (strengthened wall)			Loading in positive x-direction					Loading in negative x-direction					Total Time
			Max. base shear force	Maximum axial stress		Maximum bond- slip		Max. base shear force	Maximum axial stress		Maximum bond- slip		
				Bed-joint reinforcement	Diagonal bar	Bed-joint reinforcement	Diagonal bar		Bed-joint reinforcement	Diagonal bar	Bed-joint reinforcement	Diagonal bar	
			[kN]	[N/mm²]	[N/mm²]	[mm]	[mm]	[kN]	[N/mm²]	[N/mm²]	[mm]	[mm]	[min]
TSCM	*Without pre-/post-damage*	**Variant 1: Only bed-joint reinforcement**	27.08	42.63	-	0.12	-	-22.98	34.59	-	0.10	-	62
		Variant 2: Bed-joint reinforcement & diagonal bars	27.16	43.41	0.79	0.12	0.32	-23.07	34.29	0.53	0.10	0.24	59
	With pre-/post-damage	**Variant 3: Only bed-joint reinforcement**	26.81	39.88	-	0.10	-	-22.38	33.77	-	0.09	-	58
		Variant 4: Bed-joint reinforcement & diagonal bars	27.04	39.85	1.13	0.10	0.32	-22.46	33.68	0.48	0.09	0.21	55
EMM	*Without pre-/post-damage*	**Variant 1: Only bed-joint reinforcement**	27.00	26.67	-	0.06	-	-22.58	23.07	-	0.06	-	42
		Variant 2: Bed-joint reinforcement & diagonal bars	27.17	26.70	1.07	0.06	0.29	-22.63	23.18	0.67	0.06	0.27	40
	With pre-/post-damage	**Variant 3: Only bed-joint reinforcement**	27.04	32.79	-	0.07	-	-21.45	25.86	-	0.06	-	42
		Variant 4: Bed-joint reinforcement & diagonal bars	27.15	32.71	0.68	0.07	0.28	-21.57	26.03	0.66	0.06	0.19	45

Continuous micro-model using TSCM for mortar joints (strengthened wall)

(Crack pattern monotonic analysis for Damage Limitation state with maximum crack width w [mm] indicated)
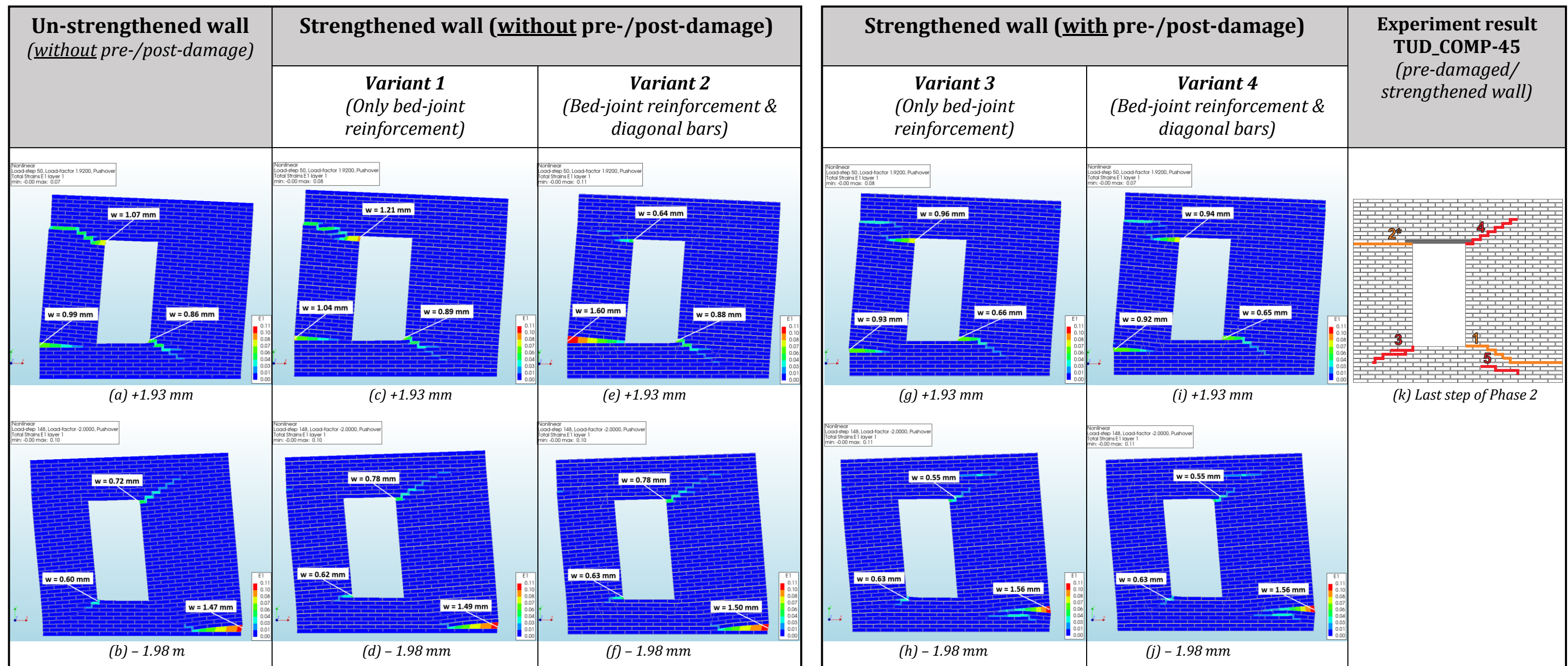
Figure 5.10: Crack pattern at maximum top displacement monotonic analysis (DL state) for continuous micro-model with TSCM for mortar joints using contour plots principal strain E1

Continuous micro-model using EMM for mortar joints (strengthened wall)

(Crack pattern monotonic analysis for Damage Limitation state with maximum crack width w [mm] indicated)
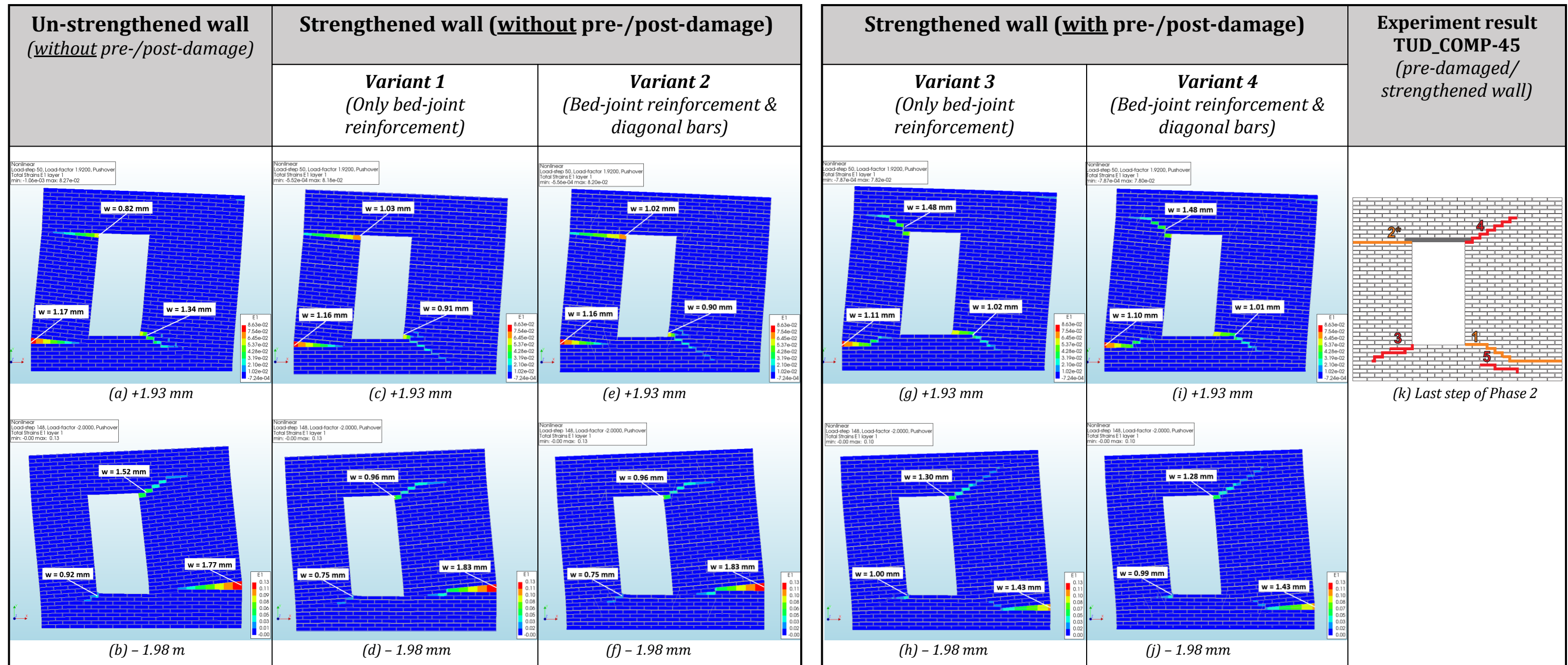
Figure 5.11: Crack pattern at maximum top displacement monotonic analysis (DL state) for continuous micro-model with EMM for mortar joints using contour plots principal strain E1

5.3 Finite element model using detailed micro-modeling approach

The detailed micro-modeling approach is used to model the strengthened wall in this chapter. The numerical model and the results are presented in a similar order like the un-strengthened walls from the previous chapter. The geometry of the FE-model including the boundary conditions are discussed in Section 5.3.1. Different adopted FE-types including information about the mesh of the model are discussed in Section 5.3.2. The adopted material models for all components are presented in Section 5.3.3. Moreover, the results of the monotonic analysis are presented and discussed in Section 5.3.4.

5.3.1 Geometry and boundary conditions

The geometry and boundary conditions of the strengthened wall are the same as for the un-strengthened wall, which are discussed in the previous chapter. The same element type and material model for each structural component are used as for the un-strengthened wall (illustrated in *Figure 4.13* of Section 4.3.1). Like the previously discussed continuous micro-model for the strengthened wall, the pre-/post-damage and the repaired/ strengthened joints can be included by modeling the geometry of these joints separately and assigning modified material properties to those joints. The difference is that these modified material properties also needs to be assigned to the interface elements where the pre-/post-damage and the repaired joints are located. The FE-model of the strengthened wall is illustrated in *Figure 5.12*. The diagonal bars are herein numbered and the rows of reinforced bed-joints are indicated with a letter. The lay-out and the diameter for the reinforcing bars and the diagonal bars are the same as for the strengthened models discussed in the previous sections.
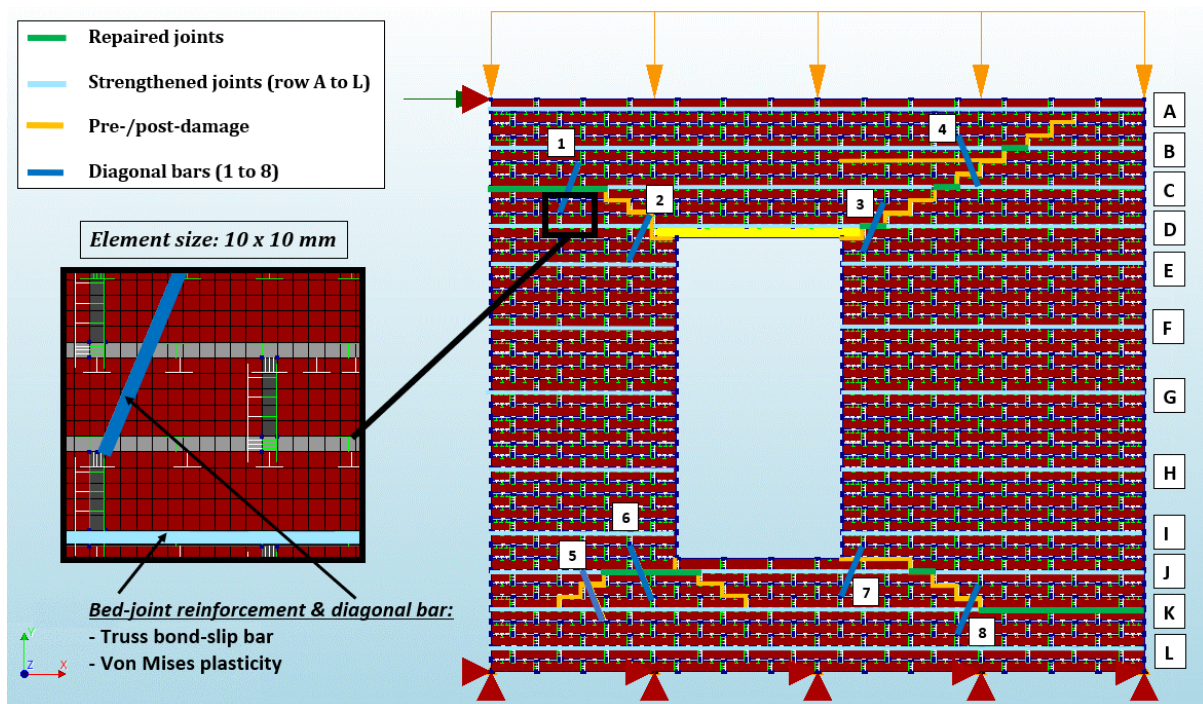
Figure 5.12: FE-model using detailed micro-modeling approach (strengthened wall)

5.3.2 Finite element discretization and mesh properties

The same FE-types are used for the strengthened wall as for the un-strengthened wall where the characteristics are listed in *Table A 3* and *Table C 3* in the corresponding appendices. Again, the steel reinforcing bars are simulated with truss elements where interface elements are incorporated between the trusses and the plane stress elements for the bed-joints. By assigning a bond-slip constitutive relation, the pull-out behavior of the steel bars can be modeled. Furthermore, a mesh size of 10 *mm* is used to match the thickness of the mortar joints in order to capture the diagonal stair-case cracks.

5.3.3 Constitutive laws

As mentioned before in Section 4.3.3 for the un-strengthened detailed micro-model, two approaches can be considered where the difference lies in the location of the nonlinearities. The detailed micro-model in which the nonlinearities are located only in the brick-mortar joint interfaces is referred to as *Approach 1*. The detailed micro-model in which the nonlinearities are located both in the brick-mortar joint interfaces as well as in the mortar joints is referred to as *Approach 2*. For both approaches, Discrete cracking is used for the brick-mortar joint interfaces and the EMM is used for the mortar joints in Approach 2. The material properties of all different joints for the EMM are listed in *Table E 3* of Appendix E. Because the mortar joints are kept linear elastic in Approach 1, only the linear material properties from the table are assigned to the different joints. Moreover, the nonlinear material properties (tensile behavior) from the table are also assigned to the brick-mortar joint interfaces for both approaches. The material properties for the steel reinforcing bars (including constitutive relation for bond-slip) are listed in *Table 17*. The material properties for the top/ bottom steel beams, concrete lintel and masonry bricks can be found in *Table 3*, *Table 4* and *Table 8*, respectively.

5.3.4 Monotonic pushover analysis

Monotonic analyses are conducted for all four variants of the strengthened wall with the detailed micro-model. The loading conditions and the configuration of numerical parameters and settings are the same as for the most optimum configuration which was found with the sensitivity analysis for the un-strengthened wall (*Table 13* from Section 4.3.5). In this section, the results of the capacity curves and the crack patterns are only shown for Approach 1 (model in which the nonlinearities are located only in the brick-mortar joint interfaces). The results for Approach 2 are presented in Appendix D. Cracking in Approach 2 mainly occurred in the form of opening of the interface elements, while cracking in the mortar joints is limited. This means that Approach 1 is a reasonable simplification of Approach 2. The obtained maximum values for different parameters are listed and compared in *Table 25* for all strengthened wall variants for both approaches.

Considering the results for Approach 1, the capacity curves for Variant 1 and 2 of the strengthened wall are compared with the un-strengthened wall in *Figure 5.13a*, while Variant 3 and 4 of the strengthened wall are compared with the experiment in *Figure 5.13b*. Some differences can be observed between Variant 1 and 2 and the un-strengthened wall. The crack at the top of the left pier is propagating across the full width of the pier for Variant 1 and 2, whereas no separation of the left pier and the top spandral can be observed for the un-strengthened wall. Moreover, the capacity curve for Variant 2 is showing a larger residual displacement at zero position compared to Variant 1. As described before in the previous chapter, the explanation for this is as follows; when the maximum top lateral displacement was

reached in the positive x-direction, the left pier was returned to its original zero position in one load-step after unloading. This happened while the L-shape portion of the wall (consisting of the right pier and the top spandrel) was slowly returning to its original zero postion. When the L-shape part of the wall met the top of the left pier again at the zero position, it pushed the left pier a bit to the left. This is the reason why the diagonal stair-case crack at the top of the left pier is also visible when loading the wall in the negative x-direction (*Figure 5.14f*). This is also the case for Variant 3 and 4 but is not occurring in the variants for Approach 2 (*Figure D 1* of Appendix D). Although small differences can be observed when looking at the crack patterns and the shape of the capacity curves, the increase in force capacity in both loading directions is small for the DL state when comparing Variant 1 and 2 with the un-strengthened wall (*Table 23*). On the other hand, the crack pattern for the strengthened wall Variant 3 and 4 are close to the experiment. The cracks mainly follow the geometry of the pre-/post-damage. Only crack number 2 is different compared to the experiment. This crack is propagating purely in the horizontal direction in the experiment while in the numerical models it follows the geometry of the pre-/post-damage and develops from a stair-case crack into a horizontal crack.

Compared to the previously discussed strengthened macro- and continuous micro-model, the maximum occurred axial stresses and bond-slips in the reinforcement bars are very small for all variants and both Approach 1 and 2 of the strengthened detailed micro-model (*Table 25*). No yielding of the reinforcement bars occurred in the DL state for all four variants since the maximum axial stresses are well below the yield strength of 205 N/mm^2. Lastly, the maximum crack width w for each main crack is also indicated in *Figure 5.14*. The obtained values of the maximum crack width for the un-strengthened wall, from the previous chapter, are compared with the strengthened wall Variant 1 and 2. The largest percentage increment, with respect to the un-strengthened wall, is +70% for crack number 3 (Variant 2), while the largest reduction is -8% for crack number 1 (Variant 1 and 2). On the other hand, the values for the maximum crack width for the strengthened wall Variant 3 and 4 are compared to the experiment in *Table 24*.

Table 23: Comparison maximum base shear forces of strengthened wall variants with un-strengthened wall and experiment for the detailed micro-model (Approach 1)

	Positive x-direction		*Negative x-direction*	
	Max. base shear force	**Percentage difference**	**Max. base shear force**	**Percentage difference**
	$[kN]$	[%]	$[kN]$	[%]
Un-strengthened wall	**25.07**	**-**	**-20.01**	**-**
Strengthened wall-Variant 1	26.35	+ 5.11%	-20.73	+ 3.60%
Strengthened wall-Variant 2	26.26	+ 4.75%	-21.90	+ 9.45%
Experimental results	**22.72**	**-**	**-20.10**	**-**
Strengthened wall-Variant 3	25.71	+ 13.16%	-20.33	+ 1.14%
Strengthened wall-Variant 4	25.41	+ 11.84%	-20.36	+ 1.29%

Table 24: Maximum crack width w [mm] comparison between the experiment (TUD_COMP-45) and strengthened wall Variant 3 and 4 for the detailed micro-model

	Crack width for pre-damaged/ strengthened wall (TUD_COMP-45)	**Crack width for strengthened wall**	
		Variant 3	*Variant 4*
	$[mm]$	$[mm]$	$[mm]$
Crack 1	**0.51**	0.65 (+27%)	0.64 (+25%)
Crack 2	**1.06**	0.63 (-41%)	0.75 (-29%)
Crack 3	**0.44**	0.81 (+84%)	0.81 (+84%)
Crack 4	**0.40**	0.82 (+105%)	0.81 (+103%)

(a)

(b)
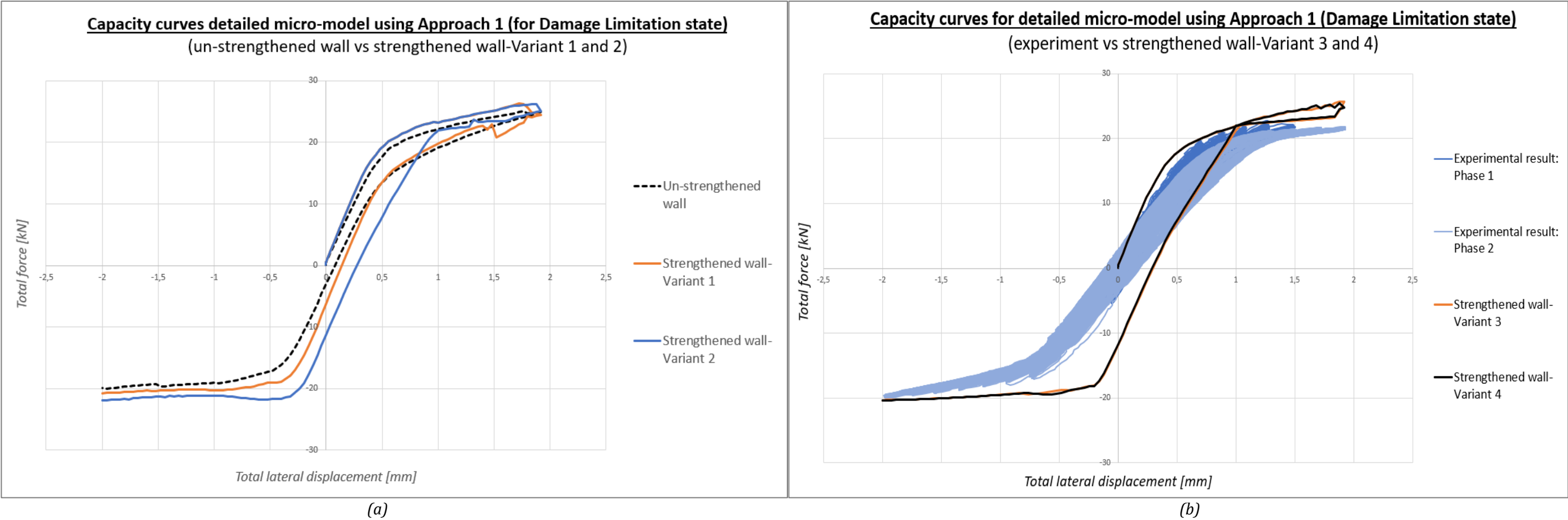
Figure 5.13: Comparison of capacity curves for detailed micro model with nonlinearity located only in interfaces: (a) un-strengthened wall vs strengthened wall-Variant 1 and 2; (b) experiment vs strengthened wall-Variant 3 and 4

Table 25: Numerical results strengthened wall detailed micro-model for all four variants

Detailed micro-model (strengthened wall)		Loading in positive x-direction					Loading in negative x-direction					Total Time
		Max. base shear force	Maximum axial stress		Maximum bond- slip		Max. base shear force	Maximum axial stress		Maximum bond-slip		
			Bed-joint reinforcement	Diagonal bar	Bed-joint reinforcement	Diagonal bar		Bed-joint reinforcement	Diagonal bar	Bed-joint reinforcement	Diagonal bar	
		$[kN]$	$[N/mm^2]$	$[N/mm^2]$	$[mm]$	$[mm]$	$[kN]$	$[N/mm^2]$	$[N/mm^2]$	$[mm]$	$[mm]$	$[min]$
Approach 1: Nonlinearity located only in brick-mortar joint interfaces												
Without **pre- /post-damage**	**Variant 1: Only bed-joint reinforcement**	26.35	0.96	-	0.03	-	-20.73	1.26	-	0.03	-	42
	Variant 2: Bed-joint reinforcement & diagonal bars	26.26	0.96	0.00	0.03	0.00	-21.90	1.84	0.00	0.03	0.01	42
With **pre- /post-damage**	**Variant 3: Only bed-joint reinforcement**	25.71	4.06	-	0.03	-	-20.33	2.46	-	0.02	-	45
	Variant 4: Bed-joint reinforcement & diagonal bars	25.41	4.26	0.00	0.03	0.01	-20.36	2.22	0.00	0.02	0.01	48
Approach 2: Nonlinearity located in both brick-mortar joint interfaces and mortar joints												
Without **pre- /post-damage**	**Variant 1: Only bed-joint reinforcement**	26.16	0.72	-	0.12	-	-20.25	0.91	-	0.02	-	48
	Variant 2: Bed-joint reinforcement & diagonal bars	25.92	1.02	0.01	0.12	0.04	-20.14	1.01	0.00	0.02	0.01	43
With **pre- /post-damage**	**Variant 3: Only bed-joint reinforcement**	23.96	5.05	-	0.06	-	-18.65	5.65	-	0.21	-	51
	Variant 4: Bed-joint reinforcement & diagonal bars	24.05	5.00	0.01	0.04	0.06	-18.45	6.47	0.01	0.19	0.05	60

Detailed micro-model Approach 1: Discrete cracking for brick-mortar joint interfaces and mortar joints linear elastic (strengthened wall)

(Crack pattern monotonic analysis for Damage Limitation state with maximum crack width w [mm] indicated)

Un-strengthened wall *(without pre-/post-damage)*	Strengthened wall (**without** pre-/post-damage)		Strengthened wall (**with** pre-/post-damage)		Experiment result **TUD_COMP-45** *(pre-damaged/ strengthened wall)*
	Variant 1 (Only bed-joint reinforcement)	**Variant 2** (Bed-joint reinforcement & diagonal bars)	**Variant 3** (Only bed-joint reinforcement)	**Variant 4** (Bed-joint reinforcement & diagonal bars)	
(a) +1.93 mm	*(c) +1.93 mm*	*(e) +1.93 mm*	*(g) +1.93 mm*	*(i) +1.93 mm*	*(k) Last step of Phase 2*
(b) – 1.98 m	*(d) – 1.98 mm*	*(f) – 1.98 mm*	*(h) – 1.98 mm*	*(j) – 1.98 mm*	
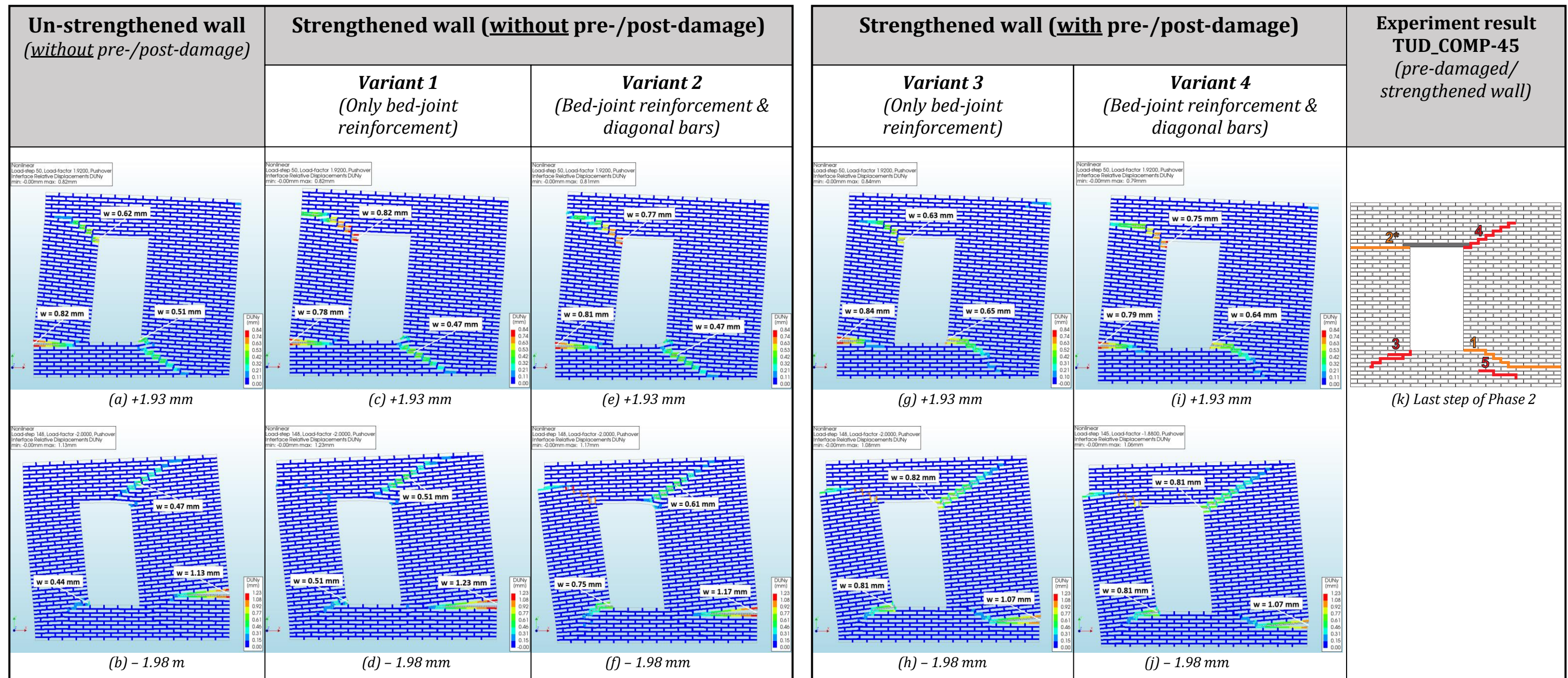
Figure 5.14: Crack pattern at maximum top displacement monotonic analysis (DL state) for detailed micro-model Approach 1 using contour plots interface relative displacement DUNy [mm] (scaling factor = 100)

5.4 Discussion numerical analyses for the Damage Limitation state

The comparison between the un-strengthened and strengthened wall from the experiment, considering the DL state, was done by interpreting the crack width and the crack length. According to Licciardello et al. ([2021](#)), an average reduction of 20~25% in crack width and 25~50% in crack length was observed for the strengthened wall compared to the un-strengthened wall. Furthermore, the presence of the bed-joint reinforcement contributes to a delay in the crack process for the DL state. However, these changes are not observed with the numerical analyses in the DL state. The crack width and crack length are very similar when comparing the un-strengthened wall with the strengthened wall from the analyses. This is the case for all three modeling approaches. Moreover, the obtained maximum base shear forces are also very close when comparing the un-strengthened wall with the strengthened wall.

The macro-modeling approach is not accurate when pre-/post-damage needs to be included in the model. This is due to the fact that the masonry wall is modeled as one homogeneous continuum where no distinction is made between the geometry of the bricks and the mortar joints. Therefore, the pre-/post-damage can only be included in the macro-model by deviding the wall into damaged and un-damaged areas by identifying the loacations of the cracks accordingly to the experiment and assigning modified material properties to those areas. For this reason, the pre-/post-damage is "smeared" over the whole damaged areas which means that the wall is expected to be weaker and thus not accurate. On the other hand, the continuous micro-model allows for the direct assignment of material properties to each structural component since the bricks and mortar joints are modeled separately.

Two different approaches are compared with each other for the detailed micro-model, namely Approach 1, in which the nonlinearity is only located in the brick-mortar joint interface elements and Approach 2, in which the nonlinearity is located in both the brick-mortar joint interface elements as well as in the mortar joints. The results for these two approaches are very similar. The cracks mainly occur in the form of opening of the brick-mortar joints interface elements, while the cracks in the mortar joints are limited. Considering the numerical results of the strengthened wall using the detailed micro-modeling approach, the maximum occurred axial stresses and bond-slips in the reinforcement bars are very small compared to the macro-model and continuous micro-model. This can be explained by the fact that the truss elements for the reinforcement bars are connected to the plane stress elements of the mortar joints and not to the brick-mortar interface elements. As was described before, because cracks mainly occur in the form of opening of the interface elements, while the cracks in the mortar joints are limited, this could explain why the reinforcement bars are not getting activated and thus low values are obtained.

Considering the macro-model and the continuous micro-model, high axial stresses are developed in the bed-joint reinforcements while exhibiting minimal bond-slip. On the contrary, low axial stresses are developed in the diagonal bars while exhibiting relatively large bond-slips.

5.5 Numerical analyses for the Near Collapse state

The continuous micro-modeling approach has been chosen to simulate the loading of the strengthened wall up to the Near Collapse state (NC) for the same reasons as discussed in Chapter 4. Again, both TSCM and EMM are used as the material models for the mortar joints in separate models and the results are compared with each other, as well as with the experiment. Both monotonic and cyclic analyses are conducted.

The loading protocol for the strengthened wall up to the NC state is depicted in *Figure 5.15*. The total loading protocol (DL state + NC state) is applied for the analyses in this Section. The loading protocol for the DL state is presented in (*Figure 4.4*) in Section 4.1.6. The applied numerical settings and parameters for both material models are listed in *Table E 1* of Appendix E. Important to note is that unlike the performed monotonic analyses for the DL state, the monotonic analyses for the NC state are preformed separately for the positive and negative x-direction.
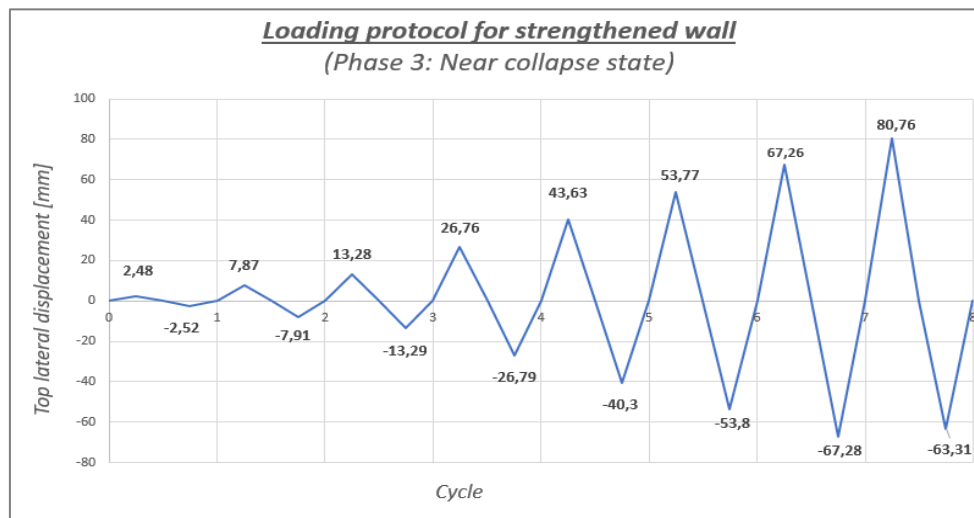
Figure 5.15: Loading protocol for strengthened wall (in NC state)

The results of the cyclic and monotonic analyses for the strengthened wall are compared with each other, as well as with the numerical results of the un-strengthened wall and the experiment. The comparison is done by interpreting the capacity curves and the crack pattern. Moreover, the behavior of the reinforcements is evaluated based on the amount of slip and the potential of yielding of the bars. All four variants (described at the beginning of the chapter) are used to investigate the effectiveness of the bed-joints reinforcement and the diagonal bars. These variants differ from each other by the implementation of pre-/post-damage and either only having bed-joint reinforcement or both bed-joint reinforcement and diagonal bars.

Capacity curves and bilinear approximation curves

First, the capacity curves for all four variants of the strengthened wall are compared with the numerical result of the un-strengthened wall. The results are illustrated in *Figure 5.17a* and in *Figure 5.17d* for the continuous micro-model using the TSCM and the EMM, respectively. The corresponding bilinear approximation curves for both material models are calculated and illustrated in *Figure 5.17b* and in *Figure 5.17e*. Moreover, the bilinear approximation parameters

are calculated, as described in Section 4.5.2, and listed in *Table 26* and in *Table 27* for the continuous micro-model using the TSCM and the EMM, respectively. The numerical results of the un-strengthened wall are herein compared with Variant 1 and 2, whereas Variant 3 and 4 are compared with the experiment (TUD_COMP-45).

No significant increment in force capacity can be observed for both material models when comparing the un-strengthened wall with the strengthened wall. This in line with the experiment. Considering the model using the TSCM for the mortar joints, the largest percentage increment, with respect to the un-strengthened wall, is +8.1% and +14.7% in the positive and negative loading direction, respectively for Variant 2. The percentage difference in force capacity between the un-strengthened and the strengthened wall is even smaller for the model using the EMM for the mortar joints, namely +1.2% in both positive and negative loading directions for Variant 2. For both material models, the maximum force capacity are very close when comparing the pre-/post-damaged variants with the variants without pre-/post-damage. Moreover, the monotonic and cyclic analyses for both un-strengthened and strengthened wall-Variant 3 are compared with each other in *Figure 5.17c* and in *Figure 5.17f* for the continuous micro-model using the TSCM and the EMM, respectively. Again, only the EMM is able to capture the hysteretic behavior when doing a cyclic analysis because the material model allows for elastic unloading. The energy dissipation for the strengthened wall in the negative x-direction is higher compared with the un-strengthened wall. Furthermore, the capacity curves for the monotonic analyses follow the out-line of the capacity curves for the cyclic analyses as the envelope curve. Lastly, the capacity curves for both material models are compared with the experiment in *Figure 5.16*. The pattern of the capacity curves are in a reasonable agreement with the experiment. However, it can be observed that the maximum force capacity is overestimated for both material models compared with the experiment. As was explained in Section 4.5.2, the numerical models are expected to be stronger than the experiment because of perfect conditions and the fact that the bricks are kept linear elastic.
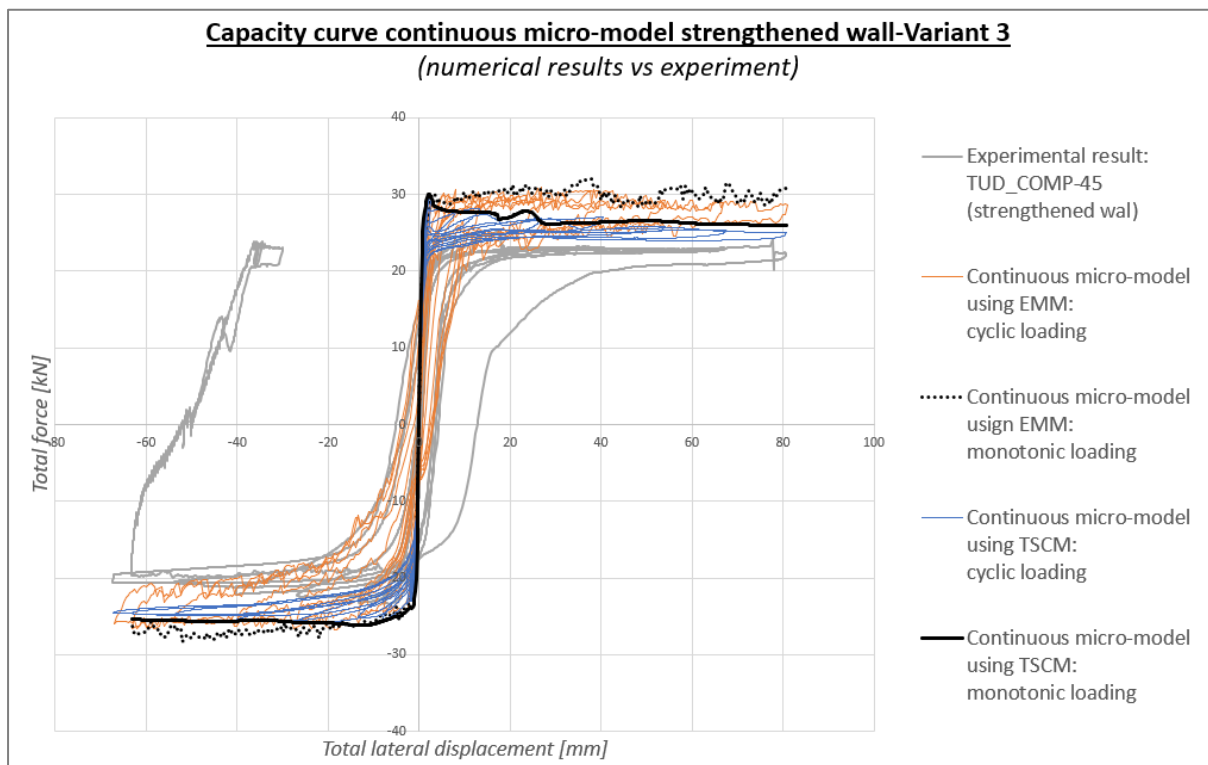
Figure 5.16: Capacity curves continuous micro-model (strengthened wall-variant 3) comparing numerical results with experimental results up to NC state

Capacity curves & bilinear approximations for continuous micro-model using *TSCM* for mortar joints

(a)

(b)

(c)

Capacity curves & bilinear approximations for continuous micro-model using *EMM* for mortar joints

(d)

(e)

(f)
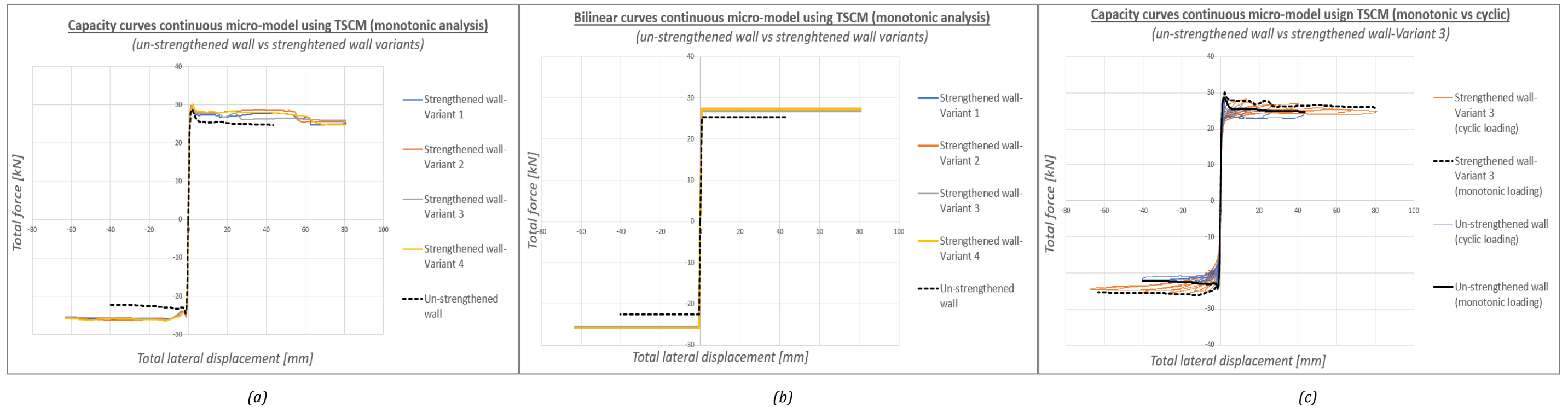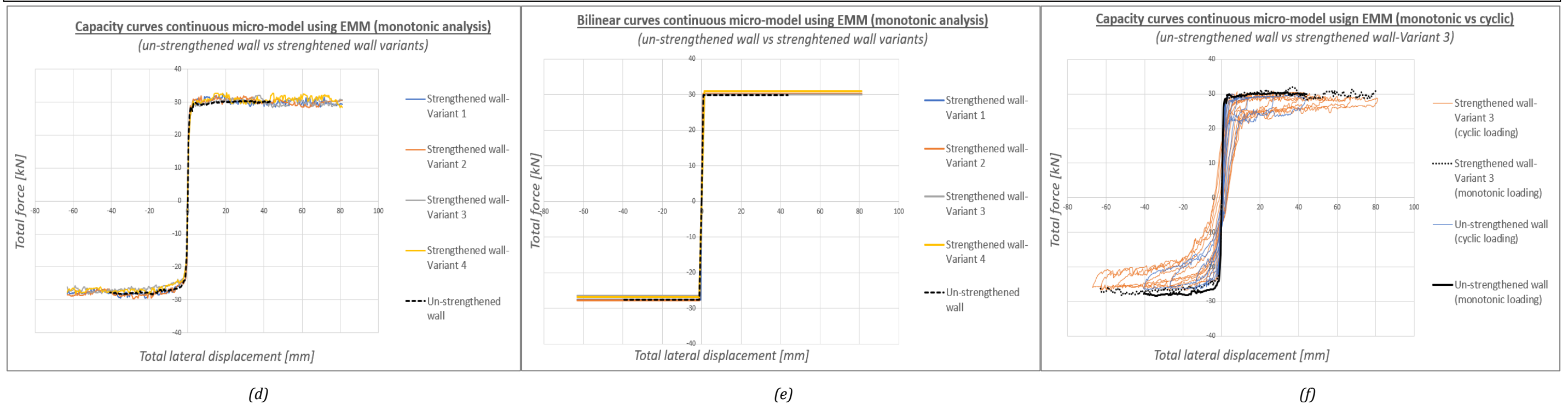
Figure 5.17: Capacity curves and bilinear approximation curves for analysis up to NC state: (a) - (c) continuous micro-model using TSCM for mortar joints; (d) - (f) continuous micro-model using EMM for mortar joints

Table 26: Bilinear approximation parameters for continuous micro-model using TSCM for mortar joints: un-strengthened wall vs Variant 1-2; experiment (Licciardello et al., 2021) vs Variant 3-4 with percentage difference for both comparisons in parentheses

		Continuous micro-model using *TSCM* for mortar joints										Experiment TUD_COMP-45	
		Un-strengthened wall without pre-/post-damage		Strengthened wall without pre-/post-damage				Strengthened wall with pre-/post-damage					
				Variant 1 (Only bed-joint reinforcement)		Variant 2 (Bed-joint reinforcement & diagonal bars)		Variant 3 (Only bed-joint reinforcement)		Variant 4 (Bed-joint reinforcement & diagonal bars)			
		Pos.	Neg.	Pos.	Neg.	Pos.	Neg.	Pos.	Neg.	Pos.	Neg.	Pos.	Neg.
Initial stiffness K_{el}	[kN/mm]	36.19	37.07	46.11 (+27.4%)	42.20 (+13.8%)	46.11 (+27.4%)	42.20 (+13.8%)	37.29 (+33.3%)	33.58 (+24.3%)	37.30 (+33.3%)	33.58 (+24.3%)	27.98	27.02
Max. base shear force V_u	[kN]	25.38	-22.58	26.83 (+5.7%)	-25.60 (+13.4%)	27.44 (+8.1%)	-25.89 (+14.7%)	26.74 (+15.4%)	-25.59 (+16.6%)	27.30 (+17.8%)	-25.87 (+18.1%)	23.18	-21.90
Elastic displacement u_{el}	[mm]	0.70	-0.61	0.58 (-17.1%)	-0.61 (0.0%)	0.60 (-14.3%)	-0.61 (0.0%)	0.72 (-13.3%)	-0.76 (-6.2%)	0.73 (-12.1%)	-0.77 (-4.9%)	0.83	-0.81
Ultimate displacement u_u	[mm]	43.60	-40.40	80.80 (+85.3%)	-63.20 (+56.4%)	80.80 (+85.3%)	-63.20 (+56.4%)	80.80 (+0.1%)	-63.20 (-0.2%)	80.80 (+0.1%)	-63.20 (-0.2%)	80.76	-63.30
Ductility factor μ_b	[−]	62.29	66.23	139.31 (+123.7%)	103.61 (+56.4%)	134.67 (+116.2%)	103.61 (+56.4%)	112.22 (+15.1%)	83.16 (+6.5%)	110.68 (+13.5%)	82.08 (+5.1%)	97.50	78.10
Ultimate drift d_{r-b}	[%]	1.62	-1.50	3.00 (+85.2%)	-2.35 (+56.7%)	3.00 (+85.2%)	-2.35 (+56.7%)	3.00 (+0.3%)	-2.35 (+0.4%)	3.00 (+0.3%)	-2.35 (+0.4%)	2.99	-2.34

Table 27: Bilinear approximation parameters for continuous micro-model using EMM for mortar joints: un-strengthened wall vs Variant 1-2; experiment (Licciardello et al., 2021) vs Variant 3-4 with percentage difference for both comparisons in parentheses

		Continuous micro-model using *EMM* for mortar joints										Experiment TUD_COMP-45	
		Un-strengthened wall without pre-/post-damage		Strengthened wall without pre-/post-damage				Strengthened wall with pre-/post-damage					
				Variant 1 (Only bed-joint reinforcement)		Variant 2 (Bed-joint reinforcement & diagonal bars)		Variant 3 (Only bed-joint reinforcement)		Variant 4 (Bed-joint reinforcement & diagonal bars)			
		Pos.	Neg.	Pos.	Neg.	Pos.	Neg.	Pos.	Neg.	Pos.	Neg.	Pos.	Neg.
Initial stiffness K_{el}	[kN/mm]	36.52	22.41	40.28 (+10.3%)	35.94 (+60.4%)	40.28 (+10.3%)	23.34 (+4.1%)	23.01 (-17.4%)	19.57 (-27.6%)	23.05 (-17.6%)	19.58 (-27.5%)	27.98	27.02
Max. base shear force V_u	[kN]	29.81	-27.54	30.07 (+0.8%)	-27.56 (+0.1%)	30.17 (+1.2%)	-27.87 (+1.2%)	29.98 (+29.3%)	-26.52 (+21.1%)	30.87 (+33.2%)	-26.78 (+22.3%)	23.18	-21.90
Elastic displacement u_{el}	[mm]	0.82	-1.23	0.75 (-8.5%)	-0.77 (-37.4%)	0.75 (-8.5%)	-1.19 (+3.3%)	1.30 (+56.6%)	-1.36 (+67.9%)	1.34 (+61.5%)	-1.37 (+69.1%)	0.83	-0.81
Ultimate displacement u_u	[mm]	43.50	-40.50	81.00 (+86.2%)	-63.00 (+55.6%)	81.00 (+86.2%)	-63.00 (+55.6%)	81.00 (+0.3%)	-63.00 (-0.5%)	81.00 (+0.3%)	-63.00 (-0.5%)	80.76	-63.30
Ductility factor μ_b	[−]	53.05	32.93	108.00 (+103.6%)	81.82 (+148.5%)	108.00 (+103.6%)	52.94 (+60.8%)	62.31 (-36.1%)	46.32 (-40.7%)	60.45 (-38.0%)	45.99 (-41.1%)	97.50	78.10
Ultimate drift d_{r-b}	[%]	1.62	-1.51	3.01 (+85.8%)	-2.34 (+55.0%)	3.01 (+85.8%)	-2.34 (+55.0%)	3.01 (+0.7%)	-2.34 (0.0%)	3.01 (+0.7%)	-2.34 (0.0%)	2.99	-2.34

Crack pattern

According to Licciardello et al. (2021), the formation of the diagonal stair-case cracks at the corners of the window opening is prevented by the precense of the bed-joint reinforcements. Moreover, the formation of horizontal cracks were triggered in the mortar joints where the reinforcement was not present. For large in-plane displacement, and arch mechanism below the window opening was also triggered by the presence of the reinforcement bars. The bed-joint reinforcements contribute to a reduction in crack width and length and leads to a more ductile behavior with an increased displacement capacity for the strengthened wall. The final crack patterns for the monotonic analyses are illustrated in *Figure 5.18* and in *Figure 5.19* for the model using the TSCM and the EMM, respectively. Variant 1 and 2 are herein compared with the numerical result of the un-strengthened wall, while Variant 3 and 4 are compared with the pre-damaged/ strengthened wall from the experiment. Important to note is that the results of the crack patterns for Variant 1 and 2 are taken at a horizontal displacement of 43.63 *mm*, which corresponds to the maximum horizontal displacement reached by the un-strengthened wall. On the other hand, the results of the crack patterns for Variant 3 and 4 are taken at a horizontal displacement of 80.76 *mm*, since the strengthened wall has a larger displacement capacity.

Some differences in the crack patterns can be observed between the two different material models. Considering the results of the model using the TSCM for the mortar joints and the comparison of Variant 1 and 2 with the numerical result of the un-strengthened wall, it can be observed that the formation of the diagonal stair-case cracks at the corners of the window opening is prevented by the presence of the reinforcements. As a result, horizontal cracks become more prominent in the bed-joints. Similar to the un-strengthened wall, the cracks in the variants of the strengthened wall are also distributed over a larger area of the masonry. Moreover, the rocking failure behavior of both piers can be observed by the horizontal cracks occurring at the base of the piers. Considering the comparison of Variant 3 and 4 with the pre-damaged/strengthened wall from the experiment, the crack pattern is in a good agreement with the experiment. The horizontal crack at the top of the left pier (crack number 2*) is captured by the numerical model. However, this horizontal crack is distributed over a wider range of rows in the bed-joints for the numerical model. The horizontal crack at the top of the right pier (crack number 8) is in a good agreement with the experiment. Furthermore, a lot of horizontal cracks running along the bed-joints at the base of the wall can be observed in the numerical models which is in line with the experiment.

Next, the results of the crack pattern for the model using the EMM for the mortar joints are discussed. The crack pattern for Variant 1 and 2 are very close to the numerical result of the un-strengthened wall since the reinforcements are not getting activated as much due to their oriented in parallel with the horizontal cracks formed in the un-strengthened wall. Similar to the numerical result of the un-strengthened wall, the horizontal cracks are distributed over a wider range of rows in the bed-joints for the strengthened wall. Considering the comparison of Variant 3 and 4 with the pre-damaged/strengthened wall from the experiment, the crack pattern is in a good agreement with the experiment. The horizontal cracks at the top of both piers (crack number 2* and 8) are simulated by the numerical model. Moreover, a lot of horizontal cracks are located at the base of the wall for which the crack length are larger compared to the model using the TSCM for the mortar joints.

The crack pattern for the monotonic and cyclic analysis are compared with each other for Variant 3 of both material models in *Figure 5.20*. Considering the comparison for the model using the TSCM for the mortar joints, it can be observed that the cracks at the top of the left pier are distributed over a wider range of bed-joints above the pier for the cyclic analysis. Furthermore, the cracks at the base of the right pier are also distributed over the pier itself. Considering the comparison for the model using the EMM for the mortar joints, the cracks at the right base of the wall are also more distributed for the cyclic analysis.

Continuous micro-model using TSCM for mortar joints (strengthened wall)

(Crack pattern monotonic analysis for Near Collapse state)

Figure 5.18: Scaled contour plots principal strain E1 [-] showing crack pattern at maximum top displacement monotonic analysis (up to NC state) for continuous micro-model using TSCM for mortar joints

Continuous micro-model using EMM for mortar joints (strengthened wall)

(Crack pattern monotonic analysis for Near Collapse state)
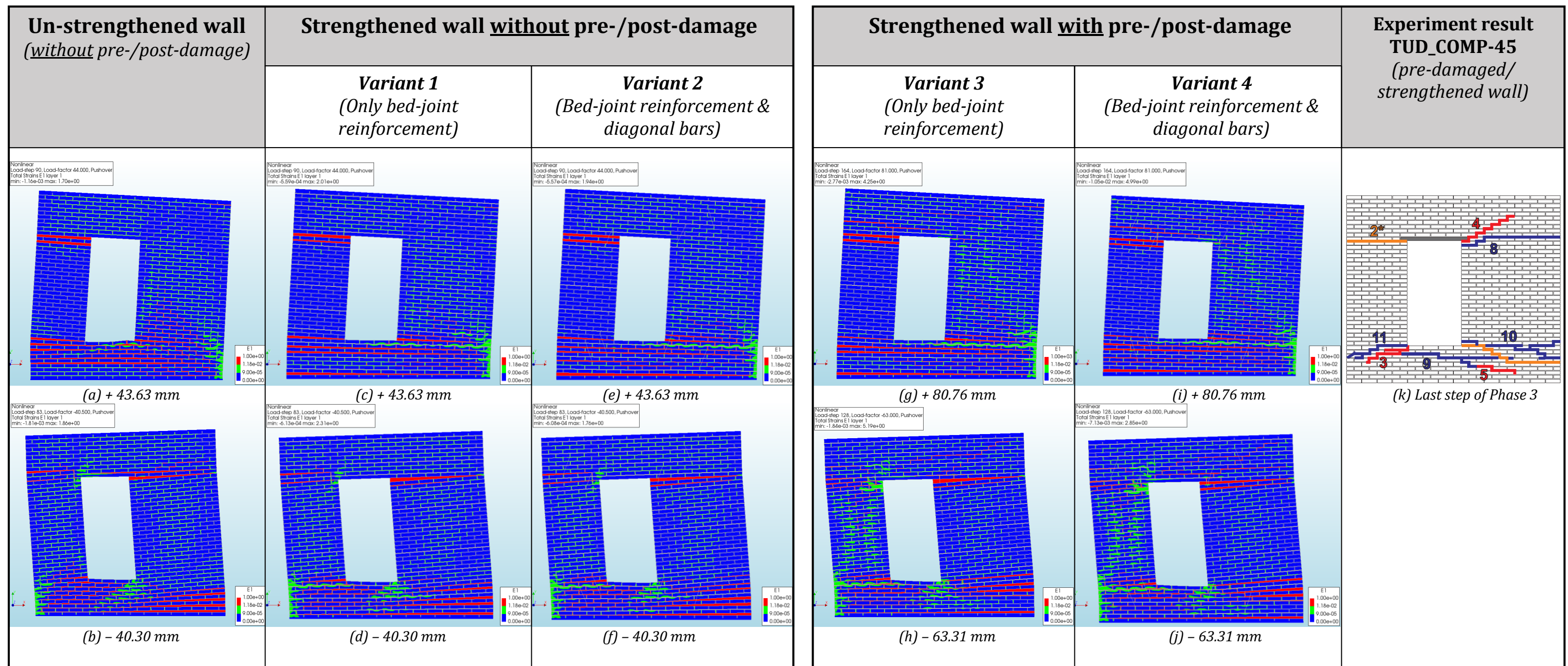
Figure 5.19: Scaled contour plots principal strain E1 [-] showing crack pattern at maximum top displacement monotonic analysis (up to NC state) for continuous micro-model using EMM for mortar joints

Continuous micro-model strengthened wall-Variant 3

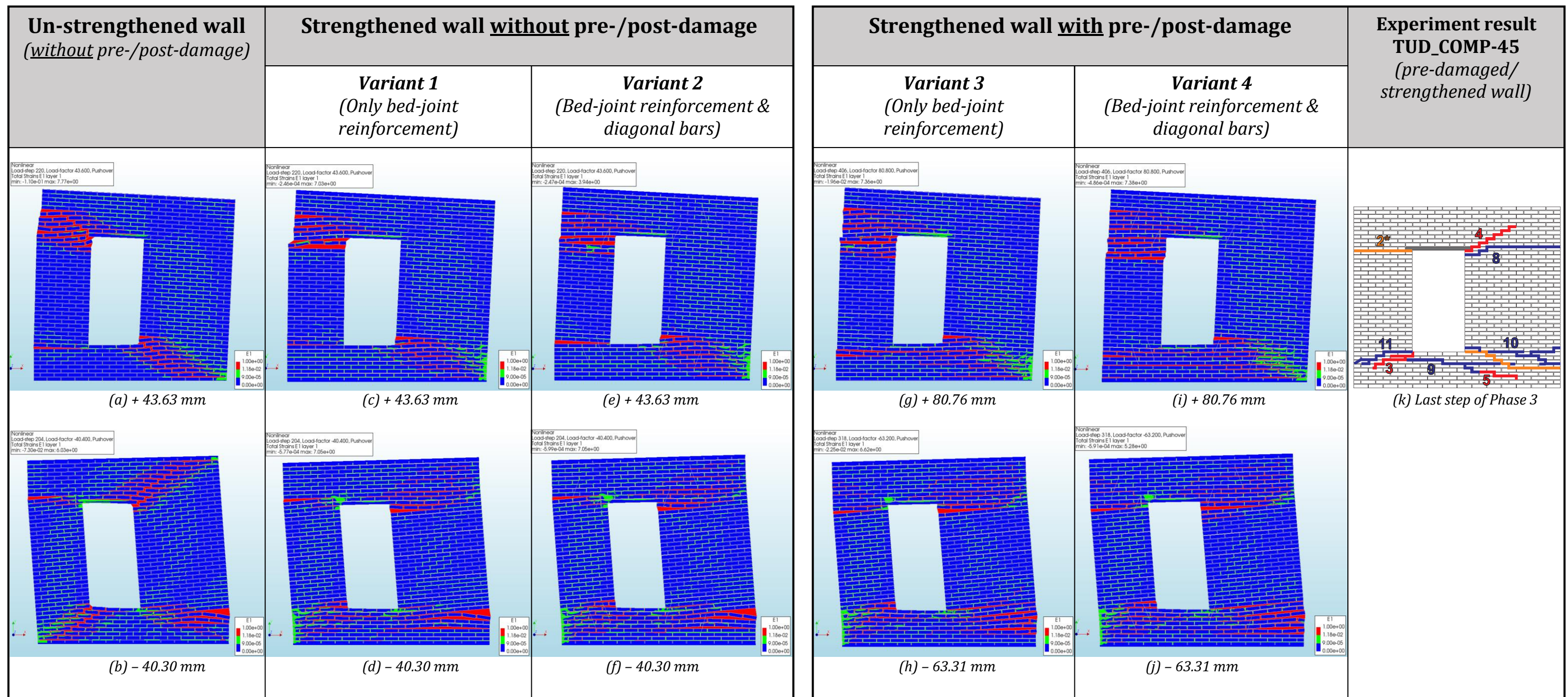*(Crack pattern monotonic analysis vs cyclic analysis for Near Collapse state)*
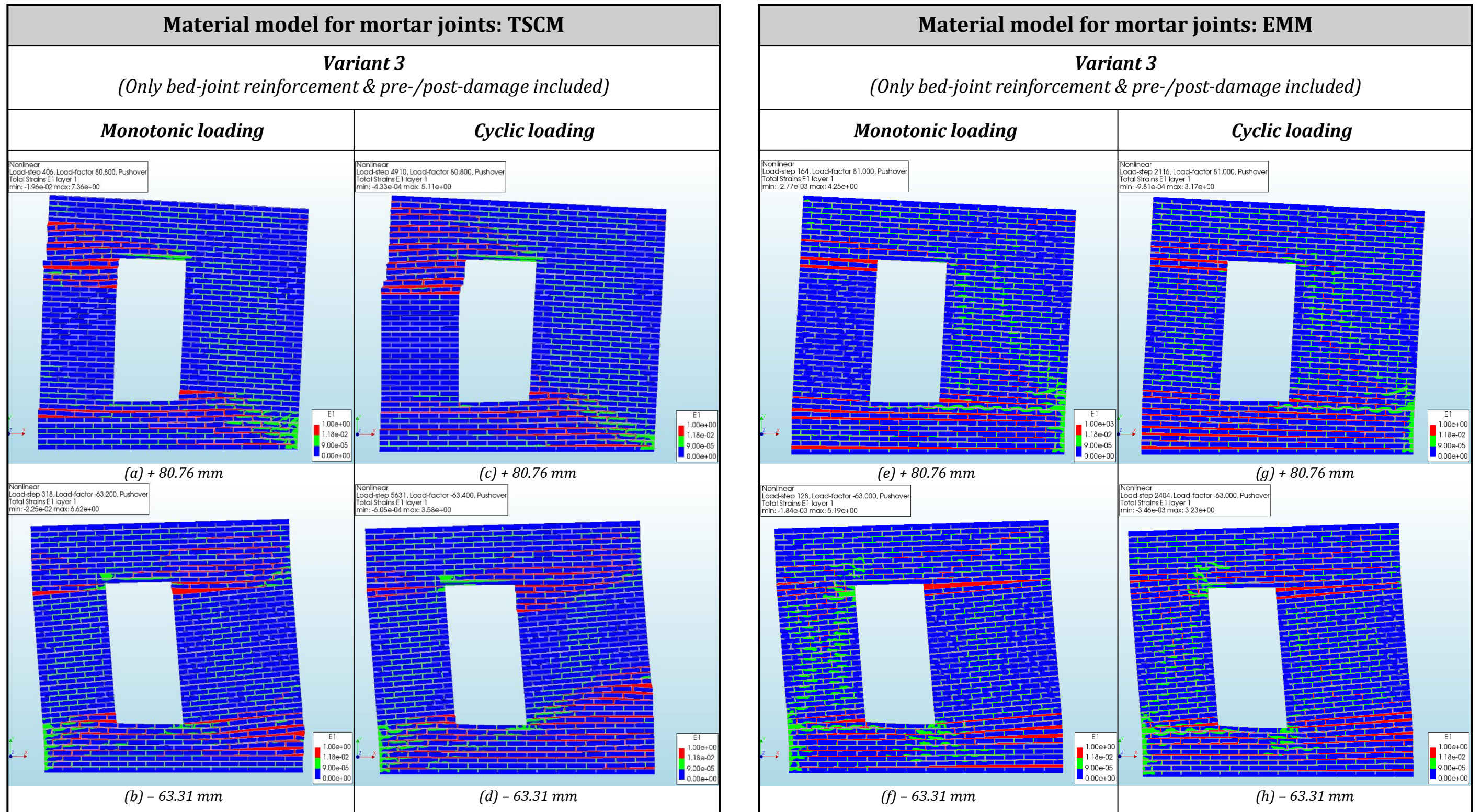
Figure 5.20: Scaled contour plots principal strain E1 [-] showing crack pattern at maximum top displacement monotonic vs cyclic analysis (up to NC state) for continuous micro-model strengthened wall-Variant 3

Axial stress and bond-slip in reinforcements

The maximum reached axial stress in every row of reinforcement and diagonal bar (if included in the model), with the corresponding locations, are indicated in *Figure 5.21* and in *Figure 5.22* for the continuous micro-model using the TSCM and the EMM, respectively. These are the results for the monotonic analyses. Important to note is that the maximum axial stresses in each row are not reached at the same top displacement. Considering the results of the model using the TSCM for the mortar joints, the locations of the maximum axial stresses are corresponding with the locations where the diagonal stair-case cracks become horizontal cracks in the strengthened wall. Since no cracks are formed in both piers, the maximum axial stresses reached in the reinforcements at these locations are small. The yield strength of 205 N/mm^2 is exceeded only at the bed-joint reinforcements which are the closest to the bottom corners of the opening. Considering the continuous micro-model using the EMM for the mortar joints, the maximum reached axial stresses in the reinforcement are relatively lower since the bars are not getting activated as much due to their oriented in parallel with the major horizontal cracks formed in the un-strengthened wall. Moreover, no yielding can be observed in any of the reinforcement bars. The locations of the largest maximum axial stress occurred for all reinforcements in the wall, for each variant of both material models, are marked in red. The axial stresses of the entire analysis are taken from these locations and the development for all variants of both material models are illustrated in *Figure E 1* and *Figure E 2* of Appendix E. Only the results for Variant 3 are presented in this chapter (*Figure 5.23*) for both material models using both monotonic and cyclic analysis. The locations of yielding of the reinforcement bars are the same when comparing the monotonic analysis with the cyclic analysis. Considering the model using the TSCM for the mortar joints, the highest developed axial stress is 210.32 N/mm^2 for the cyclic analysis and 213.71 N/mm^2 for the monotonic analysis, both in the negative x-direction. Considering the results of the model using the EMM for the mortar joints, no yielding of the reinforcement bars can be observed for both monotonic and cyclic analyses. The highest developed axial stress is 163.59 N/mm^2 for the cyclic analysis and 149.59 N/mm^2 for the monotonic analysis, both in the positive x-direction. In summary, the results of the monotonic and cyclic analysis are comparable in terms of the obtained order of magnitude for the maximum reached axial stress with the corresponding locations.

The results of the bond-slip development, at the location with the highest reached value in all reinforcements, are illustrated in *Figure 5.24* for both material models. Again, the results of the monotonic analysis are herein compared with the results of the cyclic analysis. The comparisons are also done for Variant 3 only in this section. The results of the monotonic analysis for the other variants can be found in *Figure E 3* and *Figure E 4* of Appendix E. Some differences can be observed when comparing the results of the monotonic with the cyclic analysis in terms of the locations at which the maximum slips are exhibited by the reinforcement. In general, when comparing the four variants (depicted in *Figure E 3* and *Figure E 4* of Appendix E), a larger maximum value of bond-slip is reached in the diagonal bars compared with the variants with only the bed-joint reinforcement. The maximum occurred bond-slip, in both loading directions, for both material models are within the maximum elastic branch (S_1 is 5 mm for bed-joint reinforcement). On the other hand, the maximum bond-slip in the diagonal bars are just exceeding the maximum elastic bond-slip (S_1 is 20 mm for diagonal bars) for both material models (see Appendix E).

Maximum axial stress occurred in each row of reinforcement with value and location indicated per strengthened variant

*(strengthened continuous micro-model using **TSCM** for mortar joints with monotonic analysis up to Near Collapse state)*

Strengthened wall **without** pre-/post-damage		Strengthened wall **with** pre-/post-damage	
Variant 1 (Only bed-joint reinforcement)	**Variant 2** (Bed-joint reinforcement & diagonal bars)	**Variant 3** (Only bed-joint reinforcement)	**Variant 4** (Bed-joint reinforcement & diagonal bars)
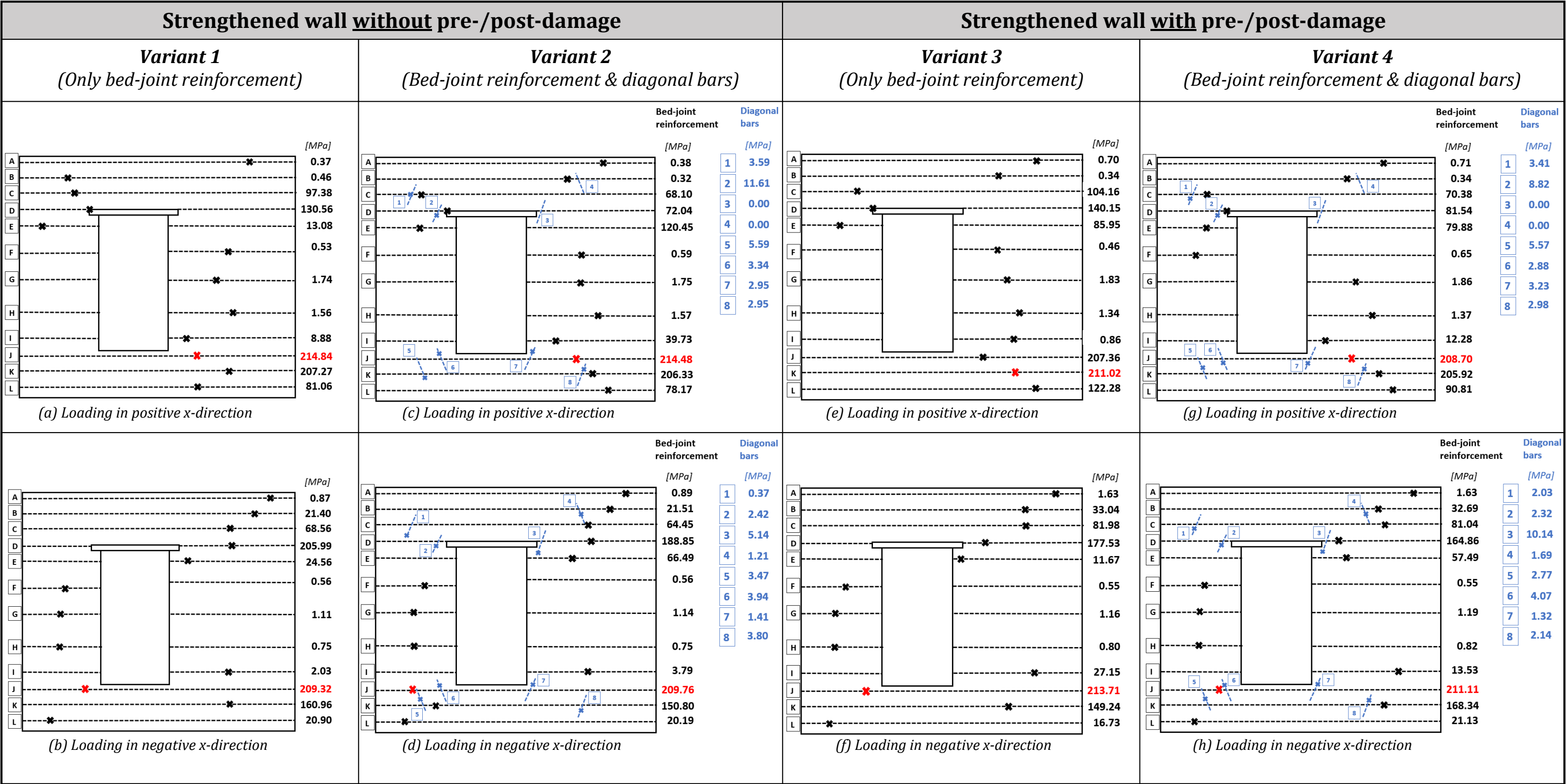
Figure 5.21: Maximum axial stress occurred in each row of reinforcement for all strengthened wall variants continuous micro-model using TSCM for mortar joints

124

Maximum axial stress occurred in each row of reinforcement with value and location indicated per strengthened variant

*(strengthened continuous micro-model using **EMM** for mortar joints with monotonic analysis up to Near Collapse state)*
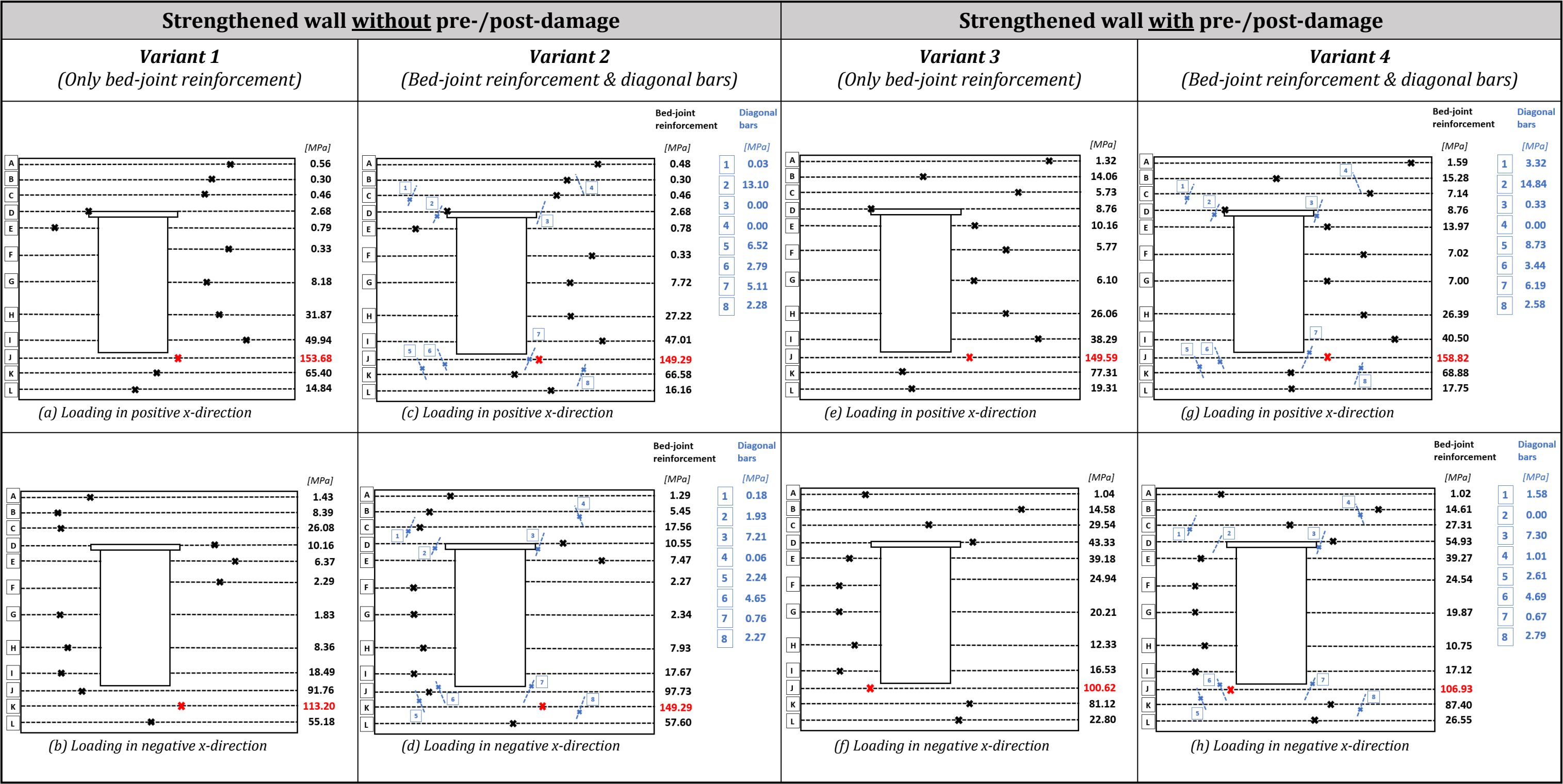
Figure 5.22: Maximum axial stress occurred in each row of reinforcement for all strengthened wall variants continuous micro-model using EMM for mortar joints

Axial stress development in bed-joint reinforcement for strengthened wall-Variant 3

*(monotonic and cyclic analysis for continuous micro-model using **TSCM** and **EMM**)*
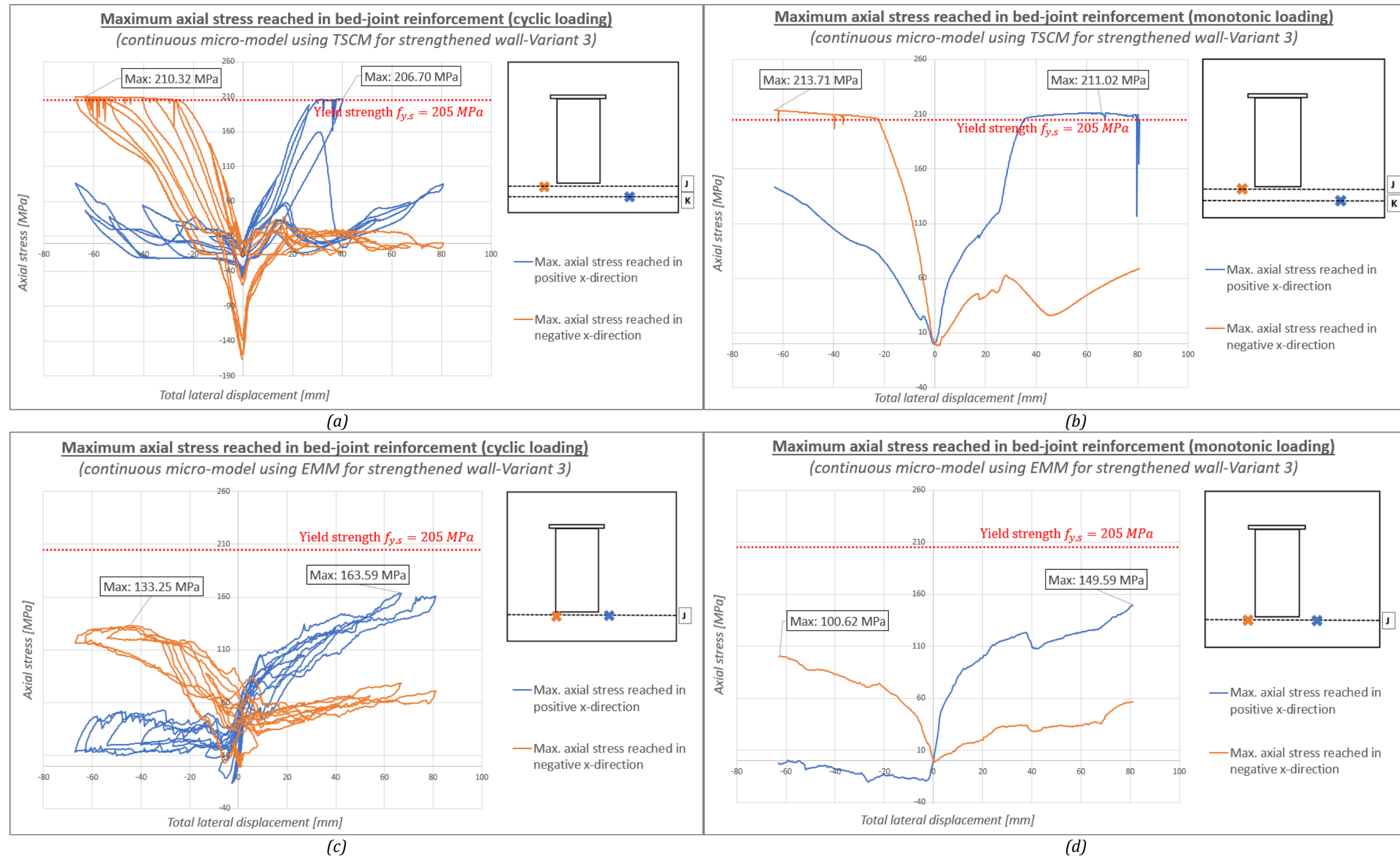
Figure 5.23: Axial stress development for strengthened wall-Variant 3: (a) cyclic analysis for continuous micro-model using TSCM; (b) monotonic analysis for continuous micro-model using TSCM; (c) cyclic analysis for continuous micro-model using EMM; (d) monotonic analysis for continuous micro-model using EMM

Bond-slip development in bed-joint reinforcement for strengthened wall-Variant 3

*(monotonic and cyclic analysis for continuous micro-model using **TSCM** and **EMM**)*
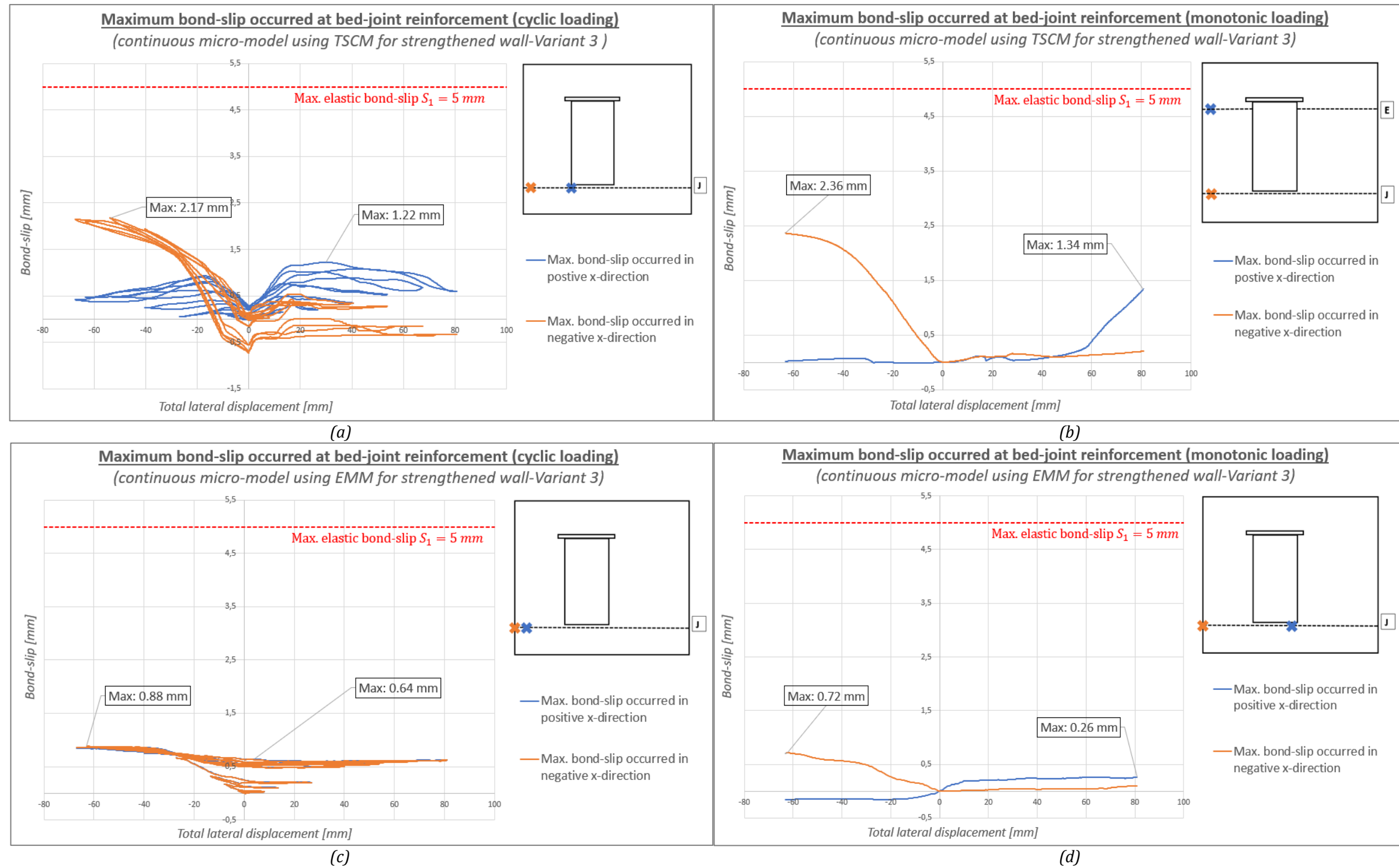
Figure 5.24: Bond-slip development for strengthened wall-Variant 3: (a) cyclic analysis for continuous micro-model using TSCM; (b) monotonic analysis for continuous micro-model using TSCM; (c) cyclic analysis for continuous micro-model using EMM; (d) monotonic analysis for continuous micro-model using EMM

Check for toe crushing

In the scope of this thesis research, the bricks in the continuous micro-models are assumed linear elastic. This means that cracking and crushing are ignored in the bricks. Important to note is that the compressive strength of masonry as a composite material is used for the bed-and head-joints, even though the geometry of all structural components (bricks and mortar) are modeled independently. The reason for this is because if the compressive strength of mortar is used for the joints, a large reduction in maximum force capacity will be observed since the compressive strength of the wall is only dependent on the mortar joints.

Crushing failure at the toe was observed for the strengthened wall at the end of the experiment where the cracks are extended in both mortar joints and bricks. However, cracks can only occur in the mortar joints in the scope of this research. Considering all strengthened wall variants for both material models, the compressive stresses in the bricks, at the bottom right corner of the wall, are lower compared to the compressive strength of bricks ($28.31\ N/mm^2$) but larger compared to masonry as a composite material ($12.93\ N/mm^2$). The results are presented in *Figure 5.25* using the contour plots for the principal stress S_2.

In order to check if the maximum occurred compressive stresses in the mortar joints are in the initial branch or the softening branch, the contour plots of the principal strain E_2 are used (presented in *Figure 5.26*). Considering the continuous micro-model using the TSCM for the mortar joints, the strain at which the maximum compressive strength is reached α_c can be calculated with *equation (28)* for a parabolic curve (according to Ferreira, 2021):

$$\alpha_c = -\frac{5}{3}\frac{f_c}{E} \tag{28}$$

, where E and f_c are the Young's modulus and the compressive strength of the bed-joints, respectively. Using the applied material properties results in $\alpha_c = -0.02155$.

Considering the continuous micro-model using the EMM for the mortar joints, the strain at which the maximum compressive strength is reached ε_{peak} can be calculated with *equation (29)* according to (Ferreira, 2021):

$$n = -\frac{E\varepsilon_{peak}}{f_c} \tag{29}$$

, where E and f_c are the Young's modulus and the compressive strength of the bed-joints, respectively. n is the factor to strain at compressive strength. Using the applied material properties results in $\varepsilon_{peak} = -0.05172$.

Considering the continuous micro-model using the TSCM for the mortar joints, it can be observed that the compressive stresses in the bed-joints, at the bottom right corner of the wall, are in the softening branch since the occurred principal strains E_2 are larger than α_c. This holds for all four variants. On the other hand, considering the continuous micro-model using the EMM for the mortar joints, it can be observed that the compressive stresses in the bed-joints, at the bottom right corner of the wall, are in the initial branch since the occurred principal strains E_2 are smaller than ε_{peak}. This holds for all four variants.

Check for toe crushing at the bottom right corner of the wall using contour plots principal stress S_2 [N/mm^2]

(monotonic analysis up to NC state in the positive loading direction for continuous micro-model strengthened wall variants)

	Strengthened wall **without** pre-/post-damage		Strengthened wall **with** pre-/post-damage	
	Variant 1 *(Only bed-joint reinforcement)*	***Variant 2*** *(Bed-joint reinforcement & diagonal bars)*	***Variant 3*** *(Only bed-joint reinforcement)*	***Variant 4*** *(Bed-joint reinforcement & diagonal bars)*
Material model: TSCM	*(a) Compressive stress:* **-12.17 N/mm^2**	*(b) Compressive stress:* **-12.08 N/mm^2**	*(c) Compressive stress:* **-12.48 N/mm^2**	*(d) Compressive stress:* **-12.22 N/mm^2**
Material model: EMM	*(e) Compressive stress:* **-12.26 N/mm^2**	*(f) Compressive stress:* **-13.14 N/mm^2**	*(g) Compressive stress:* **-12.12 N/mm^2**	*(h) Compressive stress:* **-12.49 N/mm^2**

Figure 5.25: Contour plots principal stress S_2 [N/mm^2] check for crushing at bottom right corner of all strengthened wall variants with continuous micro-model using TSCM and EMM for mortar joints

Check for toe crushing at the bottom right corner of the wall using contour plots principal strain E_2 [−]

(monotonic analysis up to NC state in the positive loading direction for continuous micro-model strengthened wall variants)
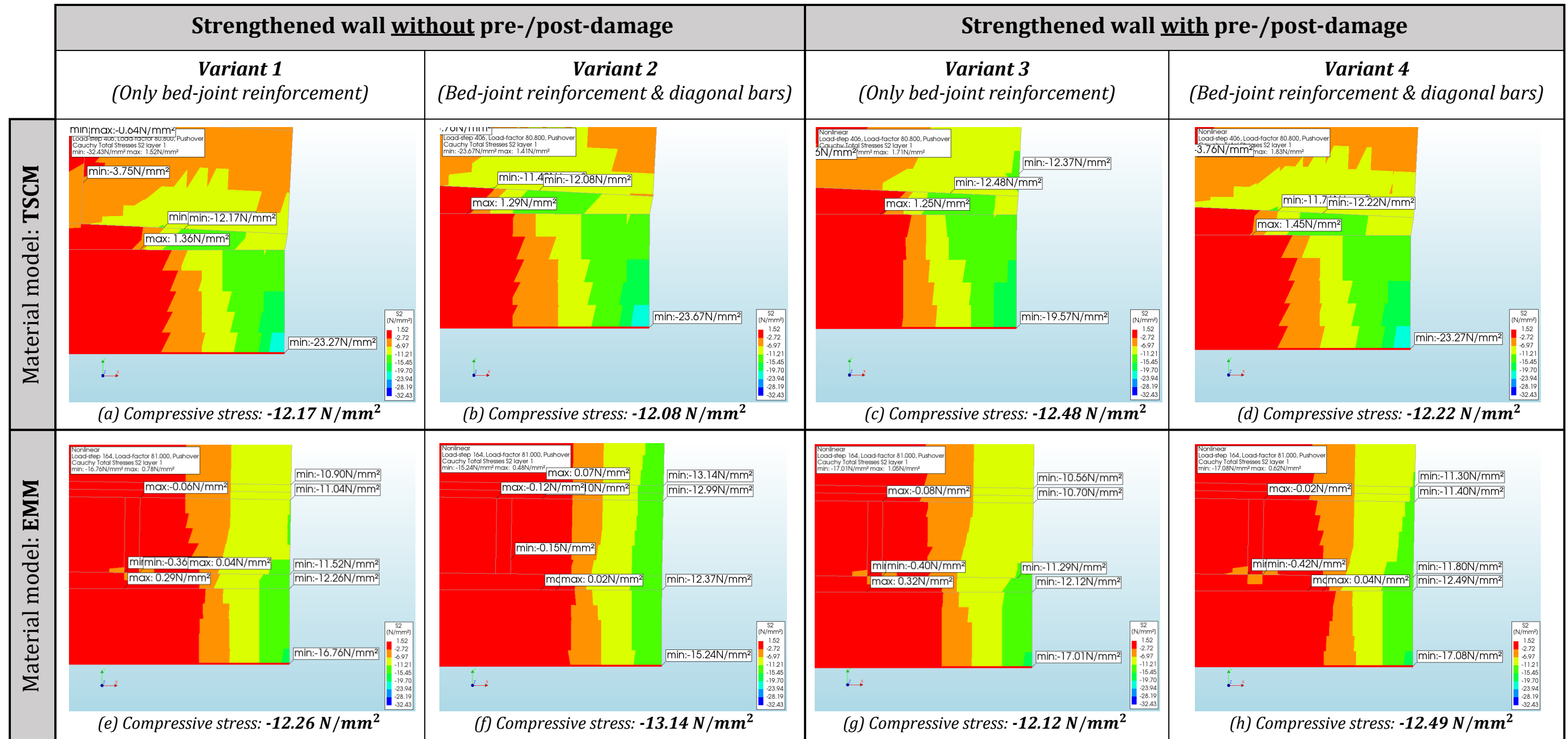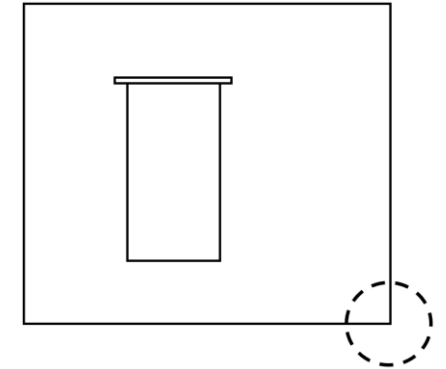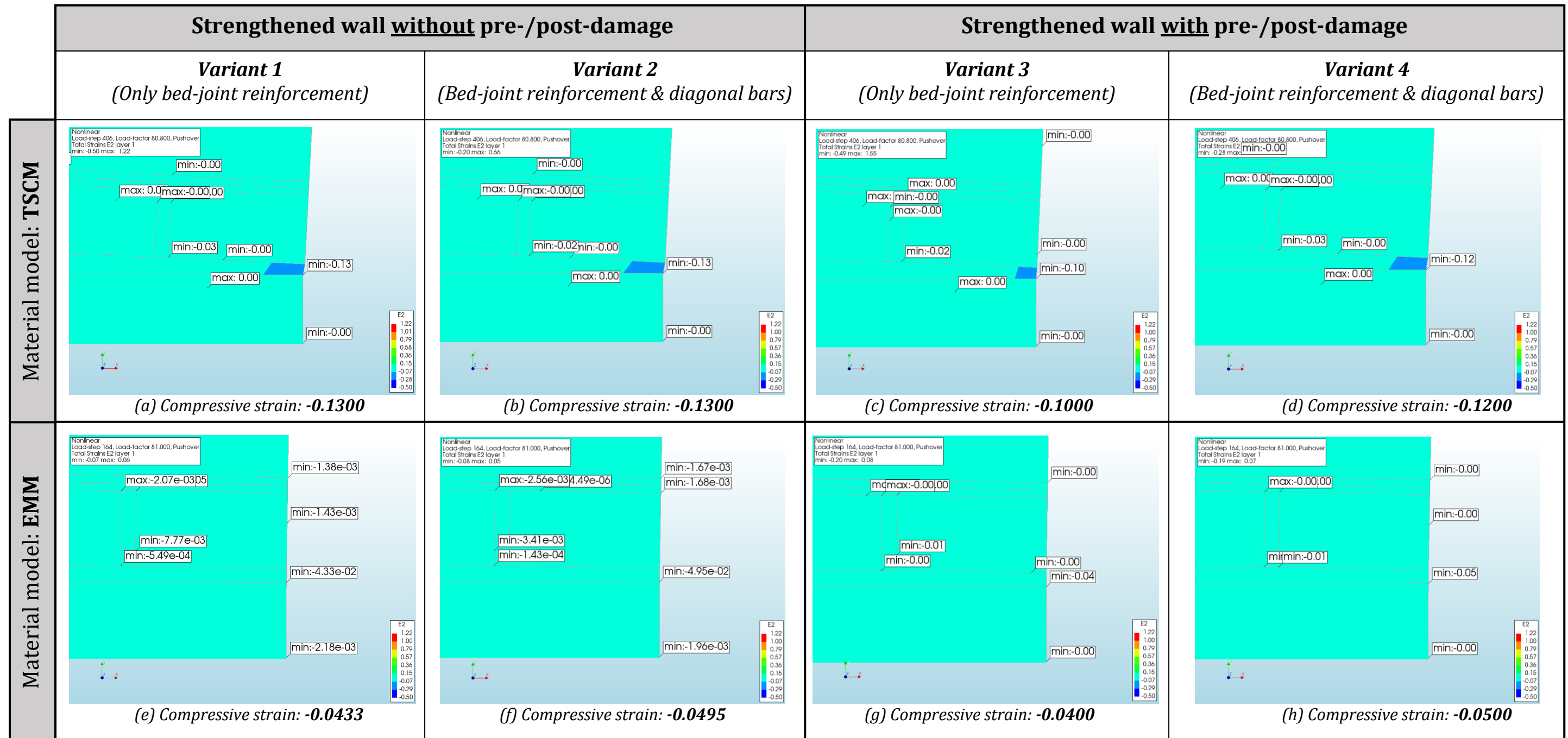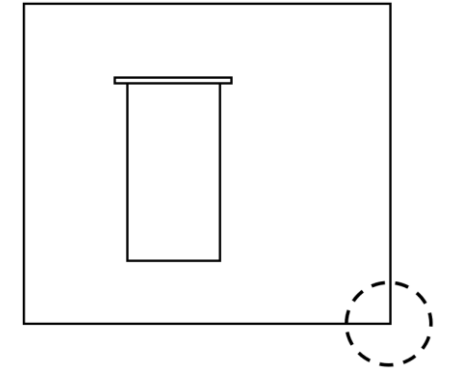

Figure 5.26: Contour plots principal strain E_2 [−] check for crushing at bottom right corner of all strengthened wall variants with continuous micro-model using TSCM and EMM for mortar joints

5.6   Conclusions

Analyses for the Damage Limitation state

Considering the analyses in the Damage Limitation state for all three modeling approaches, the crack pattern between the un-strengthened and strengthened walls, both walls without pre-/post-damage, are very similar in terms of crack width and crack length. This is in contrast with the experiment where a reduction in crack width and crack length was observed for the DL state.

The macro-model is not able to include the pre-/post-damage accurately since the bricks and the mortar joints are modeled as one homogeneous continuum. Therefore, the wall was divided into sections where modified material properties were assigned to the damaged areas in order to account for the pre-/post-damage. As a result, the cracks are "smeared" over the damaged areas and therefore the maximum force capacity of the wall is underestimated.

The detailed micro-model is not able to capture the behavior of the reinforcement bars since they are connected to the plane stress elements of the mortar joints. As was concluded also in Chapter 4, cracks in a detailed micro-model mainly occur in the form of opening of the brick-mortar joint interface elements, while smeared cracking is limited in the mortar joints. This explains why the reinforcements bars are not getting activated and therefore inaccurate low axial stresses and bond-slips are obtained.

Analyses for the Near Collapse state

The continuous micro-model is chosen for the analyses in the Near Collapse state based on the results of the Damage Limitation state. No significant increment in force capacity in both loading directions is observed between the un-strengthened and strengthened wall. The force increment is even smaller for the continuous micro-model using the *Engineering Masonry model (EMM)* for the mortar joints because this material model mainly display horizontal cracks as was observed in the un-strengthened wall from Chapter 4. The maximum axial stresses and bond-slip reached in the reinforcements are relatively lower, compared to the continuous micro-model using the *Total Strain Crack model (TSCM)* for the mortar joints, since the bars are not getting activated as much due to their oriented in parallel with the major horizontal cracks formed in the un-strengthened wall. The maximum axial stress reached in all reinforcement bars of the wall occurred near the bottom corners of the window opening. Yielding of the bars occurred at these locations only for the model using the TSCM for the mortar joints. In general, high axial stresses are developed in the bed-joint reinforcements while exhibiting minimal bond-slip. On the contrary, low axial stresses are developed in the diagonal bars while exhibiting substantial large bond-slip (exceeding the maximum elastic bond-slip).

One limitation of the model is that the bricks are kept linear elastic which means that crushing and cracking are ignored in the bricks. The compressive stresses occurred in the bricks at the bottom corner of the wall are lower than the compressive strength of the bricks, but higher than the compressive strength of masonry as a composite material. In terms of the compressive stresses in the bed-joint at the bottom right corner of the wall, it was observed that the compressive stresses are in the softening branch for the continuous micro-model using the TSCM for the mortar joints. On the other hand, it was observed that the compressive stresses are in the initial branch for the continuous micro-model using the TSCM for the mortar joints.

6

PARAMETRIC STUDY

Effects of opening size and location on the in-plane seismic response of masonry walls

A parametric study is conducted in this chapter to investigate the relationship between both opening position and opening percentage on the in-plane failure behavior of un-strengthened and strengthened masonry walls. Liu et al. ([2020](#)) performed a series of numerical analyses using Discrete Element method of many possible opening sizes and positions, such as varying the opening shape and numbers of openings, to identify their impact on the in-plane behavior of URM walls. Both load-based and displacement-based quasi-static pushover analysis procedure have been studied where the latter one is sensitive to local failures and generally showed a lower in-plane capacity, while the former one is a better representation of seismic loading but it does not allow for tracking of the post-peak response of the URM wall. According to Liu et al. ([2020](#)), as the opening percentage increases the in-plane capacity reduces, often with changes to the failure mechanism, creating more local failures and less wall integrity. For URM walls with the same opening percentage a different shape or location of the opening can result in a significant lower lateral strength and displacement capacity. URM walls with both door and window openings did not perform well even at small opening percentages. Moreover, a central opening has the least impact on the wall performance while the wall capacity is significantly reduced with openings at the bottom of the compression diagonal.

A description of the geometry and numerical model for different wall-opening configurations are given in Section 6.1. The numerical results for the wall-opening configurations are presented and discussed in Section 6.2 for the un-strengthened wall and in Section 6.3 for the strengthened wall. Lastly, the discussions and conclusions for the parametric study are provided in Section 6.4.

6.1 Description geometry and numerical model for different wall-opening configurations

Three different window opening sizes are investigated in this study, namely the original size (780 x 1510 mm) from the experiment, a medium size (1000 x 1930 mm) and a large size opening (1660 x 2050 mm) which are categorized in Group 1, Group 2 and Group 3, respectively. The dimensions of the medium and large size opening are typical of Dutch terraced houses in the region of Groningen (illustrated in the paper by Miglietta et al., [2019](#)). For all groups, five different opening locations are investigated, resulting in a total of 15 different configurations. The different configurations, in terms of the location of the central point of the opening, are indicated with a letter. For this study, the opening is only moved sideways where the height location is kept the same within each group. Configuration 1B is essentially the wall from the experiment. Configuration "B" from each group have the same distance to central point

of the opening, measured from the left edge of the wall, as the wall from the experiment. Configuration "A" of each group is the only configuration for which the opening is moved to the left. The opening in configuration "C" of each group is moved to half the width of the wall. Configuration "D" for each group is the mirrored version of configuration "B" of each group. Configuration "E" for each group is the mirrored version of configuration "A" of each group. In summary, the distance to the central point of the opening is the same for configurations "B", "C" and "D" of each group. This also holds for configuration "A" and "E", except for Group 3 in order to maintain a minimum size for the pier at the toe-side of the wall. The dimensions of the wall-opening for configuration "B" of each group are illustrated in *Figure 6.1*. The location of the central point of the opening are herein indicated for all configurations within each group. Furthermore, the dimensions of the window opening and the width of the piers for all configurations are indicated in *Table 28*.

Table 28: Dimensions of window opening and width of piers for all configurations

		Opening size (w x h)	Opening percentage	Width of left pier	Width of right pier	Distance to central point of opening
		[mm]	[%]	[mm]	[mm]	[mm]
Group 1	Config. 1A	780 x 1510	14	540	1750	930
	Config. 1B			870	1420	1260
	Config. 1C			1145	1145	1535
	Config. 1D			1420	870	1810
	Config. 1E			1750	540	2140
Group 2	Config. 2A	1000 x 1930	23	430	1640	930
	Config. 2B			760	1310	1260
	Config. 2C			1035	1035	1535
	Config. 2D			1310	760	1810
	Config. 2E			1640	430	2140
Group 3	Config. 3A	1660 x 2050	41	210	1200	1040
	Config. 3B			430	980	1260
	Config. 3C			705	705	1535
	Config. 3D			980	430	1810
	Config. 3E			1200	210	2030

Based on the numerical results of the previous chapters, the continuous micro-model is chosen to simulate the wall configurations in this chapter. The continuous micro-model is able to capture the behavior of the reinforcement bars and is able to simulate the propagation of the cracks more precisely. Again, the bricks are assumed linear elastic based on the fact that the mortar joints and the bonds between the bricks and the mortar joints usually are the weakest link in masonry. Moreover, it reduces the computational time significantly. The reinforcement bars are again simulated using truss elements embedded in the continuum plane stress elements of the bed-joints. Von Misis plasticity is assigned to all reinforcement bars to capture potential yielding in tension. The pull-out behavior of the bars are simulated through introducing interface elements between the trusses for the reinforcements and the plane stress elements for the bed-joints, and the assignment of a bond-slip constitutive relation (see *Table 17*). In terms of the material model for the mortar joints, the *Engineering Masonry model (EMM)* is able to capture the hysteretic behavior when performing a cyclic analysis with unloading. However, conducting cyclic analyses for all configurations in this study will not be practical. For this reason, monotonic analyses are conducted using the *Total Strain Crack model (TSCM)* as the material model for the mortar joints, since the EMM has to be applied in an isotropic manner which results in less accurate results for the crack pattern.

The numerical models in this chapter are essentially the same as the wall from the experiment, but with a different size and/or location of the window opening. The boundary conditions and material properties for the original configuration are presented in Chapter 4.2 for the un-strengthened wall and in Chapter 5.2 for the strengthened wall. The same lay-out of the bed-joint reinforcements from the experiment are used for the strengthened wall-opening configurations in Section 6.3. Important to note is that the diagonal bars and the pre-/post-damage are not included in the numerical models in this chapter. According to Mahmoudimotlagh ([2020](#)), the diagonal bars do not have a significant effect on the in-plane seismic response of the wall in terms of the crack pattern and the increase in force capacity. On the other hand, diagonal stair-case cracks were observed in the experiment due to the inclusion of pre-damage. However, it was observed from the numerical results in the previous chapter that the inclusion of pre-/post-damage in the models does not have a significant effect on the maximum force capacity of the wall. For this reason, the pre-/post-damage are not modeled in this parametric study. The applied numerical settings and parameters are indicated in *Table E 1* of Appendix E.
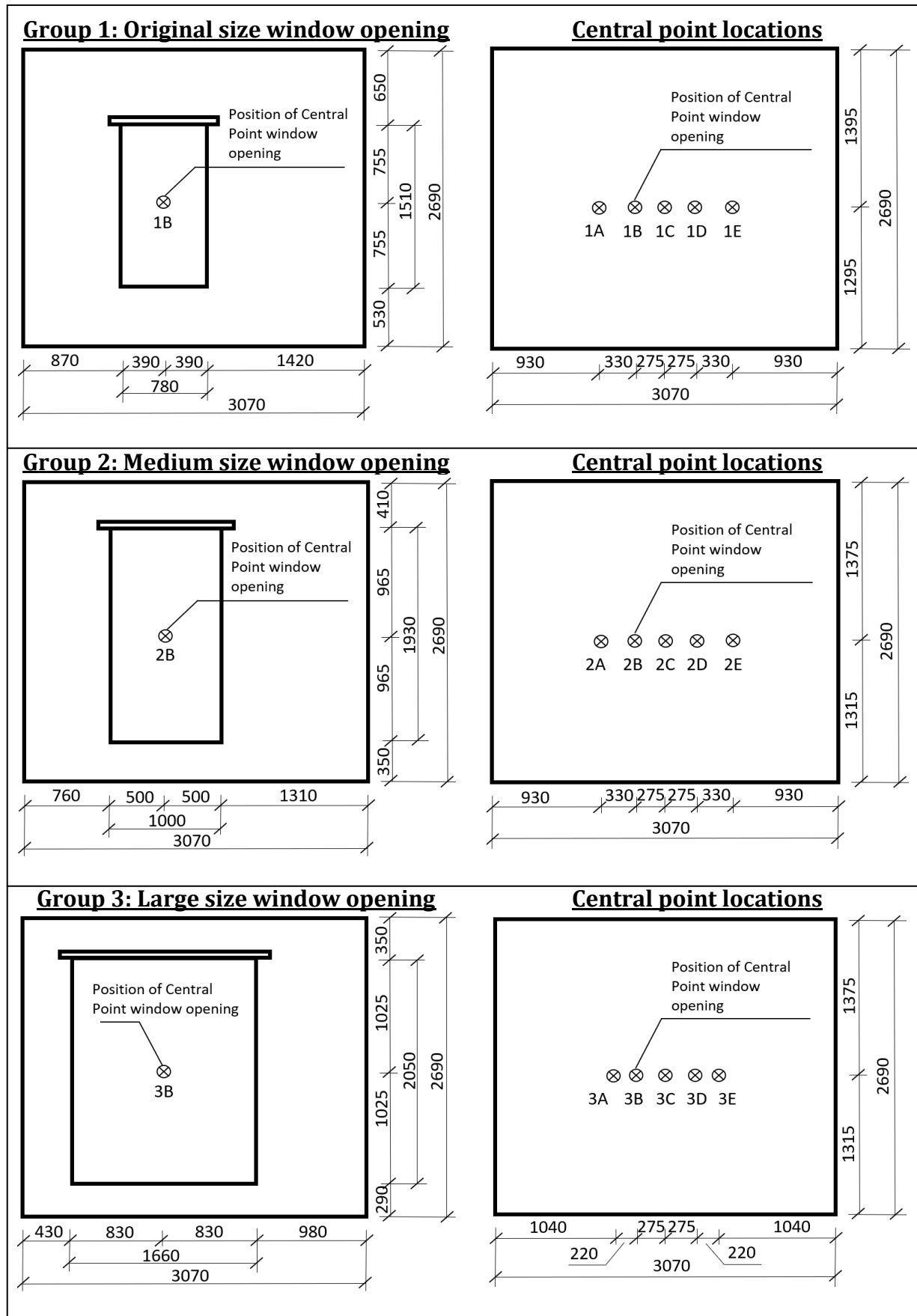
Figure 6.1: Geometry wall-opening configurations and central point locations of window opening for all 3 window opening sizes

6.2 Results for un-strengthened wall-opening configurations

The numerical results for all un-strengthened wall-opening configurations are presented in this section. The results are discussed by interpreting the capacity curves and the crack patterns. As described before, configuration "D" and configuration "E" of each group are the mirrored version of configuration "B" and configuration "A" of each group, respectively. For this reason, the results are presented only for the positive loading direction. The results in the negative loading direction are essentially the flipped and mirrored versions of the corresponding configurations.

The **capacity curves** and the corresponding bilinear approximation curves for each configurations are illustrated in *Figure 6.2* for each group separately. The bilinear approximation curves and parameters are calculated as described in Section 4.5 and the obtained values are listed in *Table 29*. The relations between the maximum base shear force V_u and the distance to the central point of the window opening are illustrated in *Figure 6.3* for each group. The comparisons are done in terms of the maximum base shear force obtained from the bilinear curves. It can be observed that as the opening percentage increases, the in-plane capacity reduces, which is in line with the results obtained by Liu et al. ([2020](#)). Moreover, as the opening is moved closer to the toe-side of the wall, the in-plane capacity also decreases. When moving the opening from the original position to half the width of the wall (configuration "B" to "C"), the maximum base shear force is staying almost constant for Group 1, while for Group 2 and 3 the force capacity is reduced. The percentage reduction for configuration "C" of each group, with respect to configuration "B" of each group, is -0.3%, -19.9% and -19.5% for Group 1, Group 2 and Group 3, respectively. When moving the opening to the left (configuration "B" to "A"), the force capacity of Group 1 and Group 2 are staying almost constant, while the force capacity for Group 3 is increased. The percentage difference, comparing configuration "A" and "B" for each group, is +0.2%, -0.3% and +28.5% for Group 1, Group 2 and Group 3, respectively. The influence of the size and location of the window opening, and thus the width of the right pier, on the force capacity can be seen with the comparison of configuration 3A with configuration 2C, 2D and 2E. The width of the right pier for configuration 3A is larger than the aforementioned configurations of Group 2. However, the force capacity is only higher than that of configurations 2D and 2E. This is exactly the same for the comparison of configuration 2B with configuration 1C, 1D and 1E. The configuration with the lowest force capacity of Group 1 (configuration 1E) is still higher than the configuration with the highest force capacity of Group 3 (configuration 3A). In general, the initial stiffness of the wall gets smaller as the pier, which is at the toe-side of the wall, gets narrower.

The final **crack pattern** for all configurations in the positive loading direction are presented in *Figure 6.4*. All configurations are showing a similar failure pattern compared with the original configuration, namely diagonal stair-case cracks developing from the corners of the window opening and propagating towards the corners of the wall. Considering the original configuration 1B, the main failure mechanism in the wall is rocking of both left pier as well as the "L-shape" portion of the wall, which consists of the right pier and the top spandrel. This is also the case for configuration 1A and 2A. All other configurations are showing rocking failure behavior of both piers in the wall. Moreover, when the width of the right pier is reduced, the horizontal crack at the base of the left pier becomes larger and gets distributed over an larger area. This can be explained by the fact that when the width of the right pier becomes smaller, the resisting capacity of the wall becomes more dependent on the left pier. Lastly, the maximum crack width for each configuration is also indicated in the figure.

Capacity curves and bilinear approximations for un-strengthened wall-opening configurations

Group 1: Original size window opening   Group 2: Medium size window opening   Group 3: Large size window opening

Figure 6.2: Capacity curves un-strengthened wall-opening configurations (a)-(c); bilinear approximations (d)-(f)

Figure 6.3: Maximum force capacity vs distance to central point of window opening for all configurations of each group for the un-strengthened walls

Table 29: Bilinear approximation parameters for all configurations of each group for the un-strengthened wall. Percentage differences with respect to configurations B of each group indicated in parentheses

		Un-strengthened walls (loading in positive x-direction)				
		Initial stiffness K_{el}	Max. base shear force V_u	Elastic displacement u_{el}	Ultimate displacement u_u	Ultimate drift d_{r-b}
		$[kN/mm]$	$[kN]$	$[mm]$	$[mm]$	$[\%]$
Group 1	Configuration 1A	40.27 (+11.3%)	25.44 (+0.2%)	0.63 (-10.0%)	43.60	1.62
	Configuration 1B	36.19	25.38	0.70	43.60	1.62
	Configuration 1C	33.75 (-6.7%)	25.30 (-0.3%)	0.75 (+7.1%)	43.60	1.62
	Configuration 1D	37.07 (+2.4%)	22.54 (-11.2 %)	0.61 (-12.9%)	43.60	1.62
	Configuration 1E	32.48 (-10.3%)	21.70 (-14.5 %)	0.67 (-4.3%)	43.60	1.62
Group 2	Configuration 2A	34.09 (+20.0%)	24.31 (-0.3%)	0.71 (-17.4%)	43.60	1.62
	Configuration 2B	28.40	24.39	0.86	43.60	1.62
	Configuration 2C	25.42 (-10.5%)	19.53 (-19.9%)	0.77 (-10.5%)	43.60	1.62
	Configuration 2D	24.43 (-14.0%)	17.62 (-27.8%)	0.72 (-16.3%)	43.60	1.62
	Configuration 2E	25.26 (-11.1%)	17.65 (-27.6%)	0.70 (-18.6%)	43.60	1.62
Group 3	Configuration 3A	21.93 (+54.0%)	19.34 (+28.5%)	0.88 (-17.0%)	43.60	1.62
	Configuration 3B	14.24	15.05	1.06	43.60	1.62
	Configuration 3C	11.09 (-22.1%)	12.12 (-19.5%)	1.09 (+2.8%)	43.60	1.62
	Configuration 3D	10.80 (-24.2%)	11.32 (-24.8%)	1.05 (-0.9%)	43.60	1.62
	Configuration 3E	11.26 (-20.9%)	11.62 (-22.8%)	1.03 (-2.8%)	43.60	1.62

Continuous micro-model using TSCM for mortar joints (un-strengthened wall)

*(monotonic analysis up to NC state in **positive** loading direction + 43.63 mm with maximum crack width w [mm] indicated)*
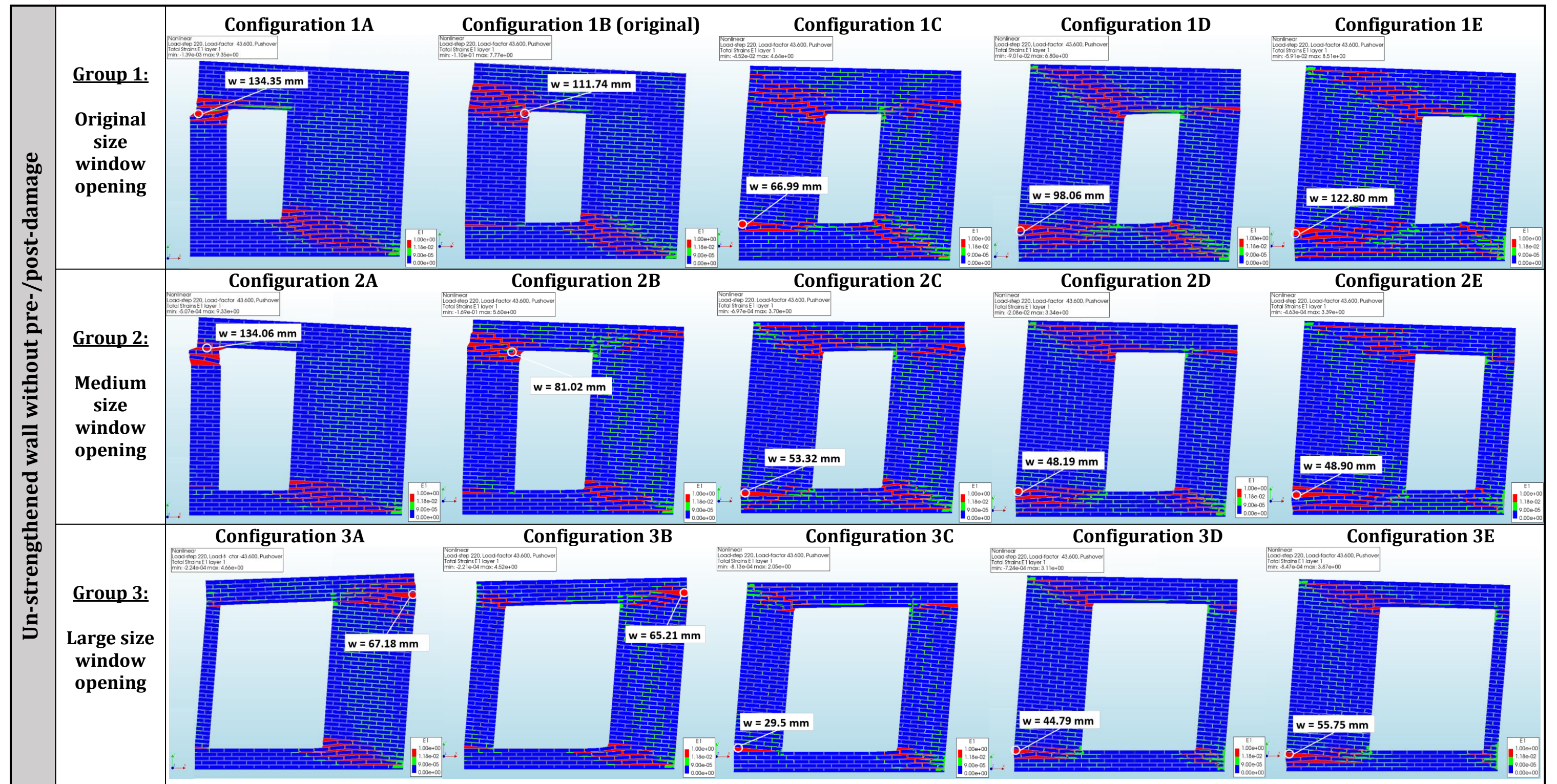
Figure 6.4: Contour plots principal strain E1 [-] showing crack pattern un-strengthened wall-opening configurations at maximum top displacement in positive loading direction using monotonic analysis (up to NC state)

6.3   Results for strengthened wall-opening configurations

The numerical results for all configurations of the strengthened walls are presented in this section. Again, the results are discussed by interpreting the crack patterns and the capacity curves. Moreover, the behavior of the reinforcements is evaluated based on the amount of slip and the potential yielding of the bars. The results are presented only for the positive loading direction for the same reason as described in the previous section.

The **capacity curves** and the corresponding bilinear approximation curves for all configurations are illustrated in *Figure 6.5* for each group separately. The bilinear approximation parameters are calculated as described in Section 4.5 and the obtained values are listed in *Table 30*. The percentage differences with respect to the un-strengthened configurations are herein indicated in parentheses. The relations between the maximum base shear force V_u and the distance to the central point of the window opening are illustrated in *Figure 6.6* for each group. Again, the comparisons are done in terms of the maximum base shear force obtained from the bilinear curves. No significant increment in force capacity with respect to the un-strengthened configurations can be observed which is also in line with the results of the experiment (Licciardello et al., 2021). The effect of the bed-joint reinforcement on the force capacity is even less noticeable as the window opening gets bigger. This can be explained by the fact that there is less wall integrity with a larger opening in the wall. Also with a larger opening, the area of bed-joints is reduced and thus the amount of reinforcements. The largest percentage increment in force capacity, with respect to the un-strengthened configurations of each group, is +13.6%, +8.4% and +5.0% for configuration 1D, configuration 2C and configuration 3C, respectively. From the results of *Table 30*, it can be observed that the bed-joint reinforcement has a relatively larger influence on the force capacity when the window opening is located close to the middle of the wall. Furthermore, the force capacity of the strengthened version of configuration 2A and 2B are very close to the un-strengthened version of configuration 1A and 1B.

The final **crack pattern** for all configurations in the positive loading direction are presented in *Figure 6.7*. It can be observed that the formation of the diagonal stair-case cracks at the corners of the window opening is prevented by the presence of the reinforcement. As a result, horizontal cracks are more prominent in the bed-joints where the reinforcement is not present. The same failure mechanism can be observed as the un-strengthened wall-opening configurations from the previous section. However, the rocking failure behavior of both piers in configuration 1C and 2B of the un-strengthened walls are changed to rocking of the left pier and the "L-shape" portion of the wall for the strengthened versions. Additionally, more horizontal cracks can be observed at the masonry portion below the window opening, especially for Group 1 with the original opening size. Similar to the configurations of the un-strengthened walls, when the width of the right pier is reduced, the horizontal crack at the base of the left pier becomes larger and gets distributed over an larger area. Again, this can be explained by the fact that when the width of the right pier becomes smaller, the resisting capacity of the wall becomes more dependent on the left pier. Furthermore, the maximum occurred crack width in each configuration is indicated in *Figure 6.7* and the values are compared with the ones for the un-strengthened wall in *Table 31*. Again, the effect of the bed-joint reinforcement is less noticeable, in terms of the maximum crack width, for walls with a large window opening since the values are increased for the strengthened walls in most cases. Some deviations in the results can be explained by the fact that the cracks are not always fully comparable since they have different shape and location when comparing the un-strengthened wall with the strengthened wall.

Capacity curves and bilinear approximations for strengthened wall-opening configurations

Group 1: Original size window opening　　Group 2: Medium size window opening　　Group 3: Large size window opening
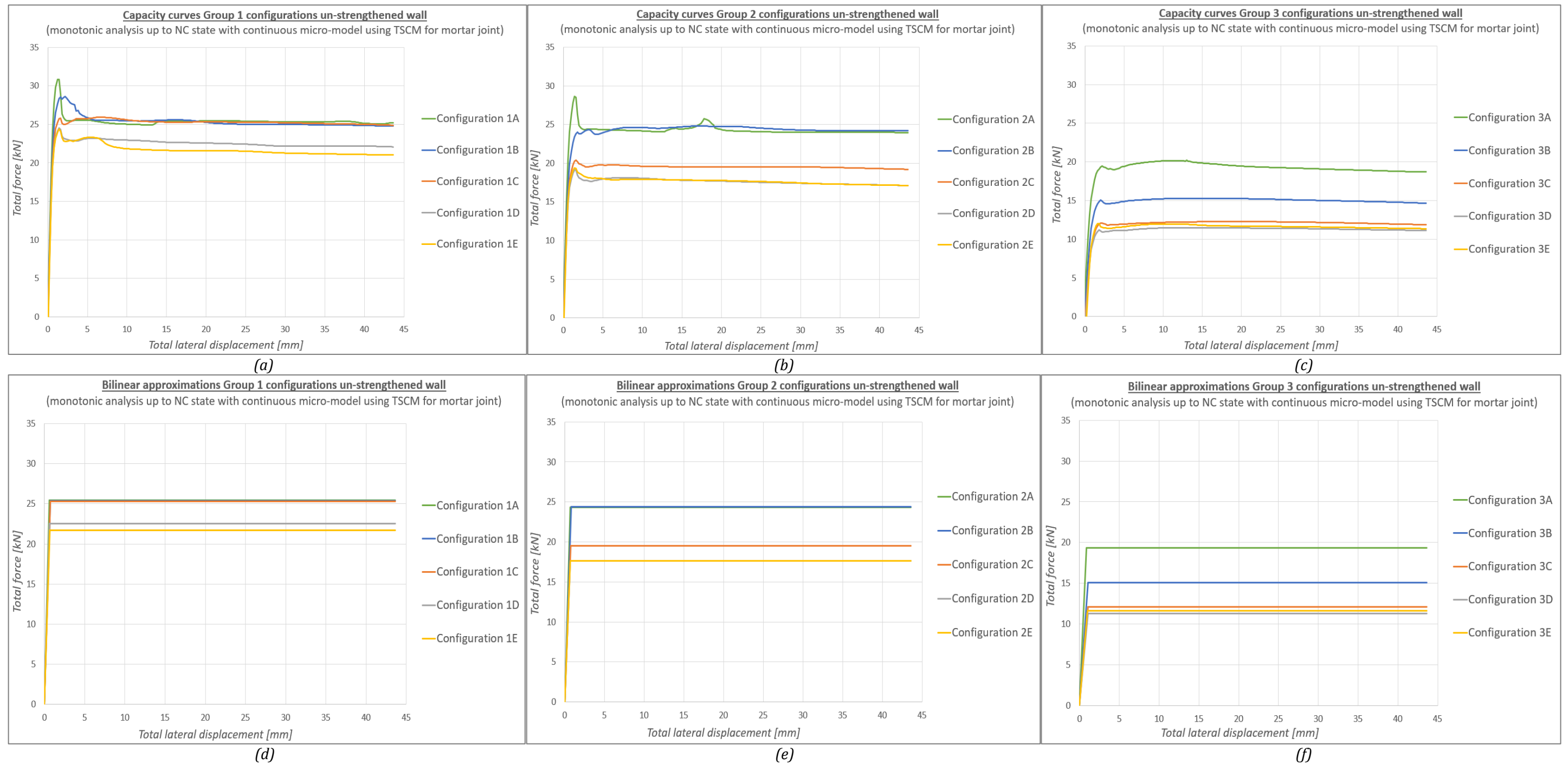

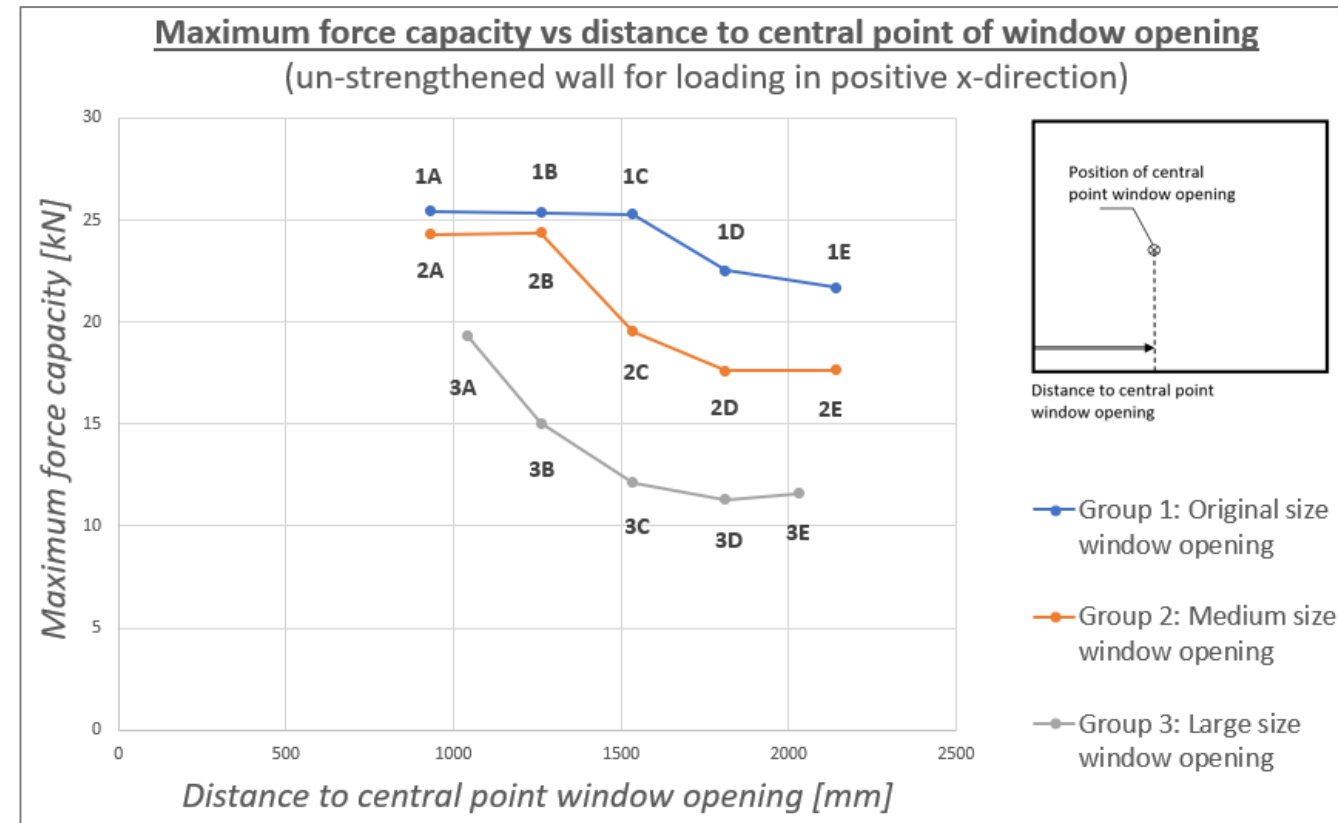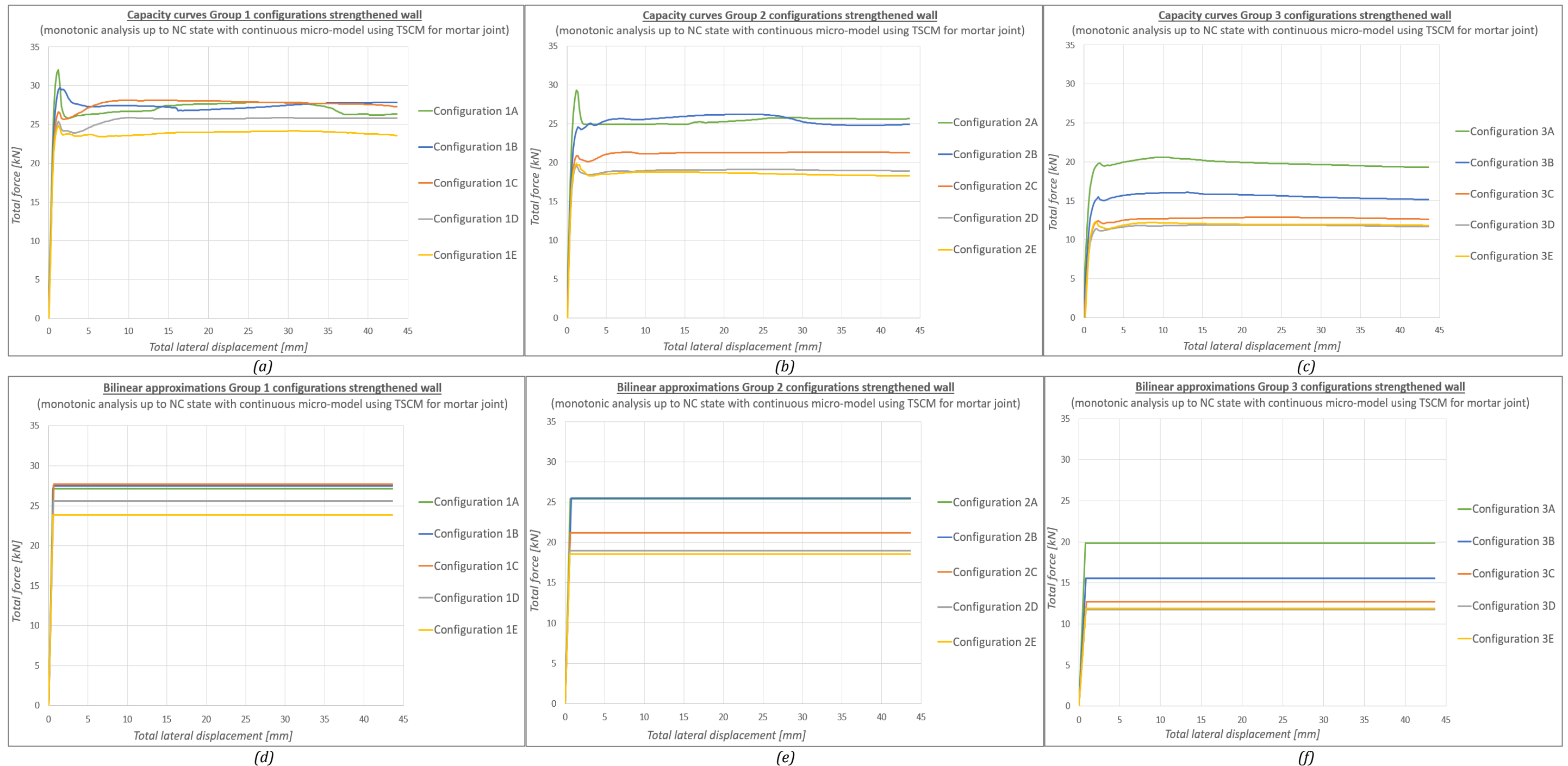Figure 6.5: Capacity curves strengthened wall-opening configurations (a)-(c); bilinear approximations (d)-(f)
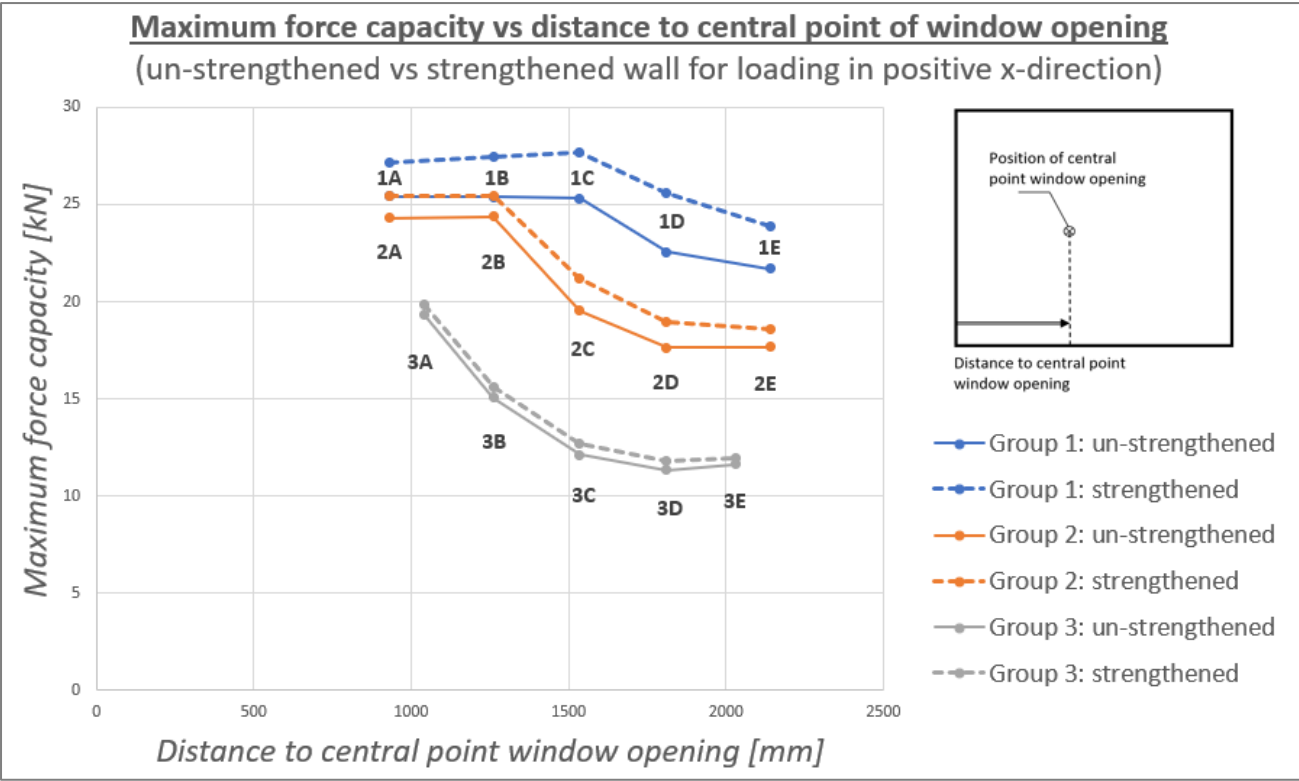
Figure 6.6: Maximum force capacity vs distance to central point of window opening for all configurations of each group for the un-strengthened and strengthened walls

Table 30: Bilinear approximation parameters for all configurations of each group for the strengthened wall. Percentage difference with respect configuration of un-strengthened version indicated in parentheses

		Strengthened walls (loading in positive x-direction)				
		Initial stiffness K_{el}	Max. base shear force V_u	Elastic displacement u_{el}	Ultimate displacement u_u	Ultimate drift d_{r-b}
		[kN/mm]	[kN]	[mm]	[mm]	[%]
Group 1	Configuration 1A	51.18 (+27.1%)	27.14 (+6.7%)	0.53 (-15.9%)	43.60	1.62
	Configuration 1B	46.11 (+27.4%)	27.46 (+8.2%)	0.60 (-14.3%)	43.60	1.62
	Configuration 1C	43.29 (+28.3%)	27.67 (+9.4%)	0.64 (-14.7%)	43.60	1.62
	Configuration 1D	42.20 (+13.8%)	25.60 (+13.6%)	0.61 (0.0%)	43.60	1.62
	Configuration 1E	41.80 (+28.7%)	23.88 (+10.0%)	0.57 (-14.9%)	43.60	1.62
Group 2	Configuration 2A	38.11 (+11.8%)	25.42 (+4.6%)	0.67 (-5.6%)	43.60	1.62
	Configuration 2B	31.93 (+12.4%)	25.46 (+4.4%)	0.80 (-7.0%)	43.60	1.62
	Configuration 2C	32.21 (+26.7%)	21.18 (+8.4%)	0.66 (-14.3%)	43.60	1.62
	Configuration 2D	31.13 (+27.4%)	18.96 (+7.6%)	0.61 (-15.3%)	43.60	1.62
	Configuration 2E	31.54 (+24.9%)	18.56 (+5.2%)	0.59 (-15.7%)	43.60	1.62
Group 3	Configuration 3A	24.31 (+10.9%)	19.84 (+2.6%)	0.82 (-6.8%)	43.60	1.62
	Configuration 3B	17.91 (+25.8%)	15.59 (+3.6%)	0.87 (-17.9%)	43.60	1.62
	Configuration 3C	13.69 (+23.4%)	12.72 (+5.0%)	0.93 (-14.7%)	43.60	1.62
	Configuration 3D	13.41 (+24.2%)	11.76 (+3.9%)	0.88 (-16.2%)	43.60	1.62
	Configuration 3E	13.50 (+19.9%)	11.94 (+2.8%)	0.88 (-14.6%)	43.60	1.62

Table 31: Maximum crack width w [mm] un-strengthened walls vs strengthened walls with percentage difference indicated in parentheses

		Maximum crack width occurred in the wall	
		Un-strengthened wall	Strengthened wall
		[mm]	[mm]
Group 1	Configuration 1A	134.35	127.85 (-4.8%)
	Configuration 1B	111.74	100.79 (-9.8%)
	Configuration 1C	66.99	64.10 (-4.3%)
	Configuration 1D	98.06	114.64 (+16.9%)
	Configuration 1E	122.80	112.75 (-8.2%)
Group 2	Configuration 2A	134.06	132.31 (-1.3%)
	Configuration 2B	81.02	82.31 (+1.6%)
	Configuration 2C	53.32	59.93 (+12.4%)
	Configuration 2D	48.19	42.69 (-11.4%)
	Configuration 2E	48.90	42.88 (-12.3%)
Group 3	Configuration 3A	67.18	115.43 (+71.8%)
	Configuration 3B	65.21	24.26 (-62.8%)
	Configuration 3C	29.50	31.35 (+6.3%)
	Configuration 3D	44.79	46.62 (+4.1%)
	Configuration 3E	55.76	60.79 (+9.0%)

Continuous micro-model using TSCM for mortar joints (strengthened wall)

*(monotonic analysis up to NC state in **positive** loading direction + 43.63 mm with maximum crack width w [mm] indicated)*
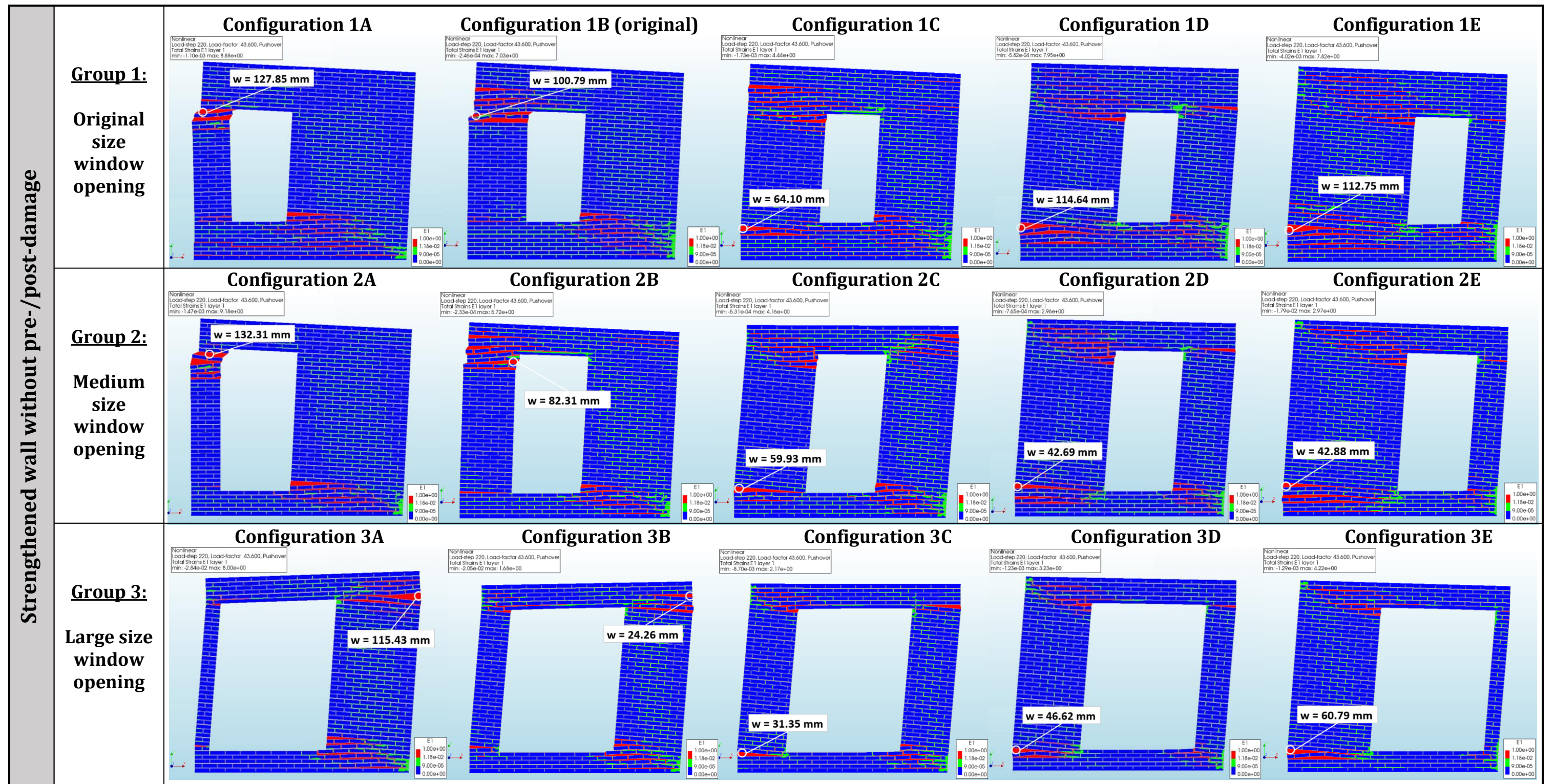

Figure 6.7: Contour plots principal strain E1 [-] showing crack pattern strengthened wall-opening configurations at maximum top displacement in positive loading direction using monotonic analysis (up to NC state)

The maximum **axial stress** reached in every row of reinforcement, with the corresponding locations, are indicated in *Figure 6.8* only for configuration "B" of each group. The results of all other configurations are presented in Appendix F. Important to note is that the maximum axial stresses in each row are not reached at the same top displacement. Nevertheless, the locations of the maximum axial stresses are corresponding with the locations where the diagonal stair-case cracks become horizontal cracks in the strengthened wall. Since no cracks are formed in both piers, the maximum axial stresses reached in the reinforcements at these locations are small. From the previous section it was observed that the bed-joint reinforcement has a relatively larger influence on the force capacity for walls with a smaller window opening. This is also reflected in the behavior of the reinforcements where the maximum occurred axial stresses are relatively lower for the walls with a larger window opening. Considering configuration 1B for both loading directions, the yield strength of 205 N/mm^2 is exceeded only in the bed-joint reinforcement below the opening at the locations near the bottom corners. On the other hand, no yielding can be observed for configuration 3B. The locations of the largest maximum axial stress occurred for all reinforcements in the entire wall, for both loading directions, are marked in red. The axial stresses of the entire analysis are taken from these locations and the development for the corresponding configurations are plotted and illustrated in *Figure 6.9(a)-(c)*. Moreover, the development of the **bond-slip** at the location where the maximum value is reached, for both loading directions, are presented in *Figure 6.9(d)-(f)*. The maximum occurred bond-slip, in both loading directions, for configuration "B" of all groups are within the elastic branch of the applied bond-slip model (see *Table 17* from section 5.1.3). The maximum elastic bond-slip S_1 is 5 mm for the bed-joint reinforcements.

6.4   Discussion and conclusions

One important aspect which was not investigated in this parametric study is the prediction of the ultimate displacement of the walls. The same prescribed maximum top displacement (+43.60 mm) is used for both un-strengthened and strengthened wall configurations. This is done in order to compare the crack patterns at the same displacement of the walls. The loading of the wall in the experiment was stopped when a large amount of out-of-plane damage was observed. However, the same stopping criteria cannot be used for the numerical models since out-of-plane deformations cannot be captured with a 2D-model using plane stress elements. This is discussed further in Section 7.2 with recommendation for further research.

It is also important to emphasize that the conclusions provided with the parametric study are derived from the limited cases treated in this study. As the opening size increases the in-plane capacity reduces. Moreover, as the opening is moved closer to the toe-side of the wall, the in-plane capacity also decreases. The rate of reduction of the force capacity, due to the location change of the window opening, varies differently for each group of opening sizes. Considering the comparison of configuration A (opening located furthest to the left) with configuration E (opening located furthest to the right), the percentage reduction in force capacity is -14.7%, -27.4% and -39.9% for Group 1 (original size opening), Group 2 (medium size opening) and Group 3 (large size opening), respectively. Furthermore, the effect of the bed-joint reinforcement on the force capacity becomes less noticeable as the window opening gets bigger. This can be explained by the fact that there is less wall integrity with a larger opening in the wall. The largest percentage increment in force capacity, with respect to the un-strengthened corresponding configuration, is +13.6%, +8.4% and +5.0% for Group 1, Group 2 and Group 3, respectively. The increment in force capacity, due to the bed-joint reinforcement, is relatively larger when the window opening is located close to the middle of the wall.

Max. axial stress occurred in each row of reinforcement for configuration B of each group with value and location indicated

(monotonic analyses up to NC state for strengthened continuous micro-model using TSCM for mortar joints)
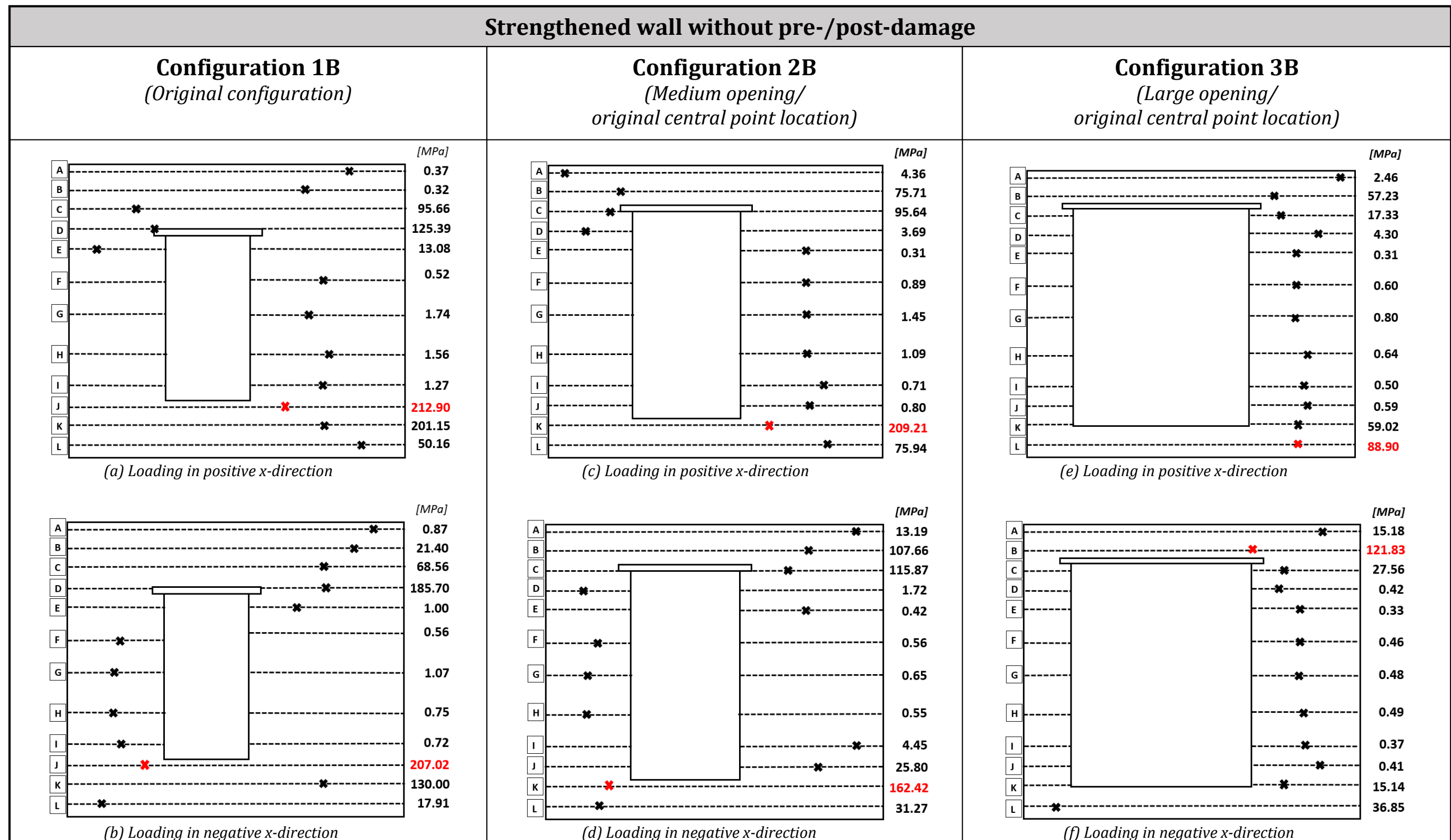
Figure 6.8: Maximum axial stress occurred in each row of reinforcement for configuration B of each group of strengthened wall

Axial stress & bond-slip development in bed-joint reinforcement for configuration B of each group

(monotonic analyses up to NC state for strengthened continuous micro-model using TSCM for mortar joints)

Configuration 1B	Configuration 2B	Configuration 3B

Axial stress development

(a)   (b)   (c)

Bond-slip development

(d)   (e)   (f)
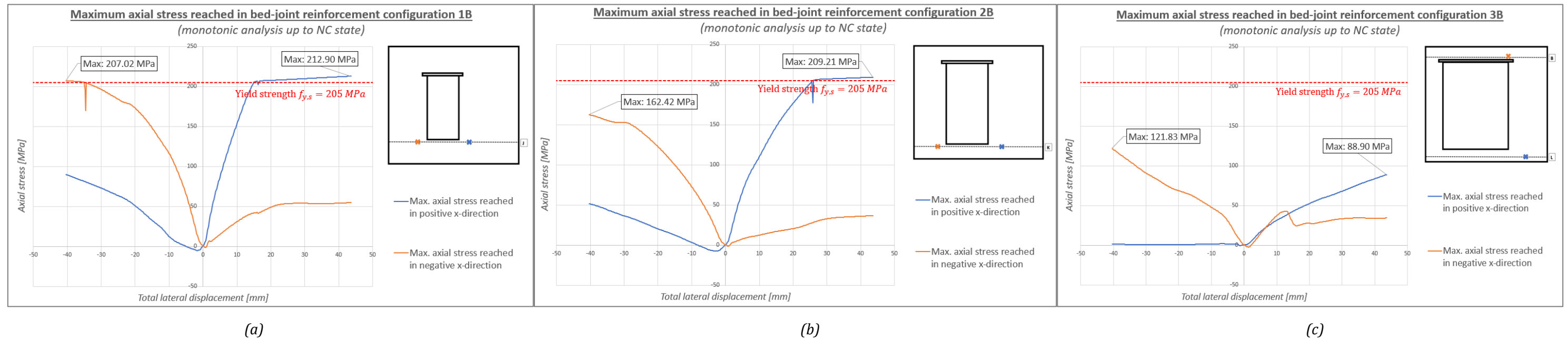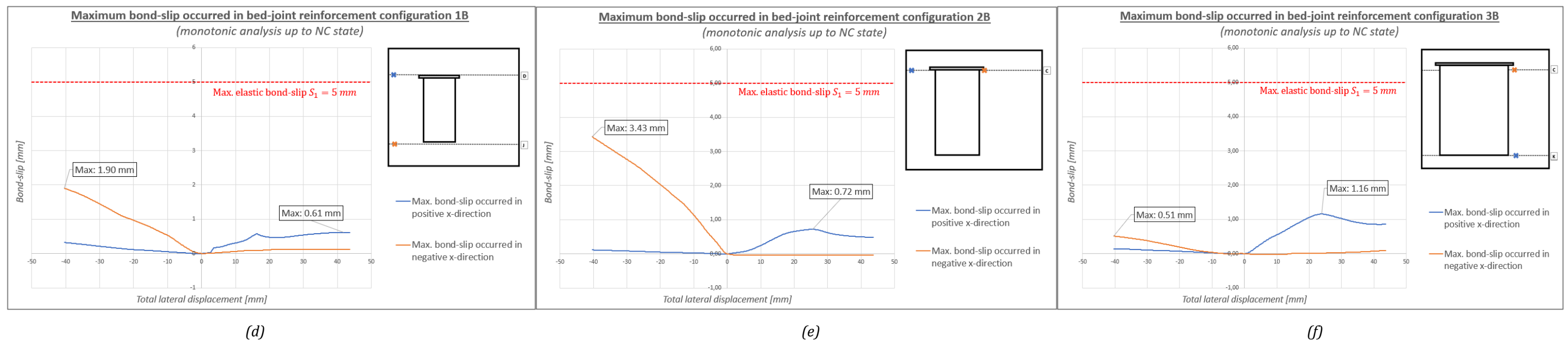
Figure 6.9: Results behavior of reinforcements for configuration B of each group: (a)-(c) axial stress development ; (d)-(f) bond-slip development

7

Conclusions and recommendations

The bed-joint reinforcement is a retrofitting technique which is commonly applied in URM structures in the Netherlands to prevent/ repair vertical cracks caused by ground settlements. However, there is a lack of extensive and systematic research on the performance of this retrofitting technique against seismic activities. Experimental tests have been conducted at Delft University of Technology (Licciardello et al., 2021) with the goal to investigate the performance of the bed-joint reinforcement technique as a strengthening measure against seismic loading for the Groningen area. A quasi-static cyclic in-plane test was conducted for both un-strengthened and strengthened wall where pre-/post-damage was included for the latter one. Through experimental testing and numerical modeling, the effectiveness of the bed-joint reinforcement technique is evaluated.

The main conclusions and recommendations formed with this thesis research are outlined in this chapter. The objective of this research was to create accurate and valid finite element models of both un-strengthened and strengthened walls from the experiments, to investigate the effect of the bed-joint reinforcement technique. Moreover, the objective was to investigate the combined effect of the bed-joint reinforcement technique and the change in size and location of the window opening on the in-plane response (parametric study). Three modeling approaches were used in the scope of this research, namely the macro-model, the continuous micro-model and the detailed micro-model. These models were compared to each other to find the best suited model for the simulation of the un-strengthened and strengthened walls. The best suited model was used to carry out the parametric study.

7.1   Conclusions

The main research question of this thesis research is formulated as follows:

Which modeling approach is best suited for simulating the in-plane seismic behavior of both URM walls and masonry walls retrofitted with the bed-joint reinforcement, and what are the influences on the in-plane response when changing the size and location of the window opening?

The main research question can be stepwise answered by finding the answers to the sub-questions. But first, a summary of the performance of each modeling approach is provided separately. Secondly, several additional and notable conclusions for the numerical analyses are provided. Subsequently, the answers to the sub-questions are given based on the discussion for each modeling approach. Lastly, a final conclusion is given for the performance of the bed-joint reinforcement technique and the contribution of this research.

The **macro-model** is the most simplified model to simulate masonry because the bricks and the mortar joints are modeled as one homogeneous continuum. In this thesis, the nonlinearity was smeared over the entire wall where the *Engineering Masonry model (EMM)* was applied as the material model to account for the orthotropic behavior. The macro-model is able to capture the main failure mechanism while having the least modeling effort and associated computational expenses compared to the other models. However, the macro-model is not accurate when pre-/post-damage needs to be included in the model because of the fact that no distinction is made between the geometry of the bricks and the mortar joints. Therefore, the pre-/post-damage can only be included in the macro-model by dividing the wall into damaged and un-damaged areas, according to the locations of the cracks from the experiment, and assigning modified material properties to those areas. For this reason, the pre-/post-damage is "smeared" over the whole damaged areas which means that the wall is expected to be weaker on a larger area and thus not accurate. Moreover, the use of high strength mortar for the embedment of the reinforcements in the strengthened joints, is also an example that cannot be included in the macro-model accurately.

The bricks and mortar joints are modeled separately in a **continuous micro-model**. This means that the modeling of the pre-/post-damage is more accurate compared to the macro-model. Both *Total Strain Crack model (TSCM)* and *Engineering Masonry model (EMM)* were applied as the material model for the mortar joints and the results were compared to each other. The *EMM* was mainly developed to capture masonry as an orthotropic material. However, since the bricks were assumed linear elastic in the scope of this thesis, the *EMM* needed to be adapted and applied in an isotropic manner to only the mortar joints. This could possibly explain why the results are less accurate, in terms of the crack pattern, compared to the results of the model using the *TSCM* for the mortar joints. The cracks, obtained from the model using the *EMM* for the mortar joints, are propagating more in the horizontal direction along the bed-joints. This explains why the axial stresses in the reinforcements are overall smaller compared to the model using the *TSCM* for the mortar joints, since the bars are not getting activated as much due to their oriented in parallel with the major horizontal cracks. On the other hand, the *EMM* is able to capture the hysteretic behavior in a cyclic analysis because the material model allows for elastic unloading, whereas the *TSCM* only allows for secant unloading. One disadvantage of the continuous micro-model is the fact that no interface elements are included at the brick-mortar bonds which means that the behavior (for example relative sliding) at these discontinuous surfaces cannot be captured.

The **detailed micro-model** is the most accurate model for simulating masonry. This is due to the fact that the bricks and mortar joints are modeled separately and also interface elements are included to account for the behavior over the discontinuous surfaces at the brick-mortar bonds. It was observed that cracks in the detailed micro-model mainly occurred in the form of opening of the interface elements, while smeared cracking in the mortar joints was limited. For this reason, the detailed micro-model is not well suited to simulate the strengthened wall because the reinforcement bars are connected to the plane stress elements of the mortar joints. Consequently, the reinforcements are not getting activated and thus inaccurate/low values are obtained for the axial stress and the bond-slip. Furthermore, *Discrete cracking* only captures the Mode-I (tensile) failure behavior because Mode-I and Mode-II (shear) are uncoupled. On the other hand, the *Combined cracking-shearing-crushing (CCSC)* material model is able to simulate fracture, frictional slip as well as crushing along the brick-mortar bonds However, this material model is not accurate for cyclic analyses because of the fact that elastic unloading in tension takes place, resulting in overly stiff cracks.

The following notable conclusions can be made based on the results of the numerical analyses:

1. Considering the Damage Limitation (DL) state of the experiment, a reduction in crack width and crack length was observed for the strengthened wall compared to the un-

strengthened wall. However, no significant changes in crack width and length can be observed with the numerical analyses in the DL state when comparing the un-strengthened wall with the strengthened wall. This is the case for all three modeling approaches.

2. The capacity curves obtained from the monotonic analyses follows the outline of the capacity curves for the cyclic analyses as the envelope curves. Furthermore, the results of the monotonic and cyclic analyses, in the DL state, are also very similar in terms of the crack patterns. This holds for all three modeling approaches and the applied material models, except for the detailed micro-model using the *CCSC* material model due to elastic unloading in tension where the cracks are not closing after each cycle. Considering the Near Collapse state, small differences can be observed where the cracks are more distributed over a wider range of bed-joints for the cyclic analyses.

3. The objective of the sensitivity analyses was to investigate the effect on the in-plane response of the masonry wall when changing different numerical settings and input parameters. The numerical settings and parameters such as the mesh size, load-step size and convergence criteria do have influence on the crack pattern. Although small differences can be spotted, the results of the sensitivity analyses consistently display the main cracks which capture the main rocking failure behavior of both piers. This is comparable with the experiments where small differences in crack pattern was also observed between wall specimens with the same geometry, material properties, loading and boundary conditions. This is due to imperfections where the material properties are not always consistent over the entire wall. Weak brick-mortar bonds can occur locally in the wall which may influence the propagation of the cracks. The same conclusion as for the sensitivity analyses can be made, namely as long as the main failure mechanism is captured, it is reasonable to consider the results to be reliable, even though small differences in crack pattern are observed.

The answers to the sub-questions are provided below:

1. ***What is the most suited finite element modeling approach (macro vs continuous micro vs detailed micro) to simulate the in-plane behavior of un-strengthened masonry walls?***

   All modeling approaches are able to simulate the main failure mechanism of the un-strengthened wall for the analyses in the Damage Limitation state. The continuous micro-model was chosen for the analyses in the Near Collapse state since the cracks are able to follow the geometry of the bed-and head-joints more accurately compared with the macro-model. Considering the comparison between the continuous micro-model and the detailed micro-model, the accuracy in obtained results is comparable in terms of the crack pattern and the capacity curve. The computational time for the analyses of the continuous micro-model is not necessarily smaller compared to the detailed micro-model (monotonic analyses longer for the continuous micro-model but cyclic analyses longer for the detailed micro-model). However, the modeling effort for the detailed micro-model is significantly larger. In the scope of this thesis research, the continuous micro-model is considered the best suited and a reasonable modeling approach to use since the modeling is only for a single wall. Based on the aforementioned summary of the performance of the continuous micro-model, the choice of material model to be applied to the mortar joints depends on the type of desired results.

2. ***What is the most suited finite element modeling approach (macro vs continuous micro vs detailed micro) to simulate the in-plane behavior of strengthened masonry walls?***

Based on the aforementioned summary of each modeling approach, the continuous micro-model is the only accurate model to simulate the strengthened wall when taken into account the modeling of the pre-/post-damage, the high strength repair mortar for the strengthened joints and capturing the behavior of the reinforcement bars.

3. ***What is the effect of changing the size and location of the opening on the in-plane behavior of both un-strengthened and strengthened masonry walls?***

It is important to emphasize that the conclusions provided with the parametric study are derived from the limited cases treated in this study. As the opening size increases the in-plane capacity reduces. Moreover, as the opening is moved closer to the toe-side of the wall, the in-plane capacity also decreases. The rate of reduction of the force capacity, due to the location change of the window opening, varies differently for each group of opening sizes. Considering the comparison of configuration A (opening located furthest to the left) with configuration E (opening located furthest to the right), the percentage reduction in force capacity is -14.7%, -27.4% and -39.9% for Group 1 (original size opening), Group 2 (medium size opening) and Group 3 (large size opening), respectively. Furthermore, the effect of the bed-joint reinforcement on the force capacity becomes less noticeable as the window opening gets bigger. This can be explained by the fact that there is less wall integrity with a larger opening in the wall. The largest percentage increment in force capacity, with respect to the un-strengthened configurations, is +13.6%, +8.4% and +5.0% for Group 1, Group 2 and Group 3, respectively. The increment in force capacity, due to the bed-joint reinforcement, is relatively larger when the window opening is located close to the middle of the wall.

Important to emphasize is that the answers given to the research questions are within the scope of this thesis research. The scope of this research is the numerical modeling of a full scale wall which was experimentally tested both un-strengthened and strengthened at Delft University of Technology. However, in case a large scale structure with multiple floors and walls needs to be modeled, the micro-models are simply not efficient because of the large modeling and computational demands. The micro-models can only be readily applied to smaller scale models such as a single masonry wall. Therefore, for large scale models or for analyses where a large number of models need to be run and the computational expense is limited, the macro-model is a more efficient model, but will likely produce less reliable results in terms of following the precise propagation of the cracks. Moreover, even though the modeling and the computational effort for the macro-model are significantly lower compared to the other modeling approaches, it is more difficult to find the right configuration of numerical settings and parameters in order to obtain accurate results. The results of the sensitivity analyses showed that the differences are larger in terms of crack pattern and capacity curves when changing certain numerical settings, whereas for the other two micro-models it stayed more or less the same (for example overlapping capacity curves). In summary, different application fields exists for all modeling approaches. The micro-models are necessary to give a better understanding about the local failure behavior in masonry, while the macro-model are better suited when a compromise between accuracy and efficiency is needed.

The numerical models were also found to corroborate the findings of the experimental tests, which showed that the bed-joint reinforcement technique has a potential to be an effective strengthening measure against seismic activity. The technique was assessed on different aspects. The force capacity and the ductility of a structure are the most important aspects for nonlinear seismic assessments. According to the experiment (Licciardello et al., 2021), the strengthening technique provided a modest increase in maximum base shear force. This was also observed from the numerical results in this research where the effect even reduces when the window opening in the wall is increased. On the other hand, a more ductile behavior and an

increased displacement capacity for the strengthened wall was observed in the experiment. This was due to the fact that the reinforcement bars were able to keep the sections of the wall together. An increase in ductility and displacement capacity of the wall is an important and desired effect because a higher ductility means that the structure is able to withstand large deformation, beyond the elastic limit, without a substantial loss in resistance. The ability to withstand large deformation means that you have more warning before total collapse of the structure and therefore more evacuation time is provided. However, the prediction of the ultimate displacement in the parametric study was not investigated (see recommendation of Section 7.2).

The previous numerical modeling studies for this specific experiment were mainly performed using the macro-model and the continuous micro-model. This could be due to the high modeling and computational demands that comes with the detailed micro-model. However, with this thesis research, another reason is found why the other models are preferred over the detailed micro-model. It has been shown that although the detailed micro-model is the most precise model to simulate the failure behavior of masonry, the model is not able to capture the behavior of the reinforcement bars in the strengthened wall. Besides the comparison study of the different numerical modeling approaches for the wall from the experiment, the other objective of this thesis research was to carry out a parametric study to extrapolate the experimental results to other configurations which are not experimentally tested. This is done to expand on the observations and results yielded in the previous studies. The performance of the bed-joint reinforcement technique was hereby investigated for different wall configurations.

7.2   Recommendations

The following recommendations for further research are formed based on the limitations within the scope of this thesis research:

1. One important aspect which was not numerically investigated in this thesis research, is the prediction of the ultimate displacement for the parametric study. The same prescribed displacement was used for both un-strengthened and strengthened configurations in order to compare the crack pattern and the increment in force capacity. The loading in the experiment was stopped when an extensive amount of out-of-plane damage was observed. The same stopping criteria cannot be used for the numerical models since out-of-plane deformations cannot be captured with a 2D-model using plane stress elements. However, a stopping criteria such as a reduction of 20% of the maximum force capacity can be used for further research.

2. The bricks are kept linear elastic for the micro-models in this research. This means that cracks can only occur in the mortar joints and the possibility of crushing and cracking in the bricks are ignored. This assumption is made based on the fact that masonry walls usually fail along the mortar joints and also to improve the efficiency of the analyses. This approach remains valid up to the point where the bricks experience local failure, which was at the last cycle of the experiment for the strengthened wall. The compressive stresses in the bricks, at the bottom right corner of the wall, were lower compared to the compressive strength of bricks but larger compared to masonry as a composite material. A new research question could hereby formed whether the continuous micro-model is stronger than the macro-model in terms of compression due to the difference in material properties (composite material vs individual structural component).

3. Cracks were extended in both mortar joints and bricks at the bottom right corner of the wall during the last cycle of the experiment. Because using smeared cracking for the

bricks requires high computational expenses, another approach that could be investigated is to place discrete interface elements vertically in the middle of the brick (D'Altri et al., 2018). For this approach, the location of the crack in the brick is predefined.

4. The focus of this research was on the in-plane response of the walls for which plane stress elements are used in two-dimensional models. However, out- of -plane deformation in the strengthened wall was observed, not only at the base of the wall (arch mechanism) but also in both piers. This out-of-plane deformation was mainly caused by the asymmetric position of the reinforcement bars within the thickness of the wall. Further investigations can be done on the comparison between the one-sided and two-sided application of the reinforcement bars using three-dimensional models.

5. The accuracy of the numerical analyses were validated based on limited cases of wall specimens from the experiment. As mentioned before, small differences in crack pattern was observed between un-strengthened wall specimens with the same geometry, material properties, loading and boundary conditions due to imperfections. On the other hand, only one wall specimen for the strengthened case was available to use as a benchmark for the validation of the numerical models. Diagonal stair-case cracks were observed in the experiment due to the inclusion of pre-damage. The validations of accuracy of the numerical models could be improved when more experiments are available.

6. The scope of this thesis is the numerical modeling of the full scale wall from the experiment. The wall is a structural component of a building. As mentioned before, in case a large scale structure with multiple floors and walls needs to be modeled, the micro-models are simply not efficient because of the large modeling and computational demands. The macro-model is therefore a more suited model to capture the global behavior of the structure. Another approach for extending the analyses from this research to buildings is to use *equivalent frame models*, where the structural elements such as the piers and spandrels are represented with beam elements which are connected to each other using rigid nodes. In this case the force-displacement curve of the structural elements are used as the constitutive law for the beam elements.

BIBLIOGRAPHY

Alejo, L., Mendes, N., & Lourenco, P. (2017). THE EFFECT OF MORPHOLOGY ON THE STRUCTURAL BEHAVIOUR OF MASONRY WALLS. Espana: Congreso de Metodos Numericos en Ingenieria.

Beardmore, R. (2012). *Masonry*. Récupéré sur Roymech: https://roymech.org/Related/Construction/Masonry.html

Buza, J. (1993). Builder 3 & 2, Volume 1. NAVEDTRA 14043.

Calderini, C., Cattari, S., & Lagomarsino, S. (2009). In-plane strength of unreinforced masonry piers. Earthquake engineering & structural dynamics, 38(2), 243-267.

Campbell, J., & Duran, M. (2017). Numerical model for nonlinear analysis of masonry walls.

Corradi, M., Speranzini, E., & Bisciotti, G. (2020). Out-of-plane reinforcement of masonry walls using joint-embedded steel cables. Bulletin of Earthquake Engineering 18: 4755-4782.

D'Altri, A. M., Miranda, S. d., Castellazzi, G., & Sarhosis, V. (2018, August 15). A 3D Detailed Micro-Modelling Approach for the In-Plane and Out-Of-Plane Analysis of Masonry Structures. Computers & Structures volume 206: 18-30.

D'Ayala, D., & Speranza, E. (2003). Definition of collapse mechanisms and seismic vulnerability of historic masonry buildings. Earthquake Spectra 19(3): 479-509.

Drougkas, A., Licciardello, L., Rots, J. G., & Esposito, R. (2020). Experimental and numerical study of historic masonry with bed-joint reinforced repoiting. EURODYN 2020: XI International Conference on Structural Dynamics. European Association for Structural Dynamics (EASD).

Drougkas, A., Licciardello, L., Rots, J. G., & Esposito, R. (2020, May 11). In-plane seismic behaviour of retrofitted masonry walls subjected to subsidence-induced damage. Delft: Engineering Structures 223.

EN-1996-1-1. (2005). EN-1996-1-1. *Eurocode 6 design of masonry structures*.

EN-1998-1-1. (2004). Eurocode 8: Desgin of structures for earthquake resistance.

Erdogmus, E., Pulatsu, B., Lourenco, P. B., Lemos, J. V., & Hazzard, J. (2020, February 18). Discontinuum analysis of the fracture mechanism in masonry prisms and wallettes via discrete element method. Meccanica 55: 505-523.

Esposito, R. (2019). CIE5148 Lecture 9. *Modelling approaches for seismic analyses*. Delft University of Technology.

Esposito, R., & Ravenshorst, G. (2017). Quasi-static cyclic in-plane tests on masonry components 2016/ 2017. Delft University of Technology.

Esposito, R., Hendriks, M. A., & Rots, J. G. (2019). CIE5148 Lecture 4. *Introduction to nonlinear finite element analysis*. Delft University of Technology.

Esposito, R., Hendriks, M., & Rots, J. G. (2019). CIE5148 Lecture 8. *Reinforced concrete*. Delft University of Technology.

Esposito, R., Jafari, S., Ravenshorst, G., Schipper, R., & Rots, J. (2018, February 11-14). Influence of the behaviour of calcium silicate brick and element masonry on the lateral capacity of structures. Sydney, Australia: 10th Australasian Masonry Conference.

Esposito, R., Messali, F., & Rots, J. (2016, April 18). TESTS FOR THE CHARACTERIZATION OF REPLICATED MASONRY AND WALL TIES. Delft University of Technology.

Esposito, R., Messali, F., Ravenshorst, G. J., Schipper, H. R., & Rots, J. G. (2019). Seismic assessment of a lab-tested two-storey unreinforced masonry Dutch terraced house. Bulletin of Earthquake Engineering 17: 4601–4623.

FEMA. (1998). FEMA 306, EVALUATION OF EARTHQUAKE DAMAGED CONCRETE AND MASONRY WALL BUILDINGS, Basic Procedures Manual. Applied Technology Council (ATC-43 Project).

Ferreira, D. (2021). User's manual-release 10.5. DIANA FEA B.V. Récupéré sur dianafea: https://dianafea.com/manuals/d105/Diana.html

Green, R. A., Bommer, J. J., Stafford, P. J., Maurer, B. W., Kruiver, P. P., Edwards, B., . . . Elk, J. v. (2020). Liquefaction Hazard in the Groningen Region of the Netherlands due to Induced Seismicity. Journal of Geotechnical and Geoenvironmental Engineering Vol. 146, Issue 8.

Hendriks, M., Rots, J., & Esposito, R. (2019). CIE5148 Lecture 4. *Introduction to NLFEA*. Delft University of Technology.

Hendriks, M., Rots, J., & Esposito, R. (2019). CIE5148 Lecture 6. *Discrete cracking v01*. Delft University of Technology.

Hendriks, M., Rots, J., & Esposito, R. (2019). CIE5148 Lecture 7 . *Smeared cracking v01*. Delft University of Technology.

Jafari, S., Rots, J. G., Esposito, R., & Messali, F. (2017). Characterizing the material properties of Dutch unreinforced masonry. Procedia Engineering 193: 250 – 257.

Khan, H. A., Nanda, R. P., & Das, D. (2017). In-plane strength of masonry panel strengthened with geosynthetic. Construction and Building Materials 156: 351-361.

Korswagen, P. A., Longo, M., & Rots, J. G. (2020). Calcium silicate against clay brick masonry: an experimental comparison of the in-plane behaviour during light damage. Bulletin of Earthquake Engineering.

Korswagen, P. A., Longo, M., Meulman, E., & Rots, J. G. (2019). Crack initiation and propagation in unreinforced masonsy specimens subjected to repeated in-plane loading during light damage. Bulletin of Earhquake Engineering.

Korswagen, P., Longo, M., & Meulman, E. (2019, December 1). Damage sensitivity of Groningen masonry structures - Experimental and computational studies - Stream 2 - Part 1. Report number C31B69WP0-14, Report, version 2.0.

Lecture, P. p. (2008). *Slideplayer*. Récupéré sur https://slideplayer.com/slide/5330292/

Licciardello, L., Rots, J., & Esposito, R. (2021). Performance of unreinforced masonry strengthened with bed joint reinforced repointing. 12th International Conference on

Structural Analysis of Historical Constructions: SAHC 2021, Online event, 29 Sep - 1 Oct, 2021 (pp. 2652-.

Liu, Z., & Crewe, A. (2020). Effects of size and position of openings on in-plane capacity of unreinforced masonry walls. Bulletin of Earthquake Engineering, 18(10), 4783-4812.

Lourenco, P. B. (1996). Computational Strategy for Masonry Structures. Delft University Press.

LS-DYNAsupport. (2021). *What are the differeces between implicit and explicit?* Récupéré sur https://www.dynasupport.com/faq/general/what-are-the-differences-between-implicit-and-explicit

Mahmoudimotlagh, S. (2020). Numerical Modeling of the In-Plane Seismic Behavior of Unreinforced Masonry Wall Retrofitted with Bed Joint Reinforcements. Delft University of Technology: MSc thesis.

Miglietta, M., Damiani, N., Grottoli, L., Guerrini, G., & Graziotti, F. (2019). Shake-table investigation of a timber retrofit solution for unreinforced masonry. Italy: XVIII ANIDIS ConferenceAt: Ascoli Piceno.

Mishra, G. (2021). *Compressive strength test on bricks*. Récupéré sur https://theconstructor.org/practical-guide/compressive-strength-test-on-brick/2790/

Nagendran, L. (2020). *Quora*. Récupéré sur https://www.quora.com/What-are-the-characteristics-of-shape-function

NAM. (2013). Technical Addendum to the Winningsplan Groningen 2013. *Subsidence, Induced Earthquake and Seismic Hazard Analysis in the Groningen Field*. Assen: NAM Nederlandse Aardolie Maatschappij B.V.

NLOG. (2016). *Groningen gasfield*. Récupéré sur https://www.nlog.nl/en/groningen-gasfield

Pulatsu, B., Ece Erdogmus, P. B., Lemos, J. V., & Tuncay, K. (2020). Simulation of the in-plane structural behavior of unreinforced masonry walls and buildings using DEM. Structures 27.

Rots, J. G., Messali, F., Esposito, R., Jafari, S., & Mariani, V. (2016). Computational modelling of masonry with a view to Groningen induced seismicity. 10th International Conference on Structural Analysis of Historical Constructions.

Rots, J. G. (1997). Structural masonry: an experimental/numerical basis for practical design rules. CRC Press.

Schreppers, G., Garofano, A., Messali, F., & Rots, J. (2017, Feb 15). DIANA Validation report for Masonry modelling. *TU Delft Structural Mechanics CiTG report CM-2016-17*. DIANA FEA BV and TU Delft.

Xu, T. (2018). *Modeling the seismic response of a two-storey calcium silicate brick masonry structure with nonlinear pushover and time-history analyses.* Delft University of Technology: MSc thesis.

APPENDICES

A
Results macro-model
(Un-strengthened wall)

Appendix A is meant as a supplement to Chapter 4.1 and provides additional information and results for the analyses of the macro-model (un-strengthened wall). The results of the crack pattern are shown using the contour plots of the principal strain E_1. The scaling factor of these contour plots are set to a value of 100. The numerical settings and parameters for the monotonic analysis (base model) are listed in *Table A 1*. The cross-sectional properties per structural component are listed in *Table A 2*. The properties of the FE-types and mesh for the base model and the model using quadratic elements are listed in *Table A 3*. The contour plots for showing the evolution of the crack pattern (base model) are presented in Section A.1. Moreover, the results of the sensitivity analysis are presented and discussed in Section A.2.
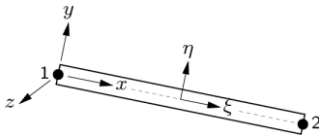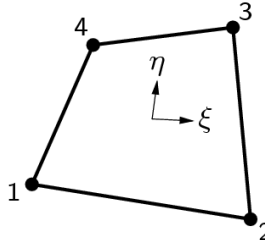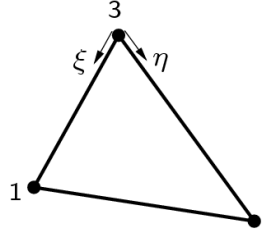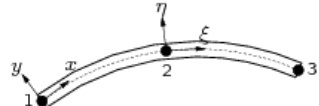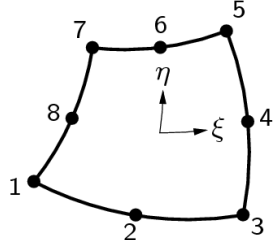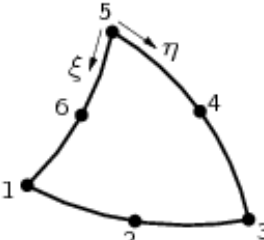
Table A 1: Numerical settings and parameters for macro-model (base model)

	Self-weight	**Overburden**	**Pushover**
Load steps	1	1	0.01(193) -0.01(391)
Max. number of iterations	10	10	100
Iteration method	Regular Newton-Raphson	Regular Newton-Raphson	Regular Newton-Raphson
Convergence norms and tolerances	Displacement (0.05) Force (0.05)	Displacement (0.05) Force (0.05)	Displacement (0.05) Force (0.05)
Satisfy all specified norms	No	No	No
Line search	Yes	Yes	Yes
Source of nonlinearity	Physical nonlinearity	Physical nonlinearity	Physical nonlinearity

Table A 2: Cross-sectional properties per element

|			Masonry wall	Concrete lintel	HEB300 (bottom steel beam)	HEB600 (top steel beam)
Thickness	t	mm	100	100	-	-
Shape			-	-	I-shape	I-shape
Height	h	mm	-	-	300	600
Width of the top flange	b_1	mm	-	-	300	300
Width of the bottom flange	b_2	mm	-	-	300	300
Thickness of top flange	t_1	mm	-	-	19	30
Thickness of bottom flange	t_2	mm	-	-	19	30
Thickness of web	t_3	mm	-	-	11	15.5

Table A 3: Characteristics FE- types for macro-model (Ferreira, 2021)

	Model using linear elements (base model)			Model using quadratic elements		
	Steel beams	Masonry wall and concrete lintel	Masonry wall	Steel beams	Masonry wall and concrete lintel	Masonry wall
Finite element type	L6BEA 2-noded Class III-beam elements	Q8MEM 4-noded plane stress elements	T6MEM 3-noded plane stress elements	CL9BE 3-noded Class III-beam elements	CQ16M 8-noded plane stress elements	CT12M 6-noded plane stress elements
Degrees of freedom per node	u_x, u_y, ϕ_z	u_x, u_y	u_x, u_y	u_x, u_y, ϕ_z	u_x, u_y	u_x, u_y
Interpolation scheme	Linear	Linear	Linear	Quadratic	Quadratic	Quadratic
Integration scheme	1-point Gauss	2 x 2	1-point	2-point Gauss	2 x 2	3-point
Shape dimension	1D	2D	2D	2D	2D	2D
Topological dimension	1D	2D	2D	1D	2D	2D
Stress components	σ_{xx}, σ_{xy}	$\sigma_{xx}, \sigma_{yy}, \sigma_{xy}$	$\sigma_{xx}, \sigma_{yy}, \sigma_{xy}$	σ_{xx}, σ_{xy}	$\sigma_{xx}, \sigma_{yy}, \sigma_{xy}$	$\sigma_{xx}, \sigma_{yy}, \sigma_{xy}$
Inclusion of shear deformations	Yes	Yes	Yes	Yes	Yes	Yes
Average element size [mm]	50	50 x 50	-	50	50 x 50	-
Total number of elements	122	2814	-	122	2814	-
Total number of nodes	2975			8764		

A.1) Evolution crack pattern monotonic analysis for macro-model (un-strengthened wall)

(base model)
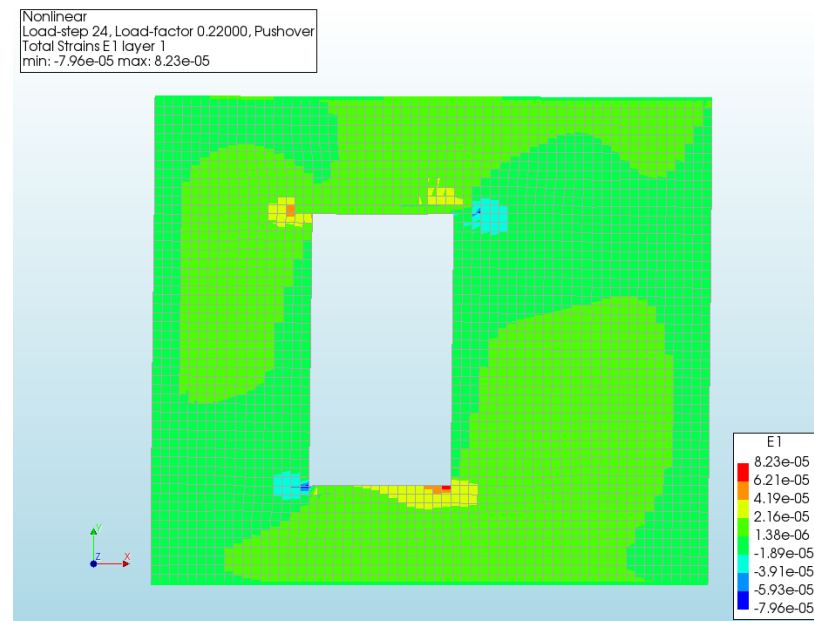
(a) Initiation cracking at the window corners in positive x-direction
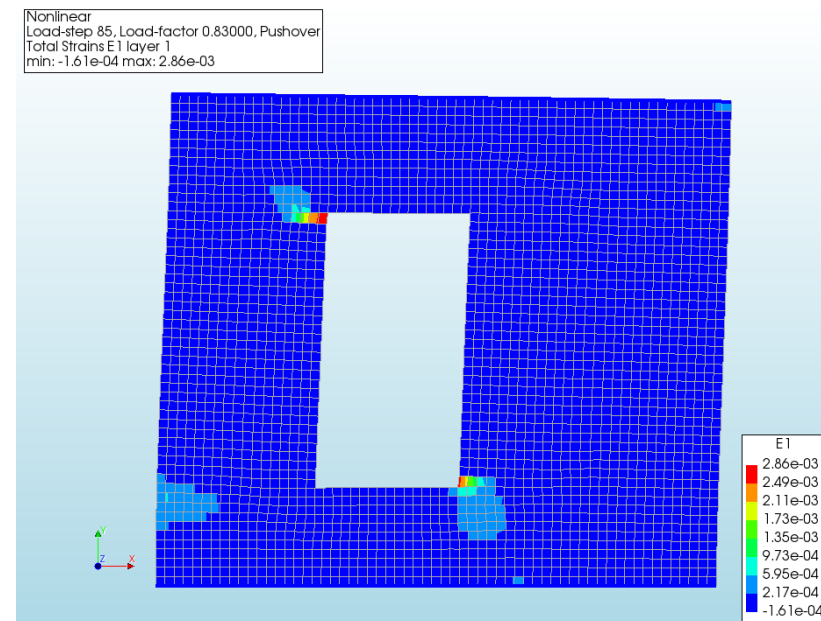
(b) Initiation cracking at the base of the left pier in positive x-direction
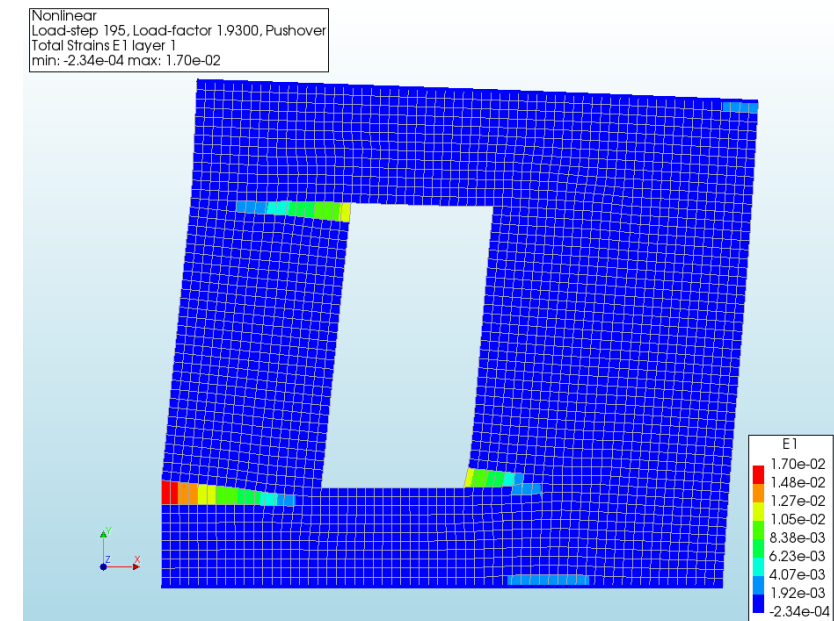
(c) Max top lateral deflection +1.93 mm
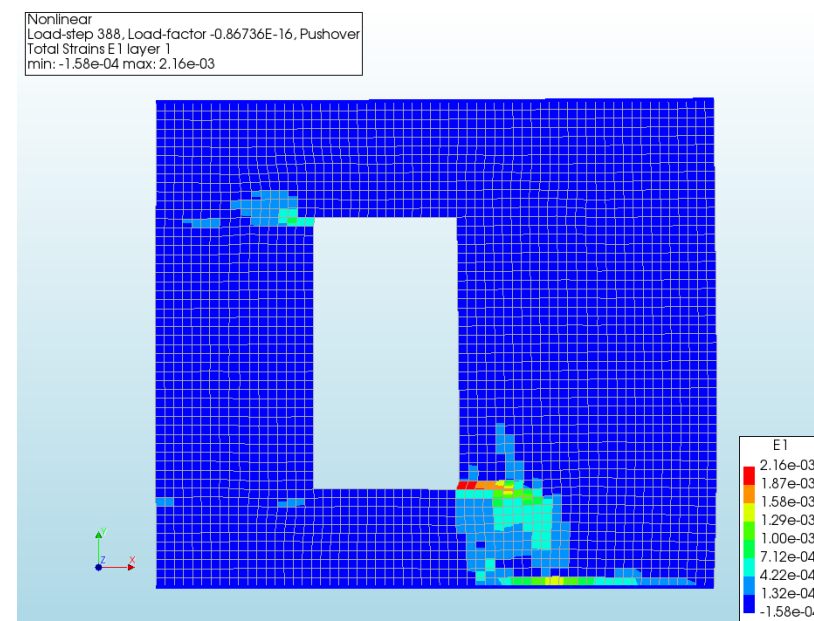
(d) Zero position
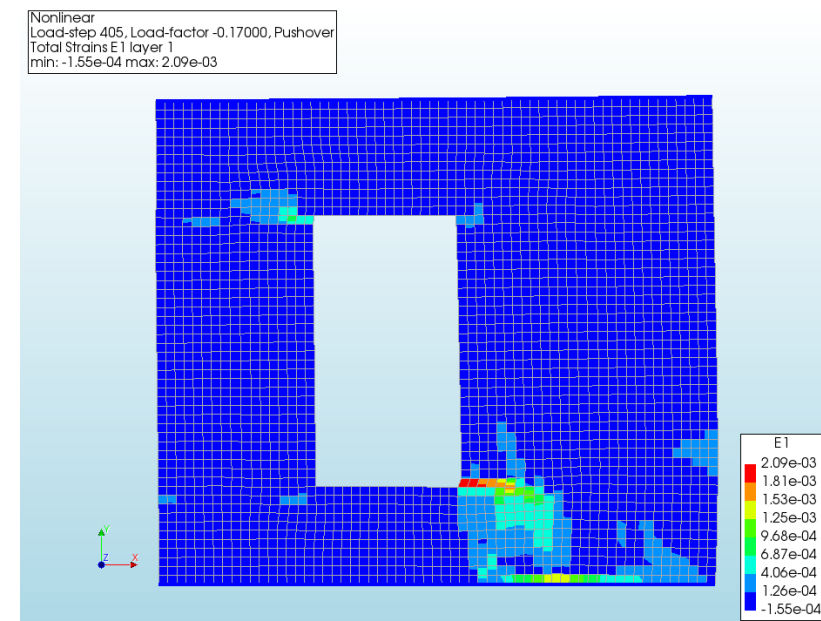
(e) Initiation cracking at base of the right pier in negative x-direction
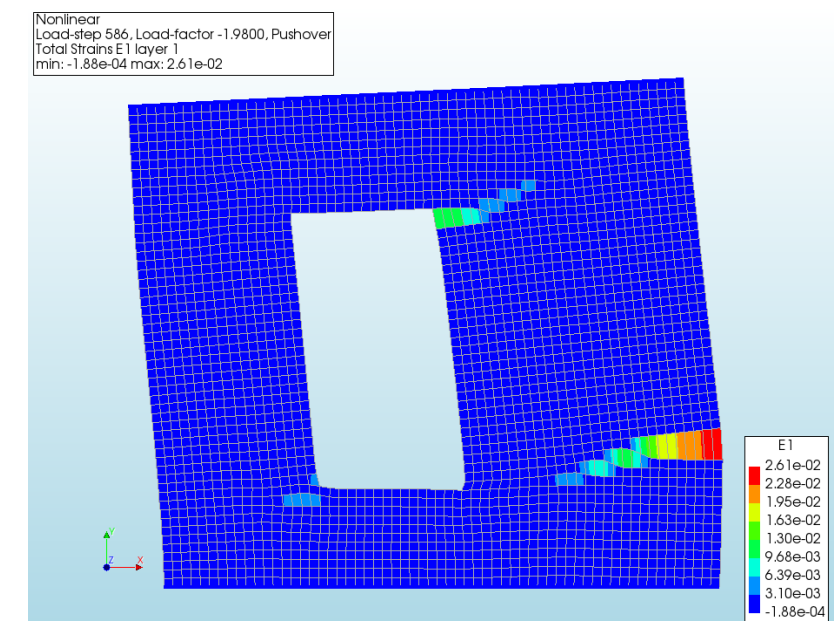
(f) Max top lateral deflection -1.98 mm

Figure A 1: Evolution crack pattern monotonic loading macro-model (un-strengthened wall) using contour plots principal strain E1 (scaling factor = 100)

A.2) Results sensitivity analysis macro-model (un-strengthened wall)

The results of the sensitivity analysis for the macro-model (un-strengthened wall) are presented in this section. The results of the contour plots, showing the cracking patterns and the capacity curves are discussed for each numerical parameter separately in the following:

1. **_Effect of the mesh size_**: It can be observed from crack pattern in the contour plots (*Figure A 2*) that the results do not improve when refining the mesh size. Important to note is that when changing the mesh size to 25 mm or 100 mm, triangular elements are included in the FE-mesh, making the cracks not propagating perfectly horizontal. Moreover, a large diagonal crack in the right pier start to develop at the end of the loading in the positive x-direction when using a mesh size of 25 mm. This explains the sudden drops in the capacity curve (*Figure A 7a*).

2. **_Effect of the element order_**: The crack pattern for the linear and quadratic elements (*Figure A 2*) are similar when looking at the positions of initiation of the cracks. However, the diagonal stair-case crack at the top right corner of the wall (loading in negative x-direction) is not simulated when using quadratic elements. Again, a large diagonal crack in the right pier start to develop at the end of the loading in the positive x-direction, which explains the sudden drop in the capacity curve (*Figure A 7b*). Furthermore, the energy dissipation is larger for the model using the quadratic elements.

3. **_Effect of the convergence tolerance and satisfaction of all specified norms_**: From the results of the contour plots (*Figure A 3*), it can be observed that the results do not improve with a convergence criterion which is set more tight. On the other hand, when the criterion is set to loose, the diagonal stair-case crack at the top right corner of the window opening is propagating more in horizontal direction. Moreover, the results are in a better agreement with the experiment when not all specified norms are satisfied. The differences can also be observed in the capacity curves (*Figure A 7c and d*)

4. **_Effect of the load-step size and different iterative method_**: The crack patterns (*Figure A 4*) and capacity curves (*Figure A 7f*) are very similar when using different load steps. The results for the Regular Newton-Raphson and the Modified Newton-Raphson are also very similar in terms of the crack patterns and the capacity curves. However, the results of the Secant (Quasi-Newton) method are not accurate.

5. **_Effect of the different sources of nonlinearity_**: The results of the crack patterns (*Figure A 4*) are similar when loading in the positive x-direction. However, the diagonal stair-case crack at the top right corner of the window opening (loading in the negative x-direction) is propagating more in the horizontal direction when the geometric nonlinearity is included for the analysis. Furthermore, the capacity curves are very similar (*Figure A 7e*).

6. **_Different options for the "Head-joint failure type"_**: The diagonal stair-case cracks at the corners of the opening are only captured with the option *"Diagonal stair-case cracks"* (see *Figure A 6*). On the other hand, it is the only option which does not capture the flexural crack at the right base of the wall (loading in negative x-direction). Finally, the capacity curves are similar for all different head-joint failure type options (*Figure A 7h*).

Results sensitivity analysis for macro-model (un-strengthened wall)
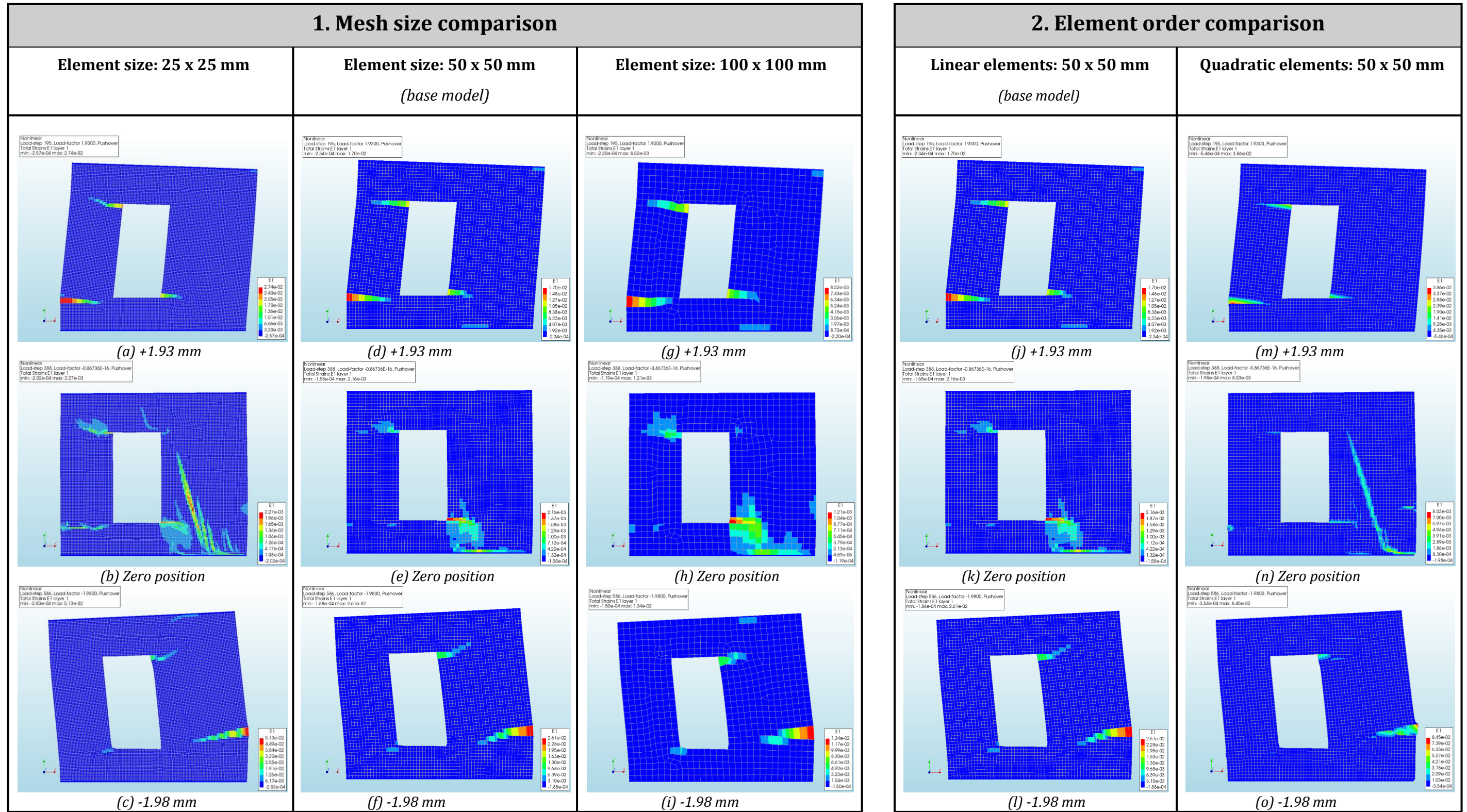
Figure A 2: Effect of the mesh size and element order comparison for macro-model (un-strengthened wall) using contour plots principal strain E1 (scaling factor = 100)

Results sensitivity analysis for macro-model (un-strengthened wall)

3. Convergence tolerance comparison			4. Satisfy all specified norms	
Displacement (0.01) Force (0.01)	**Displacement (0.05) Force (0.05)** *(base model)*	**Displacement (0.1) Force (0.1)**	**Yes**	**No** *(base model)*

(a) +1.93 mm

(d) +1.93 mm

(g) +1.93 mm

(j) +1.93 mm

(m) +1.93 mm

(b) Zero position

(e) Zero position

(h) Zero position

(k) Zero position

(n) Zero position

(c) -1.98 mm

(f) -1.98 mm

(i) -1.98 mm

(l) -1.98 mm

(o) -1.98 mm

Figure A 3: Effect of the convergence tolerance and satisfactions to all specified norms comparison for macro-model (un-strengthened wall) using contour plots principal strain E1 (scaling factor = 100)

Results sensitivity analysis for macro-model (un-strengthened wall)

Figure A 4: Effect of the load-step size and source of nonlinearity comparison for macro-model (un-strengthened wall) using contour plots principal strain E1 (scaling factor = 100)

Results sensitivity analysis for macro-model (un-strengthened wall)

Figure A 5: Effect of different iterative method comparison for macro-model (un-strengthened wall) using contour plots principal strain E1 (scaling factor = 100)

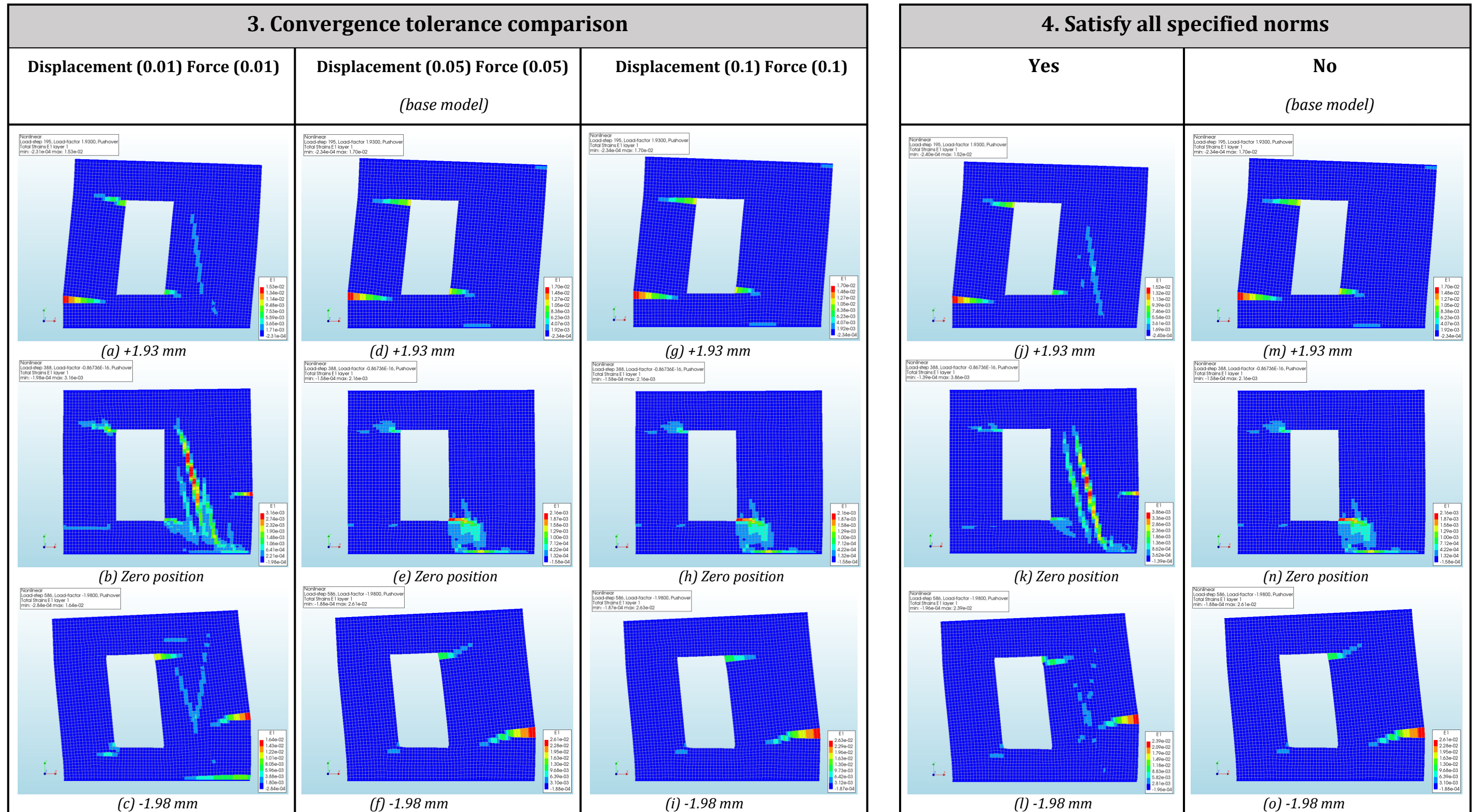# Results sensitivity analysis for macro-model (un-strengthened wall)

8. Head-joint failure type			
Head- joints failure not considered	*Direct input head-joint tensile strength*	*Diagonal stair-case cracks (base model)*	*Tensile strength head-joint defined by friction*

(a) +1.93 mm

(d) +1.93 mm

(g) +1.93 mm

(j) +1.93 mm

(b) Zero position

(e) Zero position

(h) Zero position

(k) Zero position

(c) -1.98 mm

(f) -1.98 mm

(i) -1.98 mm

(l) -1.98 mm

Figure A 6: Different options for "head-joint failure type" comparison for macro-model (un-strengthened wall) using contour plots principal strain E1 (scaling factor = 100)

167

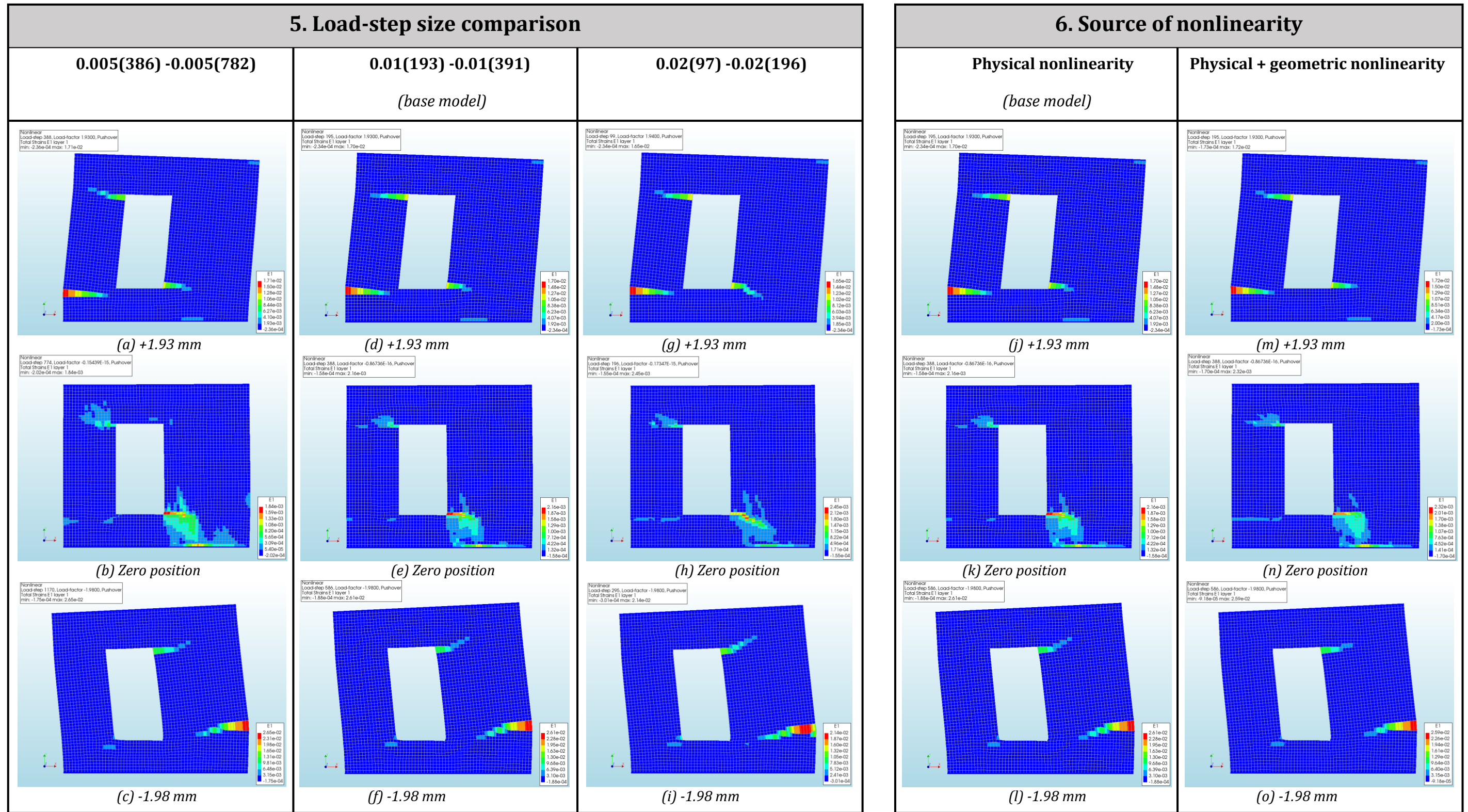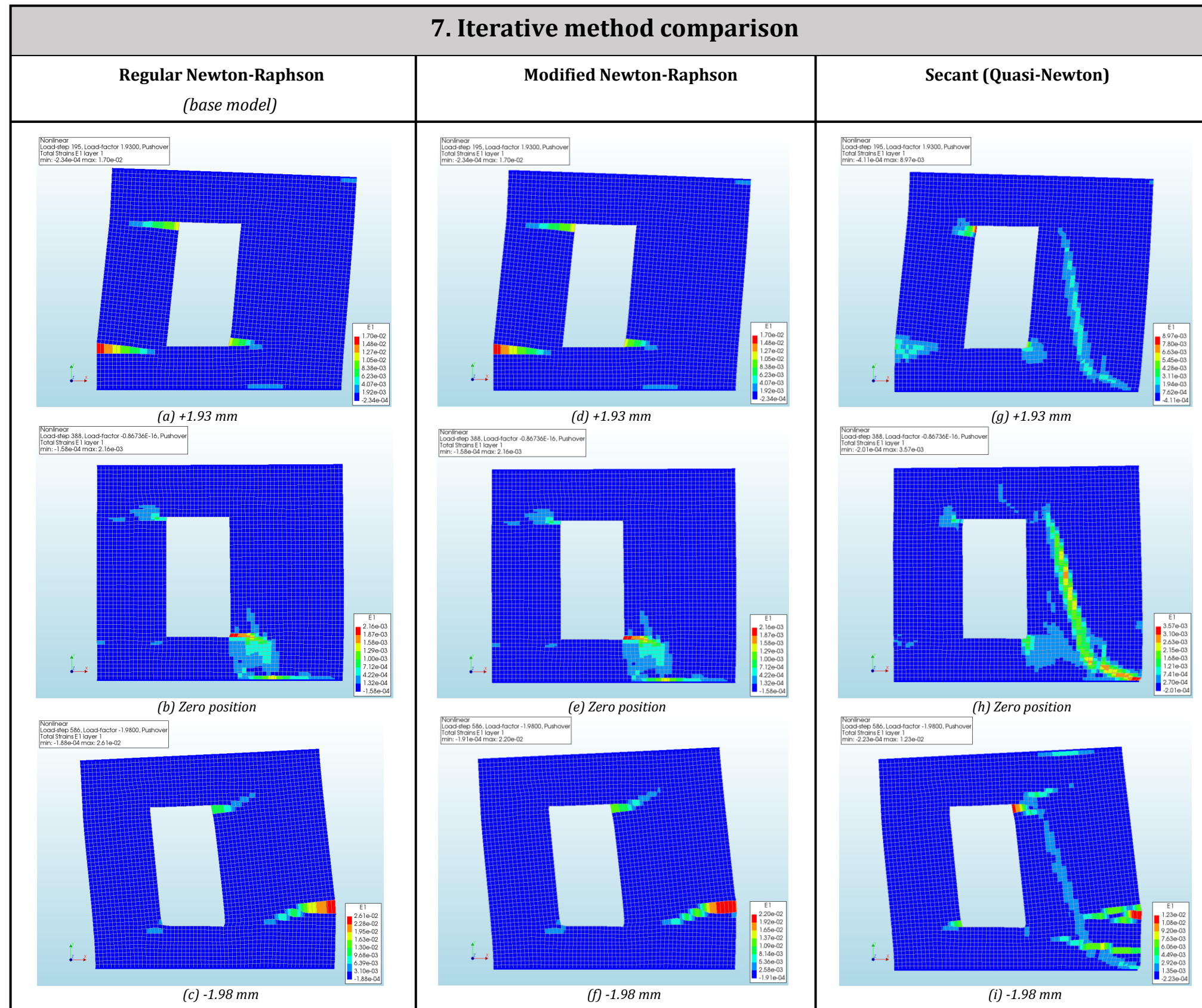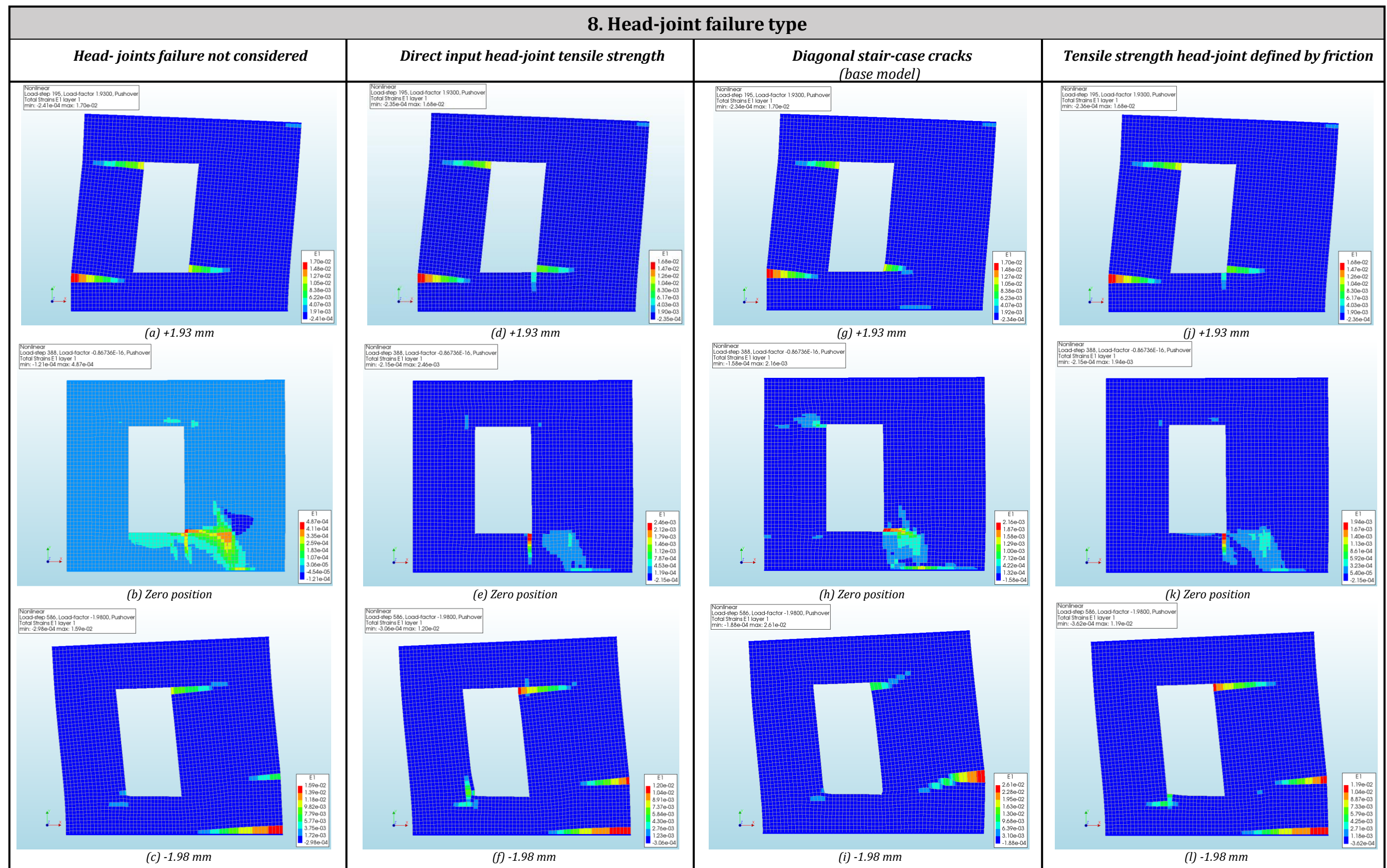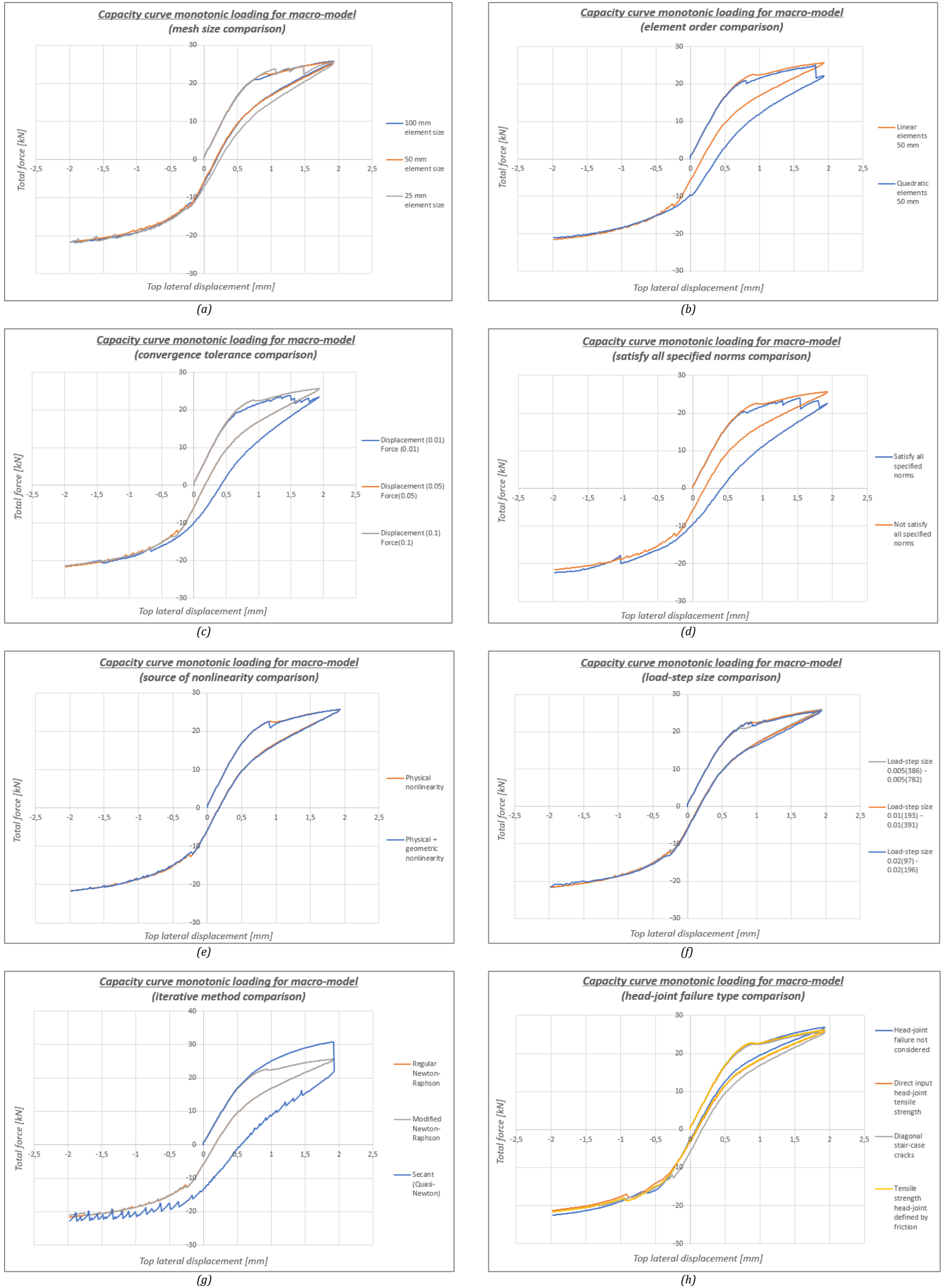# Results sensitivity analysis for macro-model (un-strengthened wall)

Figure A 7: Capacity curves comparison macro-model (un-strengthened wall)

B

Results continuous micro-model
(Un-strengthened wall)

Appendix B is meant as a supplement to Chapter 4.2 and provides additional information and results for the analyses of the continuous micro-model (un-strengthened wall). The results of the crack pattern are shown using the contour plots of the principal strain E_1. The scaling factor of these contour plots are set to a value of 100. The numerical settings and parameters for the monotonic analysis (base model) are listed in *Table B 1*. The properties of the FE mesh for the base model and the model using quadratic elements are listed in *Table B 2*. The material properties for the mortar joints using the *Engineering Masonry model (EMM)* are listed in *Table B 3*. The contour plots for showing the evolution of the crack pattern (base model) are presented in Section B.1. Moreover, the results of the sensitivity analysis are presented and discussed in Section B.2. The sensitivity analysis is conducted for the continuous micro-model using the *Total Strain Crack model (TSCM)* for the mortar joints

Table B 1: Numerical settings and parameters for continuous micro-model (base model)

	Self-weight	**Overburden**	**Pushover**
Load steps	1	1	0.04(48) -0.04(98)
Max. number of iterations	10	10	100
Iteration method	Regular Newton-Raphson	Regular Newton-Raphson	Regular Newton-Raphson
Convergence norms and tolerances	Displacement (0.01) Force (0.01)	Displacement (0.01) Force (0.01)	Displacement (0.01) Force (0.01)
Satisfy all specified norms	Yes	Yes	Yes
Line search	Yes	Yes	Yes
Source of nonlinearity	Physical nonlinearity	Physical nonlinearity	Physical nonlinearity

Table B 2: Properties mesh continuous micro-model

	Model using linear elements		Model using quadratic elements	
	Steel beams	**Masonry bricks/ mortar joints**	**Steel beams**	**Masonry bricks/ mortar joints**
Finite element type	L6BEA 2-noded Class III-beam elements	Q8MEM 4-noded plane stress elements	CL9BE 3-noded Class III-beam elements	CQ16M 8-noded plane stress elements
Average element size [mm]	10	10 x 10	10	10 x 10
Total number of elements	614	70805	614	70805
Total number of nodes	71610		214025	

Table B 3: Material properties continuous micro-model using EMM for mortar joints (analysis for the Damage Limitation state)

Material properties continuous micro-model using EMM for mortar joints				
Material class			Concrete and masonry	
Material model			Engineering Masonry Model	
Elasticity parameters				
			Bed-joints	**Head-joints**
Young's modulus	E_x	N/mm^2	1000	50
	E_y	N/mm^2	1000	50
Shear modulus	G_{xy}	N/mm^2	439	22
Mass density	ρ	kg/m^3	1708	1708
Cracking parameters				
Head-joint failure type			Direct input head-joint tensile strength	Diagonal stair-case cracks
Tensile strength	bed-joints	f_t N/mm^2	0.09	0.05
	head-joints	f_t N/mm^2	0.09	0.05
Fracture energy in tension	G_f^I	N/mm	0.00753	0.00499
Angle between stepped diagonal crack and bed-joint	α	rad	-	0.5
Crushing parameters				
Compressive strength	f_c	N/mm^2	3.81	3.81
Fracture energy in compression	G_c	N/mm	6.4	6.4
Factor to strain at compressive strength	n	-	4	4
Unloading factor, 1= secant, 0= linear	λ	-	1	1
Shear failure parameters				
Friction angle	φ	rad	0.6686	0.6686
Cohesion	c	N/mm^2	0.13	0.13
Fracture energy in shear	$G_{v,i}$	N/mm	0.3	0.3
Crack bandwidth				
Crack bandwidth specification			Rots	Rots
Crack bandwidth	h	mm	14.14	14.14

B.1) Evolution crack pattern monotonic analysis for continuous micro-model using TSCM (un-strengthened wall)

(base model)

(a) Initiation cracking at corners

(b) Initiation crack at base left pier

(c) Peak load in positive x-direction

(d) Max top lateral deflection +1.93 mm

(e) Zero position

(f) Initiation cracking at right base

(g) Peak load in negative x-direction
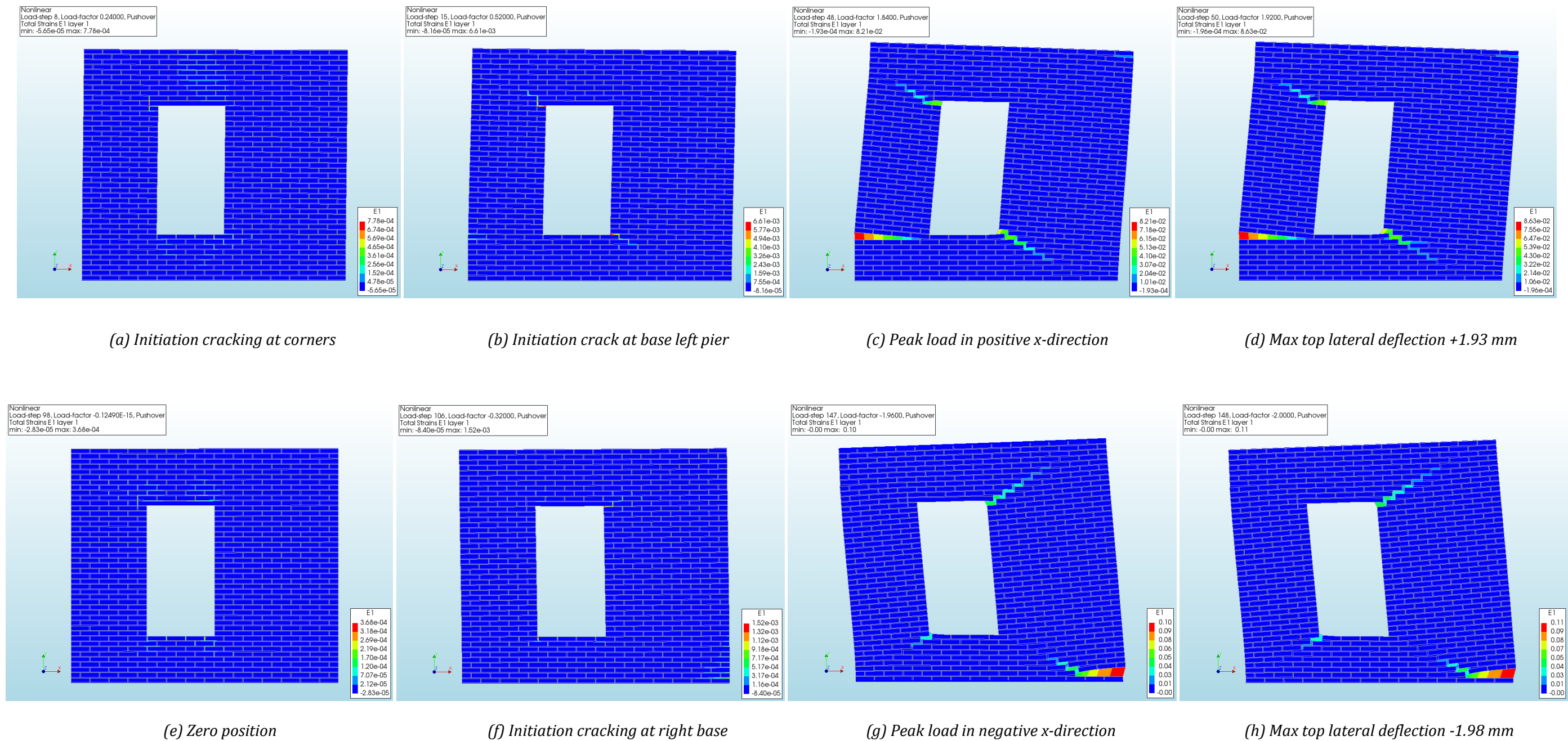
(h) Max top lateral deflection -1.98 mm

Figure B 1: Evolution crack pattern monotonic loading continuous micro-model (un-strengthened wall) using contour plots principal strain E1 (scaling factor = 100)

B.2) Results sensitivity analysis continuous micro-model (un-strengthened wall)

The results of the sensitivity analysis for the continuous micro-model (un-strengthened wall) using the TSCM for the mortar joints are presented in this section. The results of the contour plots, showing the cracking patterns and the capacity curves are discussed for each numerical parameter separately in the following:

1. ***Effect of the mesh size***: The computational time increases significantly when decreasing the mesh size to 10 mm. It is important to note that the diagonal stair-case cracks at the corners of the opening is only well captured when using a mesh size of 10 mm (*Figure B 2*). This can be explained by the fact that the elements are perfectly aligned with the thickness of the mortar joints. When choosing a mesh size which is not in line with the thickness of the mortar joints, the cracks at the corners of the opening are propagating more in the horizontal direction along the bed-joints. Furthermore, the capacity curves (*Figure B 7a*) are similar for the three options where a mesh size of 10 mm is showing relatively the largest difference in maximum base shear forces compared to the experiment.

2. ***Effect of the element order***: The computational time increases significantly when changing to quadratic elements. Moreover, the diagonal stair-case cracks at the corners of the opening are not well captured when loading in the negative x-direction (*Figure B 2*). However, the capacity curves are very similar for both element orders (*Figure B 7b*).

3. ***Effect of the convergence tolerance and the satisfaction of all specified norms***: When using a tighter convergence criterion, the diagonal stair-case crack at the top left corner of the opening start to develop horizontally along the bed-joint (loading in the positive x-direction), resulting in a rocking failure behavior of the left pier (*Figure B 4*). This crack pattern is also captured when not all specified norms are satisfied (*Figure B 5*). On the other hand, the capacity curves are similar for all options (*Figure B 7c* and *Figure B 7d*).

4. ***Effect of the load-step size and different iterative method***: The same crack pattern for the rocking failure behavior of the left pier can be observed when using smaller load-step sizes (*Figure B 3*). The crack pattern for the Regular and Modified Newton-Raphson are very similar. Only the Secant (Quasi-Newton) method is simulating the crack pattern for the rocking failure behavior of the left pier (*Figure B 5*). Again, the results for the capacity curves are very similar for all options (*Figure B 7f* and *Figure B 7g*).

5. ***Effect of the source of nonlinearity***: The results for the crack pattern (*Figure B 3*) and capacity curve (*Figure B 7e*) are very similar when using both physical and geometric nonlinearity or only physical nonlinearity.

6. ***Effect of different material input parameters:*** Different combinations of Young's modulus for the bed-and head-joints are assigned to investigate the effects on the results. The results for the crack pattern are very similar (*Figure B 6*). Furthermore, different combinations of mortar tensile strengths for the bed-and head-joints are compared to each other. The same rocking failure behavior of the left pier is simulated when using the same tensile strength for the bed-and head-joints. Furthermore, the results for the capacity curve are similar when comparing all options (*Figure B 7h*).

Results sensitivity analysis for continuous micro-model using TSCM (un-strengthened wall)
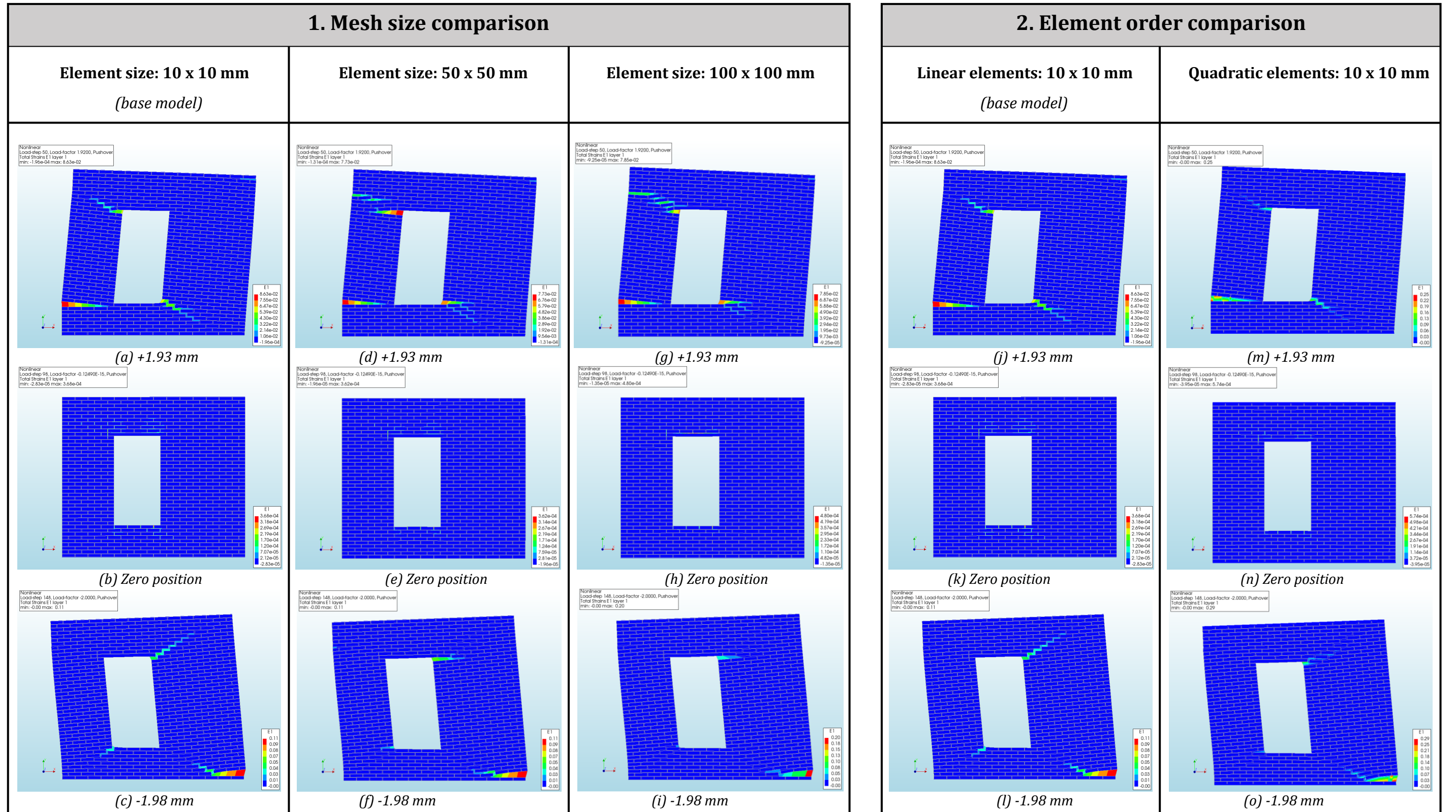

Figure B 2: Effect of the mesh size and element order comparison for continuous micro-model (un-strengthened wall) using contour plots principal strain E1 (scaling factor = 100)

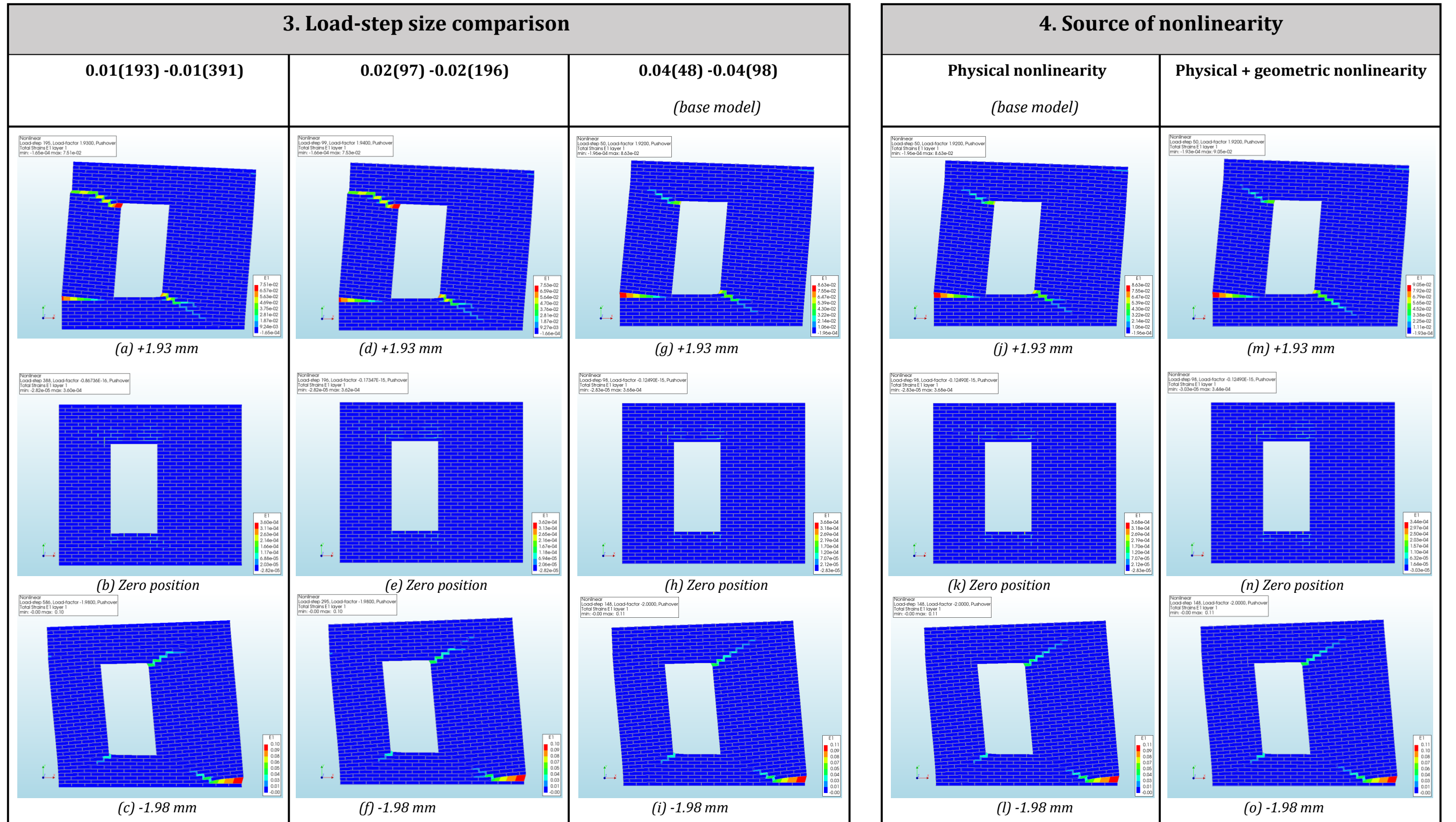# Results sensitivity analysis for continuous micro-model using TSCM (un-strengthened wall)

3. Load-step size comparison			4. Source of nonlinearity	
0.01(193) -0.01(391)	**0.02(97) -0.02(196)**	**0.04(48) -0.04(98)** *(base model)*	**Physical nonlinearity** *(base model)*	**Physical + geometric nonlinearity**

Figure B 3: Effect of the load-step size and source of nonlinearity comparison for continuous micro-model (un-strengthened wall) using contour plots principal strain E1 (scaling factor = 100)

174

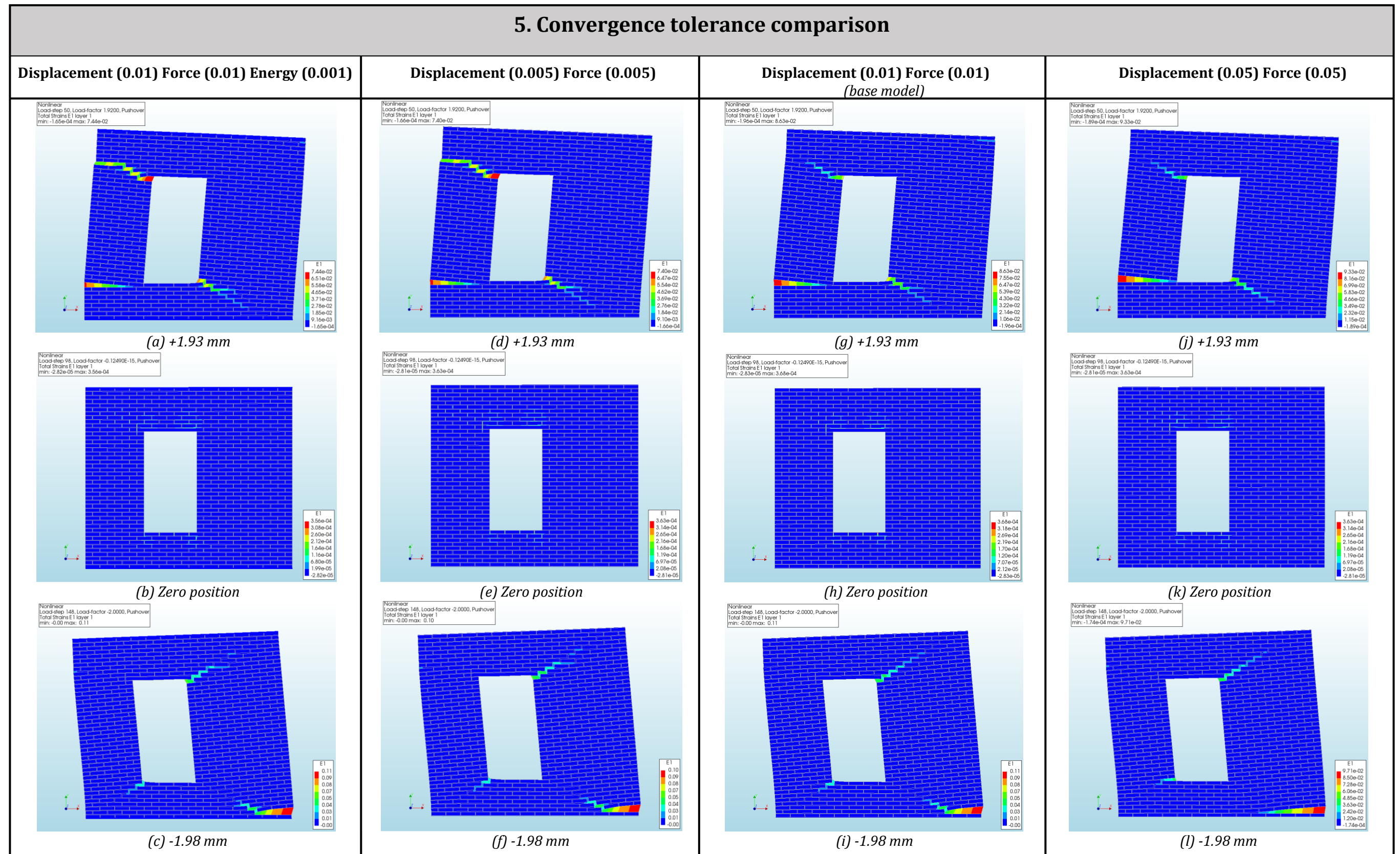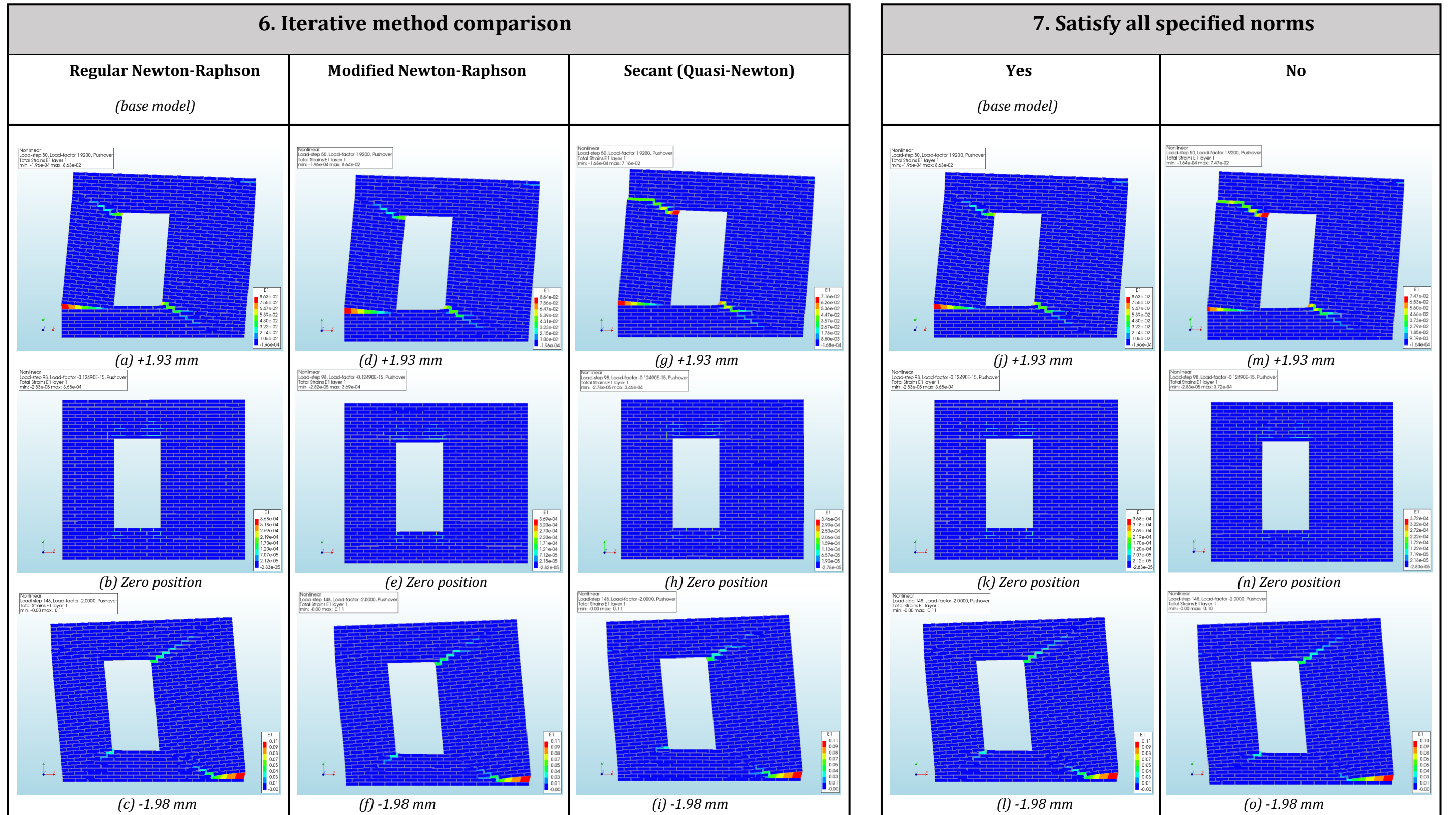# Results sensitivity analysis for continuous micro-model using TSCM (un-strengthened wall)

Figure B 4: *Effect of the convergence tolerance comparison for continuous micro-model (un-strengthened wall) using contour plots principal strain E1 (scaling factor = 100)*

175

Results sensitivity analysis for continuous micro-model using TSCM (un-strengthened wall)

Figure B 5: Effect of different iterative method and satisfactions to all specified norms comparison for continuous micro-model (un-strengthened wall) using contour plots principal strain E1 (scaling factor = 100)

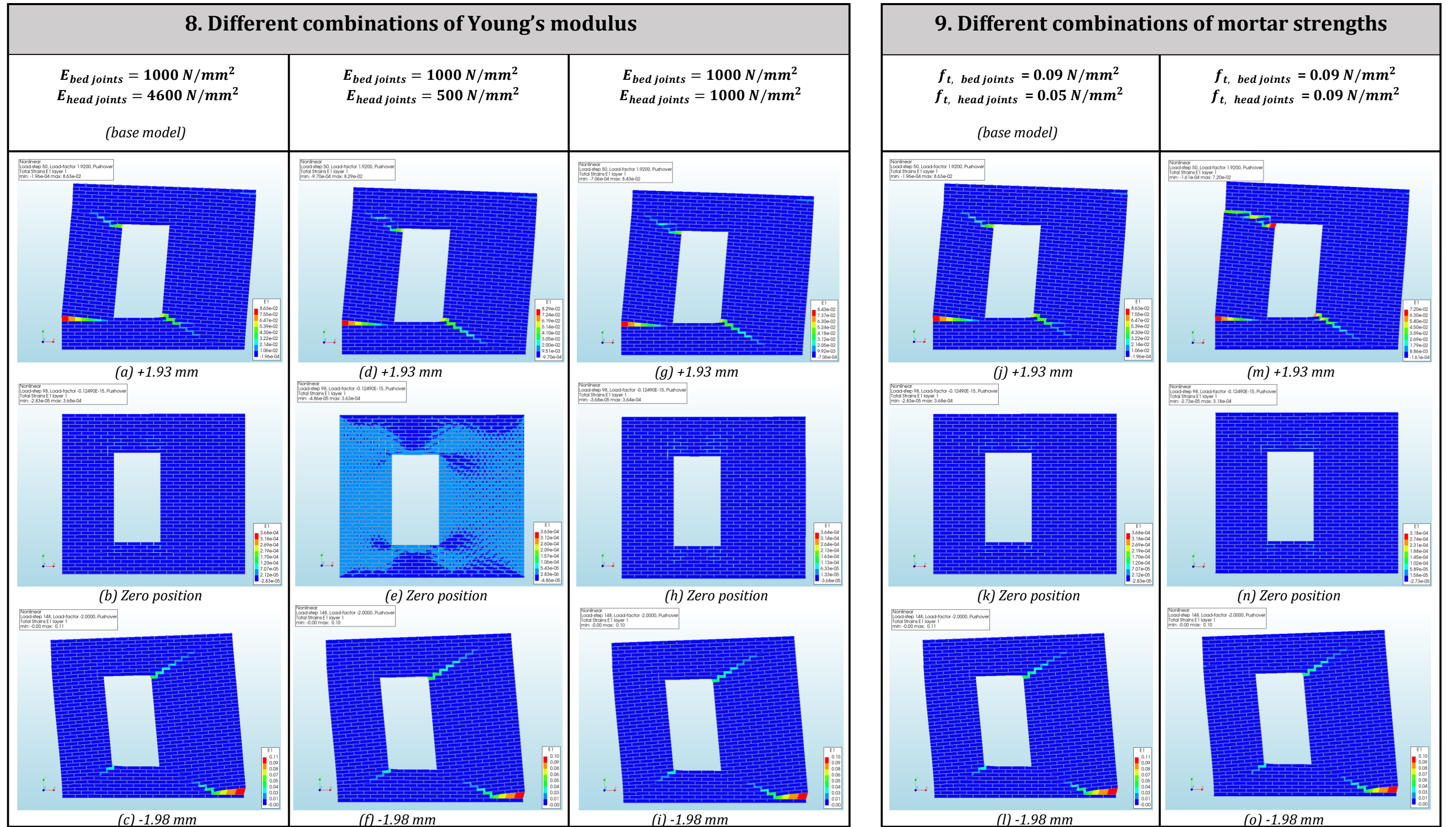# Results sensitivity analysis for continuous micro-model using TSCM (un-strengthened wall)

8. Different combinations of Young's modulus			9. Different combinations of mortar strengths	
$E_{bed\ joints} = 1000\ N/mm^2$ $E_{head\ joints} = 4600\ N/mm^2$ (base model)	$E_{bed\ joints} = 1000\ N/mm^2$ $E_{head\ joints} = 500\ N/mm^2$	$E_{bed\ joints} = 1000\ N/mm^2$ $E_{head\ joints} = 1000\ N/mm^2$	$f_{t,\ bed\ joints} = 0.09\ N/mm^2$ $f_{t,\ head\ joints} = 0.05\ N/mm^2$ (base model)	$f_{t,\ bed\ joints} = 0.09\ N/mm^2$ $f_{t,\ head\ joints} = 0.09\ N/mm^2$

| (a) +1.93 mm | (d) +1.93 mm | (g) +1.93 mm | (j) +1.93 mm | (m) +1.93 mm |
| (b) Zero position | (e) Zero position | (h) Zero position | (k) Zero position | (n) Zero position |
| (c) -1.98 mm | (f) -1.98 mm | (i) -1.98 mm | (l) -1.98 mm | (o) -1.98 mm |

Figure B 6: Effect of different material input parameters comparison for continuous micro-model (un-strengthened wall) using contour plots principal strain E1 (scaling factor = 100)
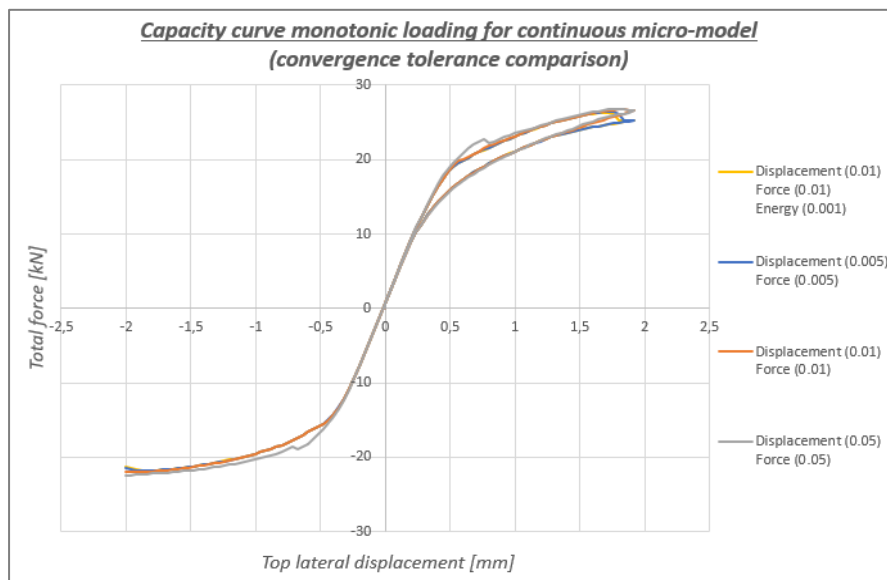
177

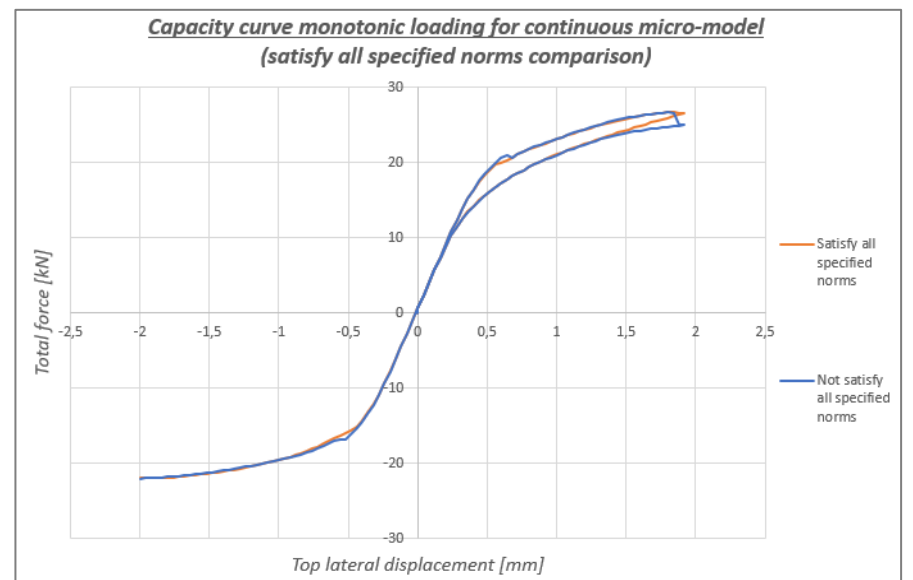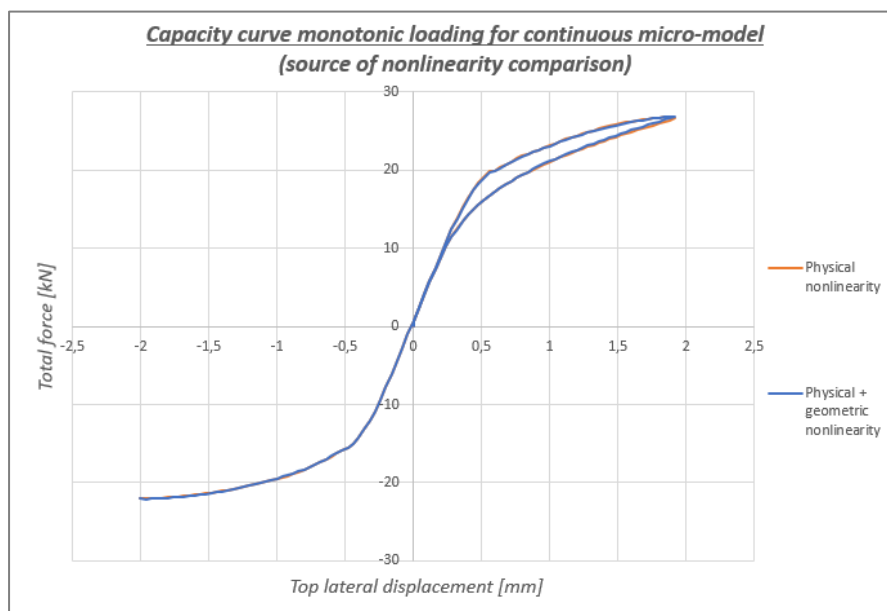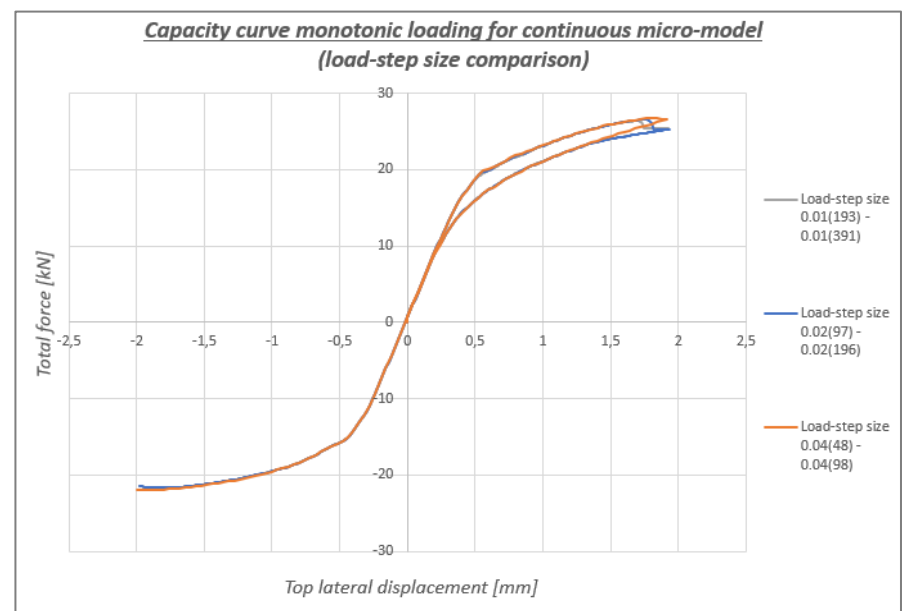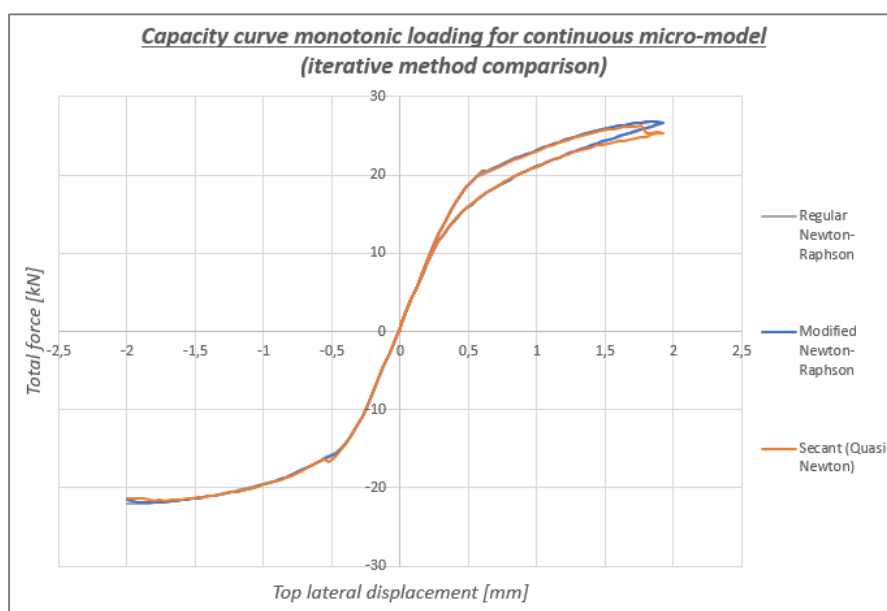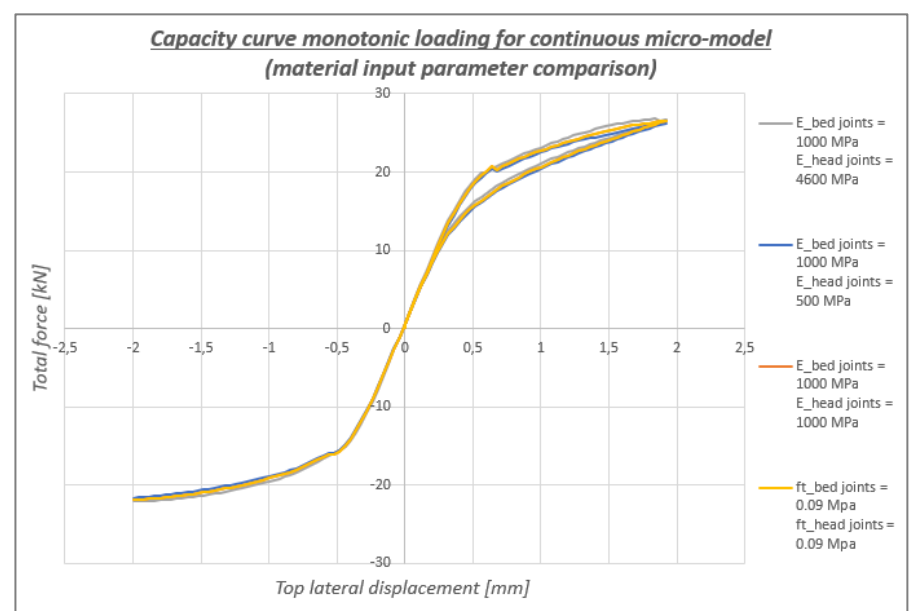# Continuous micro-model using TSCM (un-strengthened wall)
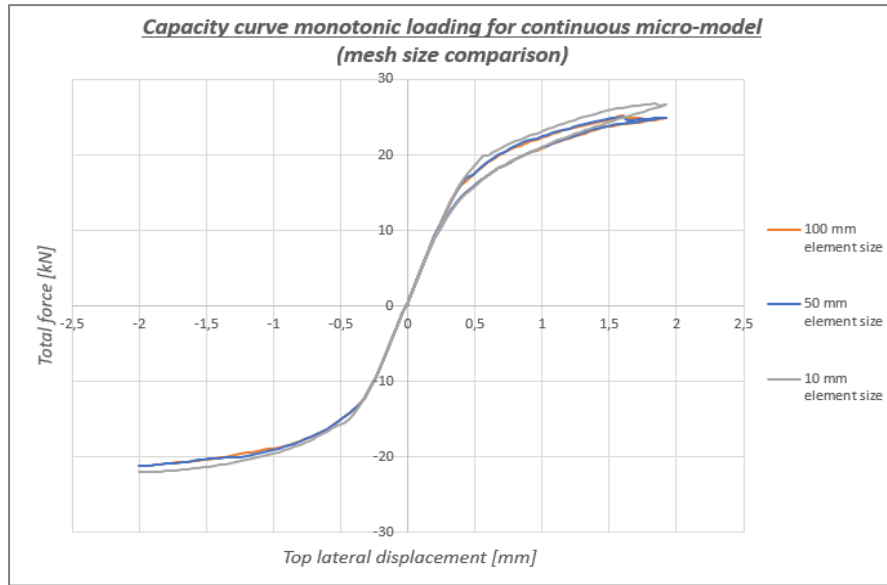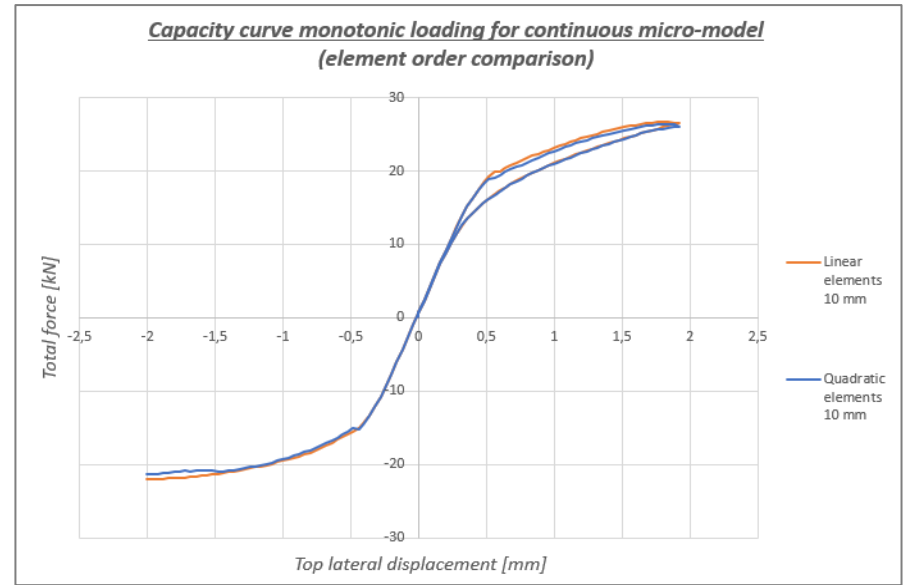
Figure B 7: Capacity curves comparison continuous micro-model (un-strengthened wall)

C

Results detailed micro-model
(Un-strengthened wall)

Appendix C is meant as a supplement to Chapter 4.3 and provides additional information and results for the analyses of the detailed micro-model (un-strengthened wall). The results of the crack pattern are shown using the contour plots of the interface relative displacement DUNy [mm]. The scaling factor of these contour plots are set to a value of 100. The numerical settings and parameters for the monotonic analysis (base model) are listed in *Table C 1*. The properties of the FE mesh for the base model and the model using quadratic elements are listed in *Table C 2*. The characteristics of the interface elements and the material properties for the brick-mortar interfaces using the *Combined Cracking-Shearing-Crushing (CCSC)* model are listed in *Table C 3* and *Table C 4*, respectively. The contour plots for showing the evolution of the crack pattern (base model) are presented in Section C.1. The results of the sensitivity analysis are presented in Section C.2. Moreover, the results of the detailed micro-model in which the non-linearities are located in both the mortar joints as well as in the brick-mortar joint interfaces, are presented and discussed in Section C.3.

Table C 1: Numerical settings and parameters for detailed micro-model (base model)

	Self-weight	**Overburden**	**Pushover**
Load steps	1	1	0.04(48) -0.04(98)
Max. number of iterations	10	10	100
Iteration method	Regular Newton-Raphson	Regular Newton-Raphson	Regular Newton-Raphson
Convergence norms and tolerances	Displacement (0.05) Force (0.05)	Displacement (0.05) Force (0.05)	Displacement (0.05) Force (0.05)
Satisfy all specified norms	No	No	No
Line search	Yes	Yes	Yes
Source of nonlinearity	Physical nonlinearity	Physical nonlinearity	Physical nonlinearity

Table C 2: Properties FE-mesh detailed micro-model

	Model using linear elements (base model)			Model using quadratic elements		
	Steel beams	Masonry bricks/ mortar joints/ concrete lintel	Interfaces	Steel beams	Masonry bricks/ mortar joints/ concrete lintel	Interfaces
Finite element type	L6BEA 2-noded Class III- beam elements	Q8MEM 4-noded plane stress elements	L8IF 2+2 nodes, line interface elements	CL9BE 3-noded Class III- beam elements	CQ16M 8-noded plane stress elements	CL12I 3+3 nodes, line interface elements
Average elements size [mm]	10	10 x 10	10	10	10 x 10	10
Total number of elements	614	70805	14491	614	70805	14491
Total number of nodes	88171			245077		

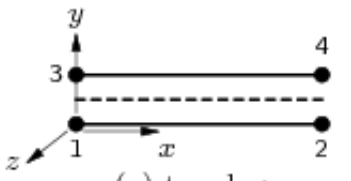*Table C 3: Characteristics interface elements for detailed micro-model (Ferreira, 2021)*
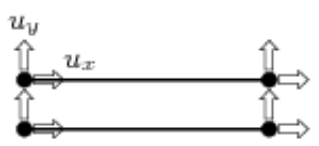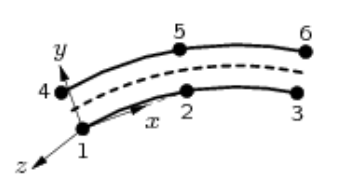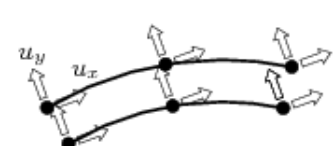
	Brick-mortar interfaces	
	Model using linear elements (base model)	Model using quadratic elements
Finite element type	L8IF 2+2 nodes, line interface elements	CL12I 3+3 nodes, line interface elements
Degrees of freedom per node	u_x, u_y	u_x, u_y
Interpolation scheme	Linear	Quadratic
Integration scheme	3-point Newton-Cotes	4-point Newton-Cotes
Shape dimension	1D	2D
Topological dimension	1D	1D
Stress components	t_n, t_t	t_n, t_t
Inclusion of shear deformations	No	No

Table C 4: Material properties brick-mortar interfaces for detailed micro-model (CCSC)

Brick-mortar interfaces						
Class	Interface elements					
Material model	Combined cracking-shearing-crushing					
Linear material properties						
Type	2D line interface					
		Bed-joints			Head-joints	
Normal stiffness modulus-y	k_n	200	N/mm^3	k_n	100	N/mm^3
Shear stiffness modulus-x	k_t	88	N/mm^3	k_t	44	N/mm^3
Combined cracking-shearing-crushing						
Cracking						
Tensile strength	f_t	0.09	N/mm^2	f_t	0.05	N/mm^2
Fracture energy	G_{ft}	0.00753	N/mm	G_{ft}	0.00499	N/mm
Shearing						
Cohesion	c	0.14	N/mm^2	c	0.14	N/mm^2
Friction angle	φ	0.669	rad	φ	0.669	rad
Dilatancy angle	ψ	0	rad	ψ	0	rad
Mode-II fracture energy						
Parameter "a"	a	0	mm	a	0	mm
Parameter "b"	b	0.3	N/mm	b	0.3	N/mm
Crushing						
Compressive strength	f_c	1e+06	N/mm^2	f_c	1e+06	N/mm^2
Factor "Cs"	C_s	9	-	C_s	9	-
Compressive inelastic law						
Compressive fracture energy	G_{fc}	1e+06	N/mm	G_{fc}	1e+06	N/mm
Equivalent plastic relative displacement	u_{eq}	1e-06	mm	u_{eq}	1e-06	mm

C.1) Evolution crack pattern monotonic analysis for detailed micro-model using Discrete cracking for interface elements (un-strengthened wall)
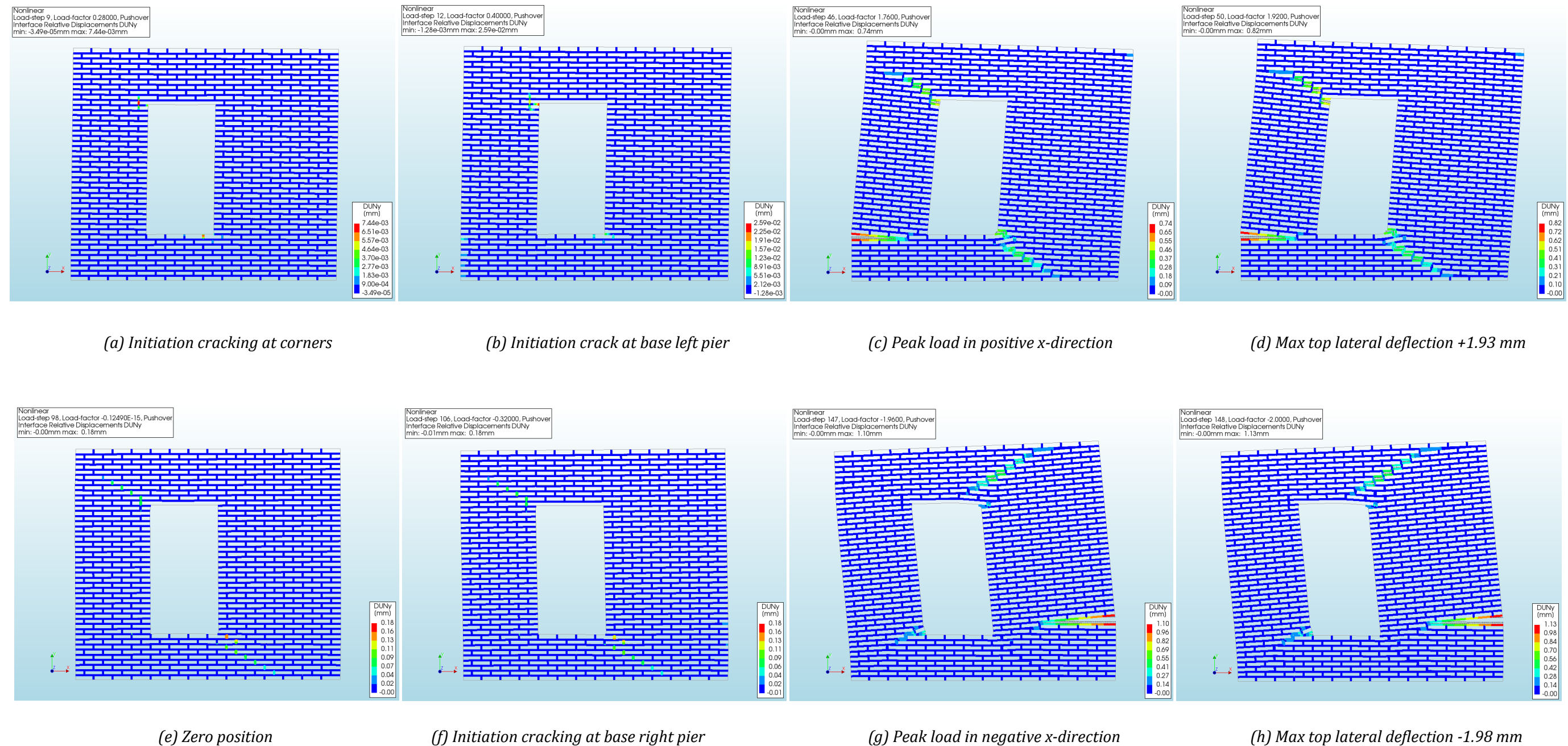
(base model)

(a) Initiation cracking at corners (b) Initiation crack at base left pier (c) Peak load in positive x-direction (d) Max top lateral deflection +1.93 mm

(e) Zero position (f) Initiation cracking at base right pier (g) Peak load in negative x-direction (h) Max top lateral deflection -1.98 mm

Figure C 1: Evolution crack pattern monotonic loading for detailed micro-model (un-strengthened wall) using contour plots interface relative displacement DUNy [mm] (scaling factor = 100)

C.2) Results sensitivity analysis for detailed micro-model using Discrete cracking (un-strengthened wall)
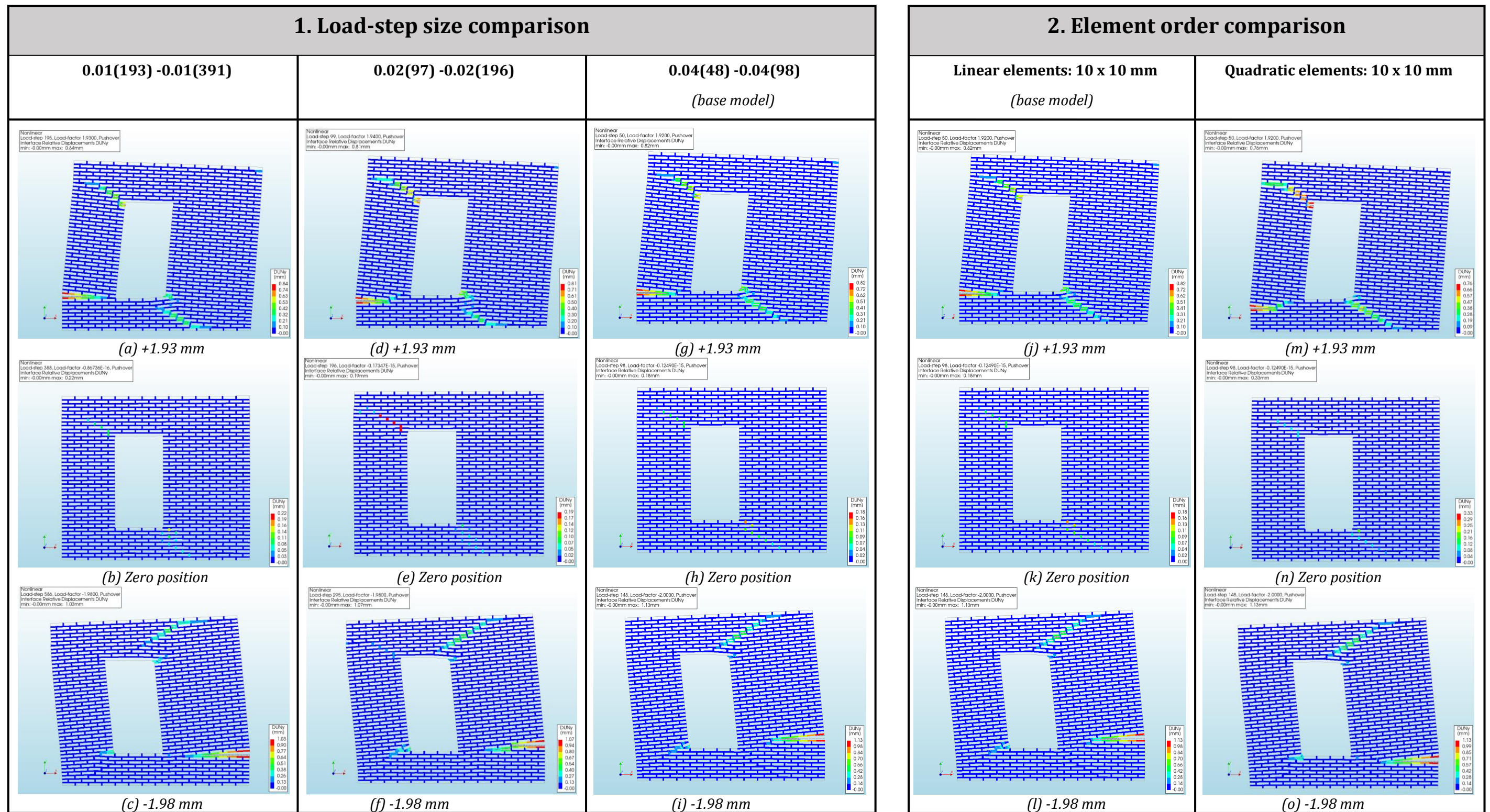

Figure C 2: *Effect of the load-step size and element order comparison for detailed micro-model (un-strengthened wall) using contour plots interface relative displacement DUNy [mm] (scaling factor = 100)*

Results sensitivity analysis for detailed micro-model using discrete cracking (un-strengthened wall)
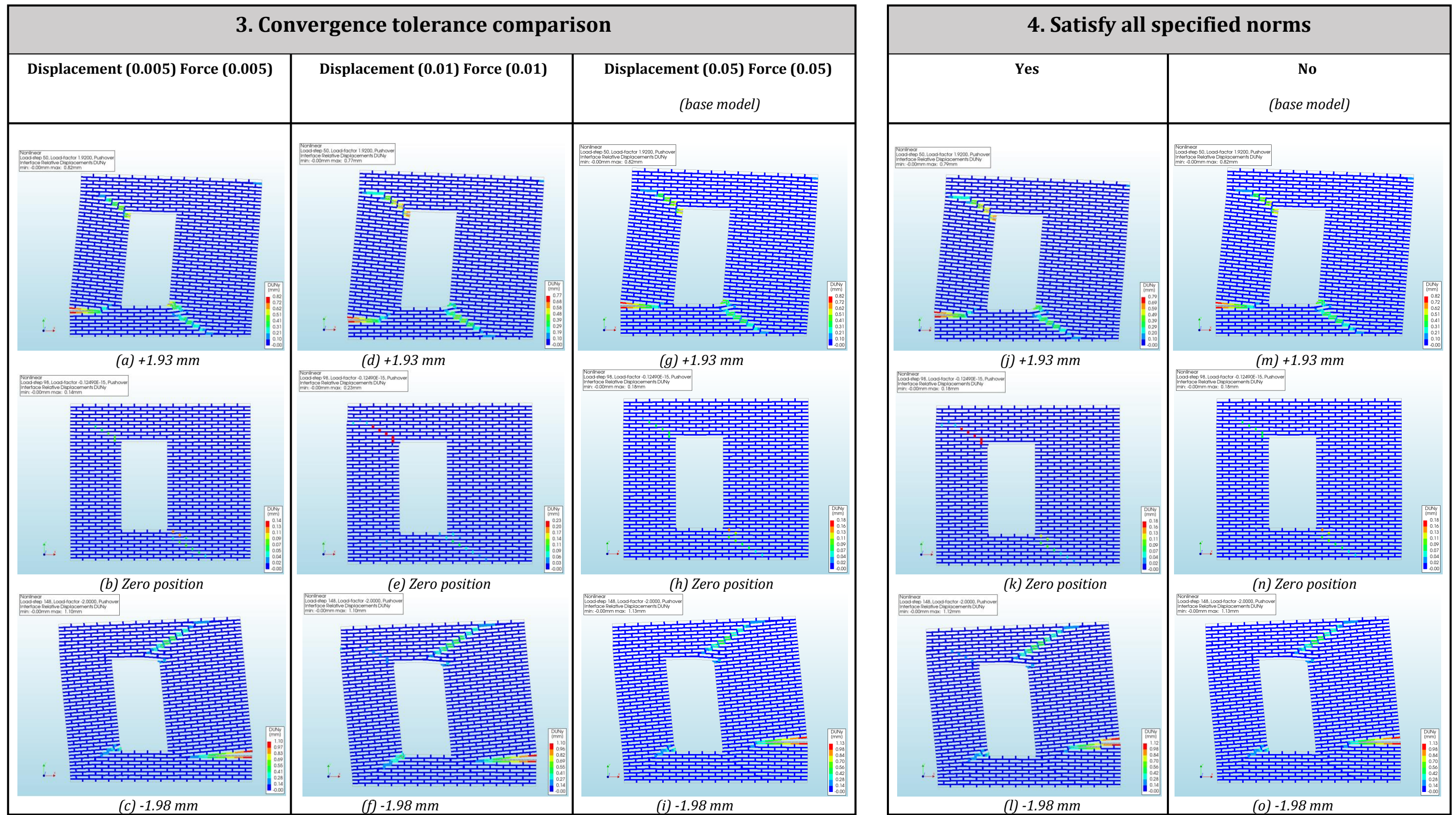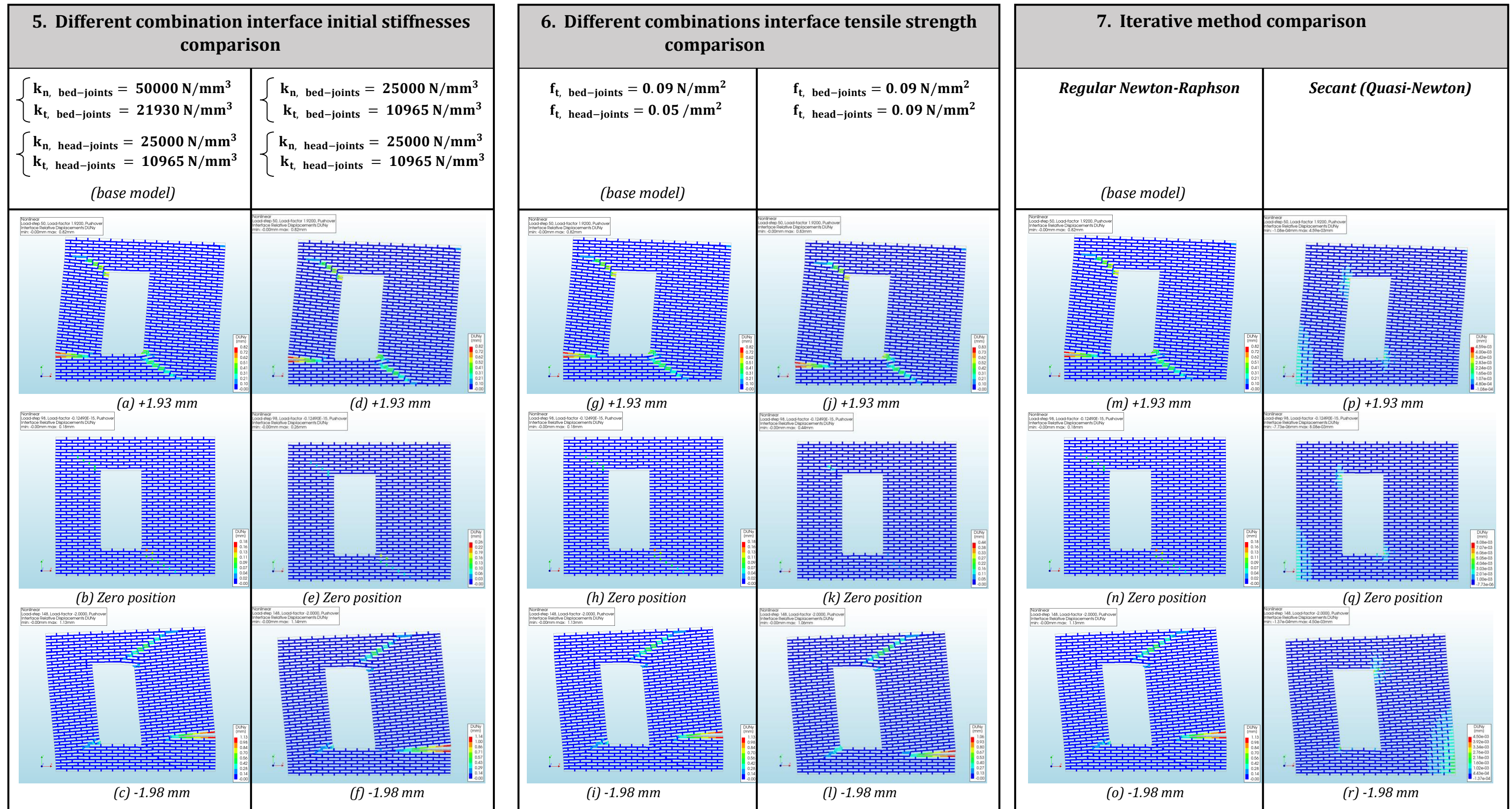
3. Convergence tolerance comparison			4. Satisfy all specified norms	
Displacement (0.005) Force (0.005)	**Displacement (0.01) Force (0.01)**	**Displacement (0.05) Force (0.05)** *(base model)*	**Yes**	**No** *(base model)*
(a) +1.93 mm	*(d) +1.93 mm*	*(g) +1.93 mm*	*(j) +1.93 mm*	*(m) +1.93 mm*
(b) Zero position	*(e) Zero position*	*(h) Zero position*	*(k) Zero position*	*(n) Zero position*
(c) -1.98 mm	*(f) -1.98 mm*	*(i) -1.98 mm*	*(l) -1.98 mm*	*(o) -1.98 mm*

Figure C 3: Effect of the convergence tolerance and satisfaction to all specified norms comparison for detailed micro-model (un-strengthened wall) using contour plots interface relative displacement DUNy [mm] (scaling factor = 100)

Results sensitivity analysis for detailed micro-model using discrete cracking (un-strengthened wall)

5. Different combination interface initial stiffnesses comparison		6. Different combinations interface tensile strength comparison		7. Iterative method comparison	
$\begin{cases} k_{n,\ bed-joints} = 50000\ N/mm^3 \\ k_{t,\ bed-joints} = 21930\ N/mm^3 \end{cases}$ $\begin{cases} k_{n,\ head-joints} = 25000\ N/mm^3 \\ k_{t,\ head-joints} = 10965\ N/mm^3 \end{cases}$ *(base model)*	$\begin{cases} k_{n,\ bed-joints} = 25000\ N/mm^3 \\ k_{t,\ bed-joints} = 10965\ N/mm^3 \end{cases}$ $\begin{cases} k_{n,\ head-joints} = 25000\ N/mm^3 \\ k_{t,\ head-joints} = 10965\ N/mm^3 \end{cases}$	$f_{t,\ bed-joints} = 0.09\ N/mm^2$ $f_{t,\ head-joints} = 0.05\ /mm^2$ *(base model)*	$f_{t,\ bed-joints} = 0.09\ N/mm^2$ $f_{t,\ head-joints} = 0.09\ N/mm^2$	*Regular Newton-Raphson* *(base model)*	*Secant (Quasi-Newton)*
(a) +1.93 mm	(d) +1.93 mm	(g) +1.93 mm	(j) +1.93 mm	(m) +1.93 mm	(p) +1.93 mm
(b) Zero position	(e) Zero position	(h) Zero position	(k) Zero position	(n) Zero position	(q) Zero position
(c) -1.98 mm	(f) -1.98 mm	(i) -1.98 mm	(l) -1.98 mm	(o) -1.98 mm	(r) -1.98 mm

Figure C 4: Effect of different material input parameters and iterative method comparison for detailed micro-model (un-strengthened wall) using contour plots interface relative displacement DUNy [mm] (scaling factor = 100)

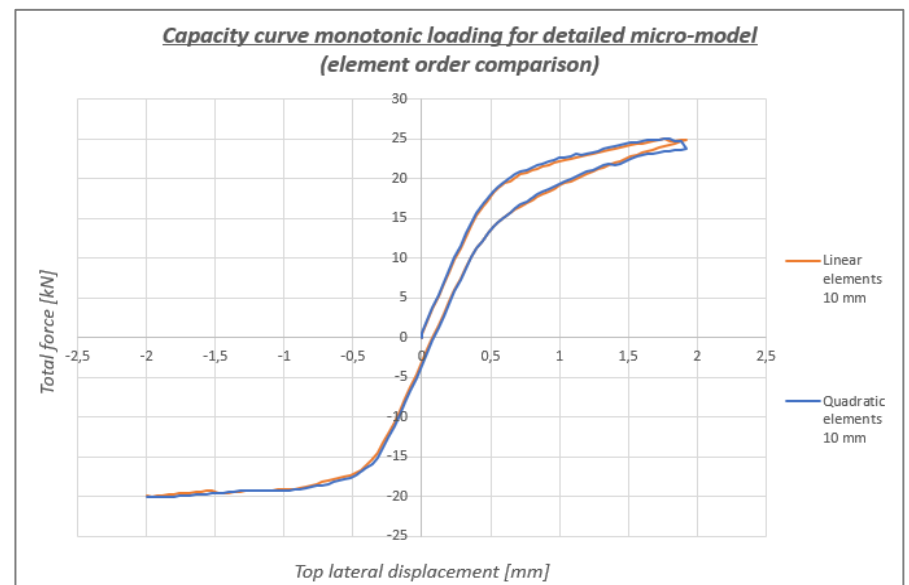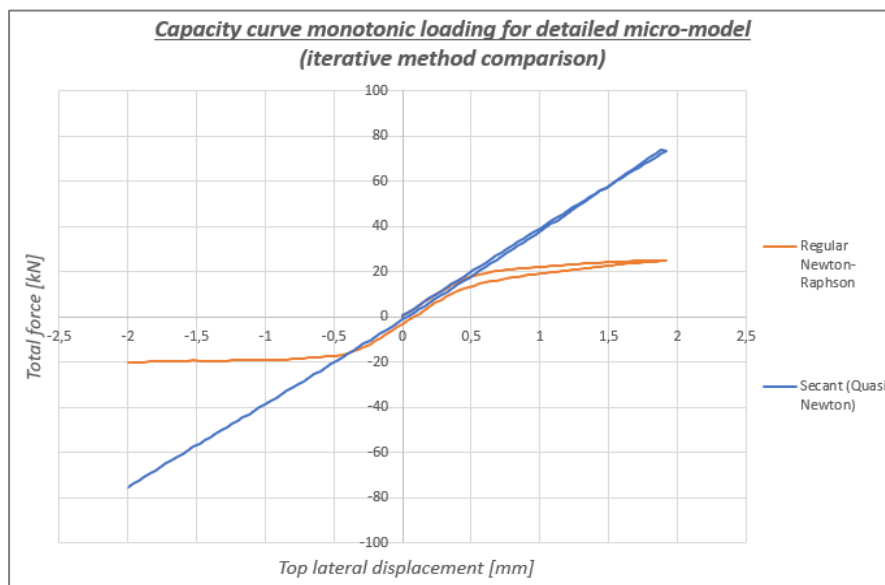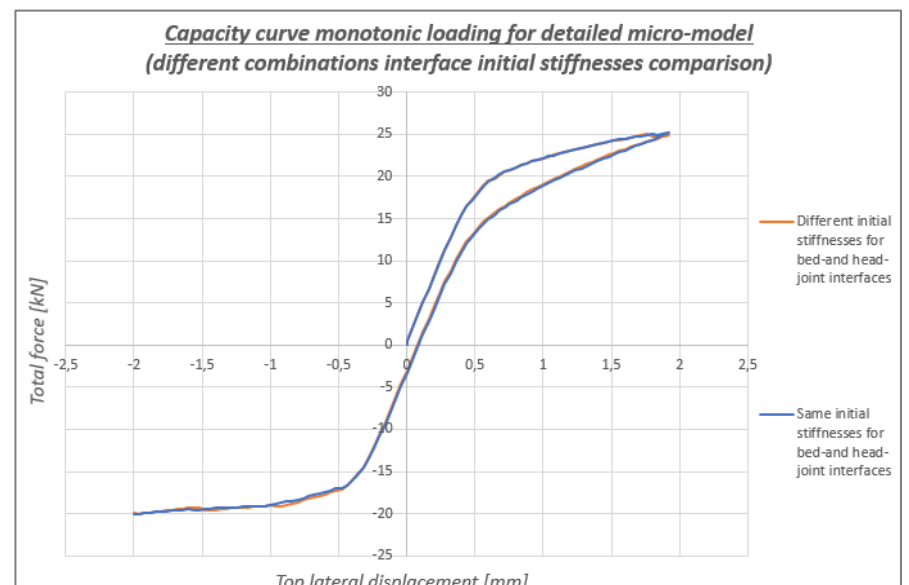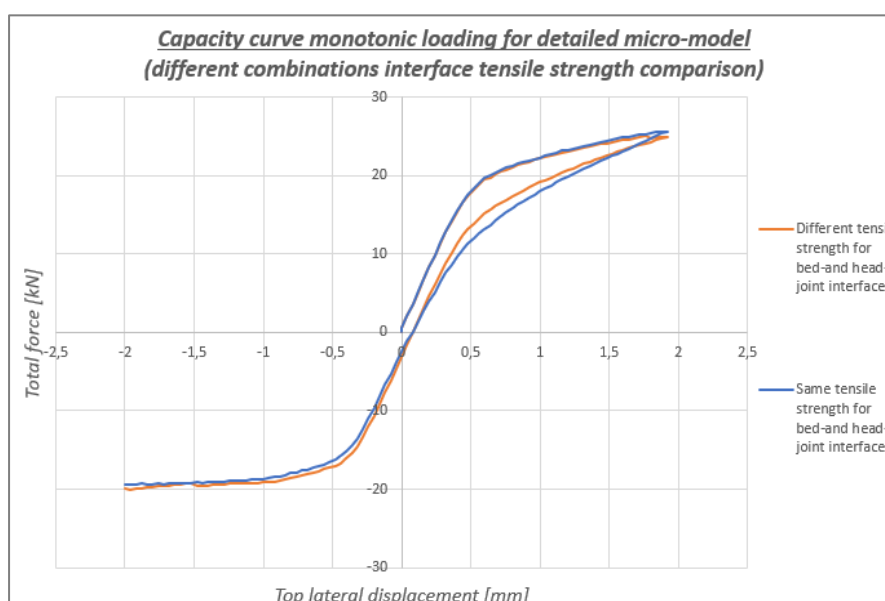# Detailed micro-model using discrete cracking (un-strengthened wall)
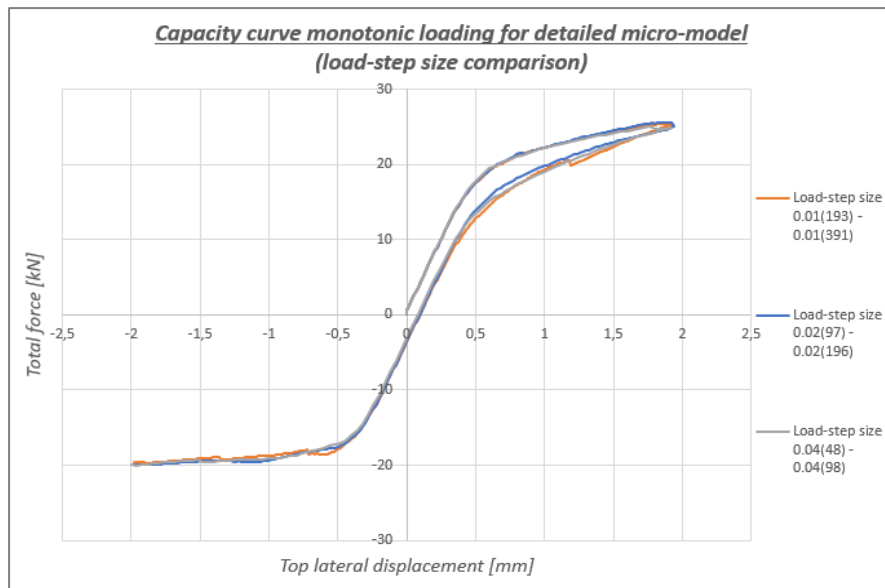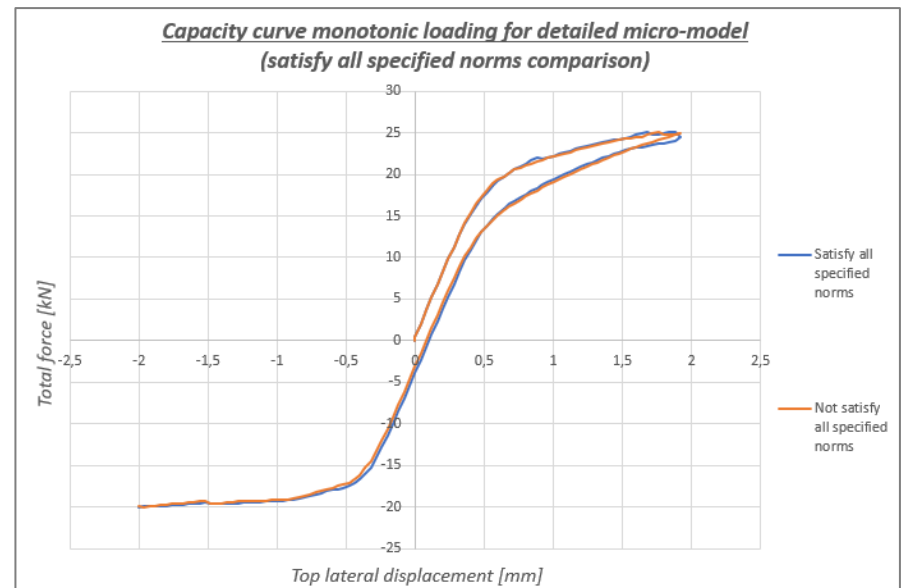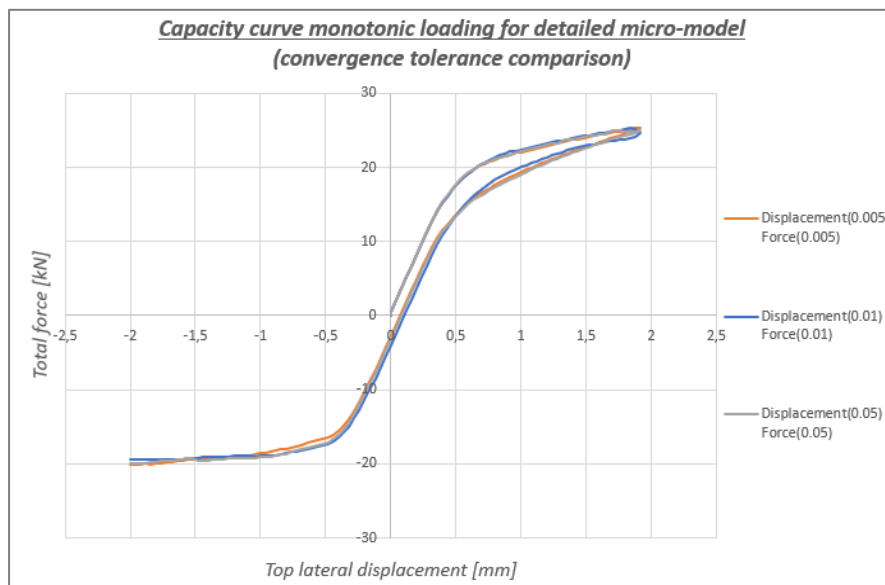
Figure C 5: Capacity curves comparison detailed micro-model (un-strengthened wall)

C.3) Detailed micro-model with the nonlinearity located in both joints and interfaces

In this section, two approaches for the Detailed micro-model are compared with each other. The difference between the two approaches is the location of the nonlinearity. The nonlinearities are only located in the brick-mortar joint interfaces for Approach 1, while discrete cracking is used for the interfaces and smeared cracking for the mortar joints in Approach 2. The EMM is herein used as the material model for the mortar joints. The results of the crack patterns are illustrated in *Figure C 7*. The crack patterns are very similar for the two approaches. Only small differences in crack length can be observed between the two approaches, but the location of the main cracks are the same. It can be observed from the results of Approach 2 that the cracks are occurring mainly in the form of opening of the interface elements, while cracking in the mortar joints are limited. Moreover, the results are also very similar in terms of the shape of the capacity curve (*Figure C 6*) and the obtained maximum base shear forces in both loading directions (*Table C 5*). Approach 2 has a slightly larger energy dissipation and the computational time is larger.
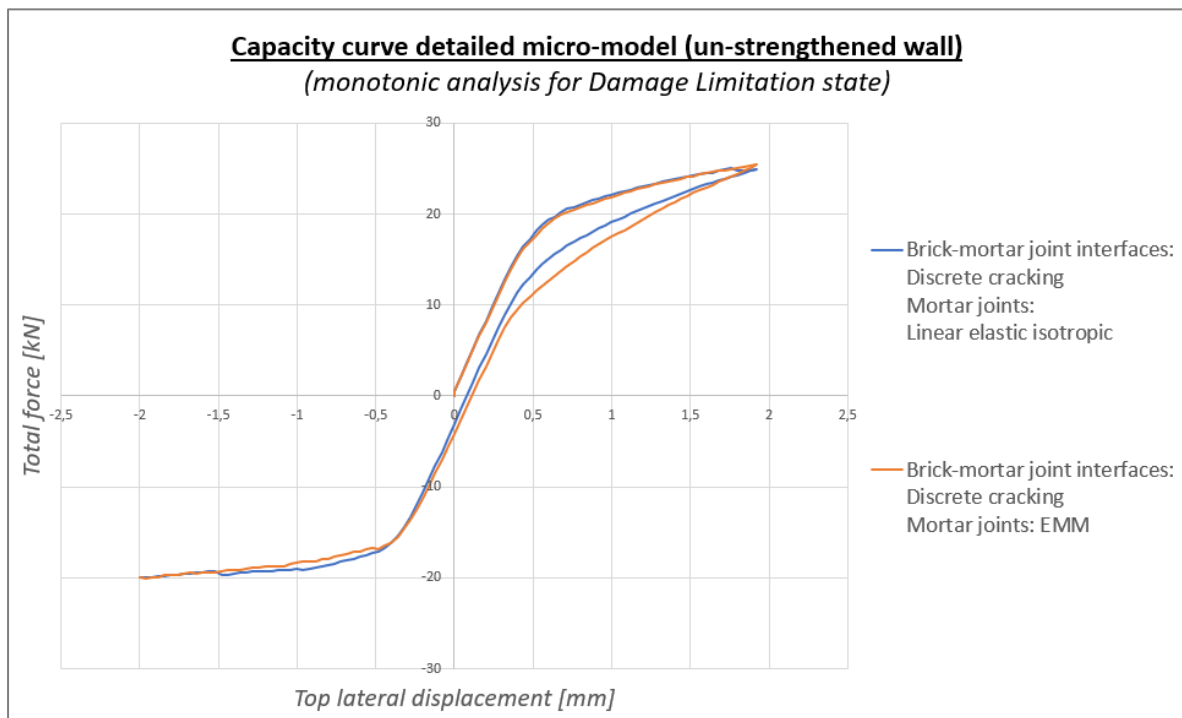

Figure C 6: Capacity curve comparing two approaches for the Detailed micro-model (un-strengthened wall)

Table C 5: Comparison of the maximum base shear forces for the two approaches of the Detailed micro-model (un-strengthened wall)

	Positive x-direction		Negative x-direction		Time
	Max. base shear force	Difference compared to experiment	Max. base shear force	Difference compared to experiment	
	[kN]	[%]	[kN]	[%]	[min]
Experimental results	**22.05**	-	**-18.72**	-	-
Approach 1	25.07	+ 13.70%	-20.01	+ 6.89%	27
Approach 2	25.44	+ 15.37 %	-20.03	+ 7.00%	42

Comparison of the two approaches for the Detailed micro-model (un-strengthened wall)
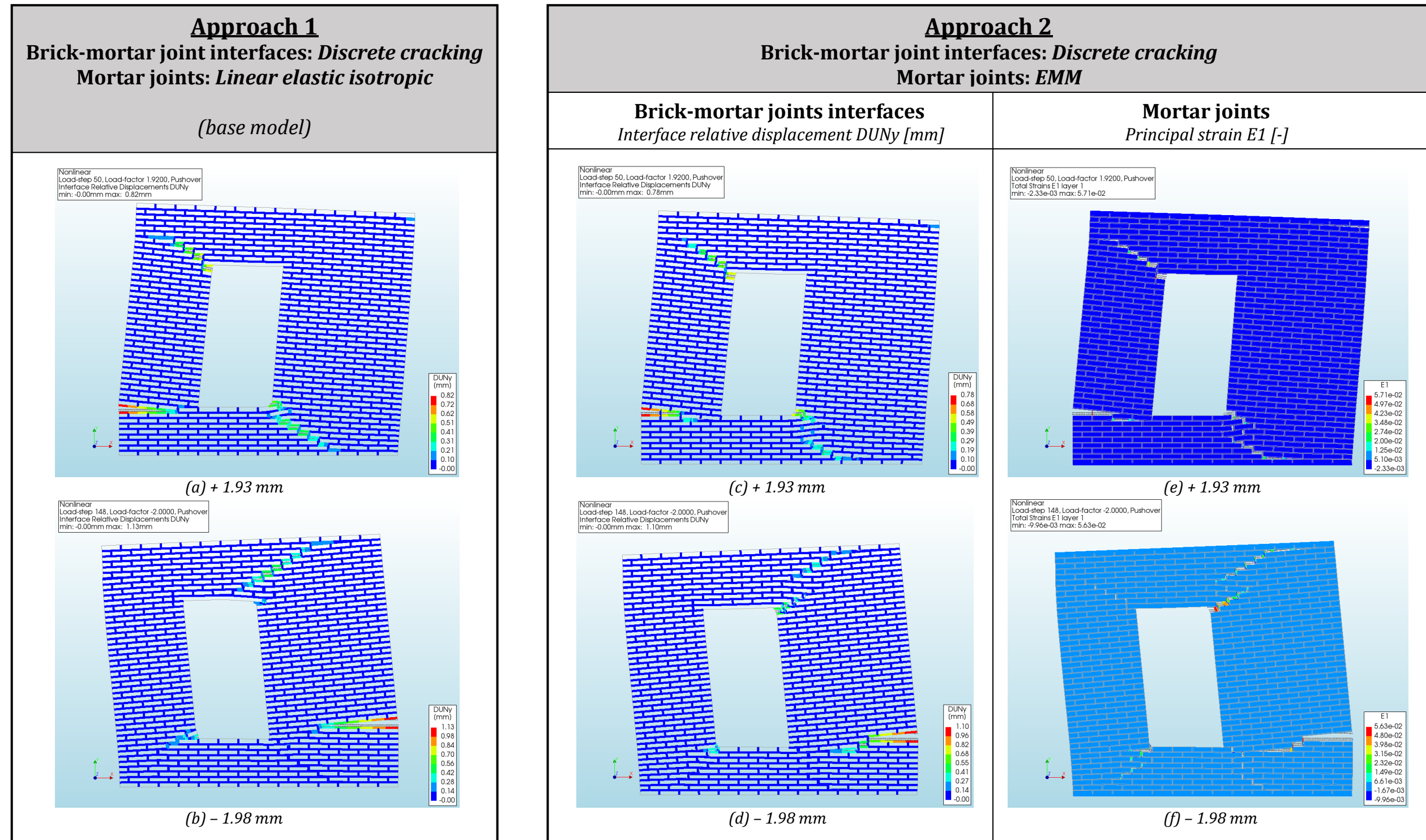
(Damage Limitation state)

Figure C 7: Crack pattern at maximum top displacement monotonic and cyclic pushover analysis (DL state) for macro-model using contour plots principal strain E1 (scaling factor = 100)

D

Results detailed micro-model
(Strengthened wall)

Appendix D is meant as a supplement to Chapter 5.3 and provides additional results for the analyses in the Damage Limitation (DL) state using Approach 2 for the detailed micro-model. In Approach 2, the nonlinearities are located both in the brick-mortar joint interfaces as well as in the plane stress elements for the mortar joints. The crack patterns for the opening of the interface elements (Discrete cracking) are illustrated in *Figure D 1*. The results of smeared cracking in the mortar joints, using the *Engineering Masonry model (EMM)*, are illustrated in *Figure D 2*.

Detailed micro-model Approach 2: Discrete cracking for brick-mortar joint interfaces and EMM for mortar joints (strengthened wall monotonic analysis for DL state)

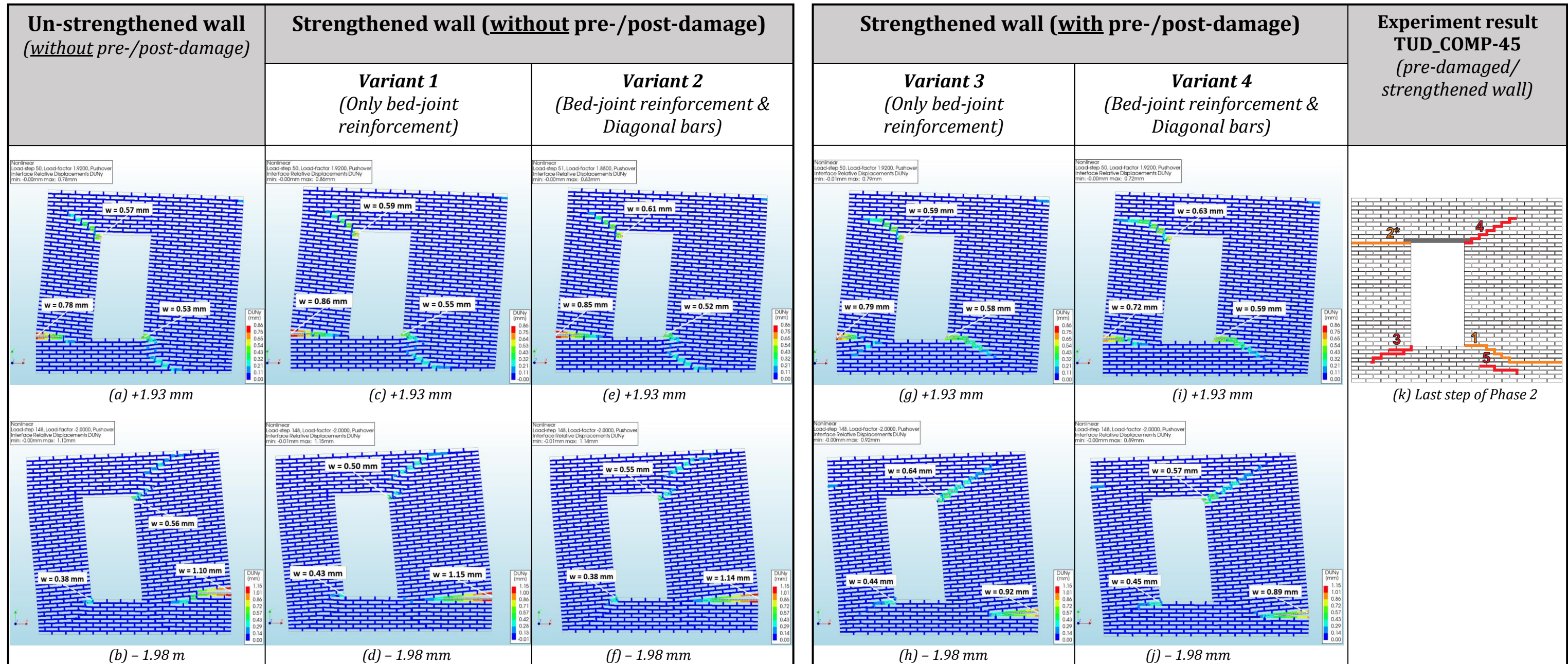## *Results part 1 of 2 : Brick-mortar joint interfaces*

Figure D 1: Crack pattern at maximum top displacement monotonic analysis (DL state) for detailed micro-model Approach 2 using contour plots interface relative displacement DUNy [mm] (scaling factor = 100)

Detailed micro-model Approach 2: Discrete cracking for brick-mortar joint interfaces and EMM for mortar joints (strengthened wall monotonic analysis for DL state)
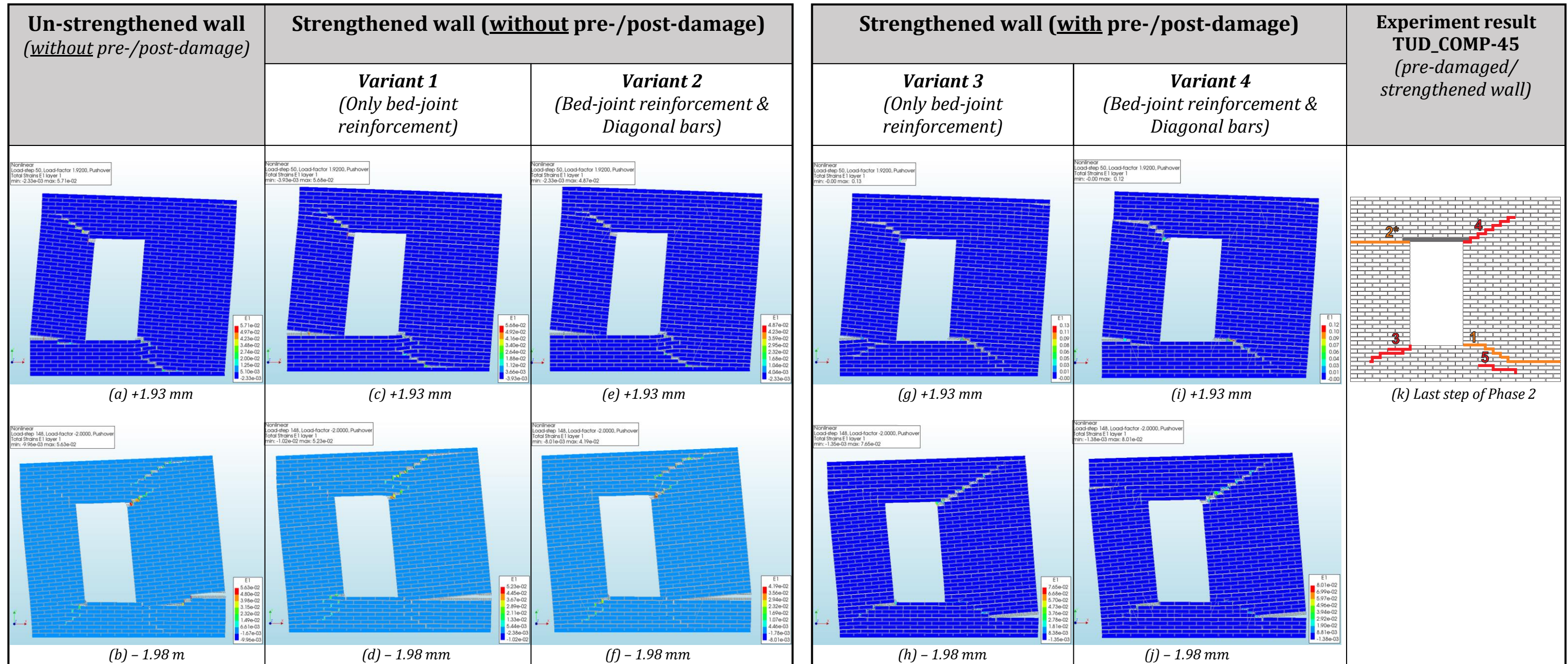
Results part 2 of 2 : Mortar joints

Un-strengthened wall (*without* pre-/post-damage)	Strengthened wall (__without__ pre-/post-damage)		Strengthened wall (__with__ pre-/post-damage)		Experiment result TUD_COMP-45 (*pre-damaged/ strengthened wall*)
	Variant 1 (Only bed-joint reinforcement)	*Variant 2* (Bed-joint reinforcement & Diagonal bars)	*Variant 3* (Only bed-joint reinforcement)	*Variant 4* (Bed-joint reinforcement & Diagonal bars)	
(a) +1.93 mm	(c) +1.93 mm	(e) +1.93 mm	(g) +1.93 mm	(i) +1.93 mm	(k) Last step of Phase 2
(b) – 1.98 m	(d) – 1.98 mm	(f) – 1.98 mm	(h) – 1.98 mm	(j) – 1.98 mm	

Figure D 2: Crack pattern at maximum top displacement monotonic analysis (DL state) for detailed micro-model Approach 2 using contour plots principal strain E1 [-] (scaling factor = 100)

Results continuous micro-model
(Analyses for the Near Collapse state)

Appendix E is meant as a supplement to Chapter 4.5 and Chapter 5.4 and provides additional information and results for the analyses up to the Near Collapse (NC) state using a continuous micro-modeling approach (for both un-strengthened and strengthened wall). The numerical settings and parameters, which are used for the monotonic and cyclic analysis in the NC state, are listed in *Table E 1* for the continuous micro-model using the *Total Strain Crack model (TSCM)* and the *Engineering Masonry model (EMM)*. These settings are used for both un-strengthened and strengthened wall. The material properties for the different mortar joints are listed in *Table E 2* for the continuous micro-model using the TSCM and in *Table E 3* for the continuous micro-model using the EMM. The results of the axial stress and bond-slip development in the reinforcement are presented in this chapter for all four variants using a monotonic analysis. The axial stress and bond-slip developments in the reinforcements are presented in *Figure E 1* and *Figure E 3*, respectively for the continuous micro-model using the TSCM. The axial stress and bond-slip developments in the reinforcements are presented in *Figure E 2* and *Figure E 4*, respectively for the continuous micro-model using the EMM.

Table E 1: Numerical settings and parameters for continuous micro-model for loading up to NC state

		Self-weight	**Overburden**	**Pushover**
Load steps	**TSCM**	1	1	0.2 for DL state 0.2 for NC state
	EMM	1	1	0.2 for DL state 0.5 for NC state
Max. number of iterations	**TSCM**	10	10	100
	EMM	10	10	50
Iteration method	**TSCM**	Regular Newton-Raphson	Regular Newton-Raphson	Regular Newton-Raphson
	EMM			
Convergence norms and tolerances	**TSCM**	Displacement (0.5) Force (0.5)	Displacement (0.5) Force (0.5)	Displacement (0.5) Force (0.5)
	EMM	Displacement (0.05) Force (0.05)	Displacement (0.05) Force (0.05)	Displacement (0.05) Force (0.05)
Satisfy all specified norms	**TSCM**	Yes	Yes	Yes
	EMM			
Line search	**TSCM**	Yes	Yes	Yes
	EMM			
Source of nonlinearity	**TSCM**	Physical & geometric nonlinearity	Physical & geometric nonlinearity	Physical & geometric nonlinearity
	EMM			

*Table E 2: Material properties continuous micro-model using TSCM for mortar joints*

Material properties continuous micro-model using TSCM for mortar joints								
Material class			Concrete and masonry					
Material model			Total strain based crack model					
Crack orientation			Rotating					
Linear material properties								
			Strengthened bed-joints	**Repaired bed-joints**	**Pre-/post-damaged bed-joints**	**Pre-/post-damaged head-joints**	**Original bed-joints**	**Original head-joints**
Young's modulus	E	N/mm^2	6630	6315	500	250	1000	500
Poisson's ratio	ν	-	0.14	0.14	0.14	0.14	0.14	0.14
Mass density	ρ	kg/m^3	1708	1708	1708	1708	1708	1708
Tensile behavior								
Tensile curve			Linear-crack energy					
Tensile strength	f_t	N/mm^2	0.09	0.032	1e-06	1e-06	0.09	0.05
Mode-I tensile fracture energy	G_f^I	N/mm	0.00753	0.003	1e-06	1e-06	0.00753	0.00499
Crack bandwidth specification			Rots	Rots	User specified	User specified	Rots	Rots
Crack bandwidth	h	mm	14.14	14.14	0	0	14.14	14.14
Compressive behavior								
Compression curve			Parabolic					
Compressive strength	f_c	N/mm^2	20.72	20.72	12.93	3.81	12.93	3.81
Compressive fracture energy	G_c	N/mm	82.75	82.75	28.63	6.4	28.63	6.4

Table E 3: Material properties continuous micro-model using EMM for mortar joints (analysis up to NC state)

Material properties continuous micro-model using EMM for mortar joints								
Material class			Concrete and masonry					
Material model			Engineering Masonry Model					
Elasticity parameters								
			Strengthened bed-joints	**Repaired bed-joints**	**Pre-/post-damaged bed-joints**	**Original bed-joints**	**Pre-/post-damaged head-joints**	**Original head-joints**
Young's modulus	E_x	N/mm^2	6630	6315	500	1000	25	50
	E_y	N/mm^2	6630	6315	500	1000	25	50
Shear modulus	G_{xy}	N/mm^2	2908	2770	219	439	11	22
Mass density	ρ	kg/m^3	1708	1708	1708	1708	1708	1708
Cracking parameters								
Head-joint failure type			Direct input head-joint tensile strength					
Tensile strength — Bed-joints	f_t	N/mm^2	0.09	0.032	1e-06	0.09	1e-06	0.05
Tensile strength — Head-joint	f_t	N/mm^2	0.09	0.032	1e-06	0.09	1e-06	0.05
Fracture energy in tension	G_f^I	N/mm	0.00753	0.003	1e-06	0.00753	1e-06	0.00499
Crushing parameters								
Compressive strength	f_c	N/mm^2	20.72	20.72	12.93	12.93	3.81	3.81
Fracture energy in compression	G_c	N/mm	82.75	82.75	28.63	28.63	6.4	6.4
Factor to strain at compressive strength	n	-	4	4	4	4	4	4
Unloading factor, 1= secant, 0= linear	λ	-	0.25	0.25	0.25	0.25	0.25	0.25
Shear failure parameters								
Friction angle	φ	rad	0.6686	0.6686	0.6686	0.6686	0.6686	0.6686
Cohesion	c	N/mm^2	0.13	0.13	0.13	0.13	0.13	0.13
Fracture energy in shear	$G_{v,i}$	N/mm	0.3	0.3	1e-06	0.3	1e-06	0.3
Crack bandwidth								
Crack bandwidth specification			Rots	Rots	User specified	Rots	User specified	Rots
Crack bandwidth	h	mm	14.14	14.14	0	14.14	0	14.14

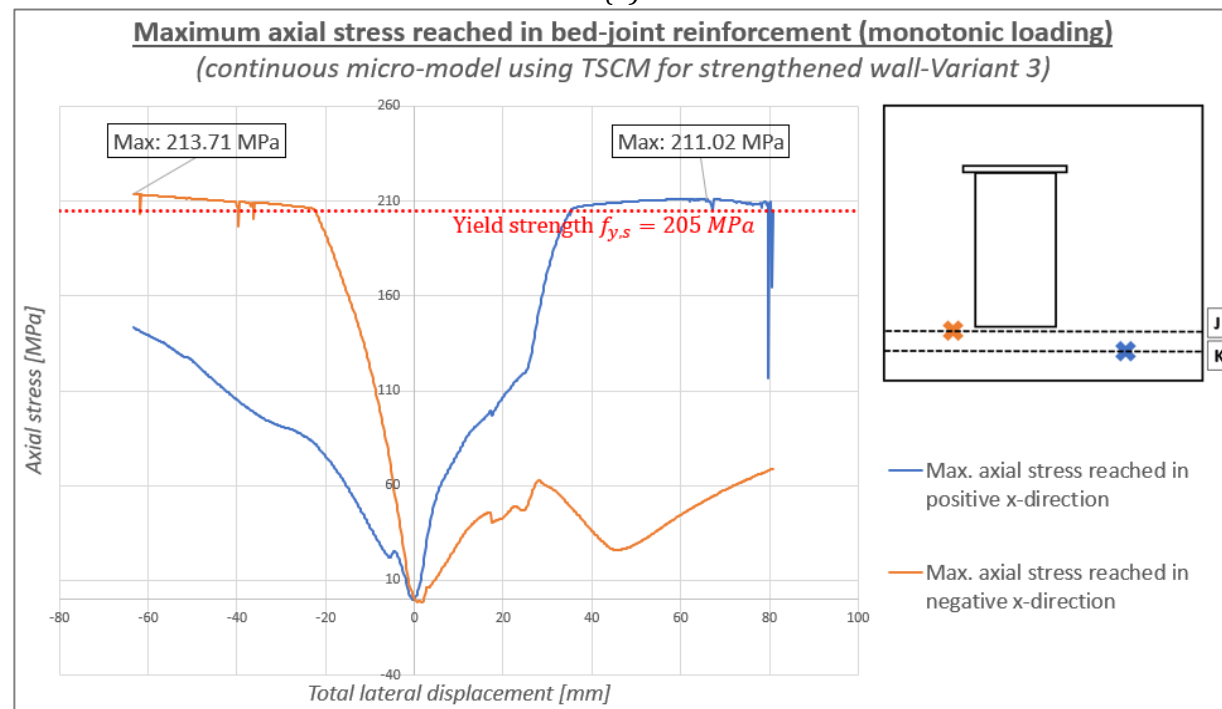# Axial stress development in bed-joint reinforcement for all strengthened wall variants

*(monotonic analysis for continuous micro-model using **TSCM** for mortar joints)*
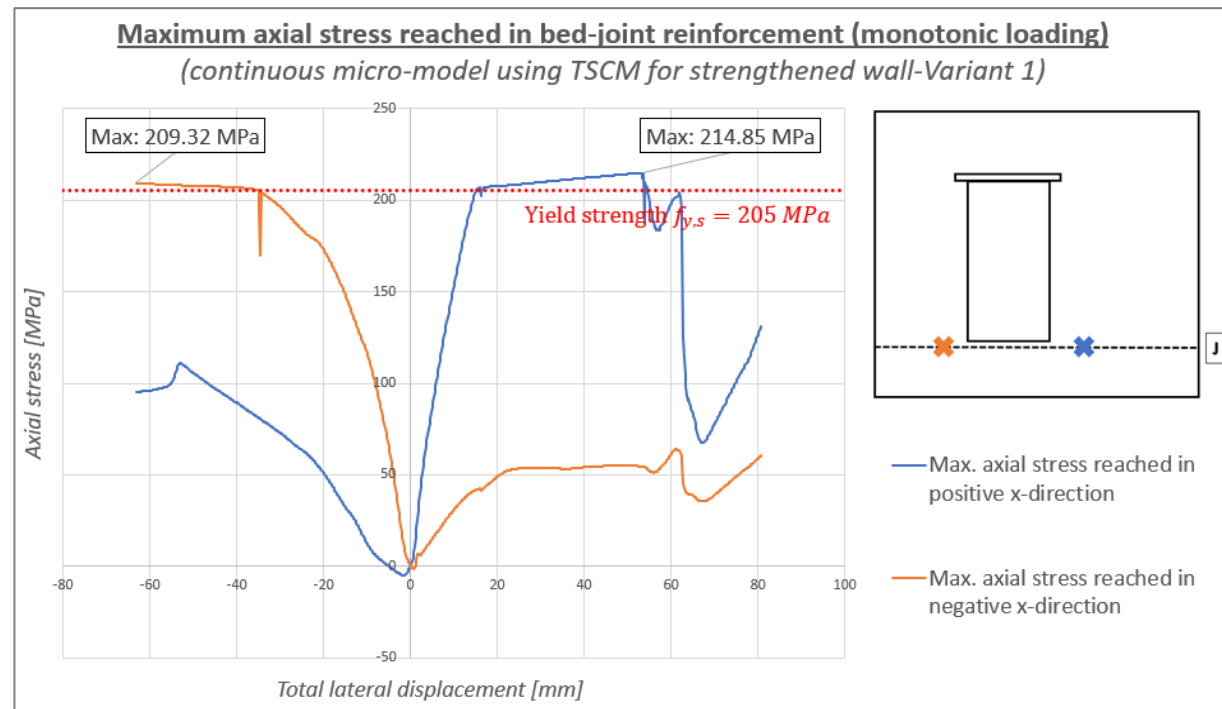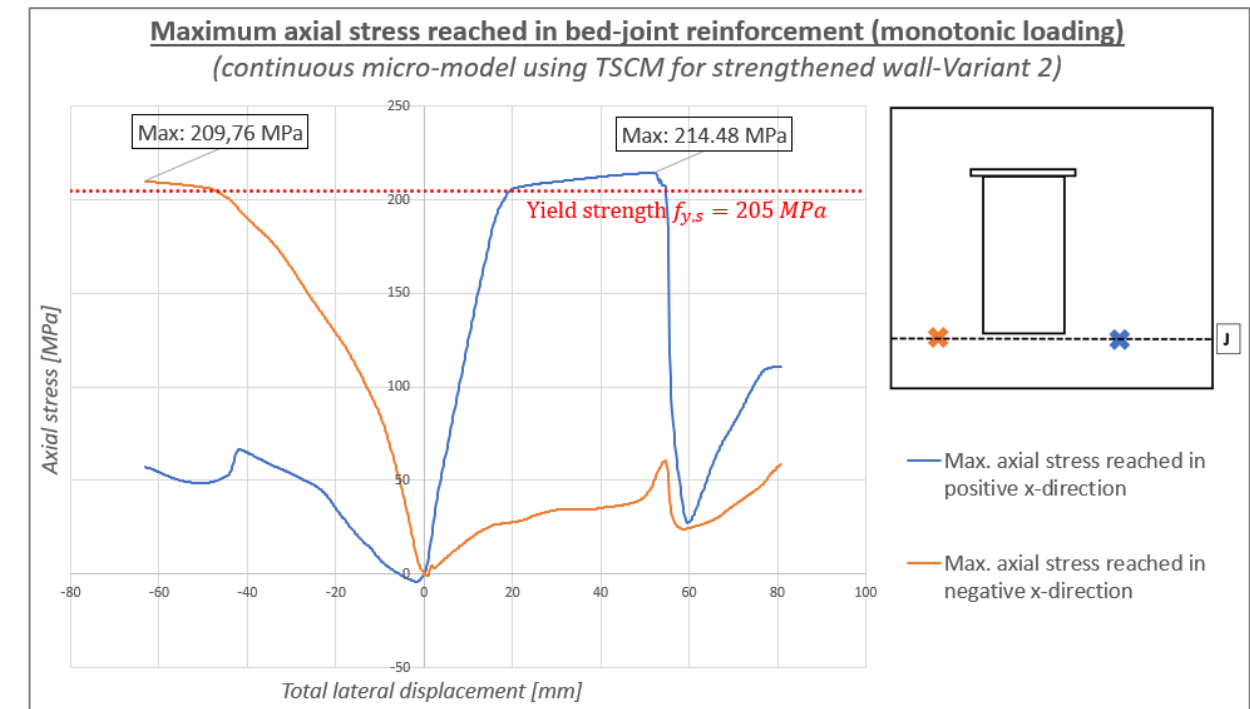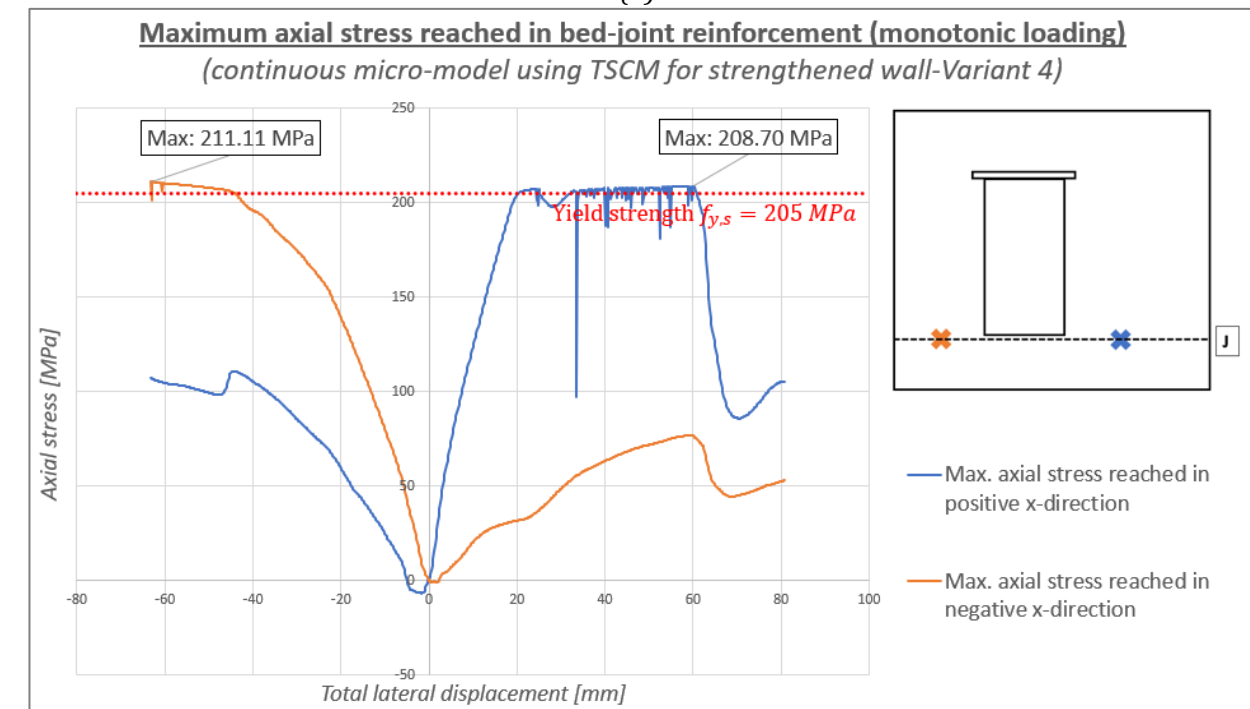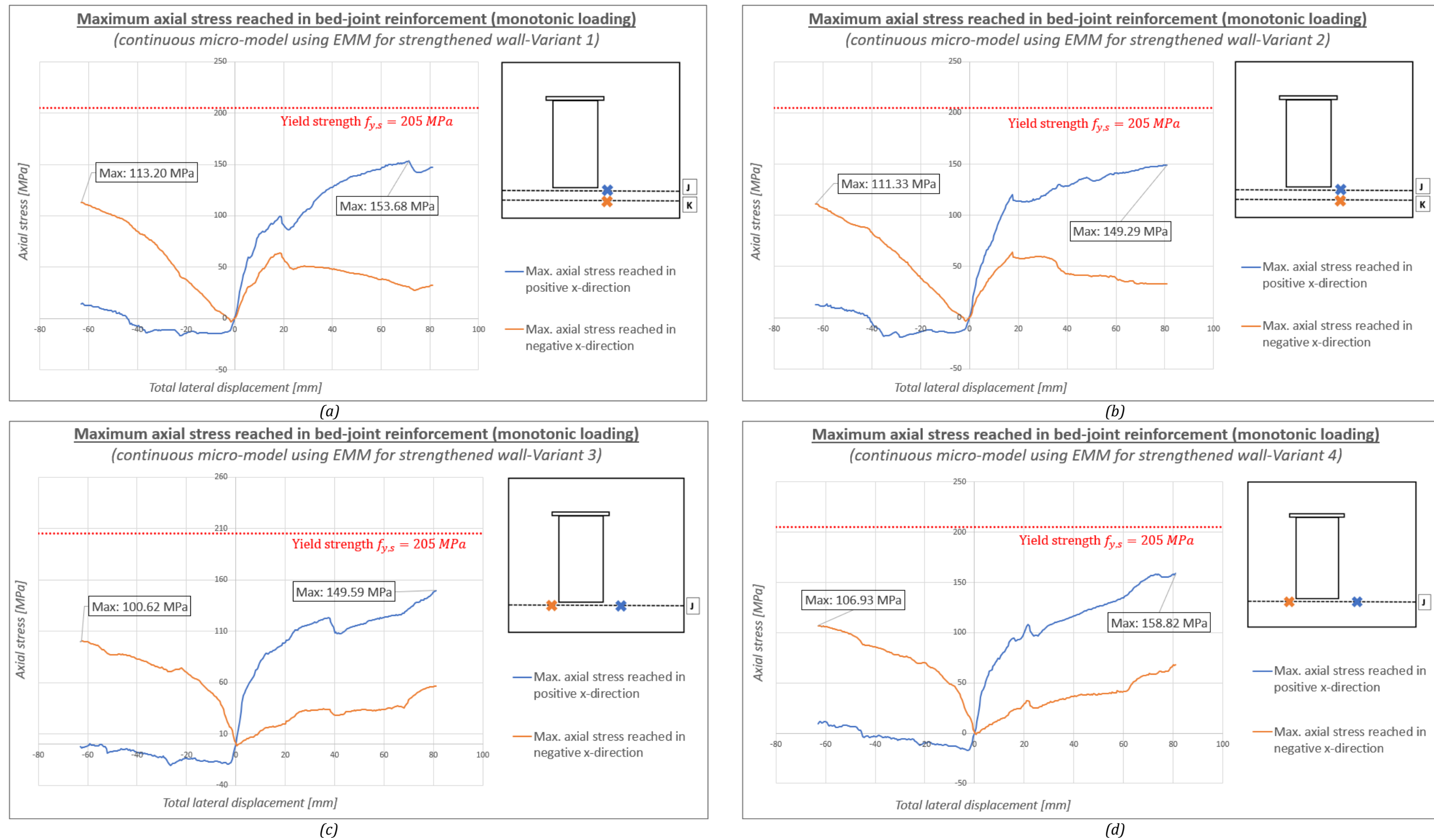

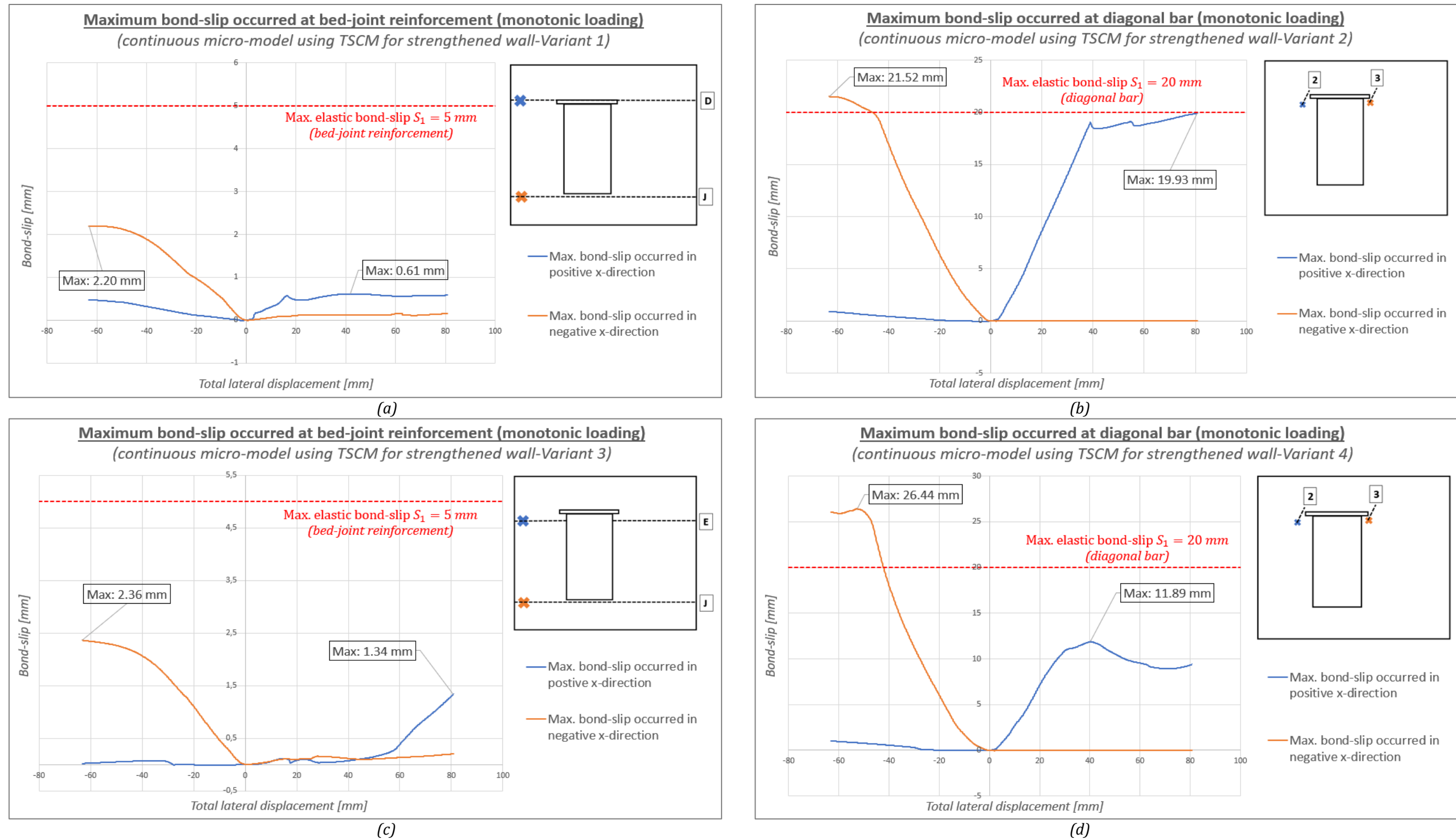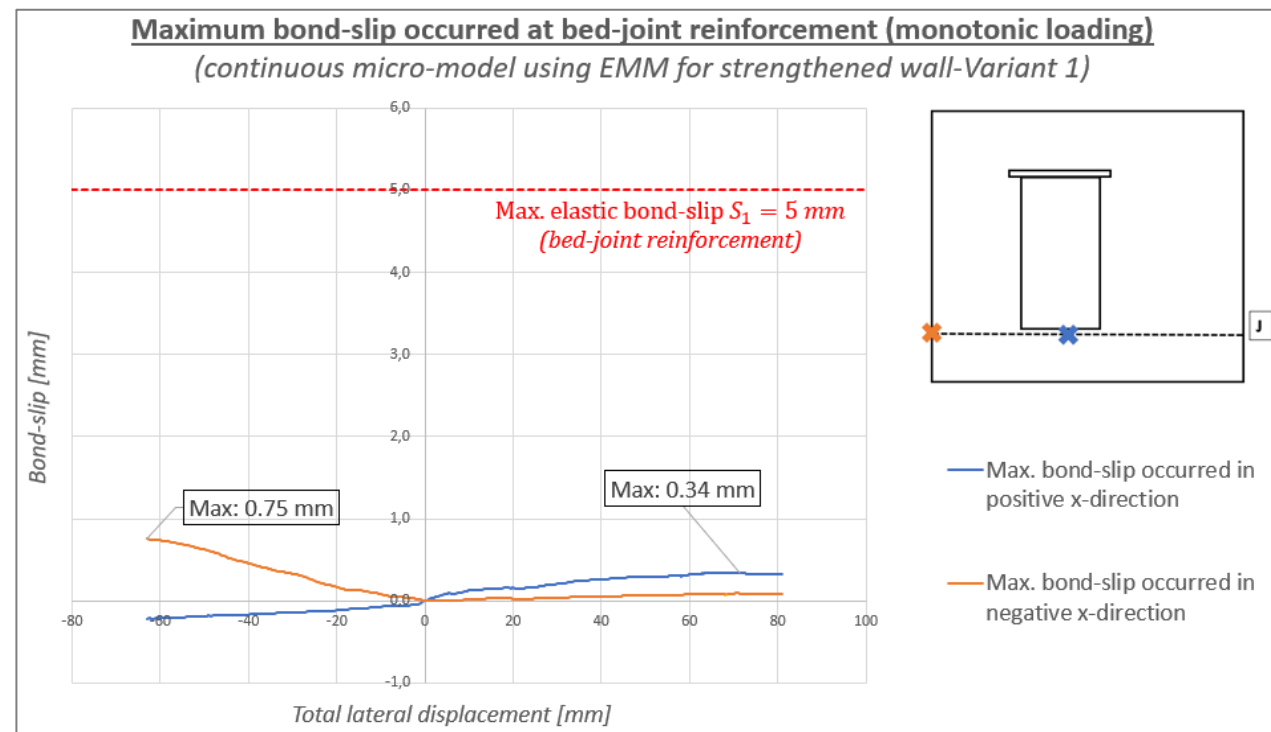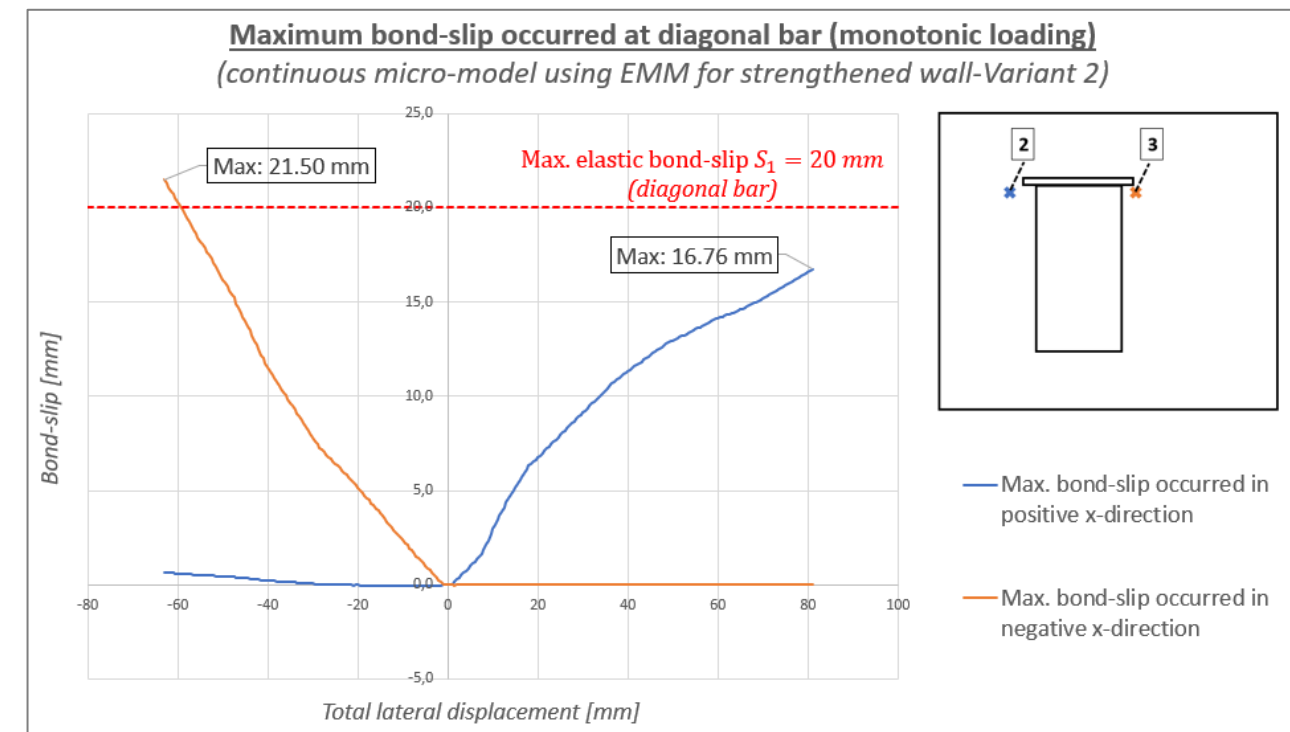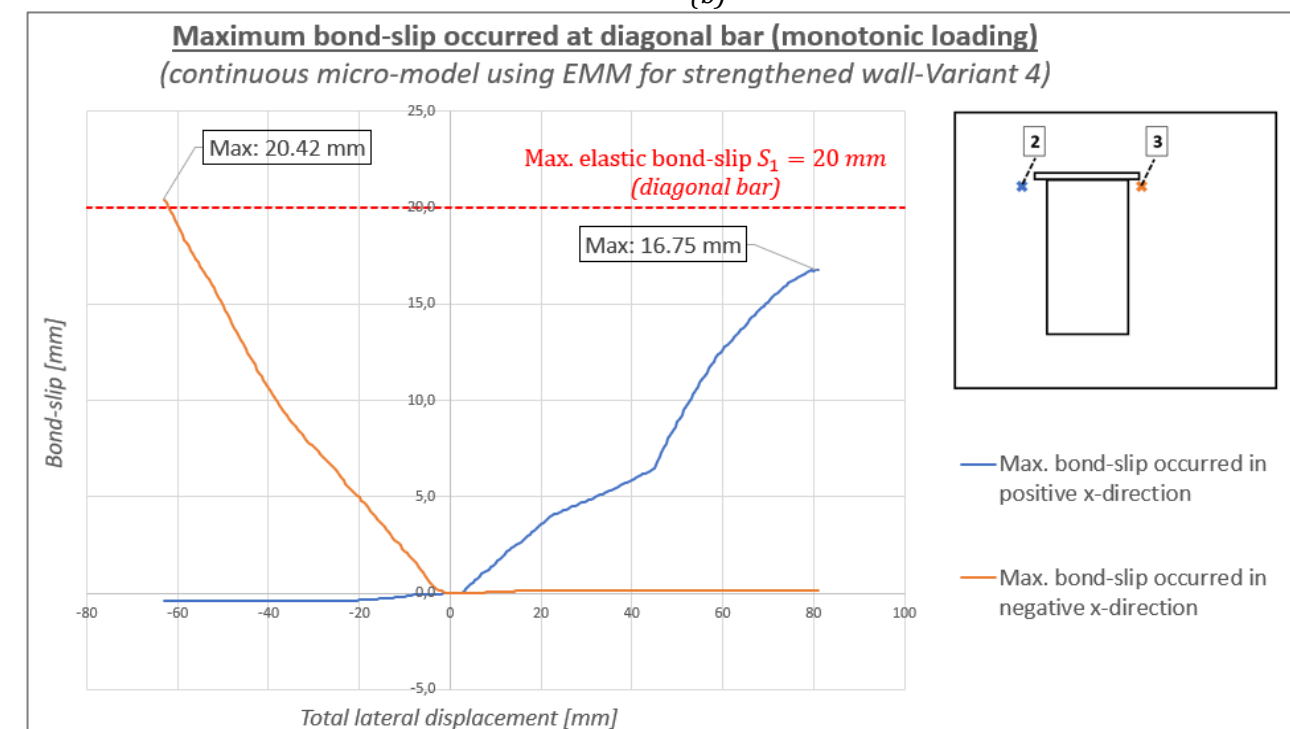*Figure E 1: Axial stress development for strengthened wall using TSCM for monotonic analysis: (a) Variant 1; (b) Variant 2; (c) Variant 3; (d) Variant 4*

Axial stress development in bed-joint reinforcement for all strengthened wall variants

*(monotonic analysis for continuous micro-model using **EMM** for mortar joints)*

Figure E 2: Axial stress development for strengthened wall using EMM for monotonic analysis: (a) Variant 1; (b) Variant 2; (c) Variant 3; (d) Variant 4

Bond-slip development in reinforcement for all strengthened wall variants

*(monotonic analysis for continuous micro-model using **TSCM** for mortar joints)*

Figure E 3: Bond-slip development for strengthened wall using TSCM for monotonic analysis: (a) Variant 1; (b) Variant 2; (c) Variant 3; (d) Variant 4

Bond-slip development in reinforcement for all strengthened wall variants

*(monotonic analysis for continuous micro-model using **EMM** for mortar joints)*
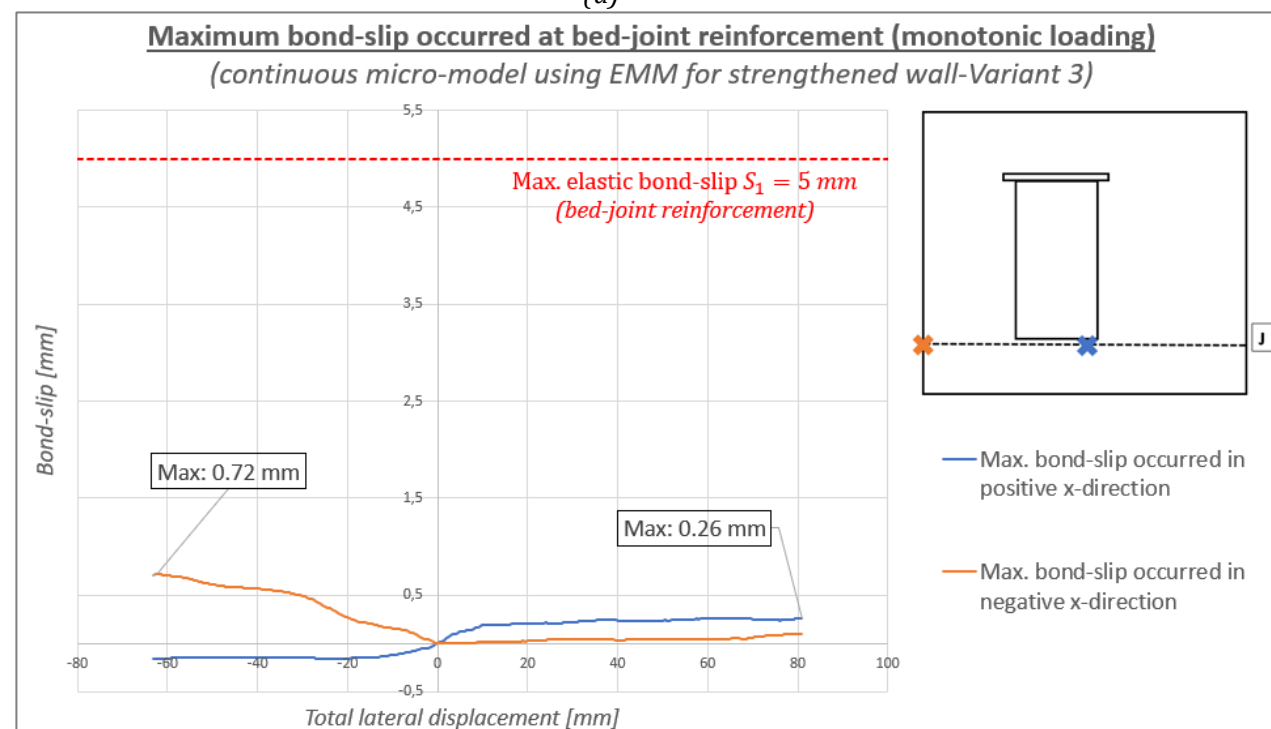
Figure E 4: Bond-slip development for strengthened wall using EMM for monotonic analysis: (a) Variant 1; (b) Variant 2; (c) Variant 3; (d) Variant 4

F

Results parametric study

Appendix F is meant as a supplement to Chapter 6 and provides additional results for all other configurations of the parametric study with the continuous micro-model using the *Total Strain Crack model (TSCM)* for the mortar joints. The maximum occurred axial stress in each row of reinforcement are presented in *Figure F 1*, *Figure F 2*, *Figure F 3* for Group 1, Group 2 and Group 3, respectively. Moreover, the axial stress and bond-slip development at the maximum occurred location in the wall are presented in *Figure F 4*, *Figure F 5*, *Figure F 6* for Group 1, Group 2 and Group 3, respectively.

Maximum axial stress occurred in each row of reinforcement with value and location indicated for Group 1

(monotonic analyses up to Near Collapse state for strengthened continuous micro-model using TSCM for mortar joints)
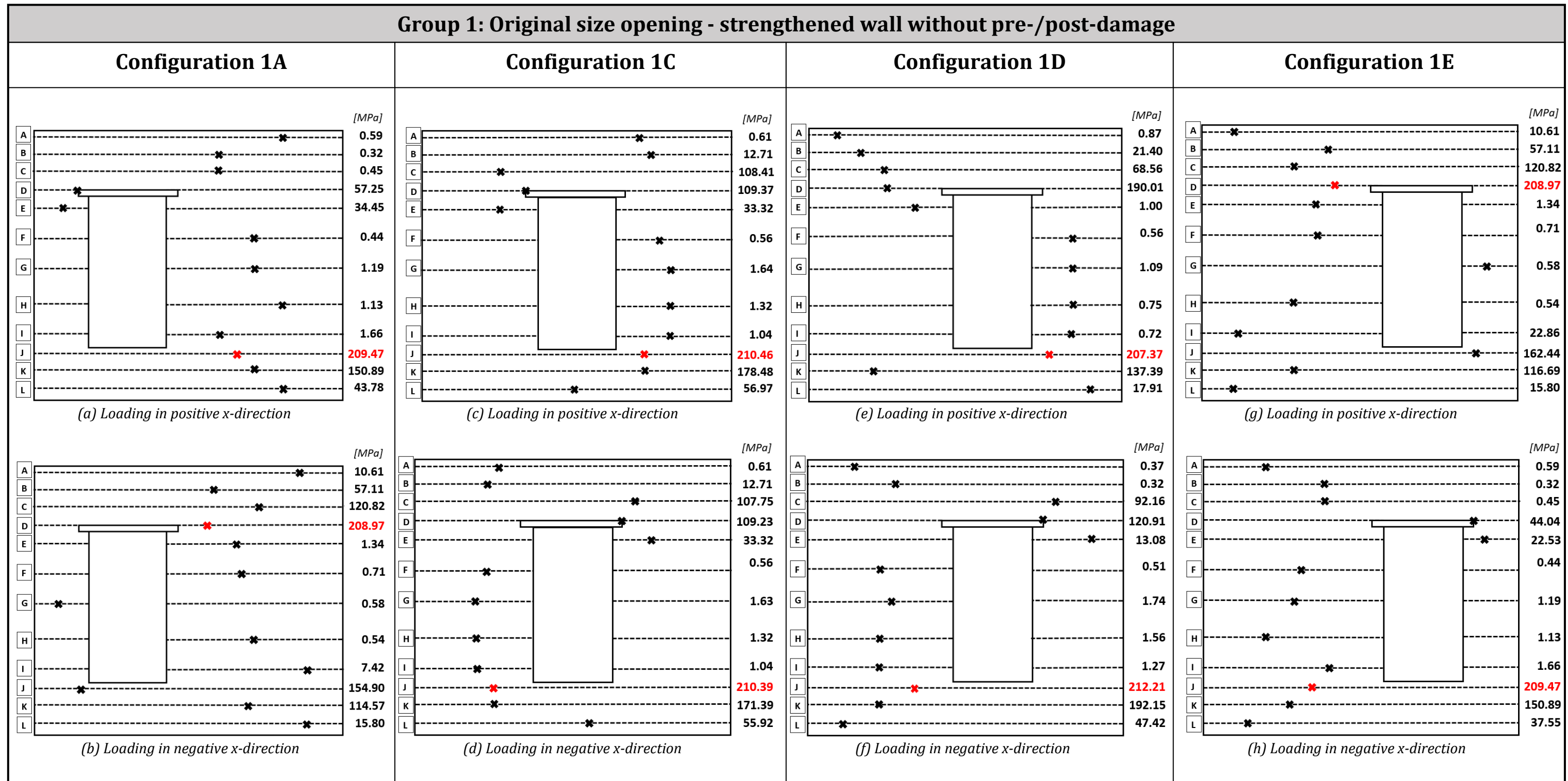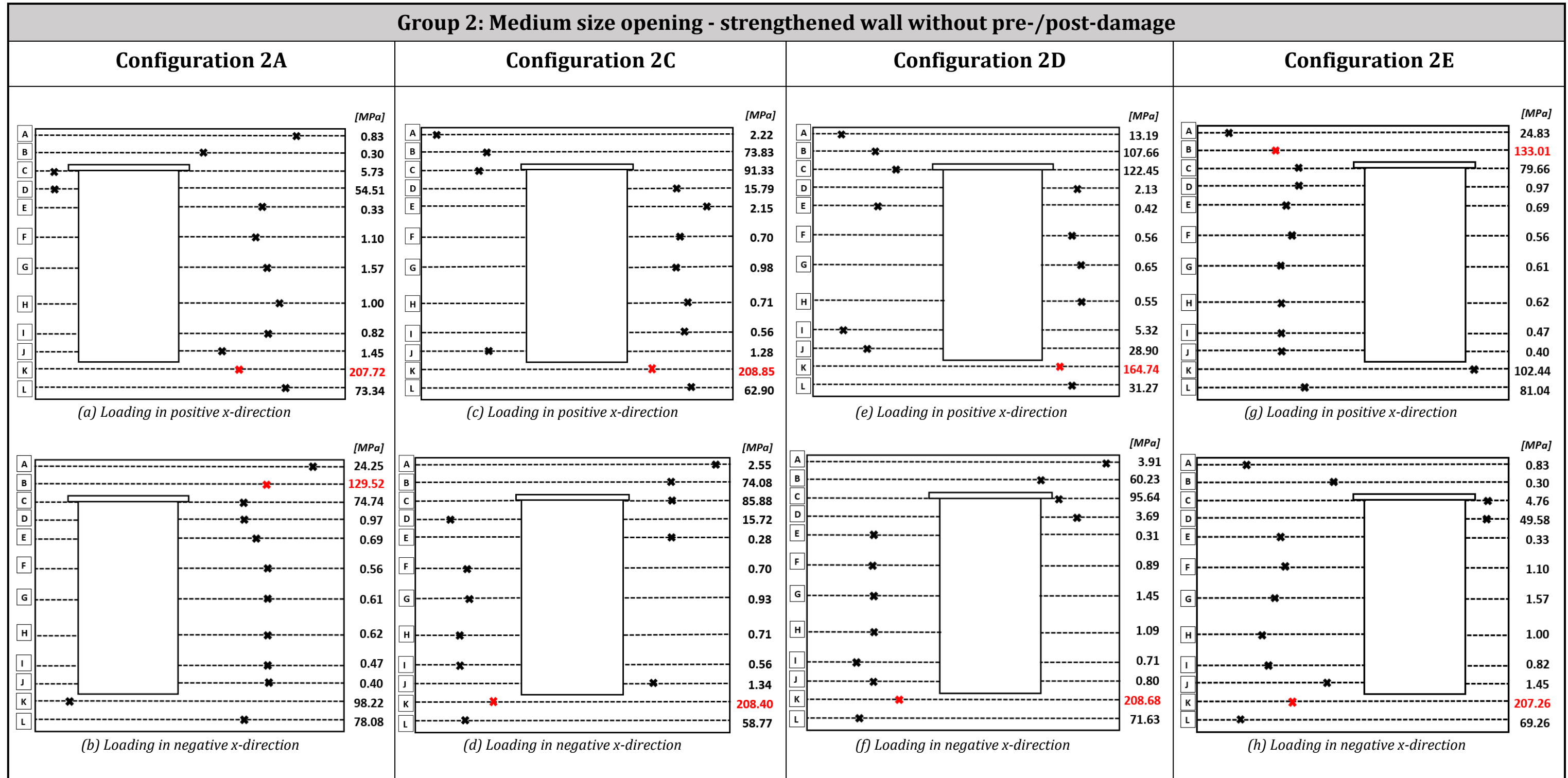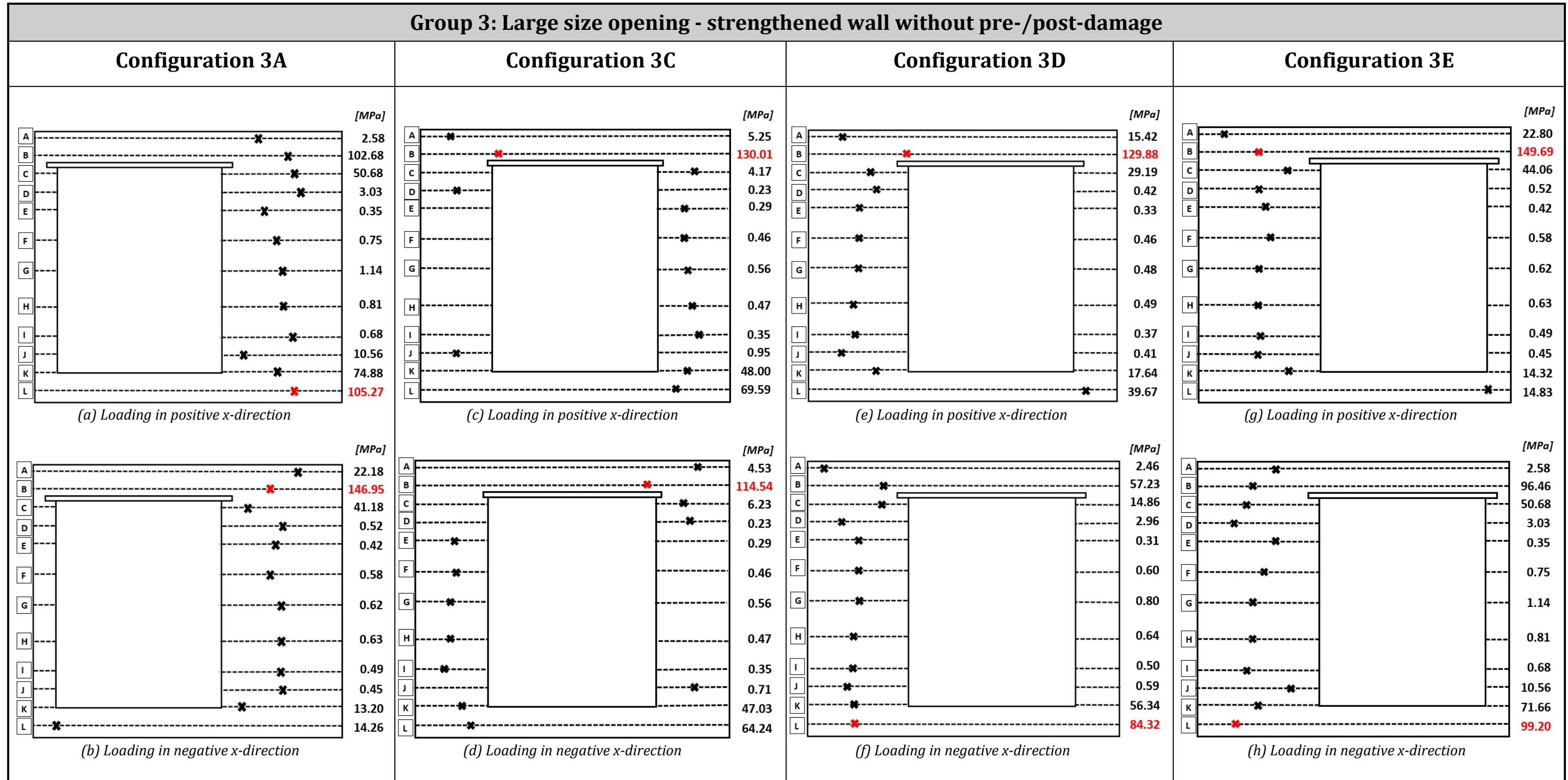

Figure F 1: Maximum axial stress occurred in each row of reinforcement for configurations of Group 1

Maximum axial stress occurred in each row of reinforcement with value and location indicated for Group 2

(monotonic analyses up to Near Collapse state for strengthened continuous micro-model using TSCM for mortar joints)

Figure F 2: Maximum axial stress occurred in each row of reinforcement for configurations of Group 2

Maximum axial stress occurred in each row of reinforcement with value and location indicated for Group 3

(monotonic analyses up to Near Collapse state for strengthened continuous micro-model using TSCM for mortar joints)

Group 3: Large size opening - strengthened wall without pre-/post-damage

| Configuration 3A | Configuration 3C | Configuration 3D | Configuration 3E |

Figure F 3: Maximum axial stress occurred in each row of reinforcement for configurations of Group 3
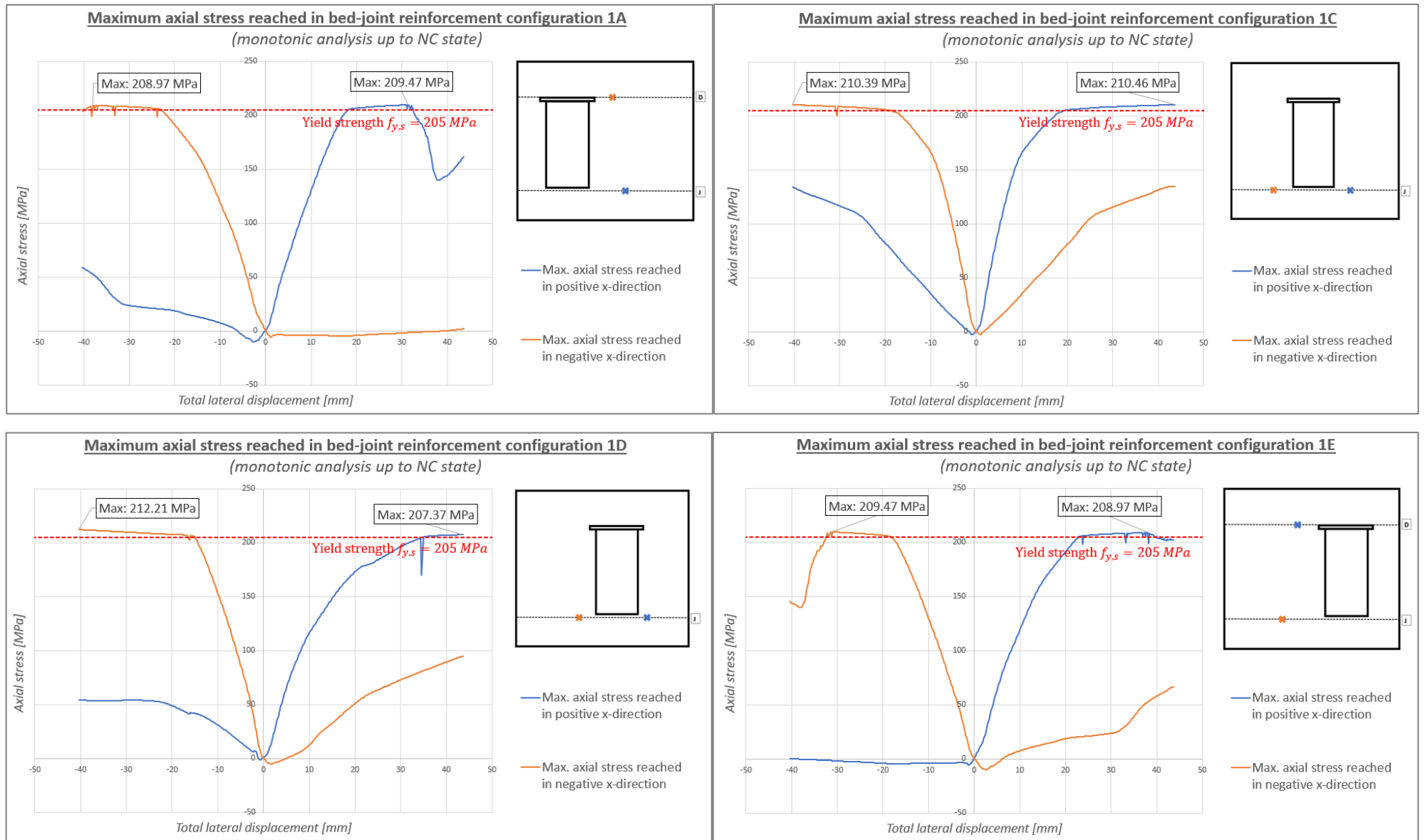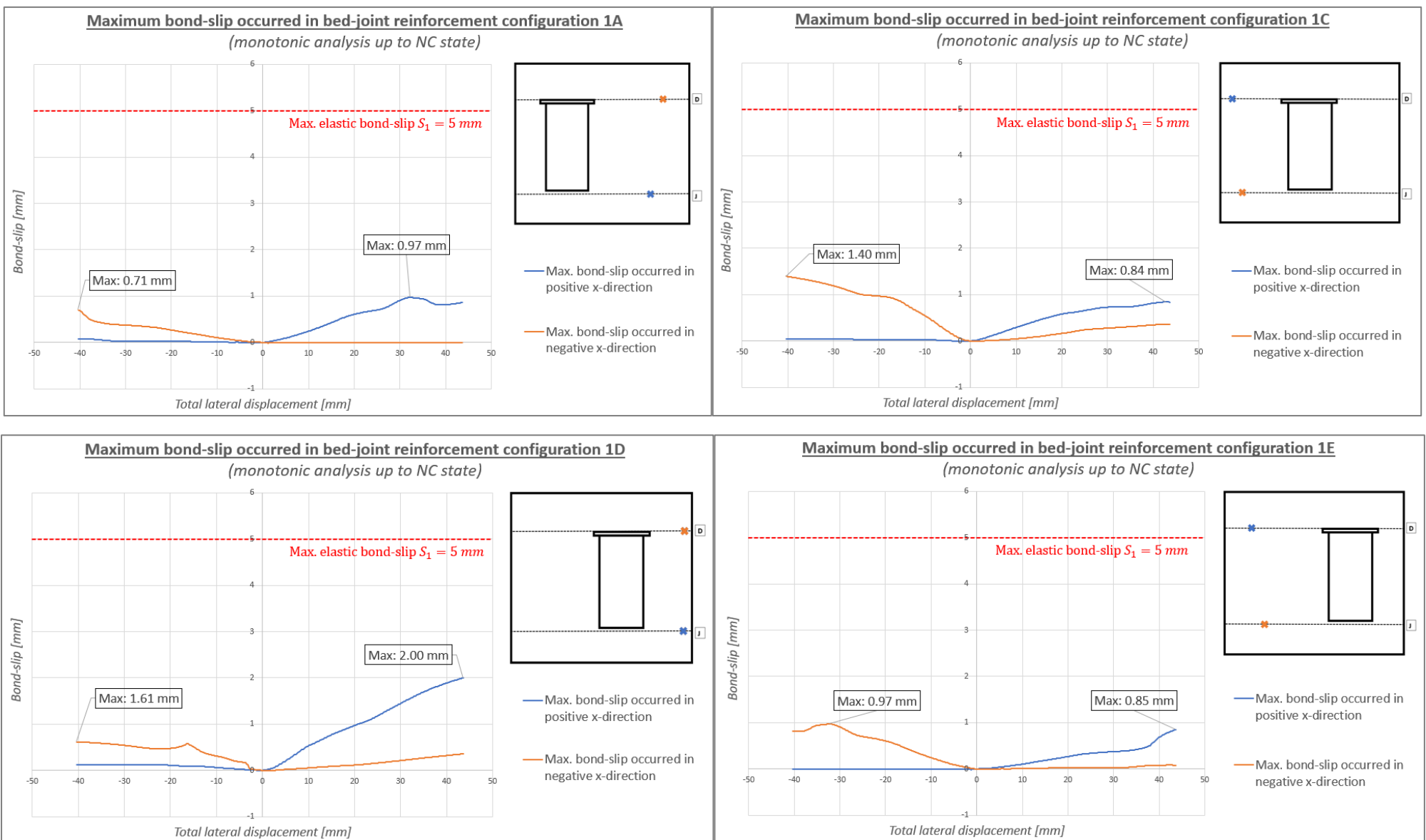
Figure F 4: Axial stress & bond-slip development in bed-joint reinforcement at maximum locations for configurations of Group 1

Axial stress development in bed-joint reinforcement for configurations of Group 2
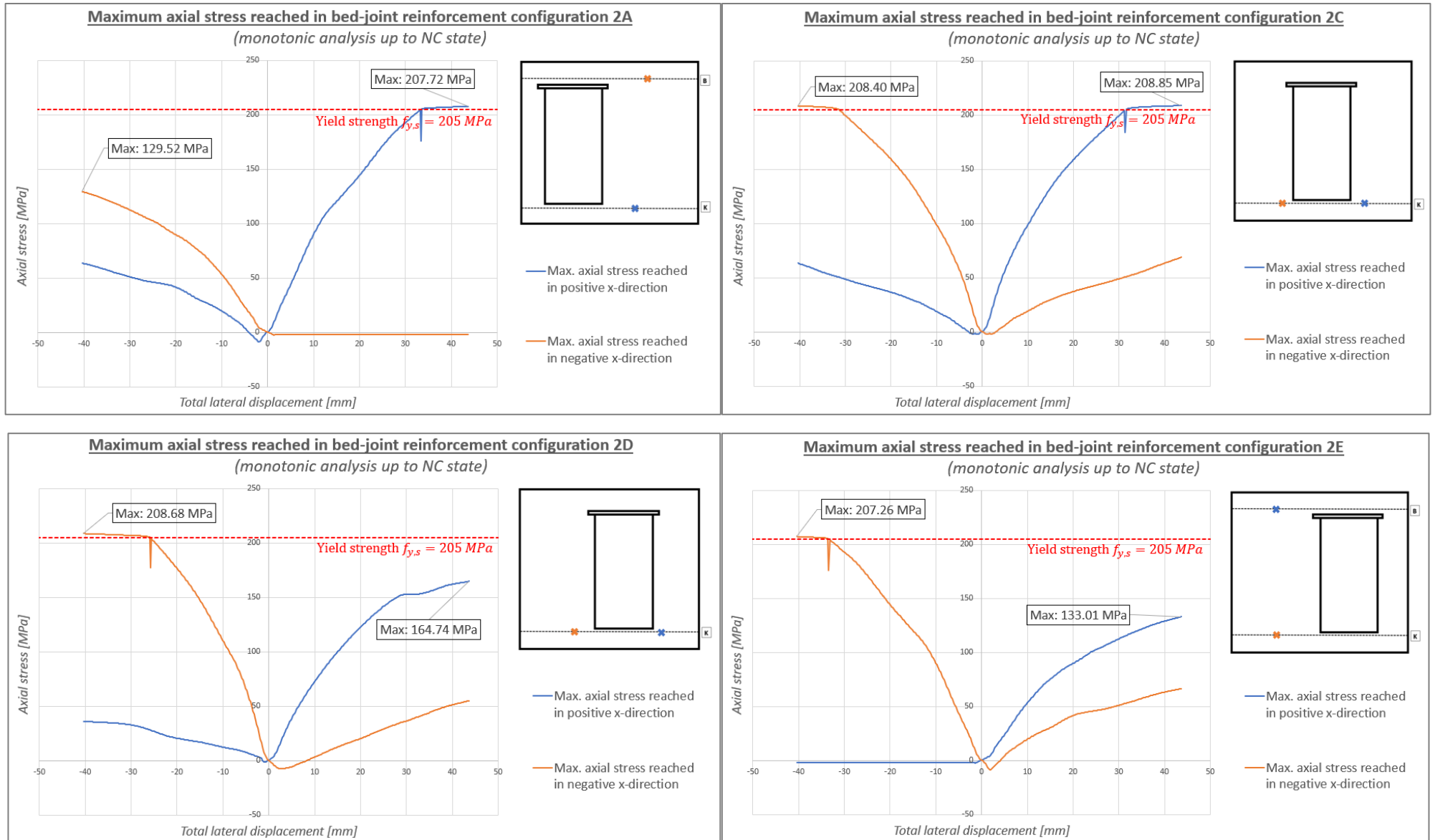
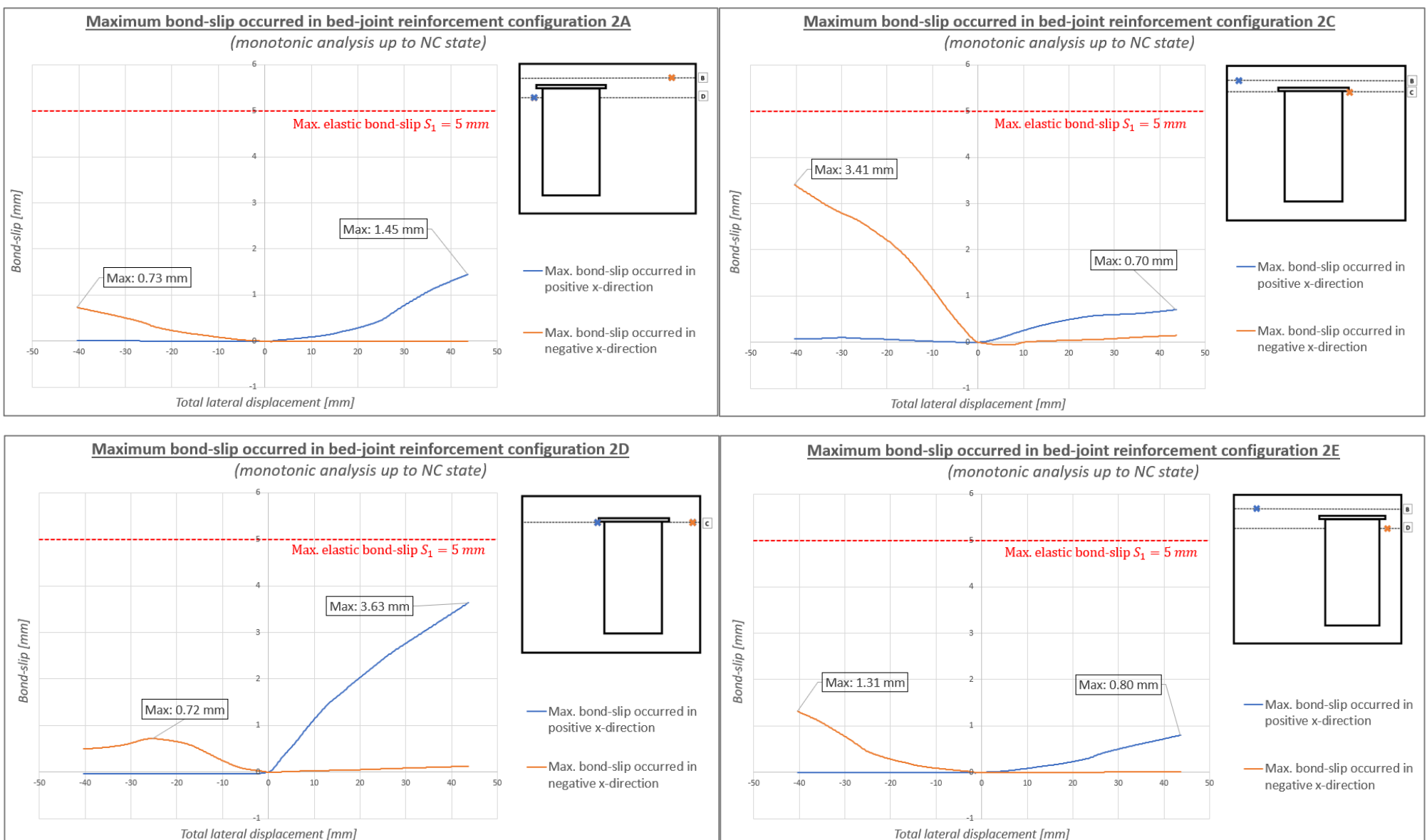## Bond-slip development in bed-joint reinforcement for configurations of Group 2
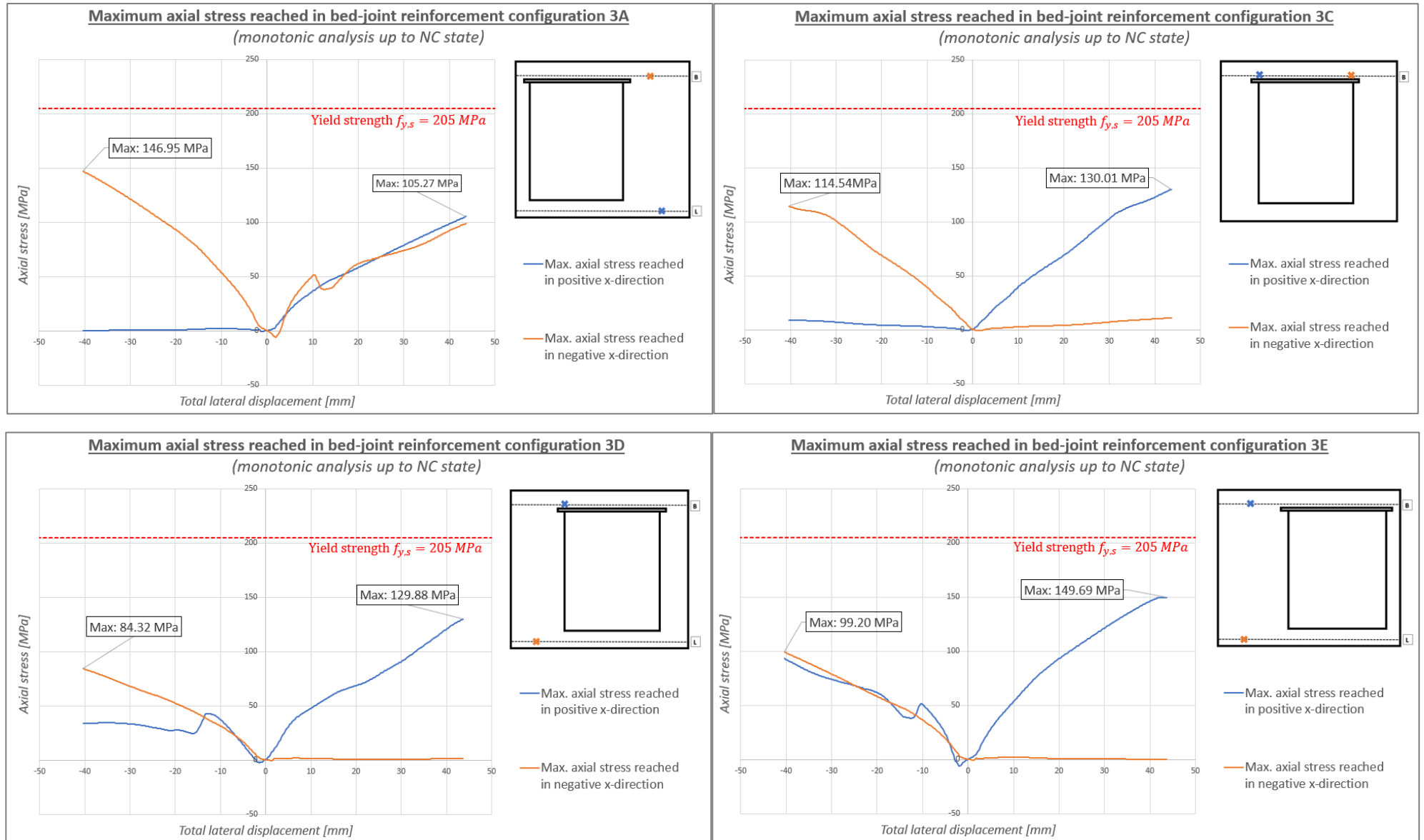

Figure F 5: Axial stress & bond-slip development in bed-joint reinforcement at maximum locations for configurations of Group 2

Axial stress development in bed-joint reinforcement for configurations of Group 3

Bond-slip development in bed-joint reinforcement for configurations of Group 3
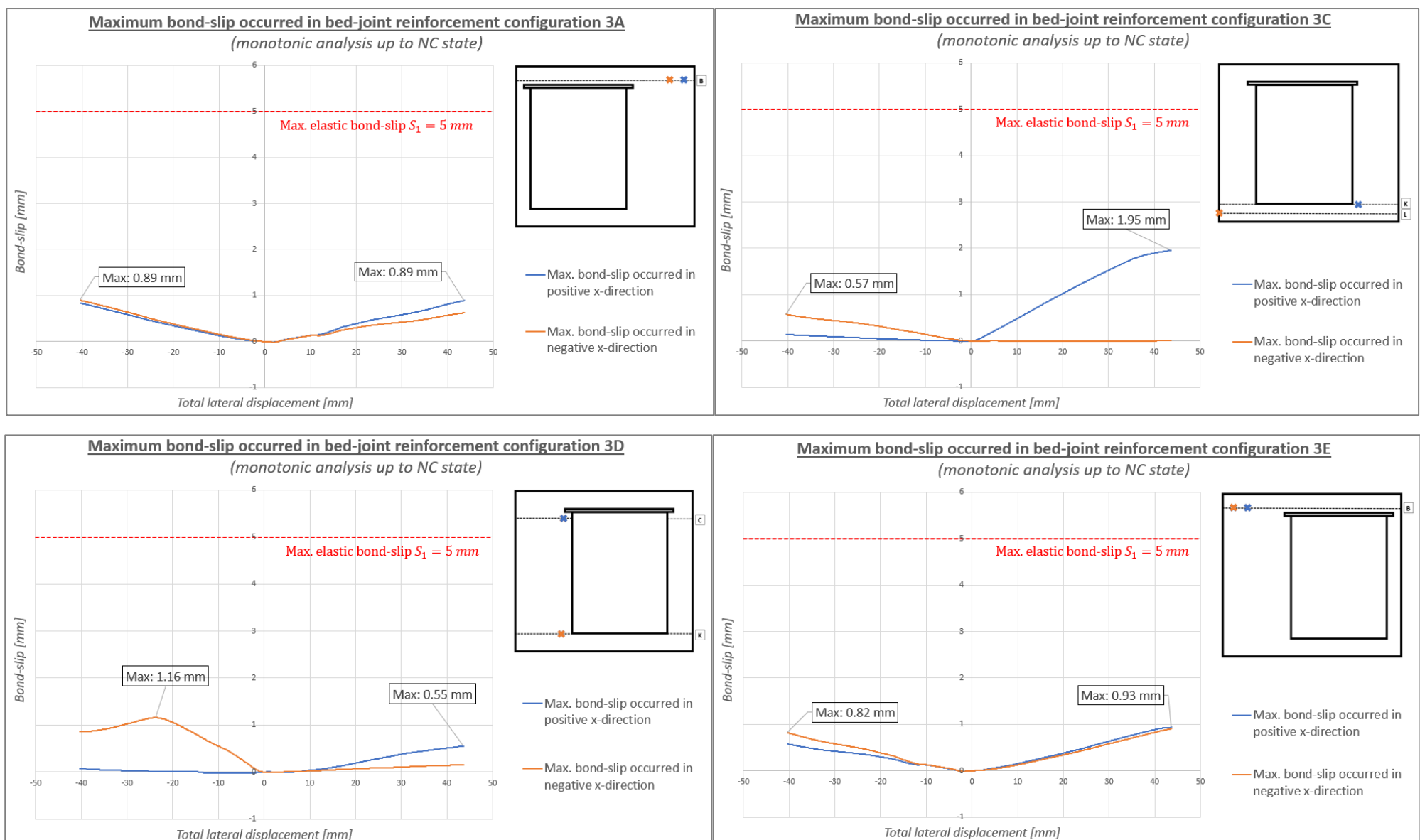

Figure F 6: Axial stress & bond-slip development in bed-joint reinforcement at maximum locations for configurations of Group 3